Atmospheric monitoring of the CH4 emissions at the European scale

Barbara Szenasi

To cite this version:

Barbara Szenasi. Atmospheric monitoring of the CH4 emissions at the European scale. Other. Université Paris-Saclay, 2020. English. NNT : 2020UPASJ006 . tel-03263871

Atmospheric monitoring of methane emissions at the European scale

Surveillance atmosphérique des émissions de méthane en Europe

Thèse de doctorat de l'université Paris-Saclay

École doctorale n° 129, Sciences de l'environnement d'Ile-de-France (SEIF)
Spécialité de doctorat: Météorologie, océanographie, physique de l'environnement
Unité de recherche: Université Paris-Saclay, CNRS, CEA, UVSQ, Laboratoire des sciences du climat et de l'environnement, 91191, Gif-sur-Yvette, France
Référent: Université de Versailles-Saint-Quentin-en-Yvelines

Thèse présentée et soutenue à Paris-Saclay, le 17 décembre 2020, par

Barbara SZÉNÁSI

Composition du jury:

M. Matthieu Roy-Barman *Professeur des universités, LSCE*	*Président*
M. Martijn Schaap *Professeur, FU Berlin*	*Rapporteur & Examinateur*
Mme. Martina Schmidt *Directrice de recherche, Heidelberg University*	*Rapportrice & Examinatrice*
M. Dominik Brunner *Professeur, Empa*	*Examinateur*
M. Hugo Denier van der Gon *Directeur de recherche, TNO*	*Examinateur*

Direction de la thèse:

M. Philippe Bousquet *Professeur, LSCE*	*Directeur de thèse*
Mme. Isabelle Pison *Directrice de recherche, LSCE*	*Co-directrice de thèse*
M. Grégoire Broquet *Directeur de recherche, LSCE*	*Coencadrant*
M. Antoine Berchet *Directeur de recherche, LSCE*	*Invité*
Mme. Rona Thompson *Directrice de recherche, NILU*	*Invitée*

Thèse de doctorat

NNT: 2020UPASJ006

Acknowledgements

Firstly, I would like to express my gratitude to Isabelle, Philippe, Antoine and Grégoire for supervising my PhD. Isabelle and Philippe, thank you for your trust in me and my capabilities, and for giving me the right amount of guidance and freedom to grow both scientifically and personally. The three years of my PhD were not always filled with excitement and happiness, and your support meant a lot to me. Antoine, thank you for always finding time for me and my questions. I have learnt a lot from you and your constructive advice helped me progress in my work. Grégoire, thank you for the valuable discussions and for making sure I stayed on track. I have improved through your supportive as well as critical suggestions. I thank you all for patiently reading the manuscript and providing me valuable feedback.

I would like to thank Marielle for advising me at the beginning of my PhD. Thank you also to Diego and Matthew for helping me getting started with CHIMERE. I am grateful to my colleagues at LSCE, especially the colleagues in the lunch and coffee groups for making my workdays livelier.

Maarten and Hugo, thank you for taking part in my thesis committee throughout the years and encouraging me to view ideas from a different perspective. I am also thankful to you for helping me in critical times. I would like to thank Martina Schmidt, Martijn Schaap, Dominik Brunner, Matthieu Roy-Barman, Rona Thompson and Hugo Denier van der Gon for accepting to be part of my PhD defence committee.

I would like to acknowledge the MEMO^2 project for making this PhD thesis possible. I enjoyed being part of as an exciting project as MEMO^2 with so many excellent scientists. I am grateful to colleagues at TNO, the Wageningen University and Utrecht University for welcoming and supporting me during my secondments. The time spent with my fellow PhD students during MEMO^2 meetings and secondments made my PhD even more fun.

I thank all my friends for their moral support throughout the years, even when I was too busy with my thesis to be a proper friend. Sara and Sophie, thank you for bringing rainbows and unicorns into my days.

Finally, I thank my family for their constant love and support that kept me motivated over the years. I am grateful to my fiancé, Enrico, for being there for me. You always made me smile when I needed it the most.

Contents

Chapter 1

Introduction

The climate of the Earth is primarily controlled by the global radiation balance. The radiation balance comprises of the incoming short-wave solar radiation and the outgoing long-wave solar radiation (Figure 1.1). The energy from incoming short-wave radiation is 340 W m^{-2} and about 30% of it is reflected back to space by the atmosphere, clouds and the surface. The rest of the radiation is absorbed by the surface (161 W m^{-2}) and the atmosphere. The energy absorbed by the surface is re-emitted by the Earth as long-wave radiation (397 W m^{-2}). A portion of this energy is emitted to space (239 W m^{-2}) and some of it (342 W m^{-2}) is absorbed by the gases in the atmosphere and scattered back to the surface as long-wave counter-radiation. This is known as the greenhouse effect. Together with the latent and sensible heat fluxes, it ensures that the average surface temperature is warmer (15° Celsius) and livable than it would be without this natural greenhouse effect (-18° Celsius). Atmospheric gases responsible for the greenhouse effect are called greenhouse gases (GHGs). These include water vapour (H_2O), carbon dioxide (CO_2), methane (CH_4), tropospheric ozone (O_3) and nitrous oxide (N_2O), which occur naturally in the atmosphere.

The incoming and outgoing radiation must be in balance in order to maintain the natural greenhouse effect and the energy balance of the Earth. The net change in the energy balance due to some perturbations is known as radiative forcing (IPCC, 2013). When the radiative forcing is positive, the incoming energy is greater than the outgoing energy, causing a warming of the Earth's atmosphere. Conversely, when a negative radiative forcing occurs, i.e. the incoming energy is smaller than the outgoing energy, the atmosphere will cool. In order to track the changes in radiative forcing, the era before the First Industrial Revolution, i.e. prior 1750, is set to a radiative forcing of zero. In 2011, the global radiative forcing was approximately 2.29 W m^{-2} (IPCC, 2013), which leads to a warming of the atmosphere compared to the pre-industrial era. This phenomenon is referred to as global warming or climate change. The current global surface temperature rise due to this additional forcing has been recently estimated as approximately 1° Celsius above pre-industrial levels by Intergovernmental Panel on Climate Change (IPCC) in their Special Report "Global Warming of 1.5 ° Celsius" (IPCC, 2018).

The global radiative forcing rise is caused by an increase of greenhouse gas emissions. This increase is due to human activities (IPCC, 2013) emitting GHGs additional to naturally occurring ones, which leads to higher atmospheric mixing ratios. The so caused energy imbalance affects not only the temperature but also the atmospheric and oceanic circulations, glacier mass balance, plant productivity and evaporation (e.g. Mercado et al., 2009; Ohmura et al., 2007; Allsopp et al., 2009). Limiting the causes of the temperature rise through mitigation efforts, the energy imbalance of the Earth could be reduced and climate change slowed down.

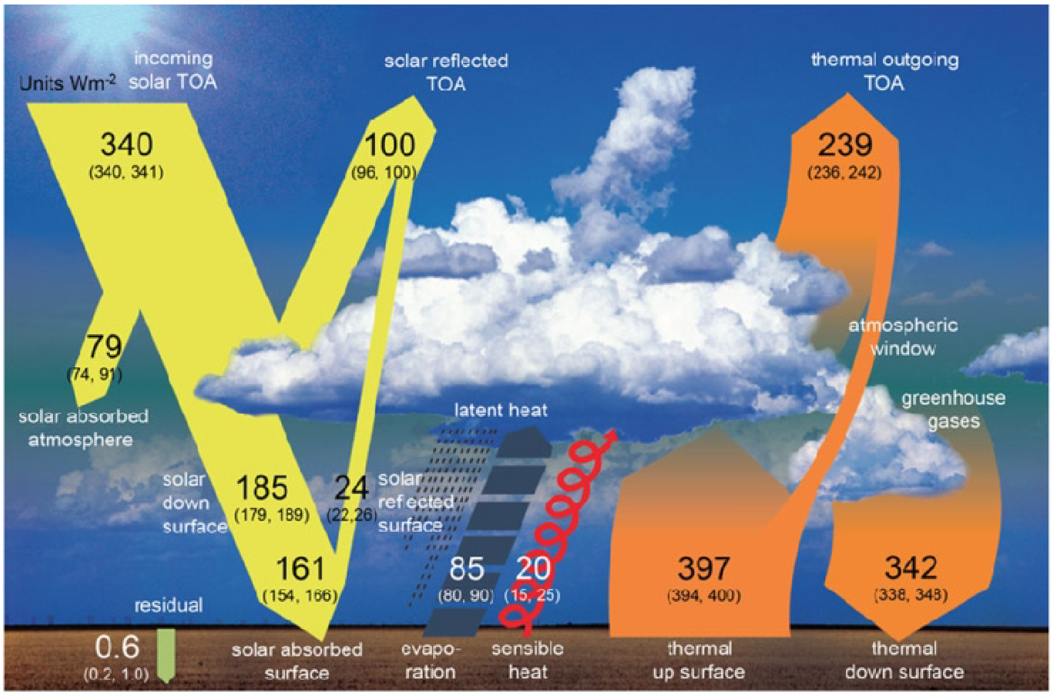

Figure 1.1: The global radiation balance of the Earth. The numbers indicate the energy flow in W m^{-2}. Source: Wild et al. (2012).

1.1 Importance of methane

A metric often used to assess the importance of a GHG in terms of radiative forcing is the global warming potential (GWP). It quantifies the global warming impact of a gas by indicating the amount of energy added by a gas over a given period of time relative to that added by the reference gas CO_2 (IPCC, 2014). Accordingly, the GWP of CO_2 is 1. CH_4 has a GWP of 28 over a period of 100 years (IPCC, 2014), meaning that the radiative forcing added by an emission of 1 ton of CH_4 is equivalent to that of an emission of 28 ton of CO_2. This makes CH_4 the second most radiatively important well-mixed anthropogenic GHG (CO_2, CH_4, N_2O and halocarbons) after CO_2. The atmospheric mixing ratio of CH_4 has increased since 1750 by 150%, resulting in a global average of 1803 ppb (parts per billion) in 2011. Between 1999 and 2006, the CH_4 mixing ratio was in a near stable state with a global average of about 1775 ppb in 2006 (Nisbet et al., 2019). Since 2007, the CH_4 mixing ratio has continued to rapidly rise with a rate of approximately 8 ppb per year and reached a global average of 1876 ppb in March 2020 (Figure 1.2). Although CO_2 has received most of the scientific attention in the last decades due to its large abundance in the atmosphere and high radiative forcing of about 1.5 W m^{-2} (in 2011; IPCC, 2013), CH_4 alone has contributed by 0.97 W m^{-2} to the total radiative forcing increase of 2.29 W m^{-2} for 2011 (IPCC, 2013).

The Paris Agreement is a global climate change agreement that aims to combat climate change by limiting the global temperature rise by the end of this century to below 2 °C compared to pre-industrial times. If CH_4 emissions follow the current trajectory of rapid increase to 2100, the global average of CH_4 mixing ratios is expected to reach approximately 2400 ppb (Nisbet et al., 2019). It would be the equivalent of about 3 °C temperature increase at the global scale, compared to pre-industrial times. This threatens the ambitions set in the Paris Agreement and requires quick action. Since methane is a relatively short-lived GHG with a lifetime of about 8-10 years (e.g. Saunois et al., 2020), it is a good target for climate change mitigation. A reduction or stabilisation of CH_4 emissions is beneficial for reaching short-term mitigation objectives as it can result in a relatively quick reduction or stabilisation of atmospheric CH_4 mixing ratios and thus of its radiative forcing.

CH_4 is a GHG that also affects air quality. For example, tropospheric near-surface oxidation of CH_4, when nitrogen oxides (NO_x) are present, produces

O_3. Ground-level O_3 influences air quality and is harmful for human health (Zhang et al., 2019). Hence, knowing and controlling CH_4 emissions would benefit the efforts in reducing tropospheric O_3 mixing ratios (Fiore et al., 2008).

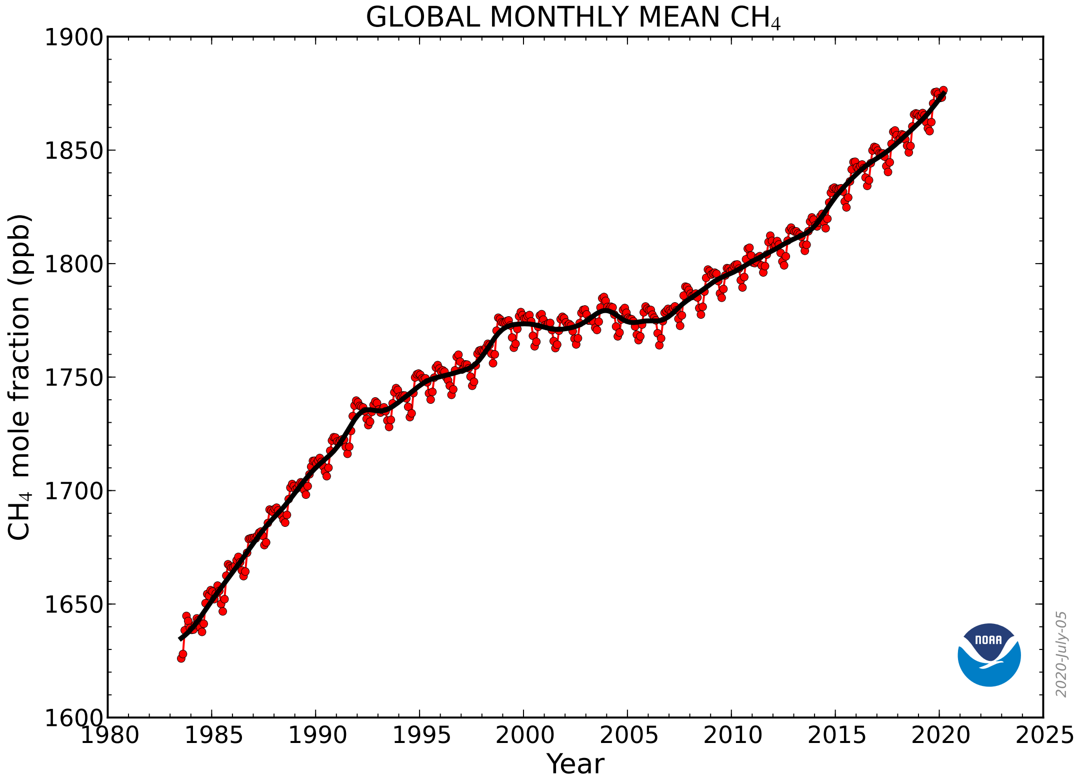

Figure 1.2: Global monthly average atmospheric methane abundance [ppb] from 1983 to 2020. The average mixing ratio is derived from marine surface sites of the Global Monitoring Division of NOAA-ESRL (National Oceanic and Atmospheric-Earth System Research Laboratory). Source: Dlugokencky, `www.esrl.noaa.gov/gmd/ccgg/trends_ch4/`

1.2 Methane budget

1.2.1 Sources and sinks

1.2.1.1 Global scale

Methane emissions are related to anthropogenic activities and natural sources. Anthropogenic sources include domestic ruminants, waste water, landfills, fossil fuels, burning of agricultural waste, biofuels from agricultural residues and rice paddies. They represent about 60% of the total global CH_4 emissions (Saunois et al., 2020). Natural sources of CH_4 are wetlands and other continental water systems (e.g. lakes, rivers), termites, biomass burning (wildfires), thawing permafrost and geological sources (such as gas and oils seeps, mud volcanoes).

Depending on their origin, the sources can be divided in three categories: microbial, thermogenic and pyrogenic.

- Microbial CH_4 is produced from organic matter by anaerobic archaea when no oxygen is available. The main anthropogenic microbial source is farming, e.g. through the application of manure, and the enteric fermentation of cattle and other ruminants. Other origins include rice paddies and wastewater treatment. Microbial CH_4 is also emitted by natural wetlands (e.g. swamps, peatlands).
- Thermogenic CH_4 is generated from the breakdown of organic matter at high temperatures and pressures. Geological gas seeps are the main source of thermogenic CH_4. Anthropogenic origins of thermogenic CH_4 include the extraction, production and distribution of fossil fuels that are associated with oil industry, coal mining and leakage of gas.
- Pyrogenic CH_4 is formed by incomplete combustion of biomass, e.g. wildfires, domestic wood burning, burning of agricultural waste and fossil fuels. Biomass burning is partly a natural source of CH_4 but is nowadays mainly human induced.

Recent estimates of methane emissions at the global scale were derived by Saunois et al. (2020) for the period 2008-2017. Following their study, the global CH_4 emissions for the studied decade are about 576 $TgCH_4$ yr^{-1}, of which 359 $TgCH_4$ yr^{-1} are of anthropogenic origin. Fossil fuel production and use is the largest global source of CH_4 that accounts for approximately 35% of the total anthropogenic CH_4 sources. Agriculture and waste sources together make up for 217 $TgCH_4$ yr^{-1} (60%) of the total anthropogenic emissions. Biomass burning is a mixed source of anthropogenic and natural sources and are estimated to be about 30 $TgCH_4$ yr^{-1}. The largest natural source of CH_4 is wetlands with emissions of 181 $TgCH_4$ yr^{-1}. Other natural sources, such as geological emissions and termites, are responsible for approximately 37 $TgCH_4$ yr^{-1} in the period 2008-2017.

The main sink of tropospheric CH_4, representing about 90% of the total sinks (Ehhalt, 1974), is the hydroxyl radical (OH) that is a highly reactive species. OH is generated by the photolysis of O_3 when water vapour is available. CH_4 oxidises through the reaction with OH in the presence of sunlight, resulting in water and CO_2. OH is responsible for the removal of about 500 $TgCH_4$ yr^{-1} (Kirschke et al., 2013). Saunois et al. (2020) estimated this loss to be approximately 553 $TgCH_4$ yr^{-1} for the period 2000-2009. Minor CH_4 sinks include photo-chemistry of CH_4 in the stratosphere, oxidation by chlorine radicals, consumption by methanotrophic bacteria in soils and photo-chemical destruction by the reaction with chlorine in the stratosphere and troposphere.

Our current understanding of the different CH_4 sources and sinks is incomplete due to the high uncertainty associated to their magnitude and spatio-temporal distribution. Based on different studies, the descriptions of the evolution of sources and sinks and hence their current global abundance are contradictory. Some studies hypothesise that the reason for the increase of atmospheric CH_4 mixing ratios after the near stability in the early 2000s is the increase of fossil emissions (Hausmann et al., 2016; Helmig et al., 2016). Other studies found that microbial sources have increased. For example, Schaefer et al. (2016) and Patra et al. (2016) suggest that increased agricultural activities are the reason behind the rise. Bousquet et al. (2011) proposed the increase of emissions from natural wetlands due to large positive anomalies of precipitation in the tropics and of temperature in high latitudes for the period 2006-2008. Nisbet et al. (2016) found a similar reason for the renewed growth of CH_4 mixing ratio and depletion of the heavy carbon isotopologue of CH_4. Their study suggests unusual meteorological conditions in the tropics led to a rise of natural wetland and agriculture emissions. The study of Saunois et al. (2017) supports these findings as their results of a top-down model ensemble indicate that about 80% of the renewed CH_4 growth is due to an emission increase in the tropics.

In addition to uncertainties in the CH_4 sources, there are large uncertainties in the sink processes. The lifetime and seasonal cycle of CH_4 is determined by the loss via radicals, primarily OH, in the troposphere. CH_4 loss is derived from estimates of tropospheric mixing ratios of OH. The lifetime of CH_4 is estimated as the total amount of CH_4 divided by the removal rate of OH (Holmes, 2018). Due to the very short lifetime of approximately 1 s of OH, it is difficult to estimate it from direct measurements. Thus, a common method for estimating OH mixing ratio is to use measurements of methyl chloroform since its main sink is OH in the troposphere and is often used as proxy for OH (e.g. Montzka et al., 2011) as its emissions and mixing ratios are assumed to be well known. Hence, OH mixing ratios are derived from measurements of methyl chloroform. Another common practice for determining the loss of atmospheric CH_4 is by atmospheric chemistry modelling (Naik et al., 2013). However, both the indirect estimation from methyl chloroform and the modelling bear uncertainties due to the high spatial and temporal variability of OH. In turn, it makes the CH_4 lifetime uncertain: 11.2 ± 1.3 years estimated for 2010 by Prather et al. (2012).

1.2.1.2 European scale

It is beneficial to study atmospheric CH_4 at the regional and sector scales to help reduce uncertainties of methane emission estimates of the various sources at the global scale. Europe offers good opportunities to more thoroughly study CH_4 emissions. It is equipped with dense monitoring networks, e.g. the Integrated Carbon Observation System (ICOS) and the Integrated non-CO2 Greenhouse gas Observing System (InGOS), and has received increasing attention for the preparation of anthropogenic emission inventories, such as the TNO-MACC (Kuenen et al., 2014), CAMS-REG emission inventories (Granier et al., 2012) and Emissions Database for Global Atmospheric Research (EDGAR) (Janssens-Maenhout et al., 2017). Therefore, Europe is chosen as the study domain of this thesis.

In the European Union (EU), emissions of CH_4 contributed to 11% of the total GHG emissions in 2018 (EEA, 2020). About 80% of CH_4 is emitted by anthropogenic sources, while natural sources account for about 20% of the total CH_4 emissions in Europe (Saunois et al., 2016a,b). The report of EEA (2020) estimated the total anthropogenic CH_4 emissions to be approximately 18 Tg in 2018 for the EU-27, Iceland and the UK (EEA, 2020, Figure 1.3). The main microbial source is connected to agricultural activities, which make up to 50% of the total anthropogenic CH_4 emissions in the EU in 2018. Emissions from landfills, waste water treatment and discharge account for 22% of the total anthropogenic CH_4 emissions. The primary natural microbial source of CH_4 in the EU is wetlands. Thermogenic methane sources, such as fossil fuel handling, represent about 11% of the total anthropogenic CH_4 emissions in the EU in 2018. Pyrogenic sources have only a small contribution (under 4%) to the total CH_4 emissions in the EU in 2018.

However, studies focusing on the European CH_4 budget have estimated CH_4 emissions to be larger than suggested by the EEA (2020). For example, Bergamaschi et al. (2018) estimated approximately 27 $TgCH_4yr^{-1}$ total CH_4 emissions for the EU-27 and the UK for the period 2006-2012, while the emission estimate according to EEA (2020) for 2012 is approximately 19 Tg. This demonstrates the need for more reliable CH_4 emission estimation methods.

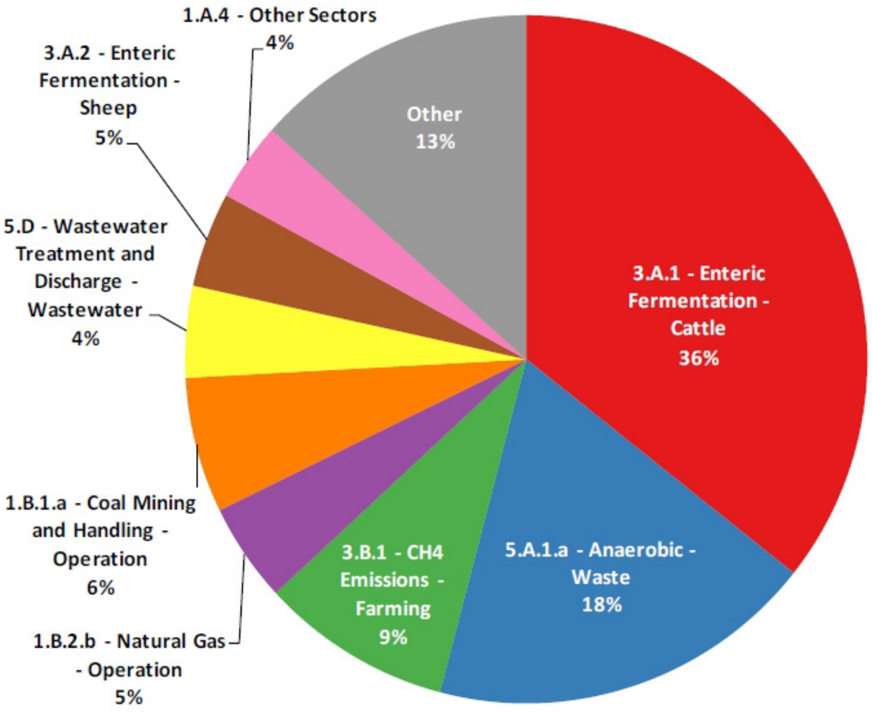

Figure 1.3: Contribution of the main methane emissions by source category in the EU in 2018. Source: EEA (2020)

1.2.2 Isotopic composition

Types of CH_4 sources can be distinguished in the above mentioned three categories (microbial, thermogenic, pyrogenic) through their isotopic contents. The stable isotope contents of CH_4 are ^{12}C, ^{13}C, ^{1}H (protium) and ^{2}H (deuterium). The isotope ratio R is the relative abundance of two isotopes of the same element. The carbon isotope ratio ^{13}R is defined as ^{13}C/^{12}C and the hydrogen isotope ratio ^{2}R is written as ^{2}H/^{1}H. The ratios provide information about the processes involved in the CH_4 formation. In general, the more heat is involved in the CH_4 formation, the more enriched it is in heavier isotopes (^{13}C, ^{2}H). For this reason, pyrogenic sources, e.g. wood burning, produce CH_4 containing more heavy isotopes and CH_4 of microbial origin is depleted in the heavier isotopes. Isotopic differences between samples are quantified by the relative difference of isotope ratios of a sample compared to an internationally recognised standard reference and denoted as delta (δ) with a unit of per mil (‰). The relative difference of the carbon isotope ratio of CH_4 is δ^{13}C-CH_4:

$$\delta^{13}C\text{-}CH_4 = \frac{\frac{^{13}C}{^{12}C}_{sample}}{\frac{^{13}C}{^{12}C}_{standard}} - 1 \tag{1.1}$$

where *standard* is the Vienna Peedee Belemnite VPDB=11180.2 ± 2.8 × 10^{-6} (Werner and Brand, 2001).

The relative difference of the hydrogen isotope ratio of CH_4 is δ^2H-CH_4:

$$\delta D\text{-}CH_4 = \frac{\frac{^2H}{^1H}_{sample}}{\frac{^2H}{^1H}_{standard}} - 1 \tag{1.2}$$

with the *standard* being the Vienna Standard Mean Ocean Water with a value of VSMOW=155.76 ± 0.08 × 10^{-6} (Werner and Brand, 2001).

In the following, the term "relative difference of isotope ratio" will be shortened to "isotope ratio" or "δ value". For clarity, whenever the isotope ratio R is described, the notations ^{13}R and ^{2}R will be used. The term "isotopic source signature" will be referred to when characterising typical δ values of an emission source.

The global mean δ^{13}C in ambient air is -47.1‰ (Rigby et al., 2012) and typical δ^{13}C values per source type are as follows (Sherwood et al., 2017):

- Microbial sources: -74.4‰ to -45.5‰
- Thermogenic sources: -87.0‰ to -14.8‰
- Pyrogenic sources: -32.4‰ to -12.5‰

However, more common global δ^{13}C values for the main European source types are (based on Whiticar, 1999; Szénási and Bousquet, 2019):

- Microbial sources:
  - Agriculture: -70.6‰ to -46.0‰
  - Waste: -73.9‰ to -45.5‰
  - Wetland: -88.9‰ to -51.5‰
- Thermogenic sources:
  - Fossil fuels: -66.4‰ to -20.0‰

The global mean δ^2H in ambient air is -86‰ (Rigby et al., 2012) and typical δ^2H values per source type span the following ranges (Sherwood et al., 2017):

- Microbial sources: -442‰ to -281‰
- Thermogenic sources: -415‰ to -62‰
- Pyrogenic sources: -232‰ to -195‰

Prevalent global δ^2H values for the main European source types cover a narrower range (based on Whiticar, 1999; Szénási and Bousquet, 2019):

- Microbial sources:
  - Agriculture: -361‰ to -295‰
  - Waste: -312‰ to -293‰

  - Wetland: -358‰ to -246‰
- Thermogenic sources:
  - Fossil fuels: -275‰ to -100‰

The above mentioned ranges of δ^{13}C and δ^{2}H are illustrated in Figure 1.4. The global average of δ^{13}C and δ^{2}H in ambient air depends on the δ^{13}C and δ^{2}H emitted from sources and lost to sinks (Quay et al., 1999). The δ^{13}C and δ^{2}H isotopic signatures during CH_4 reaction with OH are about -5.4 $\pm$ 0.9‰ (Cantrell et al., 1990) and -231 $\pm$ 45‰ (Gierczak et al., 1997), respectively. Thus, the global average of δ^{13}C and δ^{2}H in ambient air is more enriched in heavier isotopes than the various CH_4 sources. Since the typical values of isotopic signatures vary depending on the source type, stable isotope contents are beneficial for discriminating between emission sources and for a better understanding of the spatial source distribution. Isotopic measurements of CH_4 can be especially useful when they are available for periods of multiple years to among others analyse seasonal effects and inter-annual variability of CH_4 sources.

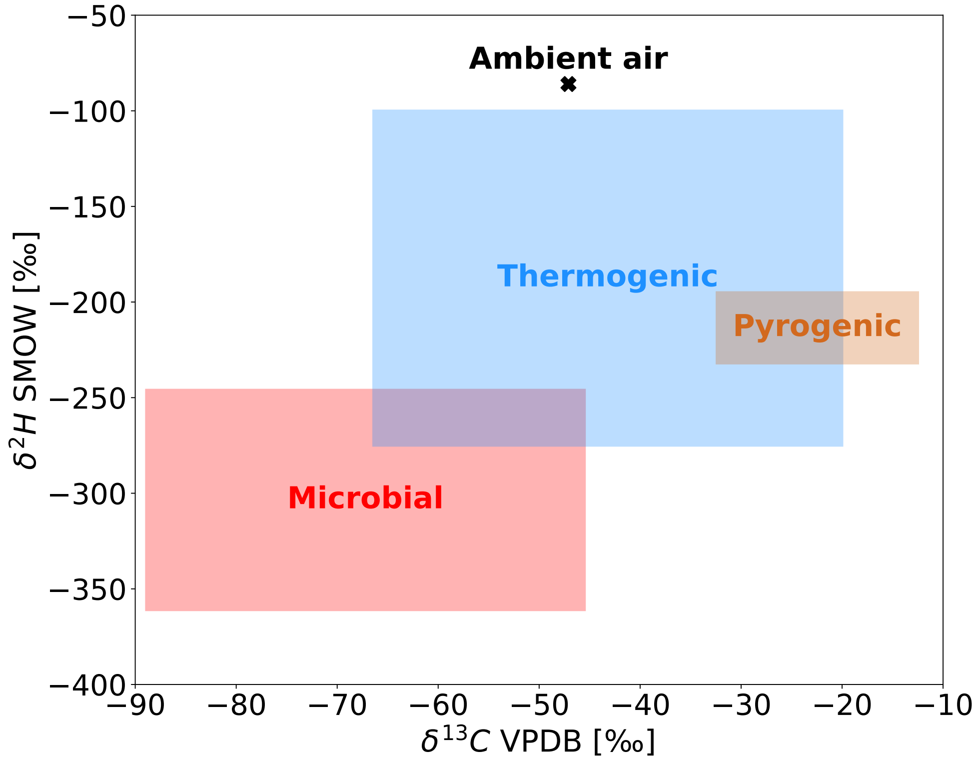

Figure 1.4: Ranges of δ^{13}C and δ^{2}H isotopic source signatures per main European source type: red=microbial, blue=thermogenic (fossil fuels), orange=pyrogenic. The global mean value of ambient air is marked by a black cross. The δ^{13}C and δ^{2}H values used here are taken from Rigby et al. (2012); Whiticar (1999); Szénási and Bousquet (2019).

1.3 Measurements of atmospheric methane

1.3.1 Methane mixing ratios

Measurements of atmospheric composition offer opportunities to better understand surface emissions of trace gases. For methane, measurements of atmospheric CH_4 mixing ratio began at multiple locations in America in 1978 (Blake et al., 1982) in order to monitor its trend. The National Oceanic and Atmospheric Administration, Earth System Research Laboratory, Global Monitoring Division (NOAA/ESRL/GMD) has monitored CH_4 mixing ratios globally since 1983 (Dlugokencky et al., 1994). Nowadays, there are several measurement networks at the global scale. In Europe, ICOS is such a network. The coverage of the ICOS network is illustrated in Figure 1.5a, which includes monitoring sites that are already part of ICOS (green), as well as sites currently being in the labelling process (orange) to become part of the ICOS network. The mission of such measurement networks is to monitor the atmospheric transport and long-term trends of atmospheric mixing ratios of GHGs. This helps detect sources and sinks and enables research to understand the evolution of GHGs. The information provided on GHGs by measurement networks supports emission mitigation strategies to combat climate change and its impacts.

Surface and low atmospheric mixing ratios of atmospheric CH_4 are typically measured by flask sampling and in-situ instruments. Mixing ratios in air sampled in flasks is examined in laboratory using gas chromatography with flame ionisation detection. Such measurements are normally performed every few weeks and allow the interpretation of the inter-hemispheric gradient, trends and seasonal cycle. In-situ instruments, such as cavity ring-down spectroscopy, have the advantage that measurements are carried out on a long-term basis at surface sites. Mobile instruments are often deployed on aircrafts or ships to obtain quasi-continuous data sets. On top of the assets of flask samples, in-situ measurements can be used for monitoring the diurnal cycle and synoptic variations.

In order to study the distribution between the various sources of methane, several methods have been used. For example, measurements of ethane are often used as a tracer for estimating CH_4 emitted by the fossil fuel sector as ethane is co-emitted with CH_4 from oil and gas sources (Franco et al., 2016). Similarly, CO is usually co-emitted with CH_4 from biomass burning and can therefore be used as a tracer of CH_4 originating from biomass burning (Gaubert et al., 2017). Another, effective tool to distinguish CH_4 sources is isotopic information (e.g. Townsend-Small et al., 2016; Fisher et al., 2017).

Atmospheric mixing ratios of methane are also monitored by infrared sensors onboard satellites. Satellites provide a near-global spatial coverage and thus an advantage to obtain information about GHGs in regions with inadequate coverage by ground-based networks. However, satellite observations still bear substantial uncertainties in the derived mixing ratios. Therefore, ground-based measurements are often preferred for studying atmospheric CH_4.

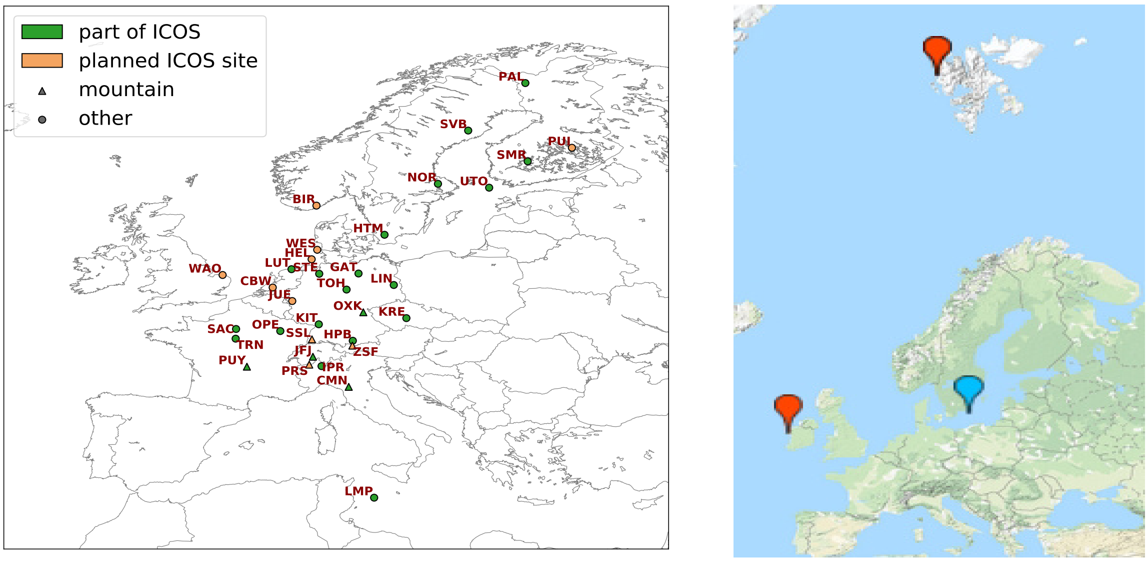

(a) CH_4 mixing ratios - ICOS **(b)** Isotopic composition

Figure 1.5: Coverage of the European network ICOS (**a**) monitoring CH_4 mixing ratios, and sites monitoring the stable isotope content (**b**) of atmospheric CH_4. Source for isotopic composition map: `https://gaw.kishou.go.jp/search/station` (last accessed: 13-07-2020).

1.3.2 Stable isotopic composition of methane

As atmospheric isotope ratios are less abundant than CH_4, isotope measurements are complex and require more advanced techniques and higher precision than CH_4 mixing ratios. As a consequence, measurements of isotope compositions are scarce both globally and in Europe. There are only three sites monitoring $\delta^{13}C$ on a regular basis in Europe, and only one of them measures $\delta^{2}H$ (Figure 1.5b). However, continuous or quasi-continuous measurements of CH_4 isotopic composition have recently been carried out (Röckmann et al., 2016; Menoud et al., 2020b) and the number of such measurements should increase in future.

δ^{13}C and δ^{2}H in methane is usually collected in air flasks and analysed on a gas chromatography isotope ratio mass spectrometry (IRMS) or a continuous flow IRMS. As CH_4 cannot be analysed directly by these systems, CH_4 is isolated from the other air components and converted to CO_2 and H_2. Ambient air is pumped through a drying agent and cooled down. After that, the sample is heated to release CH_4 and then combusted to CO_2 and H_2 that enter the analyser. There, they are compared to a standard isotope ratio R.

To ensure the compatibility of atmospheric data, the WMO IAEA (World Meteorological Organization - International Atomic Energy Agency) set a target of ±2 ppb, 0.02‰ and 1‰ for CH_4 mixing ratio, δ^{13}C and δ^{2}H, respectively (WMO, 2018). These compatibility targets are for measurements of CH_4 in background air used in global models. For regionally focused studies, extended targets are defined as ±5 ppb, 0.2‰ and 5‰, respectively.

From the analysis of CH_4 measured in ambient air, average isotopic signatures of the various CH_4 sources can be identified. To do so, measurements of atmospheric δ^{13}C and δ^{2}H are usually carried out in a target area downwind from the location of interest. For this, methods such as the Keeling plot (Keeling, 1958; Pataki et al., 2003) and Miller-Tans plot (Miller and Tans, 2003) approach are used. In the Keeling plot approach (Figure 1.6), δ^{2}H or δ^{13}C are plotted against 1/CH_4 and a linear regression analysis is used to calculate the y-axis intercept and the corresponding uncertainty, while taking into account the uncertainties in the x- and y-axis variables. The y-axis intercept is the isotopic signature of the dominant CH_4 source above background, i.e. air containing lowest level of emissions.

The atmospheric mixing ratio of a substance consists of background mixing ratio and mixing ratio produced by a source:

$$c_a = c_b + c_S \tag{1.3}$$

with c_a being the measured atmospheric mixing ratio, c_b the background mixing ratio and c_S the mixing ratio of the source. Following Pataki et al. (2003), the δ^{13}C and δ^{2}H of the measured CH_4 can be written as:

$$\delta_a c_a = \delta_b c_b + \delta_S c_S \tag{1.4}$$

where δ_a and δ_b are the isotopic composition of the total measurement and the measured background, respectively and δ_S the isotopic signature of the source. To compute the source isotopic signature, the combination of Equa-

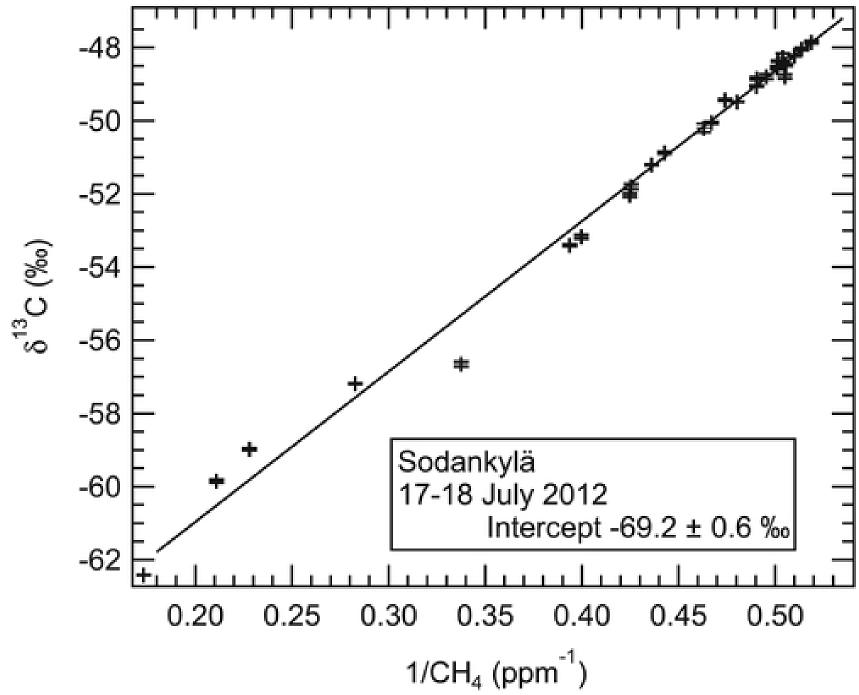

Figure 1.6: Example for a Keeling plot analysis to derive methane isotopic source signature, which is represented by the y-axis intercept of the Keeling plot. Source: Fisher et al. (2017)

tions 1.3 and 1.4 can be written as:

$$\delta_S = \delta_a - c_b(\delta_b - \delta_S)(1/c_a) \tag{1.5}$$

The Keeling analysis does not necessarily require that the CH_4 background mixing ratio and isotopic composition are known. The Miller-Tans analysis is based on the Keeling approach but has the advantage that variable background CH_4 mixing ratios can be applied (Figure 1.7): the background values can be constant or vary over time. In this method, the mixing ratio and isotopic composition of the background must be specified (Miller and Tans, 2003):

$$\delta_a c_a - \delta_b c_b = \delta_S(c_a - c_b) \tag{1.6}$$

The left side of Equation 1.6 is computed against $c_a - c_b$ on the right side of the equation in a linear regression analysis to obtain δ_S, the slope of the correlation between the two sides. The slope then represents the isotopic signature of the dominant source above background, while the uncertainties in the x- and y-axis variables are taken into account to determine the corresponding uncertainty of the isotopic source signature.

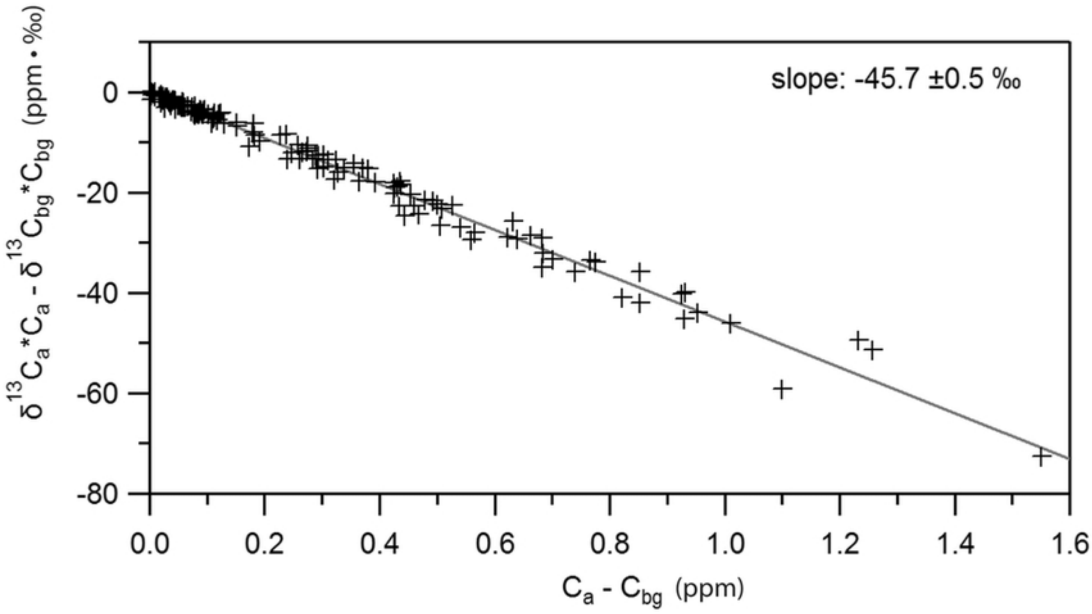

Figure 1.7: Example for a Miller-Tans plot analysis to derive methane isotopic source signature, which is represented by the slope of the Miller-Tans plot. Source: Zazzeri et al. (2017)

1.4 Modelling atmospheric methane

As atmospheric species, such as CH_4, cannot be measured everywhere frequently, their mixing ratios, as well as their spatial and temporal variability are often characterised with the aid of simulations performed by numerical chemistry-transport models (CTMs), which relate emissions to atmospheric mixing ratios. Limited-area Eulerian CTMs are well suited to study the regional scale and have been frequently used in such studies (e.g. Pison et al., 2018; Berchet et al., 2020; Denier van der Gon et al., 2015; Bergamaschi et al., 2018; Remaud et al., 2018; Locatelli et al., 2015; Timmermans et al., 2009). Hence, we choose to use a Eulerian CTM in this thesis and the main properties of such CTMs is described in this section. Eulerian CTMs simulate the transport through the discretisation of the advection-diffusion equation:

$$\frac{\delta c}{\delta t} = -u\frac{\delta c}{\delta x} + \frac{\delta}{\delta x}(K_x\frac{\delta c}{\delta x}) + E - L - D \tag{1.7}$$

where c is the mixing ratio at time t at location x, u the mean advective velocity over a given time period, K_x the turbulent diffusion coefficient, E emissions, L sinks and D deposition. The first term on the right side describes the advection process and the second term the turbulence. The advection-diffusion equation is solved on a three-dimensional grid for a given domain with parameterised subgrid-scale processes, such as convection and turbulence.

1.4.1 The chemistry-transport model CHIMERE

In this thesis, the chemistry-transport model CHIMERE is used to carry out simulations of atmospheric CH_4 mixing ratios and the atmospheric CH_4 isotope contents $\delta^{13}C$ and $\delta^{2}H$. CHIMERE is a three-dimensional Eulerian regional chemistry-transport model designed to simulate regional atmospheric mixing ratio of gas-phase and aerosol species (Menut et al., 2013; Mailler et al., 2017). For this work, CHIMERE is driven by the system PYVAR (Fortems-Cheiney et al., 2012). Figure 1.8 illustrates the general principle of a CTM, such as CHIMERE.

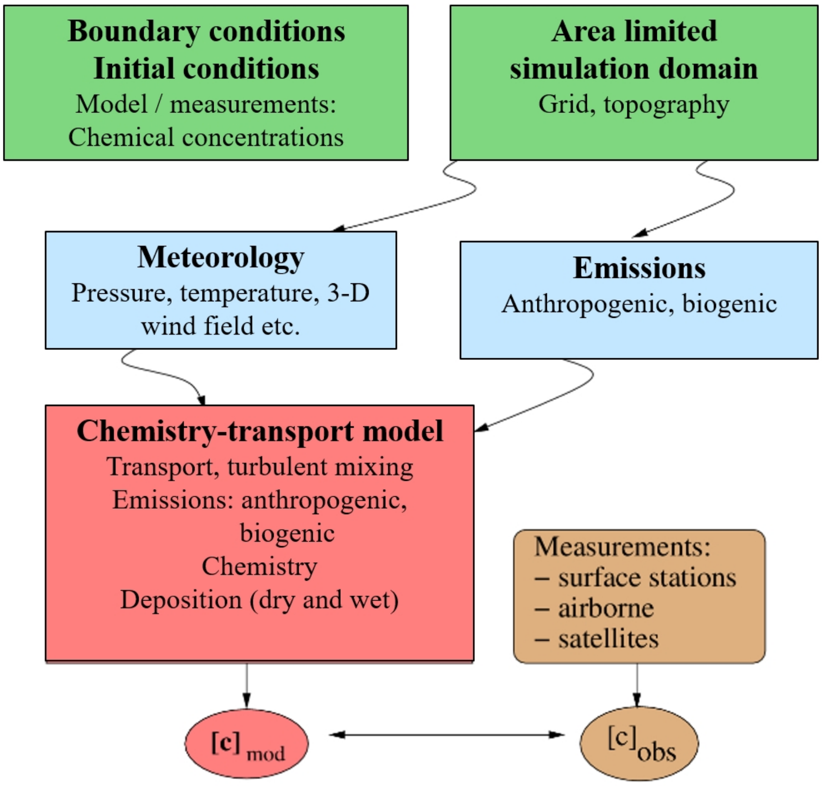

Figure 1.8: General principle of a Eulerian chemistry-transport model. The abbreviations c_{obs} and c_{mod} stand for the measured and simulated mixing ratio fields, respectively. Figure is adapted from the CHIMERE Documentation, Figure 1.1. on page 15 (CHIMERE, 2017).

The domain is arbitary and can be regional or local. The three-dimensional domain is represented by a limited number of grid-boxes and assumptions are made about the structure of the domain by spatial discretisations. The horizontal grid resolution can span from 1 km to 100 km covering urban (100-200 km) to regional (several thousand km) scales. The vertical coordinates are a linear combination of pressure p and sigma σ vertical coordinates. Sigma is the ratio of the pressure at a given location to the pressure on the surface at that given location (Simmons and Burridge, 1981). Sigma coordinates follow topographic variations in the surface and simplify the lower boundary conditions. In such vertical coordinates, the pressure levels are defined as:

$$p_k = a_k + b_k p_s \tag{1.8}$$

with p_s being the surface pressure, k the vertical model layer, a_k and b_k constants coefficients that determine the vertical coordinate (ECMWF, 2020; Eckermann, 2009). The lowest model layers are pure sigma levels, while the top levels of the model are pure pressure levels.

Boundary layer processes have a large influence on the resulting mixing ratios. Such processes, e.g. dry deposition or turbulent vertical mixing within the boundary layer, are parameterised by the sensible heat flux, the surface friction velocity and vertical diffusion profile (Troen and Mahrt, 1986). The ability of the atmosphere for the diffusion, mixing and transport of gases that are emitted to the planetary boundary layer (PBL) is determined by the PBL height. The PBL usually extends to 1-2 km height above the surface and the height depends on the turbulent air flows and is usually defined by the vertical distribution of wind, temperature and water vapour (Stull, 1988).

CHIMERE requires external forcings to perform simulations, one of which is 3-D meteorological forcing. The meteorological data files contain all the necessary variables for the simulation of atmospheric processes, for example, three-dimensional wind fields, temperature and the constant coefficients determining the vertical coordinates (ECMWF, 2020). Other external forcings are emissions and boundary and initial conditions. As the time-steps of external data usually differ from the desired times-step in a CTM, external data are temporally interpolated to yield simulation outputs in the desired time-step, which is hourly time-step in CHIMERE. As the spatial coverage of these external forcings often differs from the domain of interest, they are interpolated onto the domain of interest.

For the evolution of the mixing ratio in the domain, mixing ratios specified on the boundaries of the domain (four sides and top of the domain) and initial mixing ratios are required. Emissions can be integrated at any vertical level in the model and their temporal variation scheme can include, for example, diurnal, weekly or annual profiles. Up to date, methane emissions are provided by inventories with an annual variation, sometimes including a monthly time profile.

In this thesis, we use a domain covering main parts of Europe with [31.5° - 74°] in latitude and [-15° - 35°] in longitude. Moreover, a sub-domain is used that mainly covers parts of Northwestern Europe; [43.6° - 55.6°] in latitude and [5° - 12°] in longitude. The domains are shown in Figure 1.9. Throughout the different sub-studies in this thesis, three different horizontal resolutions are used: 0.5°×0.5°, 0.25°×0.25° (covering Europe) and 0.1°×0.1° (covering the sub-domain).

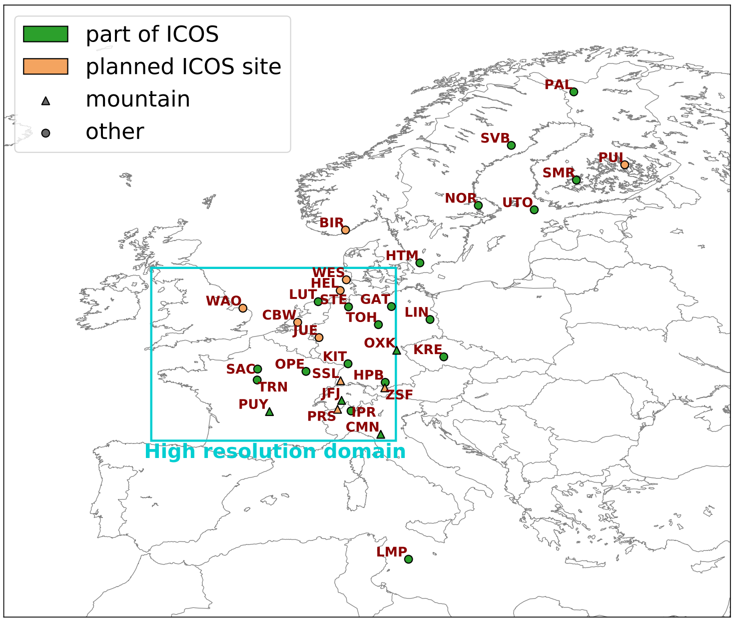

Figure 1.9: European domains used in this study for simulating CH_4 mixing ratio and its stable isotopic composition δ^{13}C and δ^{2}H. "High resolution domain" shows the sub-domain, in which simulations with a horizontal resolution of 0.1°×0.1° are performed. Monitoring sites of the ICOS network are shown as well.

1.4.2 Computing equivalents of measurements

The atmospheric mixing ratio is linked to the amount of emissions emitted to, transported and transformed in the atmosphere. CTMs compute the connection between emissions and measurements that is described through the following equation:

$$\mathbf{y} = H(\mathbf{x}) \tag{1.9}$$

with $\mathbf{y}$ being the observation vector, $\mathbf{x}$ the emission vector and H the transport model. The latter represents the atmospheric transport and mixing in the model for a given time period and space, as well as all the interpolation tools that make the comparison of model outputs to the measurements possible (e.g. averaging over time, extraction of the grid's cell matching the location of a measurement site).

In this thesis, mixing ratios of atmospheric CH_4 are simulated per source category. The δ^{13}C and δ^{2}H time series are computed by combining the simulated CH_4 mixing ratios per source category and isotopic signatures corresponding to the sources. First, the mixing ratios of the stable isotopes of carbon and hydrogen are determined for each source based on their ratios ^{13}R and ^{2}R, respectively. An example is shown for δ^{2}H:

$$^{2}R = (\frac{\delta^{2}H_{signature}}{1000‰} + 1) * VSMOW \tag{1.10}$$

$$^{2}H = {}^{2}R/(1 + {}^{2}R) * CH_4 \tag{1.11}$$

$$^{1}H = CH_4 - {}^{2}H \tag{1.12}$$

where CH_4 is the simulated CH_4 mixing ratio of a specific source and $\delta^{2}H_{signature}$ is a given isotopic signature of a specific source. The so determined ^{2}H and ^{1}H are added to obtain the total ^{2}H and ^{1}H. The total simulated δ^{2}H is then computed as:

$$\delta^{2}H = (\frac{^{2}R}{VSMOW} - 1) * 1000‰ \tag{1.13}$$

For δ^{13}C, the calculations are identical to the above mentioned ones.

1.5 Estimation of methane emissions

To gain more knowledge on atmospheric methane mixing ratios and CH_4 sources for designing and accomplishing the emission reduction efforts based on the Paris Agreement, the estimation of emissions is a key factor. In principal, there are two approaches to estimate emissions: bottom-up approaches and top-down approaches, which are described in detail in this section.

1.5.1 Bottom-up approach

In bottom-up approaches, emissions are estimated based on a large number of statistical information for source sectors and processes, which are extrapolated to larger spatial scales. The IPCC developed guidelines for estimating and reporting GHG emissions in inventories (IPCC, 2006). This method combines the so-called activity data (AD) and emission factor (EF). The activity data characterises anthropogenic socio-economic activities that cause emissions. The emission factor quantifies the sources or sinks per unit of activity. Therefore, emissions can be defined with the equation:

$$Emission = AD \times EF \tag{1.14}$$

The IPCC guidelines must be followed by countries reporting their emissions and removals (i.e. methods to remove emissions from the atmosphere) to the United Nations Framework Convention on Climate Change (UNFCCC) whose objective is the stabilisation of GHGs in the atmosphere as an international effort. Emission inventories are developed, among others, to provide information on the magnitude and spatial and temporal variations of GHGs. They usually cover global, regional (such as Europe) or country scales and provide emissions on spatial grids that can be used in numerical models to simulate atmospheric CH_4 mixing ratios. Such inventories are the TNO-MACC_III (Kuenen et al., 2014) for the European scale, the EDGAR version 4.3.2 (Janssens-Maenhout et al., 2017) and the ECLIPSE V5a (Stohl et al., 2015) for the global scale (Figure 1.10), which are used in this thesis.

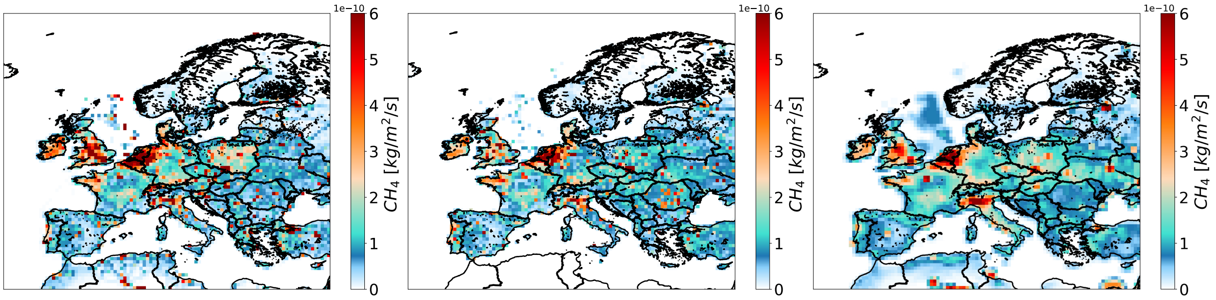

(a) EDGARv4.3.2 **(b)** TNO-MACC_III **(c)** ECLIPSE V5a

Figure 1.10: Anthropogenic emission inventories covering Europe: **a)** EDGARv4.3.2, **b)** TNO-MACC_III and **c)** ECLIPSE V5a.

These inventories provide CH_4 emissions on grids with high spatial resolutions of 0.125°×0.0625°, 0.1°×0.1° and 0.5°×0.5°, respectively. However, they distribute the sources on their spatial grids using different proxies, such as population density for e.g. waste sources. The TNO-MACC_III and ECLIPSE V5a inventories provide only annual emission time profiles. While the EDGAR inventory includes monthly time profiles as well, they are uncertain as they are based on the emission time profile of other species that co-emit with CH_4, e.g. ammonia for agricultural practices. The inventories provide emissions using different classifications for source categories that need to be regrouped when comparing simulation results made with emissions from different inventories. In this thesis, the Selected Nomenclature for Air Pollution (SNAP) level-1 categories are applied that are listed in Table 1.1. The emission inventories are further described and analysed in the following chapters of this thesis.

Table 1.1: Selected Nomenclature for Air Pollution (SNAP) level-1 categories of methane emissions.

SNAP code	Description of emission category
01	Combustion in the production and transformation of energy
02	Non-industrial combustion plants
03	Combustion in manufacturing industry
04	Production processes
05	Extraction and distribution of fossil fuels and geothermal energy
06	Solvent and other product use
07	Road transport
08	Other mobile sources and machinery
09	Waste treatment and disposal
10	Agriculture
11	Other sources and sinks (natural)

Emission inventories include uncertainties due to various causes (IPCC, 2006). Some of them are connected to the reported statistics; missing, incomplete or unclear information on reported emissions. In some situations, measurements or other data are not available to characterise individual emissions. Proxies used to spatially distribute national emissions contain further uncertainties. Numerical models that are used to generate inventories are also a source of uncertainty. Models are simplified systems that do not entirely represent real conditions. Equations used in numerical models are approximations, spatial grids or temporal scales may not be representative, and the activity data and emission factors used as inputs in models are estimates and therefore generate further uncertainties (IPCC, 2006). Moreover, uncertainties arise when interpolating emission inventories to a model grid.

Apart from the combination of emission factors and socio-economic activity data in anthropogenic emission inventories, emissions are estimated in two other ways: process-based numerical models and upscaling of models and measurements. Process-based models simulate individual emissions by representing physical, chemical or biological processes, constrained by local-scale measurements and/or laboratory experiments. Such models are often used to estimate CH_4 emissions from wetlands (e.g. Tang et al., 2010).

While they provide useful information on local scales, their use for regional to global scales is rather uncertain. These models require many parameters and inputs to represent essential processes, such as CH_4 production and oxidation in the soil. Such processes are not fully known and assumptions have to be made. Furthermore, the scarcity of direct measurements of CH_4 emissions from wetlands to initialise and parameterise the models is an additional source of uncertainty. With upscaling, local measurements made in the field or laboratory are extrapolated to the regional or global scales using numerical models. The uncertainties connected to this type of modelling are similar to the ones of process-based models. The measurements made at local scales may not be representative enough for larger scales. CH_4 emissions have a large spatial and temporal variability due to complex non-linear processes (e.g. CH_4 production, transport) that are not completely understood. As a result, upscaling methods often assume, for example, a standardised distribution of CH_4 sources within a given country or region (Sarrat et al., 2009). While emissions depend on local practices that can differ from country to country, such as types of fossil fuel produced, this kind of assumptions can lead to scaling problems.

1.5.2 Top-down approach

The goal of top-down methods is to reduce uncertainties connected to bottom-up estimated emissions and to help improve such estimates. The top-down approach optimally combines measurements of atmospheric CH_4 mixing ratios and prior knowledge on emissions from bottom-up estimates using a numerical atmospheric chemistry-transport model (Figure 1.11). This approach has been extensively used to estimate GHG emissions (Mikaloff-Fletcher et al., 2004; Bousquet et al., 2006; Berchet et al., 2020; Bergamaschi et al., 2005; Thompson et al., 2015; Bergamaschi et al., 2018; Tsuruta et al., 2019; Pison et al., 2018).

Bayes' theorem (Tarantola, 2005) usually provides the basis of top-down methods, called atmospheric inverse modelling. In this framework, atmospheric mixing ratio measurements are assimilated to optimise emissions based on synoptic deviations between measurements and simulations. An inverse modelling framework includes the respective error statistics, which are computed before the assimilation process. The optimisation of emissions largely depends on their prior estimates and their uncertainties. The optimised emissions are called the posterior emission estimates. The Bayesian

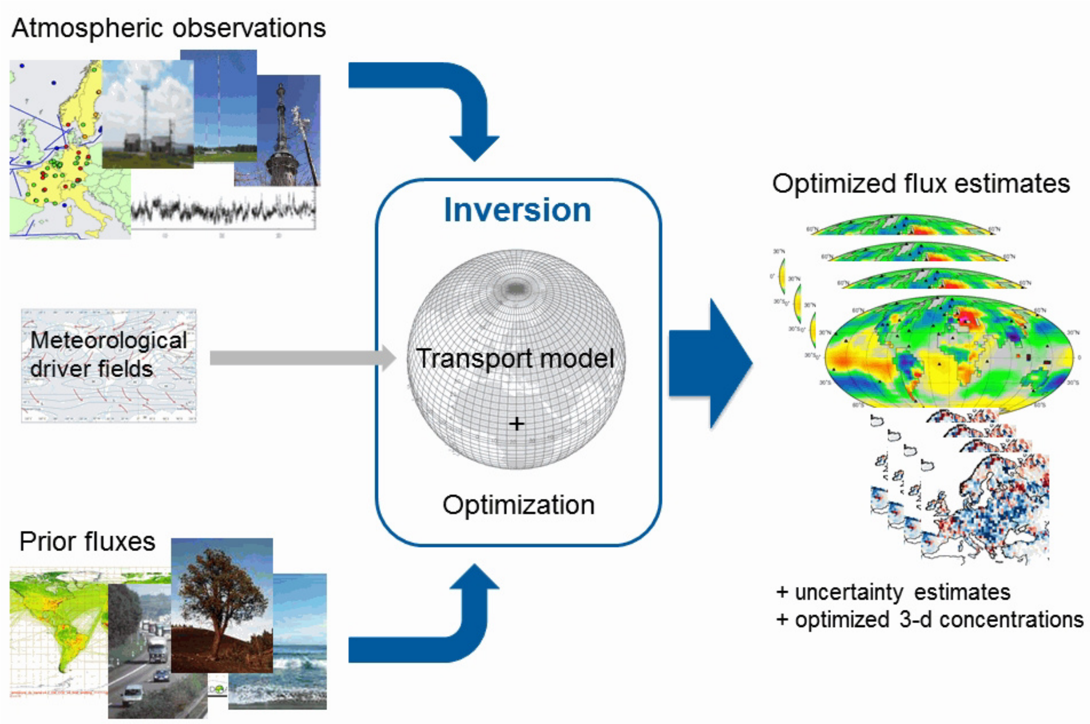

Figure 1.11: Schematic diagram of atmospheric inversions of greenhouse gas emissions (fluxes). Source: `https://www.icos-cp.eu/inverse-modelling`, last accessed on: 15-07-2020.

method is able to separate the information about emissions contained in misfits of simulation outputs and measurements from other sources of errors. The aim is to determine the conditional probability of the emission vector $\mathbf{x}$ (from Equation 1.9) that contains the emissions to be optimised, with information on atmospheric measurements of CH_4 mixing ratios described by the observation vector $\mathbf{y}$ (Enting et al., 1993, 1995):

$$p(\mathbf{x}|\mathbf{y}) \propto p(\mathbf{y}|\mathbf{x})p(\mathbf{x}) \tag{1.15}$$

with $p(\mathbf{x}|\mathbf{y})$ being the probability distribution of the posterior emission estimates, $p(\mathbf{x})$ the prior probability density function of the emission vector $\mathbf{x}$ and $p(\mathbf{y}|\mathbf{x})$ the probability density function of the observation vector $\mathbf{y}$ when $\mathbf{x}$ is assigned a certain value. When the observation operator H from Equation 1.9 (on page 18) can be considered linear and denoted as the Jacobian matrix $\mathbf{H}$, the posterior estimates of emissions $\mathbf{x}^a$ and uncertainties $\mathbf{P}^a$ can be calculated as:

$$\mathbf{x}^a = \mathbf{x}^b + \mathbf{K}(\mathbf{y}^o - \mathbf{H}\mathbf{x}^b) \tag{1.16}$$

$$\mathbf{P}^a = \mathbf{P}^b - \mathbf{K}\mathbf{H}\mathbf{P}^b \tag{1.17}$$

where $\mathbf{K}$ is the Kalman gain matrix:

$$\mathbf{K} = \mathbf{P}^b\mathbf{H}^T(\mathbf{R} + \mathbf{H}\mathbf{P}^b\mathbf{H}^T)^{-1} \tag{1.18}$$

Our study deals with linear problems because the chemistry processes are not taken into account in the simulations as the air masses in the analysed domain change rather quickly (approximately 10-14 days) compared to the atmospheric lifetime of CH_4 (approximately 8-10 years).

Emissions estimated by top-down approaches depend on the performance of chemistry-transport models and measuring instruments. For the latter, the instrument precision should be high enough to detect synoptic variations in the atmospheric signal to obtain qualitative CH_4 emission estimates. Qualitative emissions in this context mean accurate emissions in relation with the model's resolution and performance, which depends on the model inputs. The model resolution has an impact on the simulation outputs (e.g. Custodio et al., 2016; Ma et al., 2015) and estimates of emissions can differ between a higher and lower horizontal resolution configuration (Locatelli et al., 2013).

1.6 Limitations of our knowledge on atmospheric methane

Our current understanding of atmospheric methane mixing ratio evolution is limited by several aspects, which contributes to uncertainties in the CH_4 budget. This section highlights some of the limitations and uncertainties. As mentioned in Sections 1.2 and 1.5, CH_4 is formed by different processes and emitted through various types of sources, whose emission factors are highly variable in space and time. Due to that, quantification of CH_4 emissions is challenging (IPCC, 2006; Saunois et al., 2020). Although natural emissions show the largest uncertainties, anthropogenic emissions have also significant uncertainties of about 20-50% at the global scale (Saunois et al., 2020). In addition to uncertainties in sources, the sink processes of CH_4, such as the removal by OH, are not yet well understood and presents further uncertainties in the CH_4 budget (Zhao et al., 2019). Hence, due to a lack of constraints on various source and sink types, our knowledge on the contribution of different sources and sinks to the total CH_4 budget is incomplete.

The quality of emissions estimated by atmospheric inversion frameworks depends on the quality and density of atmospheric networks and on the performance of CTMs (Section 1.5.2). The limited spatio-temporal coverage of atmospheric measurements of CH_4 mixing ratios and particularly of isotopic measurements (e.g. Nisbet et al., 2019) still limits the ability of atmospheric studies to infer regional CH_4 sources and sinks. Knowledge on the spatial and temporal variability of CH_4 mixing ratios and its stable isotopic ratios $\delta^{13}C$ and $\delta^{2}H$ can be gained through their monitoring by for example ground-based networks. Although Europe is well equipped with networks monitoring atmospheric CH_4 mixing ratio, the spatial coverage of measurements remains sparse in many parts of Eastern and Southern Europe. As measurements of $\delta^{13}C$ and $\delta^{2}H$ are bound with higher instrumentational requirements and larger costs than CH_4 mixing ratio, the availability of $\delta^{13}C$ and $\delta^{2}H$ measurements remains very limited.

Atmospheric modelling incorporates additional uncertainties (e.g. physical parameterisations, representation of vertical mixing). Thus, the assessment of errors in transport models, emission inventories and measurements is critical for atmospheric inversion studies (Berchet et al., 2015; Locatelli et al., 2013; Houweling et al., 2014).

In the following sections, we address three important limitations connected to isotopic measurements and modelling errors for top-down studies.

1.6.1 Constraints on atmospheric methane sources

One of the important constraints on the roles of various sources and sinks in the methane budget is the availability of atmospheric measurements of methane isotopologues. Isotopic measurements have been proven to be useful for constraining the CH_4 budget (Nisbet et al., 2019; Townsend-Small et al., 2016). As typical isotopic source signatures vary depending on the origin of CH_4, CH_4 stable isotopic ratios, $\delta^{13}C$ and $\delta^{2}H$, can help discriminate sources of CH_4 and evaluate spatial distribution of emissions in bottom-up inventories (Zazzeri et al., 2017). Moreover isotopic measurements also appear valuable in atmospheric top-down studies as they can help improve estimates of CH_4 emissions through more constraints on source discrimination (Mikaloff-Fletcher et al., 2004). In the study of Rigby et al. (2012), it was further shown that high-frequency isotopic measurements could reduce uncertainties in emissions estimated by top-down approaches. They also provide advantages for evaluating emissions, their source apportionment and spatial distribution in inventories, as demonstrated by Zazzeri et al. (2017).

Isotopic measurements can bring constraints on atmospheric methane source sectors, which can contribute to more certain emission estimates (Rigby et al., 2012). Furthermore, information from isotopic measurements in addition to CH_4 mixing ratios can provide insights on causes of discrepancies between measurements and simulations. Such knowledge could further improve our understanding of atmospheric CH_4.

1.6.2 Requirements on instruments for source detection

Besides the limitations of the spatial coverage of atmospheric measurements of methane stable isotopic ratios, the detection of various CH_4 sources is uncertain due to limited precisions of instruments measuring $\delta^{13}C$ and $\delta^{2}H$ (Schaefer, 2019). Thonat et al. (2019) studied in a theoretical framework which instrument precision would be necessary to detect CH_4 sources through $\delta^{13}C$ measurements in the Arctic. They found that the requirements on instrument precisions can be challenging with present instruments. However, as source contributions to the total global CH_4 budget are generally larger in Europe than in the Arctic (Saunois et al., 2020), the requirements on instruments may be more favourable. This is because the uncertainty of instruments measuring isotopic composition is usually lower with higher CH_4 mixing ratios (e.g. Hoheisel et al., 2019). Hence, it is worth to investigate such instrument requirements in a European framework.

1.6.3 Error estimation for top-down studies

As mentioned in Section 1.5.2, top-down methods require that the error statistics on emissions and transport models are estimated before the assimilation of atmospheric measurements to separate the information about emissions in the discrepancies between measurements and simulation outputs of CH_4 mixing ratios. Measurements and simulation outputs can have discrepancies due to a number of causes. One cause is uncertainties in the prior emission inventories as mentioned in Section 1.5.1. Other causes include measurement errors originating from instrument precision and accuracy, and errors in transport modelling. Errors in transport modelling occur, for example, from projecting emissions to the model's grid, which may not be representative compared to measurements that can be viewed as point in case of ground-based measurements. This type of error is called the representation error (Hodyss and Nichols, 2015). Another source of representation error is the temporal resolution of transport models usually differing from that of measurements. Further errors arise from uncertainties in inputs, such as boundary conditions, and in the transport itself due to discretisations, physical parameterisations and simplifications used in models (e.g. Brophy et al., 2019).

Atmospheric inverse methods take errors into account through covariance matrices. Uncertainties, constructed from different error types, usually incorporate approximations and expert knowledge from past experience with inverse methods, which make the inverse system less objective than it should be to provide consistent emission estimates.

Several ways exist to estimate errors for atmospheric inversions of CH_4 emissions. Common methods include Monte Carlo approaches that generate multiple guesses (e.g. Super et al., 2019; Lithoxoos et al., 2012), systematic and/or objective analysis of possible uncertainties based on available data (e.g. Pison et al., 2018). Such methods are usually computationally expensive and thus difficult to reproduce, especially in case of high spatial and temporal resolutions and large amounts of measurements, which are necessary for providing reliable information to policy makers about the current state of methane in the atmosphere. Therefore, efficient tools are required to quantify uncertainties that are used in inverse models to estimate CH_4 emissions.

1.7 Objectives and research questions

1.7.1 Context of the study

The general motivation of this thesis is the increasing importance of atmospheric CH_4 in climate change (e.g. Saunois et al., 2017, 2020) and the relatively lower scientific attention given to CH_4 than to CO_2, although its mitigation could be efficient. The fact that CH_4 mixing ratio measurements in dense and relevant monitoring networks are increasingly available, especially in Europe, has additionally contributed to the ambitions of this work.

The scientific context of this thesis is the MEMO^2 project (MEthane goes MObile – MEasurements and MOdelling; `https://h2020-memo2.eu`). The main aim of MEMO^2 is the identification and evaluation of CH_4 emissions in order to support mitigation efforts set in the Paris Agreement. The region of interest is Europe as mitigation efforts occur at the regional scale and Europe is relatively well equipped with sites monitoring CH_4 mixing ratios. Within the project, new measurement and modelling tools are developed and used to detect and quantify CH_4 emissions. These include recently developed mobile analysers, state-of-the-art isotopic techniques, and newly developed high-resolution dispersion models. CH_4 emissions are measured from local sources in several countries in Europe, targeting the main sources of atmospheric CH_4. For example, agricultural sources are measured and quantified mainly in the Netherlands and emissions due to coal mining activities in Poland. The so gained knowledge from measurements is intended to be used to update emissions and improve emission estimates at the European scale. The modelling frameworks in MEMO^2 are focused on different aspects of atmospheric CH_4 from the site- and city-scale to the European scale. At the local scale, CH_4 emissions are estimated with the aid of Gaussian plume models and Direct Numerical Simulations (a computational fluid dynamics tool to simulate turbulent flows in the atmosphere) are used to study CH_4 plume composition under different conditions. At the regional scale, this project addresses various uncertainties of the European CH_4 budget, using a limited-area Eulerian CTM.

1.7.2 Objectives

In this thesis, I address several sources of uncertainties in the atmospheric methane mixing ratio evolution, aiming at improving methods for estimating CH_4 emissions at the European scale. This could contribute to improved CH_4 emission estimates and to a more comprehensive knowledge on atmospheric CH_4 in Europe.

In this work, we take benefits of CH_4 emission inventories and of the high-frequency atmospheric measurements of CH_4 mixing ratios and stable isotopic ratios $\delta^{13}C$ and $\delta^{2}H$ available for Europe. Note that we use versions of emission inventories that were available at the beginning of this thesis. In order to remain consistent throughout the thesis, we did not update them when newer versions became available. Atmospheric chemistry-transport models are advantageous for representing atmospheric CH_4 and its spatial and temporal evolution. They are useful tools for estimating emissions and designing mitigation strategies and are chosen here as the main means to study atmospheric CH_4 at the European scale. By combining atmospheric modelling and measurements, this work explores different constraints on the CH_4 budget and the potential of isotopic ratio measurements to improve estimates of CH_4 emissions at the European scale.

1.7.3 Research questions

The different chapters of this thesis address the above mentioned three crucial limitations that contribute to substantial uncertainties in the CH_4 budget.

One of the powerful tools to estimate CH_4 emissions and point towards locations that need to be emission controlled is the top-down approach (Berchet et al., 2020; Thompson et al., 2015; Bergamaschi et al., 2018; Pison et al., 2018). When such approaches combine atmospheric measurements of CH_4 mixing ratio with isotopic information, they can potentially provide even more valuable emission estimates (Mikaloff-Fletcher et al., 2004; Rigby et al., 2012). However, atmospheric inversion frameworks are subject to uncertainties in CTMs, emission inventories and measuring instruments. It is therefore critical to consistently assess the error statistics of these components. This leads to my first research question.

Research question 1: *How can we quantify errors in transport models and emission inventories for atmospheric inversions of methane emissions in Europe?*
Chapter 2 describes an analysis of several errors in transport modelling and emission inventories that can be used for inverting CH_4 emissions in Europe. The errors are estimated using a simple method over the European domain and at the location of various European measurement sites. The results of this study reveal, among others, that some inversion modelling practices should be reassessed and highlight the importance of the error estimation procedure. The study indicates that some uncertainties in atmospheric modelling originate from large errors in source apportionment of emissions.

Thus, the limited knowledge on the contribution of different CH_4 sources to the total CH_4 budget introduces additional uncertainties in the CH_4 budget. Measurements of isotopic composition can provide constraints on different source sectors and can hence be advantageous for improving emission estimates. However, isotopic measurements are scarce in Europe, which is a further limitation addressed in this thesis. Within the $MEMO^2$ project, quasi-continuous measurements of δ^2H and $\delta^{13}C$ at a coastal monitoring site and of $\delta^{13}C$ at a continental site were made available. These measurement time-series are among the very few high-frequency isotopic measurements of five months in our entire European domain. They offer an excellent opportunity to investigate the value of quasi-continuous isotopic measurements. Measurements compared to model outputs are able to well demonstrate the regional influence of CH_4 emission sources. Hence, the second study of this thesis aims at answering the following question:

Research question 2: *Are isotopic measurements useful as constraints on CH_4 sources?*
Chapter 3 focuses on the reasons for misfits between measured and simulated CH_4 mixing ratios as well as isotope ratios δ^{13}C and δ^{2}H at two locations in Europe. The main goal of the study is to learn whether any misfits between measurements and simulations can be associated with incorrect source apportionment or spatial distribution of emissions in inventories and/or with inadequate isotopic source signatures used for modelling isotopic ratios. Moreover, we aim at identifying further possible reasons for any measurement-simulation misfits.

However, using data of only two monitoring sites poses limitations and may lead to results that are not representative enough for the domain of interest. Hence, to overcome the limitations of isotopic measurement availability, simulations of one year made by the CHIMERE model are used to investigate the value of long-term in-situ isotopic measurements for more reliable estimates of CH_4 emissions in Europe.

Research question 3: *Which instrument precisions and sites are needed for isotopic measurements to be used in atmospheric inversion studies at the European scale?*
Chapter 4 studies the importance of long-term isotopic measurements by taking advantage of the European monitoring network ICOS. The value of isotopic measurements is determined by two aspects in this study: realistic instrument precision and placement of monitoring sites. As the instrument uncertainty sets limitations on CH_4 emission estimates, we examine the instrument precision needed to detect signals of δ^{13}C and δ^{2}H. For that, four reasonable instrument precisions for both δ^{13}C and δ^{2}H are examined. Whether the placement of monitoring sites is beneficial, is analysed by how often signals can be detected in the study year and what type of sources can be detected at the sites. For a complete understanding of CH_4 emissions, the detection and measurement from different types of sources is crucial.

Chapter 2

Characterisation of errors for top-down estimates of methane emissions

2.1 Preamble

2.1.1 Context and aim of the study

In this chapter, we address the limitation connected to the assessment of errors in atmospheric transport modelling, as introduced in Section 1.6. This study focuses on the influence of the transport model performance on top-down estimated emissions and aims at estimating errors in emission inventories and transport modelling that can be used in atmospheric inversions to estimate CH_4 emissions at the European scale.

2.1.2 Methodology

In this study, an error in emission inventories and four errors in transport models are assessed by applying the method of Wang et al. (2017). Following this method, multiple simulations are performed with the CHIMERE transport model using different horizontal resolutions, three emission inventories covering Europe, two products of boundary and initial conditions and CH_4 mixing ratio simulation outputs of two limited-area transport models CHIMERE and LOTOS-EUROS (Manders et al., 2017). The errors in emission inventories and transport models are the following:

- error in emission inventories: estimated from different emission inventories;
- background error: determined by simulation outputs of CH_4 mixing ratio made with two boundary and initial condition products;

- representation error: calculated from simulation outputs carried out with different horizontal resolutions;
- transport error: assessed with the aid of simulation outputs performed with two transport models;
- transported-emission error: estimated from simulation outputs of CH_4 mixing ratio made with different emission inventories.

To investigate whether an atmospheric inversion framework is able to tackle targeted CH_4 emissions over Europe, we compute the ratio of the transported-emission error to the other three transport model errors. Furthermore, spatial and temporal correlations of errors, if attainable, are explored. The errors are estimated at the location of measurement sites in Europe and over the European model domain for 2015.

2.1.3 Main results

The computation of the background error showed that its structure is homogeneous and its variability low. Thus, it can be discriminated from other types of errors. The background error can be represented by long temporal and spatial scales of more than a month and over 2400 km, respectively. Due to its homogeneity, the background error can be controlled alongside the emissions. The analysis of the transport error resulted in spatial correlations of 150-550 km and temporal correlations of 5-50 days, depending on the inventory used for the simulations of CH_4 mixing ratios. Our results indicate that sources of transport error may be controlled alongside the emissions. Both the representation error and transported-emission error feature temporal correlations under 15 days. The representation error shows no spatial correlations, while the transported-emission error shows spatial correlation lengths of about 100 km. Comparing the transport error to the transported-emission error suggests that the representation error can be treated in the observation error statistics. We estimate the error in emission inventories at the source sector and country scale. At both scales, the analysis resulted in a heterogeneous error. The study of spatial correlation lengths indicates 100-150 km for the agriculture sector, and negligibly small correlations for the waste and fossil fuel related sectors.

2.1.4 Conclusions and impact

The estimated errors allow us to gain insights into how these errors could be treated and included in a data assimilation system for inverting CH_4 emissions in Europe. The results implied that the background error may be controlled alongside the emissions, which is usually done in inversion studies. Similarly, our results for the representation error are in agreement with the usual methods of atmospheric inversion studies, in which they are included in the observation error statistics. However, controlling sources of the transport error alongside the emissions is challenging in most state-of-the-art inversion systems.

The examination of the error in emission inventories shows that the inventories are in agreement regarding the agriculture emissions. In contrast to that, there are substantial differences between the spatial distribution and magnitude of waste and fossil fuel related sources over Europe. To reduce uncertainties in CH_4 emissions, additional constraints on methane sources can be achieved by the application of atmospheric measurements of CH_4 isotopologues as isotopic source signatures differ depending on the CH_4 source type.

2.2 A pragmatic protocol for characterising errors in atmospheric inversions of methane emissions over Europe

Article submitted to *Tellus B: Chemical and Physical Meteorology* on 13 August 2020:

Barbara Szénási[1], Antoine Berchet[1], Isabelle Pison[1], Grégoire Broquet[1], Hugo Denier van der Gon[2], Arjo Segers[2], Maarten Krol[3,4], Joanna J.S. Hullegie[2], Anja Kiesow[5], Dirk Günther[5], A.M. Roxana Petrescu[6], Marielle Saunois[1], Philippe Bousquet[1], and Isabelle Pison[1]

[1] Laboratoire des Sciences du Climat et de l'Environnement, LSCE-IPSL (CEA-CNRS-UVSQ), Université Paris-Saclay, Gif-sur-Yvette, France

[2] TNO, Department of Climate, Air and Sustainability, Utrecht, the Netherlands

[3] Wageningen University & Research, Wageningen, The Netherlands

[4] Institute for Marine and Atmospheric Research Utrecht (IMAU), Utrecht University, the Netherlands

[5] German Environment Agency, Unit Emission Situation, 06844 Dessau, Germany

[6] Earth and Climate Cluster, Department of Earth Sciences, Faculty of Science, Vrije Universiteit Amsterdam, The Netherlands

Abstract. This study aims at estimating errors which are to be accounted for in atmospheric inversions of methane (CH_4) emissions at the European scale. A technically ready and computationally inexpensive method is used. Four types of errors are estimated: (i) background error, due to the bound-

ary and initial conditions, (ii) representation error, due to the difference of representativity between a model's grid-cell and atmospheric mixing ratio measurements, (iii) transport error, due to the numerical representation of atmospheric transport and meteorological inputs and (iv) transported-emission error, due to the misrepresentation of emissions on the spatial and temporal model grid. Furthermore, the errors in the emission inventories are estimated at the country and source sector scales. The method is implemented by running a set of simulations of hourly CH_4 mixing ratios for 2015 using two area-limited transport models at three horizontal resolutions with three emission inventories and two sets of boundary and initial conditions as inputs. The obtained error estimates provide insight into how these errors could be treated in an inverse modelling system for inverting CH_4 emissions over Europe. The main results include that error patterns cover a number of measurement sites and errors are heterogeneous and depend on sector and country.

2.2.1 Introduction

Methane (CH_4) contributed up to 11% to the total greenhouse gas (GHG) emissions of the European Union (EU) in 2017 (EEA, 2019), after carbon dioxide (79%). In Europe, CH_4 is released to the atmosphere by a variety of anthropogenic (more than 80%) and natural ($\sim$ 20%) sources (Saunois et al., 2016a,b). Anthropogenic CH_4 mainly originates from the activity of anaerobic bacteria in waste water treatment, landfills and through manure management and enteric fermentation of ruminants. Anthropogenic CH_4 is also released during fossil fuel extraction, production and distribution, non-industrial combustion (e.g. heating), the use of biofuel, as well as through biomass burning from agricultural activities and the treatment of agricultural waste. The largest anthropogenic emission sources in the EU are enteric fermentation, manure management and anaerobic waste treatment, accounting for $\sim$54% of the total anthropogenic sources in 2017 (EEA, 2019). Natural sources include methanogenesis in natural wetlands mostly, and to a lesser extent CH_4 release in natural gas seeps and by wildfires, through incomplete combustion of the biomass.

Due to CH_4's relatively short lifetime of 8-10 years (e.g. Saunois et al., 2020), it is a good target for short-term climate change mitigation. In order to design efficient mitigation strategies, it is necessary to have an advanced understanding on the magnitudes, trends, as well as spatial, temporal and sector distributions of CH_4 emissions at the relevant space and time scales. Emissions are primarily estimated and characterised by the so-called bottom-up approaches; i) aggregating socio-economic statistical information in the case of anthropogenic emission inventories (Kuenen et al., 2014), ii) using process-based numerical models calibrated with local-scale measurements and lab experiments (Ringeval et al., 2010), or iii) upscaling local models and measurements (Peltola et al., 2019). However, the large variety of anthropogenic sources associated with high heterogeneity, both in space and time, of their activity data and emission factors lead to imperfect knowledge. All emission data sets have significant but ill-quantified uncertainties, of which the statistical characterisation is particularly difficult (Jonas et al., 2011).

An alternative to bottom-up approaches is proposed by atmospheric inversions. The aim of such a top-down approach is to reduce uncertainties on existing emission data sets. They are built to optimally merge atmospheric measurements, numerical modelling of atmospheric transport and chemistry and prior knowledge on emissions. Atmospheric inversions commonly apply Bayesian inversion methods (Tarantola, 2005) using emission data sets as prior knowledge and assimilating atmospheric mixing ratio data in a chemistry-transport model (CTM) to update this a-priori knowledge into an optimised posterior emission estimate. In principle, the Bayesian framework makes it possible to obtain the information about the emissions contained in the misfits between the model simulations and the measurements from the other sources of errors, assuming that the statistics of the different types of errors are correctly characterised. Misfits between model simulations and measurements originate from (i) errors in measurements (instrument precision and accuracy), (ii) uncertainties in the chosen prior emission inventory, (iii) projection of emissions to the CTM’s grid, (iv) representativity of simulated mixing ratios in a model grid cell compared to measurements, which can generally be viewed as representative of a point (for in-situ measurements) or a line (for remote sensing data), compared to the typical spatial and temporal resolution of CTMs, (v) boundary conditions used in the CTM for the case of regional CTMs with limited-area domains of simulation, (vi) uncertainties in the modelling of the transport in the CTM itself (discretisation and numerical solving of continuous equations, physical parameterisations and simplifications, uncertainties in the meteorological forcing), as well as (vii) aggregation errors, which are due to the spatial and temporal resolutions of the inversion, which are different from (usually coarser than) the spatial and temporal resolutions of the CTM.

To date, atmospheric studies for the inversion of CH_4 emissions use configurations which have been specifically adapted to each inversion system and inverse problem to be solved (e.g. Bergamaschi et al., 2005; Thompson et al., 2015; Henne et al., 2016; Bergamaschi et al., 2018; Tsuruta et al., 2019; Wang et al., 2019). In particular, uncertainties in inverse systems are based on approximations, past experience and expert knowledge, which can be biased towards including some specific error-generating processes and ignoring others, e.g. taking into account errors due to the vertical mixing in the model and not the errors due to the representation of sub-grid-scale processes. Recent studies have proposed automatic methods representing uncertainties in inversion systems in a more comprehensive way (e.g. Ganesan et al., 2014; Berchet et al., 2015; Lunt et al., 2016; McNorton et al., 2020; Pison et al., 2018). These studies are based on Monte Carlo approaches, systematic exploration of possible uncertainties and/or objective analysis of available data to estimate uncertainties. They primarily optimise the uncertainties in all sources of model-data misfits along with the posterior emissions and its uncertainties. Still, underlying assumptions are strong (such as structure of errors and their correlation) and methods are computationally very expensive, making their application hard to replicate, especially for high dimensional problems with emissions at high spatial and temporal resolutions and with large amounts of observations to assimilate.

The replicability and operationality of the uncertainty assessment is especially critical in the field of regional atmospheric inversions of methane emissions, with high pressure to deliver reliable results to policy makers in the framework of the Paris agreement. As the volume of observations will further increase (Varon et al., 2019; Hu et al., 2018; Bousquet et al., 2018), our capability of manually attributing uncertainties will be more and more compromised. Indeed, in the EU, the increasing availability of continuous in-situ observations (mainly in the ICOS network, `https://www.icos-cp.eu/`), of ground-based remote-sensing data (e.g. total columns in Wunch et al., 2019) and of high-resolution satellite products, makes it necessary to build generic and efficient tools to quantify uncertainties.

In the present work, our aim is to obtain uncertainty estimates, which can be used in the framework of the inversion of CH_4 emissions in Europe by assimilating in-situ measurements from surface stations, with a methodology that is computationally inexpensive, easy to reproduce and update to account for new products (e.g. new prior emission inventories, meteorology products at high resolutions), extended measurement periods, new measurement sites and large-size data sets (e.g. satellite data). The uncertainty estimates obtained here should help setting-up inversions by providing insights on *i)* how to account for sources of errors that are not emission related and *ii)* how to specify error statistics (magnitude, temporal and spatial patterns of errors). The uncertainty estimates are computed at the CTM's grid resolution and at hourly scales, which are the finest targeted resolution for the foreseen inversions. The spatial and temporal scales targeted by the inversion can also be coarser than the CTM's: in Europe, a primary target for CH_4 could be estimates of emissions at the country scale per main sector per year or per month.

Following Wang et al. (2017), we base our error analysis and practical implementation on comparisons between simulation outputs and in-situ measurements of CH_4 mixing ratios, as generated from an ensemble of model simulations. The ensemble of simulations is based on three inventories of European CH_4 emissions, two CTMs with three different horizontal resolutions and two sets of lateral boundary conditions (LBCs) and covers the year 2015. The data sets and the models are described in Section 2.2.2. The methodology to compute error estimates is explained in Section 2.2.3. We analyse the magnitude of errors and investigate to what extend they are correlated in time and space. The results are presented and discussed in Section 2.2.4, with emphasis on the relations between the different errors. Finally, Section 2.2.5 concludes about possible error characterisations and ranges and ways to use these results in atmospheric inversions of European CH_4 emissions.

2.2.2 Data and Model Description

2.2.2.1 Measurements

In this study, focused on the year 2015, we use hourly atmospheric measurements of CH_4 mixing ratios at sites at which measurements are available for at least six months in the year. We choose 2015 for the analysis as a large number of measurements are available for this year. The selected 31 measurement sites in Europe are listed in Table 2.1 and their locations are shown in Figure 2.1.

In order to identify links between error statistics and locations and sur-

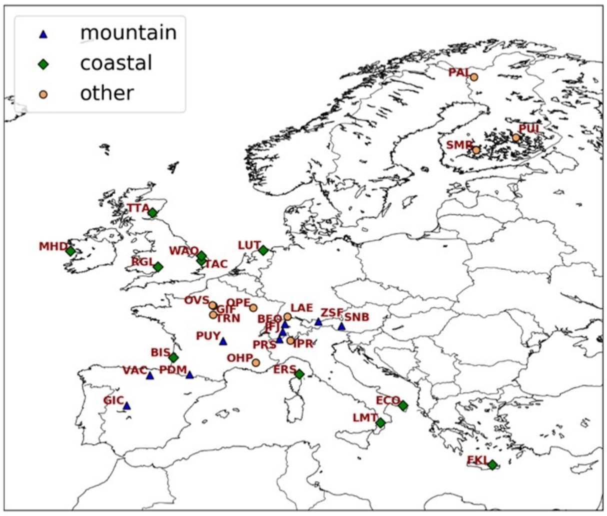

Figure 2.1: Locations of the 31 selected measurement sites (with at least six months of data available for 2015, see details in Table 2.1). Blue triangles indicate mountain sites, green diamonds coastal sites and orange circles indicate 'other' sites that are not included in the first two categories.

rounding topography of the measurement sites, we group the measurement sites in three categories: mountain sites, coastal sites and other sites (in most cases, tall towers at rural sites in a relatively flat environment). When a measurement site provides several sampling heights, we use the highest level to limit the effects of local emissions. That, combined with poorly resolved vertical transport near the surface, may lead to biased inversions (Broquet et al., 2011).

2.2.2.2 Emissions

Three annual anthropogenic emission data sets are used: TNO-MACC_III (Kuenen et al., 2014), EDGARv4.3.2 (Janssens-Maenhout et al., 2017) and ECLIPSE V5a (Stohl et al., 2015) emission inventories. At the start of this study, the inventories did not include the year 2015 so that we use the emissions from the most recent year available in each inventory (Table 2.2).

For this study, CH_4 emissions are grouped into Selected Nomenclature for Air Pollution (SNAP) level-1 sectors to have a common ground for the three inventories, as they use different classifications. In our European domain, agriculture (SNAP 10) is the main emitting sector, followed by the waste sector (SNAP 9). Other relevant emission sources for CH_4 are non-industrial combustion plants (SNAP 2) and the production, extraction and distribution of fossil fuels (SNAP 5). The latter two sectors were added into one category that is named "fossil fuel related emissions" hereafter (Table 2.3). The total anthropogenic emissions in EDGARv4.3.2 are up to 20% larger than in

Table 2.1: List of measurement sites located in the studied domain with at least six months of data available for 2015 (see locations in Figure 2.1).

Trigram	Name of site	Contributor	Country	Coordinates (lat, lon)	Altitude (m asl + inlet height)
Mountain sites					
GIC	Gredos	WDCGG/IC3	Spain	40.35, -5.18	1456
JFJ	Jungfraujoch	EMPA	Switzerland	46.54, 7.987	3580
PDM	Pic du Midi	LSCE	France	42.9372, 0.1411	2877
PRS	Plateau Rosa	RSE	Italy	45.93, 7.70	3480
PUY	Puy de Dôme	InGOS/LSCE	France	45.7719, 2.9658	1465
SNB	Sonnblick	WDCGG/UBA	Austria	47.05, 12.95	3106
VAC	Valderejo	WDCGG/IC3	Spain	2.88, -3.21	1122
ZSF	Zugspitze / Schneefernerhaus	UBA	Germany	47.42, 10.98	2656
Coastal sites					
BIS	Biscarrosse	LSCE	France	44.38, -1.23	120
ECO	Lecce Environmental-Climate Observatory	WDCGG	Italy	40.3358, 18.1245	36
ERS	Ersa	LSCE	France	42.9692, 9.3801	533
FKL	Finokalia	ECPL[a]	Greece	35.3378, 25.6694	150
LMT	Lamezia Terme	WDCGG	Italy	38.8763, 16.2322	6
LUT	Lutjewad	InGOS	The Netherlands	53.4036, 6.3528	1
MHD	Mace Head	NOAA/ESRL	Ireland	53.33, -9.9	8
RGL	Ridge Hill	University of Bristol	UK	51.9974, -2.5398	199
TAC	Tacolneston	University of Bristol	UK	52.5177, 1.1388	56
TTA	Angus	University of Bristol	UK	56.555, -2.9864	313
WAO	Weybourne	NILU[d]	Norway	52.95, 1.121	31
Other sites					
BEO	Beromünster	UBERN	Switzerland	47.19, 8.18	1009
CGR	Capo Granitola	WDCGG	Italy	37.6667, 12.65	5
GIF	Gif-sur-Yvette	LSCE	France	48.71, 2.1475	160
IPR	Ispra	InGOS/JRC	Italy	45.8147, 8.636	210
LAE	Lägern Hochwacht	UBERN	Switzerland	47.82, 8.4	872
OHP	Observatoire de Haute Provence	OSU[b]	France	43.931, 5.712	650
OPE	Observatoire pérenne de l'environnement	LSCE	France	48.5619, 5.5036	390
OVS	OVSQ[c]	LSCE	France	48.7779, 2.0486	150
PAL	Pallas-Sammaltunturi	NOAA/ESRL	Finland	67.97, 24.12	560
PUI	Puijo	FMI[d]	Finland	62.9096, 27.6549	232
SMR	Hyytiälä	University of Helsinki	Finland	61.8474, 24.2947	181
TRN	Trainou	InGOS/LSCE	France	47.9647, 2.1125	131

[a] ECPL: Environmental Chemical Process Laboratory
[b] OSU: Observatoire des Sciences de l'Univers Institut Pythéas
[c] OVSQ: Observatoire de Versailles Saint-Quentin-en-Yvelines
[d] FMI: Finnish Meteorological Institute
[e] NILU: Norwegian Institute for Air Research

Table 2.2: Description of the anthropogenic emission inventories used in this study

Inventory	**TNO-MACC_III**	**EDGARv4.3.2**	**ECLIPSE V5a**
Coverage	Europe	Global	Global
Spatial resolution	0.125°×0.0625°	0.1°×0.1°	0.5°×0.5°
Temporal resolution	Yearly	Monthly and yearly	Yearly
Available years	2000-2011	1970-2012	1990-2050
Year used	2011	2011	2010

TNO-MACC_III and ECLIPSE V5a but the relative contributions of the three main sectors are very similar across the inventories (Table 2.3). The agriculture sector dominates (about 39 to 46% of the total CH_4 emissions). The top panel of Figure 2.2 shows the spatial distribution of the average annual emissions of the three inventories for the total and the main emission sectors.

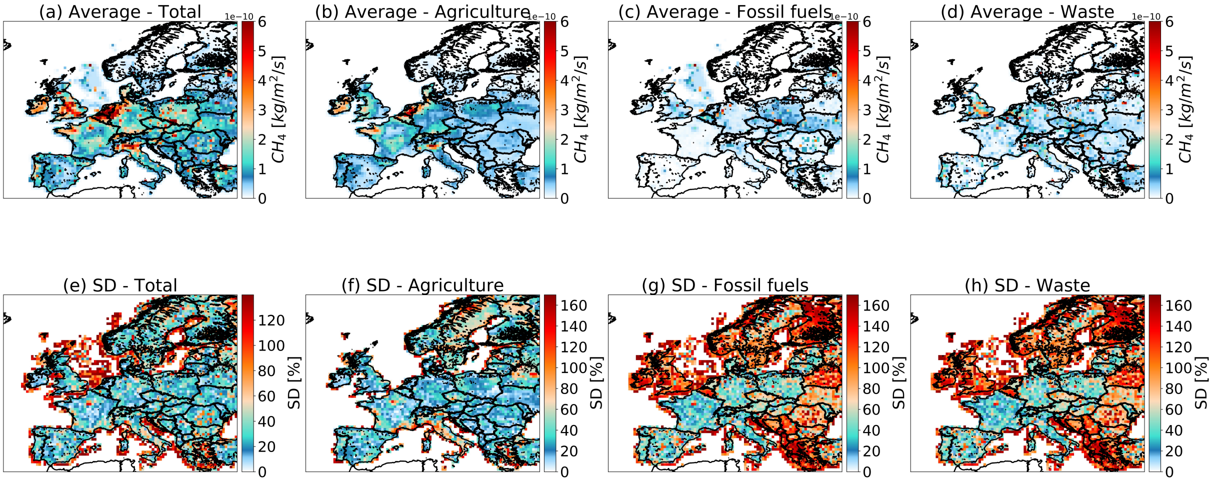
(a) Average - Total (b) Average - Agriculture (c) Average - Fossil fuels (d) Average - Waste

(e) SD - Total (f) SD - Agriculture (g) SD - Fossil fuels (h) SD - Waste

Figure 2.2: Average (top, in kg.m^{-2}.s^{-1}) and standard deviations (SDs, bottom, in % of the average) of yearly CH_4 emissions from the TNO-MACC_III, EDGARv4.3.2 and ECLIPSE V5a anthropogenic inventories: total and three main emission sectors (see Section 2.2.2.2 for definition).

2.2.2.3 Chemistry-Transport Models

Table 2.3: Total and sectoral emissions [$TgCH_4year^{-1}$] of the TNO-MACC_III, EDGARv4.3.2 and ECLIPSE V5a anthropogenic inventories in our European domain. The three main sectors used in this study are described in column 'Details'.

SNAP code	Details	Emissions ($TgCH_4year^{-1}$)			% of total anthropogenic emissions		
		TNO-MACC_III (2011)	EDGARv4.3.2 (2011)	ECLIPSE V5a (2010)	TNO-MACC_III	EDGARv4.3.2	ECLIPSE V5a
2&5	Non-industrial combustion plants & Distribution of fossil fuels and geothermal energy	6.1	7.3	5.9	24.0	23.9	22.6
9	Waste treatment and disposal	7.7	10.8	7.8	30.3	35.3	29.9
10	Agriculture	10.9	12.1	12.0	42.9	39.5	45.8
all	Total anthropogenic	25.4	30.6	26.1	97.2	98.7	98.5

We use two regional CTMs: CHIMERE (Menut et al., 2013; Mailler et al., 2017) driven by the system PYVAR (Fortems-Cheiney et al., 2019) and LOTOS-EUROS (Manders et al., 2017) in a European domain covering [31.5° - 74°] in latitude and [-15° - 35°] in longitude (Figure 2.1). The main characteristics of the set-up of the two models can be found in Table 2.4. The meteorological data used to drive both models are obtained from the European Centre for Medium-Range Weather Forecast (ECMWF) operational forecast product. For the CHIMERE simulations, the boundary and initial concentrations of CH_4 are taken either from the analysis and forecasting system developed in the Monitoring Atmospheric Composition and Climate (MACC) project (Marécal et al.,

2015) or are pre-optimized LBCs. The pre-optimized LBCs are 4D fields of CH_4 concentrations resulting from the inversion by Bousquet et al. (2006), using the global scale Laboratoire de Météorologie Dynamique (LMDz) model (Hourdin et al., 2006). The most recent year available from this inversion system is 2010, which we use to provide large-scale patterns and seasonal cycles at the boundaries of our domain for 2015. The CH_4 boundary and initial conditions of the LOTOS-EUROS model are taken from the CAMS CH_4 reanalysis product (Segers and Houweling, 2017). The global concentration fields and meteorological products were interpolated to our models' resolutions both spatially and temporally.

Table 2.4: Set-ups and input data for the atmospheric chemistry-transport models CHIMERE and LOTOS-EUROS for the simulations in 2015. The resolutions indicated for Meteorology and Boundary and initial conditions are the original ones, from which the data is interpolated on the Horizontal resolutions.

Model	**CHIMERE**	**LOTOS-EUROS**
Meteorology	ECMWF	ECMWF
Horizontal resolution	10×10 km	7×7 km
Frequency of data availability	3 hours	3 hours
Boundary and initial conditions	LMDz or MACC	CH_4: CAMS CH_4 flux reanalysis, full chemistry runs: MACC
Vertical levels	19 & 71	34
Horizontal resolution (lon × lat)	3.75°×2.5° & 0.653°×0.653°	3°×2°
Frequency of data availability	48 hours & 3 hours	3 hours
Number of levels	29	20
Top pressure	300 hPa	240 hPa
Anthropogenic emissions	EDGARv4.3.2 or TNO-MACC_III or ECLIPSE V5a	EDGARv4.3.2 or TNO-MACC_III or ECLIPSE V5a
Horizontal resolutions (lon × lat)	0.5°×0.5°or 0.25°×0.25°or 0.5°×0.25°	0.5°×0.25°
Period simulated	2015	2015

2.2.3 Methodology

2.2.3.1 Definition of Error Sources

We study five errors, described below; four of them are in the concentration space and one is in the emission space:

Error in the emission space:

- e_p, called hereafter the prior error, which is the error of the emissions in the inventories, particularly due to the spatial distribution of the emissions at the sector and country scales. This error source includes the errors due to the projection of the inventories on the model's grid and due to the use of different methodology, socio-economic input data, emission factors and products used for the spatial distribution of emissions in various inventories. We do not study the temporal distribution of e_p as emissions do not vary throughout the year in the inventories used here.

Errors in the concentration space:

- $\varepsilon_{\mathrm{flx}}$, called hereafter the transported-emission error. This error source is due to the impact of the errors in the emission inventories on the simulated mixing ratios in the transport model domain. The error e_{p} is linked to $\varepsilon_{\mathrm{flx}}$ mainly through the projection of the inventories on the model's grid and the atmospheric transport of these emissions by the model;
- $\varepsilon_{\mathrm{repr}}$ the representation error, due to the model having a resolution that is coarser than the scales at which emissions vary and of which in-situ measurements are representative;
- ε_{t} the transport error, due to discretisation with sub-grid scale parametrisations and other approximations of the fundamental equations of the atmospheric transport used in a model as well as the meteorological forcing (computed off-line for the CTMs used here, by the numerical weather forecast system of ECMWF) and the choice of physical approximations in a given model.
- $\varepsilon_{\mathrm{LBC}}$, called hereafter the background error, is due to the choice of lateral boundary conditions (LBCs, four sides and top of the domain) and initial conditions

This list of errors does not include the aggregation error described in Wang et al. (2017), which is based on Kaminski et al. (2001) and Bocquet et al. (2011). This error is linked to the inversion targeting emissions at a resolution coarser than the CTM's resolution. To our knowledge, inversion systems do not use the CTM's native spatio-temporal resolution as a target resolution. In many cases, the CTM's grid cells are grouped into coarser spatial structures (e.g. national or regional groups) and in most cases, the temporal profiles of emissions are grouped by time periods (from a few hours to days or even years), below which a constant profile is kept throughout the inversion procedure. Inversions with the capability to handle large control vectors, like variational inversions, often control the emissions at a resolution close to that of the transport model (e.g. Broquet et al., 2011; Fortems-Cheiney et al., 2012), at least spatially. In that case, $\varepsilon_{\mathrm{flx}}$ covers most of the aggregation error. In contrast, for inversions handling low resolution control vectors (e.g. Pison et al., 2018), like when using analytical inversion systems, the aggregation error can dominate over many other type of errors (Wang et al., 2017). Here, considering our future use of a variational inverse modelling system in which all spatial and temporal scales can be targeted (from the grid-cell and hourly scales to the whole domain and period of interest), we do not further investigate the aggregation error. Our aim is to estimate the dominant contributions to the total observation and prior errors in order to propose a lower bound for uncertainties and consistent structures of errors.

To evaluate whether an atmospheric inversion is relevant to tackle the targeted CH_4 emissions, we compare the magnitudes and structures of $\varepsilon_{\mathrm{repr}}$, ε_{t} and $\varepsilon_{\mathrm{LBC}}$ to $\varepsilon_{\mathrm{flx}}$. The relation of $\varepsilon_{\mathrm{flx}}$ to the other errors in the concentration space is valuable as $\varepsilon_{\mathrm{flx}}$ contains the expected signal from emissions in the simulated mixing ratios. Several cases are possible:

- $\varepsilon_{\mathrm{flx}}$ has distinct spatio-temporal structures and /or dominates all other types of error: emissions are so ill-quantified, i.e. e_{p} is large and is not smoothed out when projected by the model to the concentration space (through mainly the projection of the inventory on the model's grid and the simulation of the atmospheric transport), that they introduce large errors on the simulated mixing ratios. Therefore, any data brings valuable knowledge on emissions in an inversion. This can be the case of particular sectors with little or no reliable information on emissions;
- errors have similar structures and some errors are of the same magnitude as $\varepsilon_{\mathrm{flx}}$: the inversion may lead to inconclusive ambiguous results;
- errors have similar structures and some errors are large compared to $\varepsilon_{\mathrm{flx}}$: the inversion is likely to bring only limited information and only on very large scale aggregated CH_4 budgets; in that case, it may be possible to control the sources of these errors alongside the CH_4 emissions to better optimise the latter; for instance, regional inversions classically include LBCs in their control vector to avoid biases in the LBCs impacting emission estimates. In Section 2.2.4.1, we elaborate on this issue.

2.2.3.2 Estimates of the Representation Error $\varepsilon_{\mathrm{repr}}$, the Transport Error ε_{t}, the Transported-Emission Error $\varepsilon_{\mathrm{flx}}$, and the Background Error $\varepsilon_{\mathrm{LBC}}$ from Simulated CH_4 Mixing Ratios

Following Wang et al. (2017), from the available modelling components (Table 2.4), a total of 11 CHIMERE and 3 LOTOS-EUROS simulations are run as listed in Table 2.5. In each grid cell c, one estimate of a given ε_{i}, for $i \in \{\mathrm{repr}, \mathrm{t}, \mathrm{flx}, \mathrm{LBC}\}$, consists of a time-series of hourly differences between two simulations, ϕ and ψ, of CH_4 concentrations which differ by only one aspect:

$$\varepsilon_{i,c}^{(\phi,\psi)} = \left([\mathrm{CH_4}]_{c,h}^{\phi} - [\mathrm{CH_4}]_{c,h}^{\psi} \right)_{h \in H} \tag{2.1}$$

with H an ensemble of hours among all the 8760 hours in 2015.

Table 2.5: Simulations performed with the set-ups of the two chemistry-transport models (CTMs) described in Table 2.4. The ID(s) attributed to each simulation indicate(s) when it is used for computing differences between different resolutions (R1X-R2X, with X=A, B, C), inventories (I1X-I2X), transport models (T1X-T2X) or boundary conditions (L1-L2). See Section 2.2.3.2 for details.

CTM	Boundary conditions	Emissions	Resolution (lon × lat)	ID
CHIMERE	MACC	EDGARv4.3.2	0.5°×0.5°	R1A, I1A, I2C
CHIMERE	MACC	EDGARv4.3.2	0.25°×0.25°	R2A
CHIMERE	MACC	EDGARv4.3.2	0.5°×0.25°	T1A
CHIMERE	MACC	TNO-MACC_III	0.5°×0.5°	R1B, I2A, I1B
CHIMERE	MACC	TNO-MACC_III	0.25°×0.25°	R2B
CHIMERE	MACC	TNO-MACC_III	0.5°×0.25°	T1B
CHIMERE	MACC	ECLIPSE V5a	0.5°×0.5°	R1C, I2B, I1C
CHIMERE	MACC	ECLIPSE V5a	0.25°×0.25°	R2C
CHIMERE	MACC	ECLIPSE V5a	0.5°×0.25°	T1C
CHIMERE	MACC	EDGARv4.3.2	0.5°×0.5°	L1
CHIMERE	LMDZ	EDGARv4.3.2	0.5°×0.5°	L2
LOTOS-EUROS	CAMS	EDGARv4.3.2	0.5°×0.25°	T2A
LOTOS-EUROS	CAMS	TNO-MACC_III	0.5°×0.25°	T2B
LOTOS-EUROS	CAMS	ECLIPSE V5a	0.5°×0.25°	T2C

The 14 simulations available are grouped to compute:

- three estimates of $\varepsilon_{\text{repr}}$: $(R1A-R2A)$, $(R1B-R2B)$, $(R1C-R2C)$; each calculation is based on two horizontal resolutions, 0.5°×0.5° and 0.25°×0.25°, and one inventory per estimate. The differences are computed in the grid cells of the finer resolution after projecting the coarser resolution on the fine resolution grid (one grid cell at 0.5°×0.5° corresponds to four grid cells at 0.25°×0.25°).
- three estimates of ε_{t}: $(T1A-T2A)$, $(T1B-T2B)$, $(T1C-T2C)$; each calculation is based on the two CTMs computed at the same horizontal resolution (0.5°×0.25°) and one inventory per estimate.
- three estimates of ε_{flx}: $(I1A-I2A)$, $(I1B-I2B)$, $(I1C-I2C)$; each calculation is based on a pair of the three inventories computed with the model CHIMERE at 0.5°×0.5°.
- one estimate of ε_{LBC}: $(L1-L2)$, based on the two available LBC data set runs with CHIMERE at 0.5°×0.5°.

As the present work is a first step towards regional inversion using real in-situ observations, all estimates of errors are also calculated in the grid cells matching the horizontal and vertical location of existing measurements in Europe (see Table 2.1). To determine the model layer that best fits the height of the measurements for each site, the RMSE between measured and simulated hourly mixing ratios from 2015 was computed for all the model layers; the layer with the lowest RMSE was then taken to compute error estimates. Note that choosing another layer than the one with the lowest RMSE would lead to an increase of the errors in the concentration space.

2.2.3.3 Metrics Characterising Errors

To be able to summarise the estimates of the error time series, we define aggregated metrics used later in Section 2.2.4. The chosen metrics are the bias, the standard deviation of errors, the spatial correlation of errors as well as the temporal correlation of errors on a given sub-sample H of hours in 2015 (see details on the choice of H in Section 2.2.3.4).

For every estimate (ϕ, ψ) of a given error $i \in \{\mathrm{repr}, \mathrm{t}, \mathrm{flx}, \mathrm{LBC}\}$, we compute the bias $b_{\varepsilon_{i,c,H}^{(\phi,\psi)}}$ and the standard deviation $\sigma_{\varepsilon_{i,c,H}^{(\phi,\psi)}}$ as:

$$\begin{cases} b_{\varepsilon_{i,c,H}^{(\phi,\psi)}} & = \overline{\varepsilon_{i,c}^{(\phi,\psi)}} = \frac{1}{Card(H)} \sum_{h\in H} \varepsilon_{i,c,h}^{(\phi,\psi)} \\ \sigma_{\varepsilon_{i,c,H}^{(\phi,\psi)}} & = \sqrt{\frac{1}{Card(H)} \sum_{h\in H} (\varepsilon_{i,c,h}^{(\phi,\psi)} - b_{\varepsilon_{i,c,H}^{(\phi,\psi)}})^2} \end{cases} \tag{2.2}$$

with $Card(H)$ being the size of the sample H.

The spatial correlations of an estimate (ϕ, ψ) of a given error $i \in \{\mathrm{repr}, \mathrm{t}, \mathrm{flx}, \mathrm{LBC}\}$ are obtained from the bias-corrected correlations for pairs of grid cells (c_1, c_2):

$$corr_{i,(c_1,c_2),H}^{(\phi,\psi)} = \frac{\frac{1}{Card(H)} \sum_{h\in H} \left(\varepsilon_{i,c_1,h}^{(\phi,\psi)} - b_{\varepsilon_{i,c_1,H}^{(\phi,\psi)}}\right) \left(\varepsilon_{i,c_2,h}^{(\phi,\psi)} - b_{\varepsilon_{i,c_2,H}^{(\phi,\psi)}}\right)}{\sigma_{\varepsilon_{i,c_1,H}^{(\phi,\psi)}} \times \sigma_{\varepsilon_{i,c_2,H}^{(\phi,\psi)}}} \tag{2.3}$$

The correlations are represented as the average of all correlations from all possible pairs for a given distance interval (Section 2.2.4.1):

$$corr_{i,d,H}^{(\phi,\psi)} = \overline{\left\{ corr_{i,(c_1,c_2),H}^{(\phi,\psi)} \qquad \forall (c_1, c_2) \setminus ||c_1 c_2|| \in [d, d+50\mathrm{km}[\right\}} \tag{2.4}$$

The temporal auto-correlation R for a given temporal delay k is computed as follows:

$$R_{i,c,H}^{(\phi,\psi)}(k) = \frac{\frac{1}{Card(H)} \sum_{h\in H} \left(\varepsilon_{i,c,h}^{(\phi,\psi)} - b_{\varepsilon_{i,c,H}^{(\phi,\psi)}}\right) \left(\varepsilon_{i,c,h+k}^{(\phi,\psi)} - b_{\varepsilon_{i,c,H}^{(\phi,\psi)}}\right)}{\sigma_{\varepsilon_{i,c,H}^{(\phi,\psi)}}} \tag{2.5}$$

In most inversion studies, the temporal correlation of errors is assumed to follow an exponential decay. In our case, the auto correlations quickly decrease before converging to zero but do not necessarily closely follow an exponential decay. Nevertheless, for a simple representation of the temporal correlation, we take the time after which the auto correlation drops below e^{-1}.

For better readability, the spatial distribution of the metric of a given error $i \in \{\mathrm{repr}, \mathrm{t}, \mathrm{flx}, \mathrm{LBC}\}$ is not displayed for all possible estimates (e.g. for all pairs of inventories). Instead, we show the average of the metric of interest on all estimates of the error (one for $\varepsilon_{\mathrm{LBC}}$, and three for all other errors, as detailed in Section 2.2.3.2) in Sections 2.2.3.4 and 2.2.4.1.

2.2.3.4 Temporal Sampling of Error Time Series

To investigate whether a diurnal cycle is present in the error metrics, we compute the estimates of $\varepsilon_{\mathrm{repr}}$, ε_{t}, $\varepsilon_{\mathrm{flx}}$, $\varepsilon_{\mathrm{LBC}}$ for 8 sub-samples W_j of simulated hourly concentrations over 3-hour long time-windows j:

$$W_j = [(3j)\mathrm{hours}; (3j+3)\mathrm{hours}] \tag{2.6}$$

To detect whether there is a period in the day which is more favourable for assimilating observations on regional scale, we compute the ratios of the averages of $\varepsilon_{\mathrm{repr}}$, ε_{t} and $\varepsilon_{\mathrm{LBC}}$ with respect to $\varepsilon_{\mathrm{flx}}$, for each time-window j, in each grid cell c:

$$r_{i,c}^{j} = \frac{\overline{\varepsilon_{i,c}^{j}}}{\overline{\varepsilon_{flx,c}^{j}}} \text{ with } i \in \{\mathrm{repr}, \mathrm{t}, \mathrm{LBC}\} \tag{2.7}$$

We subsequently determine the minimum and maximum of $r_{i,c}^{j}$ for each $i \in \{\mathrm{repr}, \mathrm{t}, \mathrm{LBC}\}$ to signal the time-window for which the ratio of errors to $\varepsilon_{\mathrm{flx}}$ is the smallest. These values are shown for the locations c of the measurement sites in Figure 2.3. In the 'mountain' sites category, the optimum ratios are mostly found during the night and early morning (15 over 24 ratios), the rest being during the afternoon. However, most ratios are bigger than 2, confirming that 'mountain' sites are less sensitive to local emissions, and provide information on the larger spatial scales. The smallest ratios are found during the afternoon, which suggests that some days, the planetary boundary layer (PBL) can reach the corresponding sites, allowing them to constrain local or regional emissions. For the other categories of sites, the smallest ratios are generally found in the morning with 28 occurrences over

69 between 6h-12h, which indicates that more precise information on local to regional emissions would be retrieved by inversions using morning data at these sites. This result differs from the choice generally made in inversions, based on expert knowledge, to select only afternoon observations for non-mountain sites to limit the impact of poorly-modelled shallow PBL during the night and early morning. Indeed, the vertical mixing and its impact on the diurnal cycle of mixing ratios are a significant source of error in CTMs (Koffi et al., 2016; Dabberdt et al., 2004). However, both CTMs in this study use ECMWF data so that errors on the vertical mixing likely follow the same diurnal pattern. It is therefore not possible to go further in the analysis of the impact of the errors on the vertical mixing at the sub-diurnal scale. In order to stay compatible with the usual choice of afternoon observations for non-mountain sites, in the following, we compute $\varepsilon_{\mathrm{repr}}$, ε_{t}, $\varepsilon_{\mathrm{flx}}$, $\varepsilon_{\mathrm{LBC}}$ in each grid cell c from simulated hourly concentrations between 13 h and 17 h UTC included. For mountain sites, we take the simulated hourly concentrations between 00 h and 04 h UTC included. The sample of hourly concentrations H to compute error metrics has then $5\ \mathrm{hours} \times 365\ \mathrm{days} = 1825$ elements. Our computation of the transport error thus focuses on the horizontal aspect, rather than the vertical one.

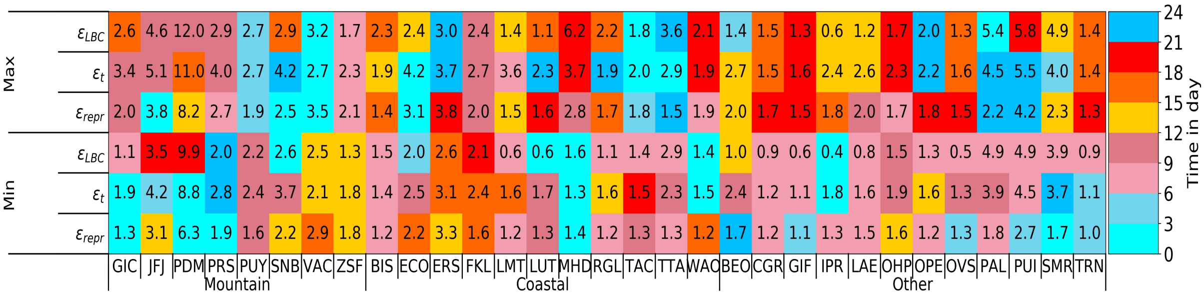

		GIC	JFJ	PDM	PRS	PUY	SNB	VAC	ZSF	BIS	ECO	ERS	FKL	LMT	LUT	MHD	RGL	TAC	TTA	WAO	BEO	CGR	GIF	IPR	LAE	OHP	OPE	OVS	PAL	PUI	SMR	TRN
Max	ε_{LBC}	2.6	4.6	12.0	2.9	2.7	2.9	3.2	1.7	2.3	2.4	3.0	2.4	1.4	1.1	6.2	2.2	1.8	3.6	2.1	1.4	1.5	1.3	0.6	1.2	1.7	2.0	1.3	5.4	5.8	4.9	1.4
	ε_t	3.4	5.1	11.0	4.0	2.7	4.2	2.7	2.3	1.9	4.2	3.7	2.7	3.6	2.3	3.7	1.9	2.0	2.9	1.9	2.7	1.5	1.6	2.4	2.6	2.3	2.2	1.6	4.5	5.5	4.0	1.4
	ε_{repr}	2.0	3.8	8.2	2.7	1.9	2.5	3.5	2.1	1.4	3.1	3.8	2.0	1.5	1.6	2.8	1.7	1.8	1.5	1.9	2.0	1.7	1.5	1.8	2.0	1.7	1.8	1.5	2.2	4.2	2.3	1.3
Min	ε_{LBC}	1.1	3.5	9.9	2.0	2.2	2.6	2.5	1.3	1.5	2.0	2.6	2.1	0.6	0.6	1.6	1.1	1.4	2.9	1.4	1.0	0.9	0.6	0.4	0.8	1.5	1.3	0.5	4.9	4.9	3.9	0.9
	ε_t	1.9	4.2	8.8	2.8	2.4	3.7	2.1	1.8	1.4	2.5	3.1	2.4	1.6	1.7	1.3	1.6	1.5	2.3	1.5	2.4	1.2	1.1	1.8	1.6	1.9	1.6	1.3	3.9	4.5	3.7	1.1
	ε_{repr}	1.3	3.1	6.3	1.9	1.6	2.2	2.9	1.8	1.2	2.2	3.3	1.6	1.2	1.3	1.4	1.2	1.3	1.3	1.2	1.7	1.2	1.1	1.3	1.5	1.6	1.2	1.3	1.8	2.7	1.7	1.0

Figure 2.3: Three-hour long time-window in the day for the maximum (top part) and minimum (bottom part) of the ratio of $\varepsilon_{\mathrm{repr}}$, ε_{t}, $\varepsilon_{\mathrm{LBC}}$ to $\varepsilon_{\mathrm{flx}}$ for the year 2015 at the 31 selected measurement sites (details in Table 2.1). The colour depicts the time-window in the day and the number gives the ratio at that time [UTC].

2.2.3.5 Indicators of e_{p} Characteristics

The consistency of the spatial distributions of the three inventories is represented through the average and standard deviation (in % of the average) of methane emissions per sector s in each grid cell c (Figure 2.2):

$$\overline{f_{s,c}} = \frac{1}{3}\left(f_{s,c}^{ED} + f_{s,c}^{TM} + f_{s,c}^{EC}\right) \tag{2.8}$$

$$SD_{s,c} = \frac{\sqrt{\frac{1}{3}\left((f_{s,c}^{ED} - \overline{f_{s,c}})^2 + (f_{s,c}^{TM} - \overline{f_{s,c}})^2 + (f_{s,c}^{EC} - \overline{f_{s,c}})^2\right)}}{\overline{f^{s,c}}} \times 100 \tag{2.9}$$

with f^{XY} the annual emissions from EDGARv4.3.2 ($XY = ED$), TNO-MACC_III ($XY = TM$) and ECLIPSE V5a ($XY = EC$).

To investigate whether the prior error e_{p} for a given sector includes spatial correlations, and, if so, whether these correlations can be represented with correlation lengths, the correlations of the $SD_{s,c}$ for the three main sectors s are computed (Section 2.2.4.2). The correlations between sectors are investigated at the European and at the country scales. All correlations are analysed for significance and are considered significant when the p-value is $\leq$ 0.01. At the European scale, the correlations between two sectors (hereafter named 'cross-sector correlations') are computed, for each pair of sectors (s_1, s_2), from the two sets of three maps of differences in emissions for this sector, i.e. between the series consisting of the list of differences between pairs of inventories, in all grid cells c of the European domain:

$$\delta_{s,c}^{I} = f_{s,c}^{A} - f_{s,c}^{B} \text{ for } (I,A,B) \in \{(1,ED,TM),(2,ED,EC),(3,TM,EC)\} \tag{2.10}$$

$$corr_{s_1,s_2}^{Europe} = \frac{\frac{1}{3}\frac{1}{N}\sum_{c=1}^{N}\sum_{I=1}^{3}\delta_{s_1,c}^{I}\delta_{s_2,c}^{I}}{\sqrt{\left(\frac{1}{3}\frac{1}{N}\sum_{c=1}^{N}\sum_{I=1}^{3}\delta_{s_1,c}^{I}{}^2\right)\left(\frac{1}{3}\frac{1}{N}\sum_{c=1}^{N}\sum_{I=1}^{3}\delta_{s_2,c}^{I}{}^2\right)}} \tag{2.11}$$

The cross-sector correlations are then represented as a matrix (Section 2.2.4.2).

To enable the computation of the correlations between two sectors (s_1, s_2) and between two countries, the correlations between sectors and between countries (hereafter named 'cross-sector cross-country correlations') are obtained from two series which describe the 66 possible pairs of countries among 12 selected countries (as defined in Table 2.6):

$$\begin{aligned} \delta_{(s,C)}^{I} = & f_{s,C}^{A} - f_{s,C}^{B} \\ & \text{for } (I,A,B) \in \{(1,ED,TM),(2,ED,EC),(3,TM,EC)\} \\ & \text{and } C \in 12 \text{ selected countries} \end{aligned} \tag{2.12}$$

$$(L_1, L_2) \text{ lists of countries } / (C_a, C_b) \in L_1 \times L_2 \text{ describe the 66 pairs of countries} \tag{2.13}$$

$$corr_{s_1,s_2}^{countries} = \frac{\frac{1}{3}\frac{1}{66}\sum_{(C_a,C_b)\in(L_1\times L_2)}\sum_{I=1}^{3}\delta_{(s_1,C_a)}^{I}\delta_{(s_2,C_b)}^{I}}{\sqrt{\left(\frac{1}{3}\frac{1}{66}\sum_{C_a\in L_1}\sum_{I=1}^{3}{\delta_{s_1,C_a}^{I}}^{2}\right)\left(\frac{1}{3}\frac{1}{66}\sum_{C_b\in L_2}\sum_{I=1}^{3}{\delta_{s_2,C_b}^{I}}^{2}\right)}} \tag{2.14}$$

The cross-sector cross-country correlations are then represented as a matrix (Section 2.2.4.2). Contrary to a classical correlation matrix representation, in which only pairs of sectors or pairs of countries are taken into account, the diagonal terms of the matrices in Section 2.2.4.2 are not equal to 1 as they represent the average correlation between pairs of countries for given sectors and are therefore always smaller than 1.

An inter-annual analysis of e_p is not possible here as the CH_4 emissions in the inventories used for this study do not vary within the year. Finally, the uncertainties of the above elements, associated to the three spatially distributed emission inventories, are evaluated by comparison to the total UNFCCC national estimates and estimates from top-down (TD) studies (Section 2.2.4.2).

2.2.4 Results and Discussion

2.2.4.1 Errors in the Concentration Space: Representation Error ε_repr, Transported-Emission Error ε_flx, Transport Error ε_t, and Background Error ε_LBC

Absolute Values of ε_LBC, ε_repr, ε_t and ε_flx

Figure 2.4 shows the spatial patterns of ε_LBC, ε_repr, ε_t and ε_flx over the domain, including the average bias, SD and the ratios of ε_repr, ε_t and ε_LBC to ε_flx. The annual SDs of ε_LBC, ε_repr, ε_t and ε_flx at the locations of the measurement sites are shown in Figure 2.5. Despite of having the largest bias (3-34 ppb, Figure 2.4g) compared to the biases of the other errors, ε_LBC has the smallest and most homogeneous annual SD over Europe (15-32 ppb, Figure 2.4h). This confirms that LBCs are a critical obstacle to any reliable regional inversion. Nevertheless, their uniform structure with low variability makes it possible to differentiate the LBC errors from other errors (both emission-induced and other types), and thus to optimise them in the inversion.

Patterns due to the emissions show up both in ε_repr and ε_t. The SD of ε_repr ranges between 1 and 80 ppb over land and reaches high values at several grid cells that contain emission hot-spots such as capitals in Europe, e.g. Madrid, Paris and Warsaw. Maxima are found in high-emitting zones, such as the Silesian Coal Basin in Poland or the Po-Valley in Italy (Figure 2.4b). A maximum value of 80 ppb occurs in St. Petersburg. Indeed, a hot-spot of emissions appears in St. Petersburg in the total emission map of the TNO-MACC inventory, due to fossil fuel related emissions (see Figure 2.2a and Figure 2.2c): 54% of the total GHG emissions in St. Petersburg come from energy sources (ISAP, 2019).

The SD of $\varepsilon_{\text{repr}}$ is in general much smaller over the sea than over the land, with values under 10 ppb, due to limited sea emissions. Nevertheless, higher values for the SD of $\varepsilon_{\text{repr}}$ are found in the North Sea where numerous oil and gas offshore platforms are located. The SD of ε_{t} ranges between 10 and 140 ppb over land. High values are found over the largest emission hot-spots and areas (Figure 2.4e) rather than in areas where the transport modelling is in principle more challenging, such as coasts or mountainous zones (high values for the Alps appear only in Italy and Switzerland). The patterns in $\varepsilon_{\text{repr}}$ and ε_{t} biases and SDs are linked to large gradients of concentrations induced by steep gradients of emissions, which have an impact even at a resolution as large as 0.5°×0.5°. Patterns due to meteorological situations and synoptic events may occasionally generate large errors but these events are averaged out at the yearly scale studied here.

Emission hot-spots and high-emitting zones are key regions of interest for policy makers. The capacity of retrieving information on the emissions through inversions in these areas would then be particularly useful. However, the very steep spatial emission gradients encountered at scales smaller than the smallest scale used in our work (0.25°) may lead to even higher $\varepsilon_{\text{repr}}$ and ε_{t} than derived here. Hence, observations near hot-spots should be used with caution within an inversion over Europe at horizontal resolutions coarser than 0.25°×0.25°.

The SD of ε_{flx} ranges between 2 and 140 ppb and is the highest over grid cells where the emissions in the three inventories differ the most, e.g. over the Po-Valley, the Silesian Coal Basin, Istanbul (Figure 2.4k). Wunch et al. (2019) have shown that there is an uncertainty in the spatial distribution of the emissions, based on the comparison of EDGAR v4.2 FT2010 and TNO-MACC_III over parts of Europe, the differences being larger near large cities. Nevertheless, ε_{flx} is not necessarily the highest near large cities in our case because of the horizontal resolutions used in the simulations remain larger

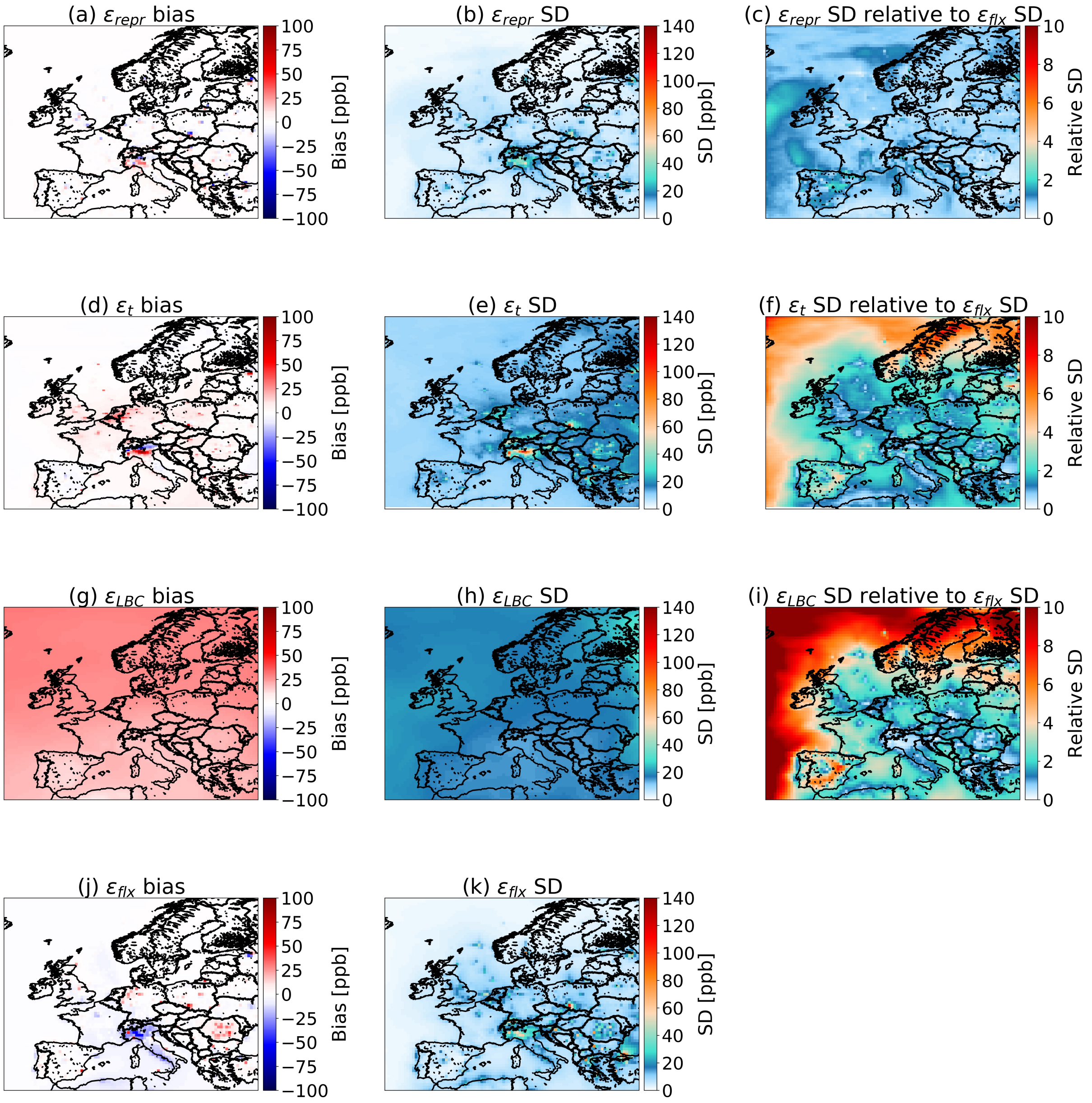

Figure 2.4: Average bias (first column) and standard deviation (SD, middle column) for 2015 of (from top to bottom) $\varepsilon_{\mathrm{repr}}$, ε_{t}, $\varepsilon_{\mathrm{LBC}}$ and $\varepsilon_{\mathrm{flx}}$ in ppb and ratios of $\varepsilon_{\mathrm{repr}}$, ε_{t} and $\varepsilon_{\mathrm{LBC}}$ SDs to $\varepsilon_{\mathrm{flx}}$ SD. Results are shown at 0.5°×0.5°.

than the typical scale of European mega-cities. Further investigations on the patterns in the prior error e_{p} are made in Section 2.2.4.2.

Ratios of $\varepsilon_{\mathrm{LBC}}$, $\varepsilon_{\mathrm{repr}}$ and ε_{t} Relative to $\varepsilon_{\mathrm{flx}}$

The ratios of the SDs of $\varepsilon_{\mathrm{LBC}}$, $\varepsilon_{\mathrm{repr}}$ and ε_{t} relative to the SD of $\varepsilon_{\mathrm{flx}}$, called hereafter $r_{SD}^{\varepsilon_{\mathrm{LBC}}}, r_{SD}^{\varepsilon_{\mathrm{repr}}}, r_{SD}^{\varepsilon_{\mathrm{t}}}$ (Figure 2.4i, Figure 2.4c, Figure 2.4f), are used as indicators of whether $\varepsilon_{\mathrm{flx}}$ dominates the other types of error. $r_{SD}^{\varepsilon_{\mathrm{repr}}}$ is the smal-

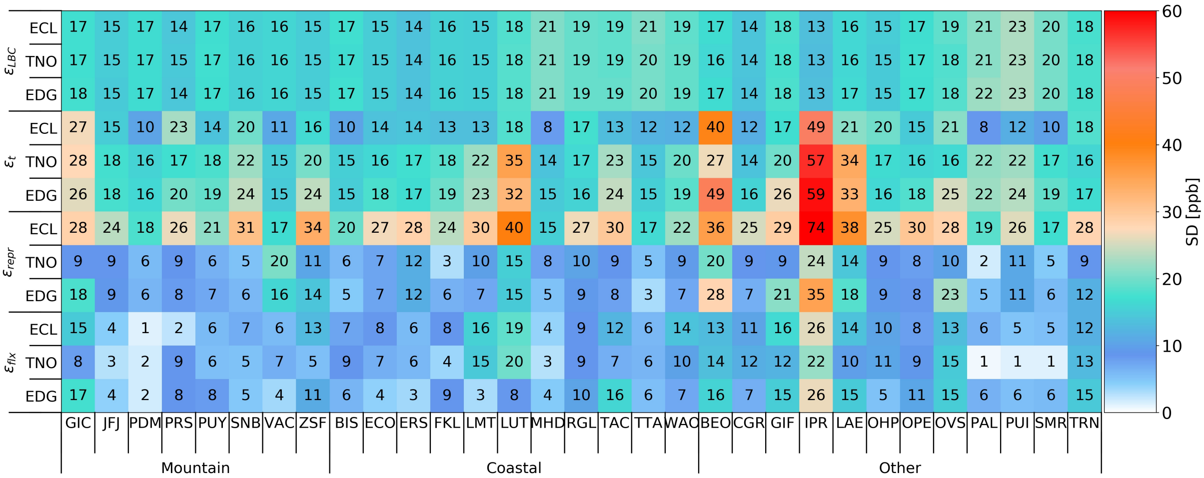

		GIC	JFJ	PDM	PRS	PUY	SNB	VAC	ZSF	BIS	ECO	ERS	FKL	LMT	LUT	MHD	RGL	TAC	TTA	WAO	BEO	CGR	GIF	IPR	LAE	OHP	OPE	OVS	PAL	PUI	SMR	TRN
ε_{LBC}	ECL	17	15	17	14	17	16	16	15	17	15	14	16	15	18	21	19	19	21	19	17	14	18	13	16	15	17	19	21	23	20	18
	TNO	17	15	17	15	17	16	16	15	17	15	14	16	15	18	21	19	19	20	19	16	14	18	13	16	15	17	18	21	23	20	18
	EDG	18	15	17	14	17	16	16	15	17	15	14	16	15	18	21	19	19	20	19	17	14	18	13	17	15	17	18	22	23	20	18
ε_t	ECL	27	15	10	23	14	20	11	16	10	14	14	13	13	18	8	17	13	12	12	40	12	17	49	21	20	15	21	8	12	10	18
	TNO	28	18	16	17	18	22	15	20	15	16	17	18	22	35	14	17	23	15	20	27	14	20	57	34	17	16	16	22	22	17	16
	EDG	26	18	16	20	19	24	15	24	15	18	17	19	23	32	15	16	24	15	19	49	16	26	59	33	16	18	25	22	24	19	17
ε_{repr}	ECL	28	24	18	26	21	31	17	34	20	27	28	24	30	40	15	27	30	17	22	36	25	29	74	38	25	30	28	19	26	17	28
	TNO	9	9	6	9	6	5	20	11	6	7	12	3	10	15	8	10	9	5	9	20	9	9	24	14	9	8	10	2	11	5	9
	EDG	18	9	6	8	7	6	16	14	5	7	12	6	7	15	5	9	8	3	7	28	7	21	35	18	9	8	23	5	11	6	12
ε_{flx}	ECL	15	4	1	2	6	7	6	13	7	8	6	8	16	19	4	9	12	6	14	13	11	16	26	14	10	8	13	6	5	5	12
	TNO	8	3	2	9	6	5	7	5	9	7	6	4	15	20	3	9	7	6	10	14	12	12	22	10	11	9	15	1	1	1	13
	EDG	17	4	2	8	8	5	4	11	6	4	3	9	3	8	4	10	16	6	7	16	7	15	26	15	5	11	15	6	6	6	15
		Mountain								Coastal											Other											

Figure 2.5: Standard deviations (SDs) of $\varepsilon_{\text{repr}}$, ε_{t}, ε_{flx} and ε_{LBC} for 2015 at the 31 selected measurement sites (details in Table 2.1). The colour and number give the same information.

lest relative error at about 1 over the entire domain (Figure 2.4c); $r_{SD}^{\varepsilon_{\text{LBC}}}$ and $r_{SD}^{\varepsilon_{\text{t}}}$ are often 2-6 (Figure 2.4i, Figure 2.4f) and therefore dominate ε_{flx}. Even though information about the statistics of these errors makes it possible to characterise these errors correctly, the resulting observation error matrix may be too complex due to technical limitations, e.g. it is too big for the system to deal with it in an affordable computing time. In this case, it is possible to include other variables, alongside the targeted emissions, in the control vector. In our case, the ratios of ε_{LBC}, $\varepsilon_{\text{repr}}$ and ε_{t} relative to ε_{flx} indicate that $\varepsilon_{\text{repr}}$ could be treated in the observation error statistics whereas the sources of ε_{LBC} and ε_{t} may better be controlled alongside the emissions in the inversion. Including LBCs in the control vector is usually done in regional inversions, but optimising the transport alongside emissions remains challenging in most state-of-the-art inversion systems, although first attempts exist (e.g. Zheng et al., 2018).

Temporal Patterns in ε_{LBC}, $\varepsilon_{\text{repr}}$, ε_{t} and ε_{flx}

Annual biases appear in ε_{LBC}, $\varepsilon_{\text{repr}}$, ε_{t} and ε_{flx} (Figure 2.4g, Figure 2.4a, Figure 2.4d and Figure 2.4j). As we have very few samples of errors (only three inventories), the average estimate is likely not representative of an actual bias, but rather indicates strong temporal correlations of errors. ε_{flx} and $\varepsilon_{\text{repr}}$ auto-correlations have characteristic time scales generally less than 15 days (Figure 2.6 and Figure 2.7), which correspond to the synoptic scale. ε_{t} scales range mainly between 5 and 50 days and ε_{LBC} scales are larger than one month over more than half the domain. In general, over continents, ε_{flx}, $\varepsilon_{\text{repr}}$

and ε_{t} have similar temporal scales. The similarity of structures requires that the magnitude of $\varepsilon_{\mathrm{flx}}$ is larger than the magnitudes of $\varepsilon_{\mathrm{repr}}$ and ε_{t} to ensure efficient filtering by the inversion system.

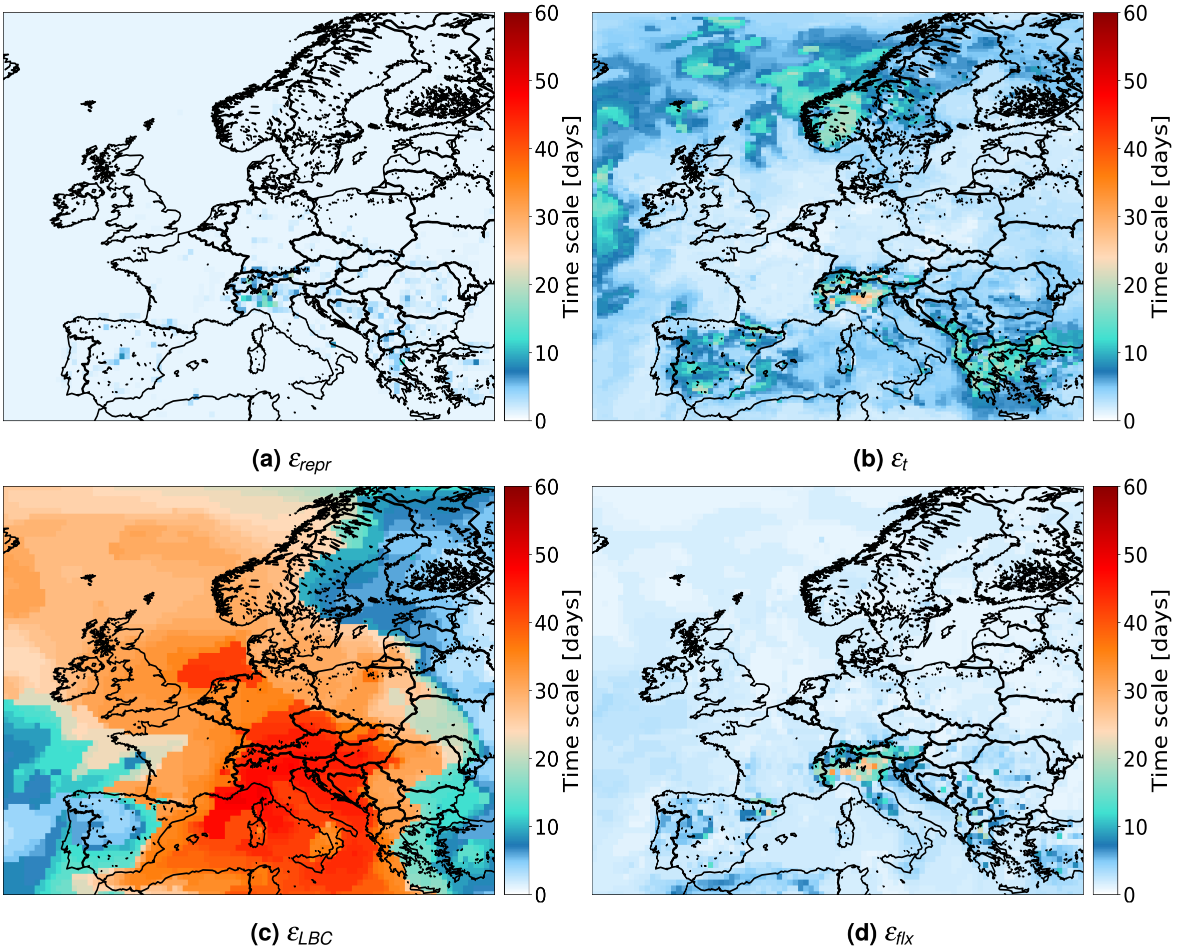

(a) ε_{repr} **(b)** ε_{t}

(c) ε_{LBC} **(d)** ε_{flx}

Figure 2.6: *Characteristic time scales (in days) of the decrease of temporal auto-correlation for ε_{repr}, ε_{t}, ε_{flx} and ε_{LBC} over the domain for 2015.*

Spatial Correlations in $\varepsilon_{\mathrm{LBC}}$, $\varepsilon_{\mathrm{repr}}$, ε_{t} and $\varepsilon_{\mathrm{flx}}$

The average spatial correlation structures of the different errors are presented in Figure 2.8. The longest characteristic scale is found for $\varepsilon_{\mathrm{LBC}}$ (2450 km) and the shortest for $\varepsilon_{\mathrm{flx}}$ (100 km) and $\varepsilon_{\mathrm{repr}}$ (≈50-100 km). The length of ε_{t} is intermediate (≈150-550 km). Lengths shorter than the size of one grid cell (≈50 km) indicate that spatial correlations may be neglected, as is the case for $\varepsilon_{\mathrm{repr}}$ for EDGAR and TNO-MACC. This suggests that a network of stations with a density higher than one station per 500 km would allow an inversion system to filter LBC and transport errors as their characteristic lengths are larger than 500 km with EDGAR and TNO-MACC. However, our results show that distinguishing between representation and transported-emission errors is challenging without a very dense network.

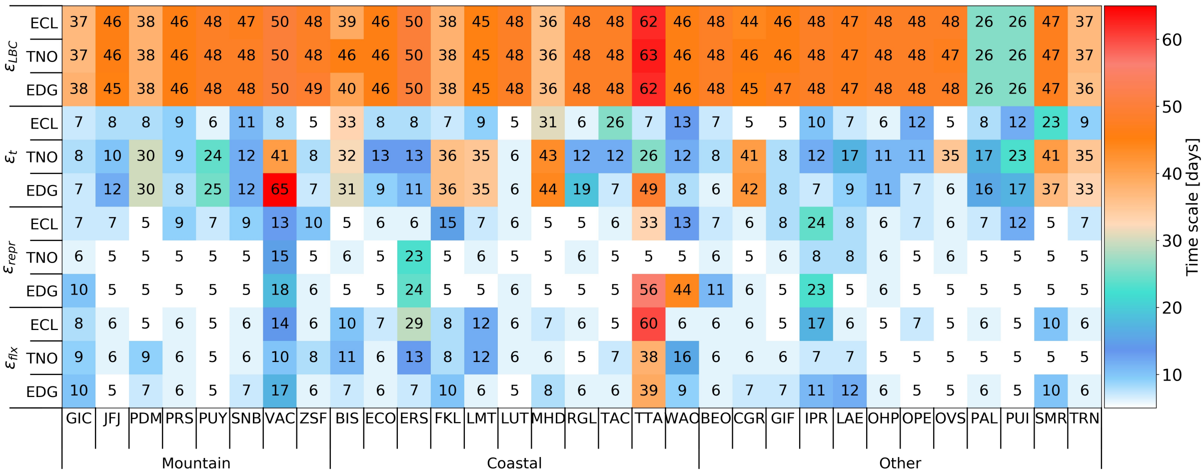

		GIC	JFJ	PDM	PRS	PUY	SNB	VAC	ZSF	BIS	ECO	ERS	FKL	LMT	LUT	MHD	RGL	TAC	TTA	WAO	BEO	CGR	GIF	IPR	LAE	OHP	OPE	OVS	PAL	PUI	SMR	TRN
ε_{LBC}	ECL	37	46	38	46	48	47	50	48	39	46	50	38	45	48	36	48	48	62	46	48	44	46	48	47	48	48	48	26	26	47	37
	TNO	37	46	38	46	48	48	50	48	46	46	50	38	45	48	36	48	48	63	46	48	46	46	48	47	48	48	47	26	26	47	37
	EDG	38	45	38	46	48	48	50	49	40	46	50	38	45	48	36	48	48	62	46	48	45	47	48	47	48	48	48	26	26	47	36
ε_{t}	ECL	7	8	8	9	6	11	8	5	33	8	8	7	9	5	31	6	26	7	13	7	5	5	10	7	6	12	5	8	12	23	9
	TNO	8	10	30	9	24	12	41	8	32	13	13	36	35	6	43	12	12	26	12	8	41	8	12	17	11	11	35	17	23	41	35
	EDG	7	12	30	8	25	12	65	7	31	9	11	36	35	6	44	19	7	49	8	6	42	8	7	9	11	7	6	16	17	37	33
ε_{repr}	ECL	7	7	5	9	7	9	13	10	5	6	6	15	7	6	5	5	6	33	13	7	6	8	24	8	6	7	6	7	12	5	7
	TNO	6	5	5	5	5	5	15	5	6	5	23	5	6	5	5	6	5	5	5	6	5	6	8	8	6	5	6	5	5	5	5
	EDG	10	5	5	5	5	5	18	6	5	5	24	5	5	6	5	5	5	56	44	11	6	5	23	5	6	5	5	5	5	5	5
ε_{flx}	ECL	8	6	5	6	5	6	14	6	10	7	29	8	12	6	7	6	5	60	6	6	6	5	17	6	5	7	5	6	5	10	6
	TNO	9	6	9	6	5	6	10	8	11	6	13	8	12	6	6	5	7	38	16	6	6	6	7	7	5	5	5	5	5	5	5
	EDG	10	5	7	6	5	7	17	6	7	6	7	10	6	5	8	6	6	39	9	6	7	7	11	12	6	5	5	6	5	10	6
		Mountain								Coastal											Other											

Figure 2.7: Characteristic time scales (in days) of the decrease of temporal auto-correlation for $\varepsilon_{\text{repr}}$, ε_{t}, ε_{flx} and ε_{LBC} with the three inventories at the 31 selected measurement sites (details in Table 2.1) for 2015.

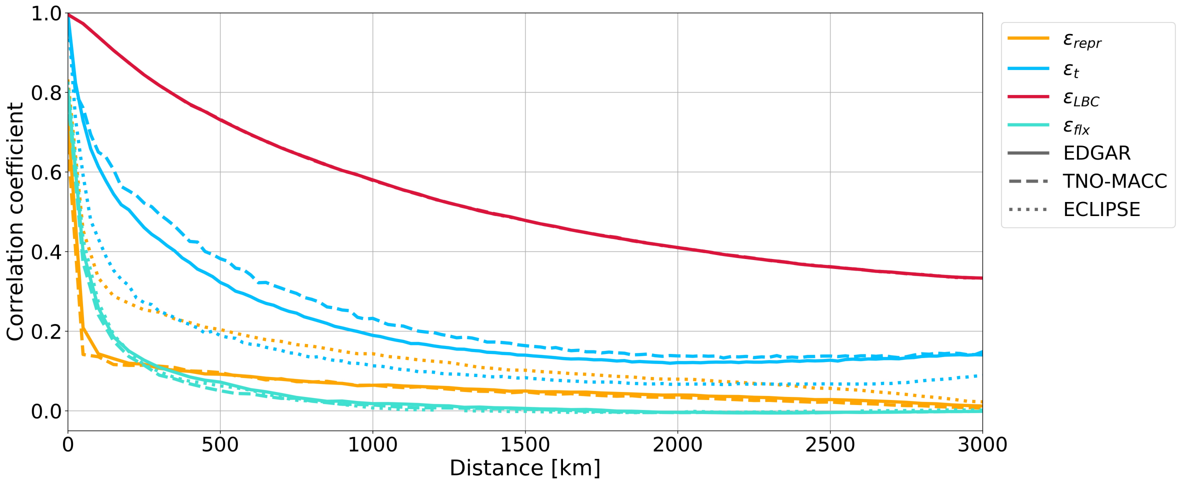

Figure 2.8: Spatial correlations over the whole domain for the three estimates of $\varepsilon_{\text{repr}}$, ε_{t} and ε_{flx} (indicated by the name of the emission inventory used, see Section 2.2.3.2 for details) and for the estimate of ε_{LBC}.

Most studies, such as Bergamaschi et al. (2018), Tsuruta et al. (2017), Locatelli et al. (2013) or Fortems-Cheiney et al. (2012), assume the concentration errors to be spatially uncorrelated, which is not what we would recommend following our results. In our case, not taking into account correlations due to error patterns common to various measurement locations would artificially increase the weight of observations in the cost function used in the inversion and erroneously attribute all correlated patterns to the emissions. This implies that non-diagonal correlation matrices should be used for the inversion, for which smart implementations are required.

2.2.4.2 Prior Emission Uncertainties e_{p}

Absolute Values of e_{p}

Some studies assume e_{p} to be homogeneous over the whole domain or per land-use categories, e.g. Bergamaschi et al. (2015) with 500% in monthly emissions (in their free inversion setting), Tsuruta et al. (2017) with 80% over land and Thompson et al. (2017) with 50% for total emissions. With the three inventories used here, e_{p} depends on the location and emission sector, as shown by the large SDs (up to 170%) for waste in almost all countries, for fossil fuel related sectors in some countries only (e.g. the United Kingdom, the Netherlands) compared to low values for agriculture in almost all countries (Figure 2.2f, Figure 2.2g, Figure 2.2h). The emissions in the 3 inventories differ most in the waste and the fossil fuel related sectors, with SDs of 58 to 122% and 35 to 124% (Table 2.6) at the national scale in the 12 selected countries. This can be explained by the different distributions of area and point sources used for these two sectors in the three inventories. The SDs are lowest in the agriculture sector with values $<$57%.

Table 2.6: Standard deviation relative to the average [%] between the three anthropogenic emission inventories for selected countries.

Country	Agriculture [%]	Waste [%]	Fossil fuel related sector [%]
AUT: Austria	29	99	54
BEL: Belgium	19	62	113
DEU: Germany	22	93	50
DNK: Denmark	29	62	48
ESP: Spain	28	104	48
FIN: Finland	48	122	124
FRA: France	37	83	35
GBR: United Kingdom	29	78	104
IRL: Ireland	16	99	118
ITA: Italy	57	80	41
NLD: The Netherlands	22	72	70
PRT: Portugal	34	58	46

The main hot-spots and high-emitting zones could be assumed to be often better known and therefore better located and specified in the inventories. This is the case for high-emitting zones such as the Netherlands or Brittany in France (Figure 2.2a), where the emissions are mainly due to the agricultural sector (Figure 2.2b): the spatial patterns of the three inventories are consistent (SDs $<$50%, Figure 2.2e, Figure 2.2f). Nevertheless, some high-emitting zones or hot-spots are not represented consistently in all three inventories: e.g. the off-shore fossil fuel sector in the North Sea (Figure 2.2c and Figure 2.2g).

Large differences between emission inventories are also found in low emitting areas, as denoted by the large SDs around the coasts (Figure 2.2a). With differences between emissions over land and sea being large, the effect of different horizontal resolutions becomes large at the coasts. With a CTM horizontal resolution lower than that of the inventory, land based emissions are attributed to grid cells encompassing actually land and sea areas. This problem is smaller with higher CTM horizontal resolutions. In general, the approach used for the spatial projection of emissions onto the CTM's grid impacts the patterns in the interpolated field (conservation of the mass over particular land-use categories for example) so that the interpolation method itself leads to errors. These discrepancies are a source of errors that impact specifically the assimilation of data from coastal measurement sites and need to be addressed in each system.

Spatial Correlations in e_p

The spatial correlations of the prior emission errors (Figure 2.9) indicate that an exponential decay function with a correlation length of $\approx$100-150 km could be used to model the errors for agriculture. For the waste sector and the fossil fuel related sectors, considering that the size of the model grid cells is approximately 50 km×50 km, we assume that spatial correlations can be neglected. Tsuruta et al. (2019) and Bousquet et al. (2011) (inversion INV1) assumed that the errors in emissions e_p are spatially uncorrelated, which is in agreement with our analysis for the fossil fuel related sectors. In the study of Bergamaschi et al. (2015) (inversion S1), uncertainties of 100% per grid cell and month and spatial correlation scale lengths of 200 km are applied to individual emission sectors. Compared to this setting, our analysis results in a lower average uncertainty and comparable spatial correlation lengths for agriculture and waste. Theoretically, higher uncertainties and lower spatial correlation lengths give more freedom for the inversion to optimise emissions.

Cross-Sector and Cross-Sector Cross-Country Correlations in e_p

Cross-sector correlations in e_p over the whole domain are presented in Figure 2.10a. These correlations are computed with a good level of significance and are very weak ($r < 0.1$), reflecting the overall independence of the

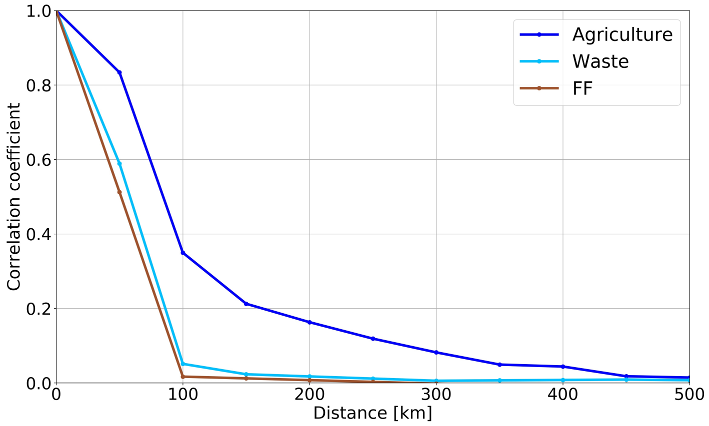

Figure 2.9: Spatial correlation lengths of the prior errors for the agriculture, waste and fossil fuel related (FF) sectors (see Section 2.2.2.2 for definition) per grid cell at the 0.5°×0.5° horizontal resolution.

sectoral emissions in the bottom-up inventories. We also compute cross-country cross-sector correlations (Figure 2.10b) for a subset of 12 countries (see country list in Table 2.6). The agriculture sector is correlated with no other sectors, which is consistent with the cross-sector correlations over the whole domain. However, the fossil fuel and waste sector exhibit non-negligible cross-country and cross-sector correlations ($r = 0.34$). These small correlations are likely indirect effects of spatial correlations embedded when building the bottom-up inventories, for example when using proxies such as population density for various sectors.

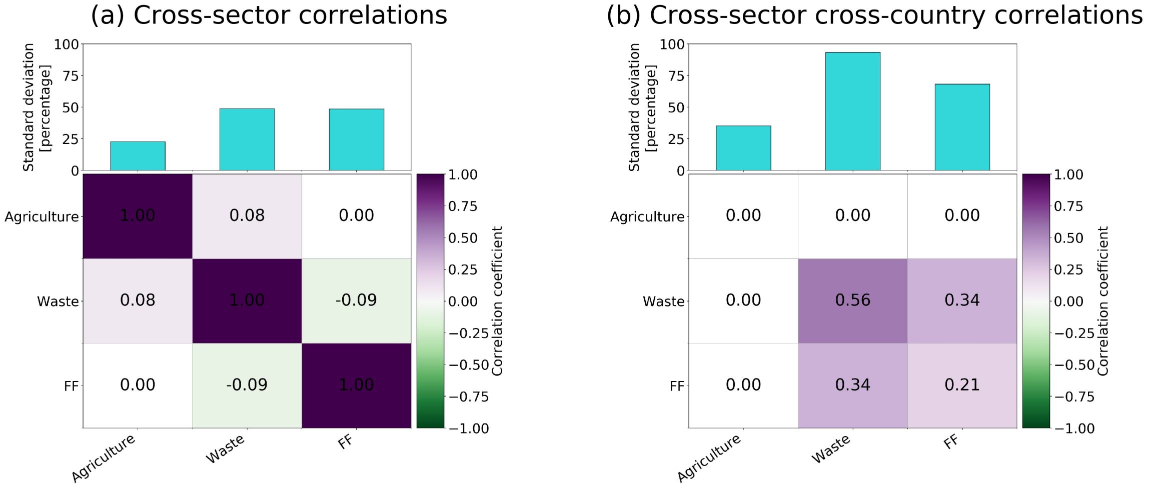

Figure 2.10: Correlations (colour matrices): cross-sector correlations over the European domain (left) and cross-sector cross-country correlations for 12 selected countries (right, see Table 2.6 for list). White = correlation not significant, green = negative correlation, violet = positive correlation. The matching standard deviations (in % of the average) are given in the top bar charts.

National-Scale Uncertainties: Comparison to Estimates from Other Studies

The national average emissions of the three inventories and the uncertainties estimated in this study are compared to the emissions and uncertainties in the UNFCCC national inventory reports (NIR) for the selected 12 countries (Figure 2.11). Compared to the NIRs, average emissions of the three inventories are for most countries underestimated in the agriculture sector but overestimated in the waste and fossil fuel related sectors. However, the average country totals of the emissions of the three inventories are still in the range of the NIR uncertainties, which is expected as the inventories are constructed by using similar information as in the NIRs.

Furthermore, the uncertainties in the NIRs are highest in the waste sector for most countries, in agreement with our estimated uncertainties. This suggests that the current knowledge of the activity data and emission factors of the waste emission sector remains less complete than that of the agriculture and fossil fuel related sectors. To deal with the large temporal and spatial variability of the emissions in the waste sector, specific climate and operational practices should be taken into account (National Academies of Sciences, Engineering, and Medicine, 2018).

To evaluate the results of this study, a comparison to top-down estimates from other studies at the national scale is also attempted (Table 2.7). Unfortunately, only a few studies estimate TD emissions at national scale for the countries that we have data available for. Thus, the comparison is only possible for France (Pison et al., 2018), Finland (Tsuruta et al., 2019), the United Kingdom and Ireland together and Germany (Bergamaschi et al., 2010). For these countries, estimates are statistically consistent at ± 1-sigma except for France. The years covered by these studies differ. However, we are interested mainly in the uncertainties and we assume that they do not vary much over the years available.

The uncertainties reported in TD studies are either larger (FRA and GB+IRL) or much larger (DEU, FIN) than the uncertainties estimated in this work for these four countries. This might be due to the inversions being too conservative and using large estimates of prior errors, which leads to large uncertainty estimates for the posterior emissions and/or this may be due to our error estimates being underestimated because of the similarities in the three inventories available for this study.

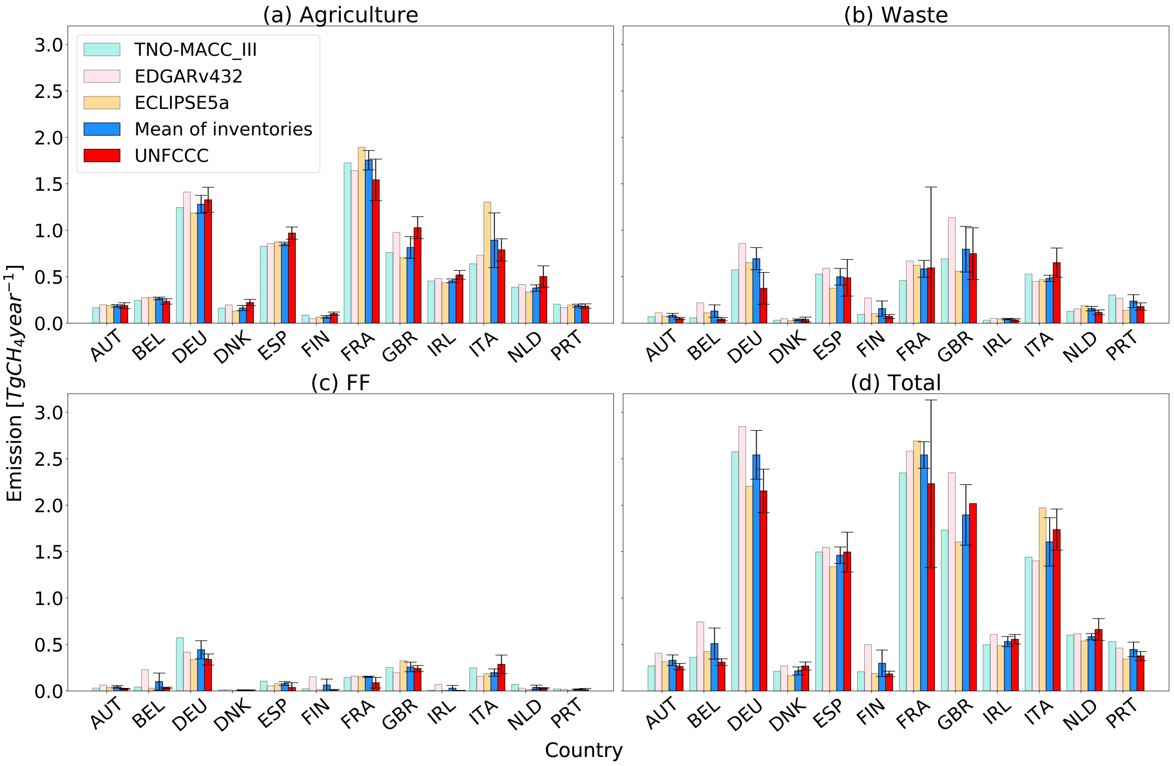

Figure 2.11: Anthropogenic CH_4 emissions ($TgCH_4$/year) of different source sectors of the TNO-MACC_III (2011), EDGARv4.3.2 (2011) and ECLIPSE V5a (2010) inventories and their average compared to the anthropogenic emissions of the UNFCCC (2017) for 12 selected countries (see Table 2.6 for list). The error bars indicate the uncertainties on the UNFCCC emissions and the uncertainties estimated here on the average inventory emissions. The uncertainty on total emissions of the United Kingdom could not be assessed as not all the necessary information is available in the NIR.

2.2.5 Conclusions and Recommendations

In this study, we aim at estimating errors that need to be taken into account in atmospheric inversions of CH_4 emissions at the European scale. We have used a simple (i.e. technically ready and not expensive in computing time) and easy to update method that consists of performing a set of simulations using two limited-area CTMs at three different horizontal resolutions with inputs based on three emission inventories and two sets of boundary and initial conditions. We have performed the analysis for the year 2015. Four types of errors have been estimated by computing differences of simulated hourly mixing ratios:

- the background error ε_{LBC}, due to the lateral boundary and initial conditions used by the area-limited CTMs;
- the representation error $\varepsilon_{\text{repr}}$, due to the difference of representativity between a model's grid-cell and atmospheric mixing ratio measure-

Table 2.7: Total anthropogenic emissions [$TgCH_4year^{-1}$] and associated uncertainties as 1-σ SD [$TgCH_4year^{-1}$ and %] from this study compared to top-down (TD) emission estimates and uncertainties from other studies and to the UNFCCC emissions and uncertainties.

	Germany	**Finland**	**France**	**United Kingdom and Ireland**
Our study	2.54 ± 0.26 (10%)	0.30 ± 0.14 (47%)	2.54 ± 0.14 (6%)	2.42 ± 0.61 (25%)
UNFCCC	2.15 ± 0.24 (11%)	0.18 ± 0.03 (17%)	2.23 ± 0.90 (40%)	2.57
TD studies	3.67 ± 1.25 (34%) [a]	0.31 ± 0.34 (110%) [b]	3.9 ± 0.31 (8%) [c]	3.29 ± 1.09 (33%) [a]

[a] Bergamaschi et al. (2010) (inversion S1, anthropogenic, average over the study years)
[b] Tsuruta et al. (2019) (anthropogenic)
[c] Pison et al. (2018) (sectoral run)

ments;

- the transport error ε_t, due to discretisation, parametrisations of the fundamental equations of the atmospheric transport used in a model and to the meteorological inputs used by the CTMs;
- the transported-emission error ε_{flx}, due to the misrepresentation of emissions on the spatial and temporal grid of the model.

To be consistent with the usual choice of data based on expert-knowledge, the errors have been computed from afternoon values (13 h to 17 h UTC included) for non-mountain sites and from night-time values (00 h to 04 h UTC included) for mountain sites, either in all the first-level grid-cells of the European domain or at the locations (horizontal and vertical grid cell) of 31 selected measurement sites. We have shown that this choice is not always optimal depending on stations and that it should be reassessed by inverse modellers.

The obtained error estimates allow us to gain insights into how these errors could be treated in a data assimilation system for inverting CH_4 emissions over Europe, as summarised in Table 2.8:

- ε_{LBC} appears to be simple to take into account because of its uniform structure with low variability, which makes it possible to differentiate it from the other errors. ε_{LBC} can be considered as a parameter to invert, in the observation error statistics, or could even be corrected beforehand. The relative magnitude of ε_{LBC} compared to ε_{flx} indicates that, in the inversion framework, the sources of ε_{LBC} may better be controlled alongside the emissions. This is consistent with what is usually done in regional inversions, which include lateral boundary and initial conditions in their control vector. At the scale studied here, long temporal ($>$1 month) and spatial ($>$2400 km) correlation lengths could be used to represent ε_{LBC}.

Table 2.8: Summary of the errors estimated in this study: main recommendations to treat each error in an inversion system for targeting CH_4 emissions in Europe at the yearly scale and orders of magnitude of correlation lengths which can be used to simply represent some of them.

Error	**Magnitude relative to $\varepsilon_{\mathrm{flx}}$**	**Recommended treatment**	**Temporal correlation lengths**	**Spatial correlation lengths**
$\varepsilon_{\mathrm{flx}}$	1	controlled (emissions are the main target of the inversion)	$<$15 days (due to meteorology, other sources of error in time not accounted for)	$\approx$100 km
$\varepsilon_{\mathrm{repr}}$	$\approx$1	in the observation statistics	$<$15 days	none
ε_{t}	2-6	controlled alongside the emissions	5-50 days	150 -550 km
$\varepsilon_{\mathrm{LBC}}$	2-6	controlled or in the prior statistic or pre-treated	$>$1 month	$>$2400 km
e_{p}	not studied	in the prior statistics	not accounted for	for agriculture: 100-150 km for other sectors: negligible
			other correlations: cross-sector agriculture & waste; fossil-fuel related & waste cross-sector cross country fossil-fuel related & waste	

- $\varepsilon_{\mathrm{repr}}$ and ε_{t} may be underestimated in our set of simulations close to hot-spots and high-emitting zones. This is due to the horizontal resolutions used for the simulations being coarser than the scale at which CH_4 emission patterns actually vary. Steep gradients of concentrations induced by steep gradients of emissions encountered in certain types of activity sectors (e.g. waste) can, therefore, not be represented well in our models' configurations. Even though hot-spots and high-emitting zones are key-regions for policy makers, in which a reduction of uncertainties on emissions brought by the inversions would be very useful, our study shows that observations near these areas should be used with caution with horizontal resolutions coarser than 0.25°×0.25°. The relative magnitudes of $\varepsilon_{\mathrm{repr}}$ and ε_{t} compared to $\varepsilon_{\mathrm{flx}}$ indicate that $\varepsilon_{\mathrm{repr}}$ can be treated in the inversion within the observation error statistics whereas the sources of ε_{t} may better be controlled alongside the emissions in the inversion. Nevertheless, optimising transport characteristics at the same time as emissions remains challenging in most state-of-the-art inversion systems. Moreover, spatial (from 150 to 550 km depending on the prior inventory) and temporal (from 5 to 50 days) correlation lengths would have to be used for ε_{t}, which may be an issue because of the technical challenge of inverting non-diagonal large matrices.

- $\varepsilon_{\mathrm{flx}}$ may be represented by short spatial correlation lengths ($\approx$100 km i.e. twice our coarsest resolution). Since emissions do not vary through the year in the inventories used here, temporal aggregation errors could not be studied and temporal patterns in $\varepsilon_{\mathrm{flx}}$ are only due to meteorology. In this case, the use of short temporal correlation lengths ($<$15 days) is recommended.

The spatial correlation lengths estimated here show that the error patterns cover a number of measurement sites, whereas the errors in in-situ fixed measurements are generally assumed to be uncorrelated in inversion systems.

Moreover, we have estimated the error in the emission inventories, e_{p}, particularly at the country and sector (agriculture, waste and fossil fuel related emissions) scales. Due to the assumptions and proxies used for the spatial distribution of area and point sources in the inventories, they differ the most for the waste and fossil fuel related sectors and agree better for agriculture at the European scale. This is particularly due to some high-emitting zones or hot-spots not being represented consistently, i.e. their locations and/or emissions vary between the three inventories. Discrepancies also arise from the projection of emissions onto the model's grid along the coasts, which may impact specifically the assimilation of data from coastal measurement sites. All cases where emission gradients between two neighbouring types of land-use are steep will lead to such an issue. Spatial correlation lengths that are recommended to represent e_{p} for agricultural emissions are $\approx$100-150 km. Cross-sector and cross-sector cross-country correlations show the impact of spatial correlations that are used in the inventories. Our simple analysis based on the 3 available inventories indicates that errors are heterogeneous and depend on the sector and country, which is in contrast with most inversion studies where the assumed uncertainties are homogeneous, with only land being different from sea. Finally, there is a need for an in-depth analysis and/or update of the spatial distribution of current emission inventories and for a more complete error estimation study dedicated to the inventories.

Following the method chosen here, further work should target the following:

- $\varepsilon_{\mathrm{repr}}$ and ε_{t} should be analysed on finer horizontal resolutions, mainly with the objective of assimilating satellite imaging
- ε_{t} should be more finely analysed with different meteorological inputs,

particularly to investigate the vertical mixing, which is known as a large source of error (Dabberdt et al., 2004).

- $\varepsilon_{\mathrm{flx}}$ and e_{p} could be improved by adding simulations based on other emission inventories; either including new inventories that may become available, or the same inventories with added features such as seasonal or hourly time profiles. Although natural emissions are small compared to anthropogenic contributions in Europe, they are not negligible everywhere, particularly in northern regions with natural wetlands. Their errors could be studied with the same methodology as the anthropogenic emissions.

Acknowledgements. We are grateful to the colleagues at TNO for their valuable support. We thank Matthew Lang, Diego Santaren and Audrey Fortems-Cheiney for their helpful advice. Calculations were performed using the resources of LSCE, maintained by François Marabelle and the LSCE IT team. We thank the PIs of the measurement sites we used in this study for maintaining methane measurements and for sharing their data through the following contributors: World Data Centre for Greenhouse Gases (WDCGG), Institut Català de Ciències del Clima (IC3), Swiss Federal Laboratories for Materials Science and Technology (Empa), Laboratoire des Sciences du Climat et de l'Environnement (LSCE), Ricerca sul Sistema Energetico (RSE), Integrated non-CO2 Greenhouse gas Observing System (InGOS), Integrated Carbon Observation System (ICOS), Umweltbundesamt (UBA), Environmental Chemical Process Laboratory (ECPL), National Oceanic and Atmospheric Administration (NOAA) Earth System Research Laboratories (ESRL), University of Bristol, Norwegian Institute for Air Research (NILU), University of Bern, Joint Research Centre (JRC), Observatoire des Sciences de l'Univers Institut Pythéas (OSU), Finnish Meteorological Institute (FMI), and University of Helsinki.

Funding. This project is part of the MEMO^2 (MEthane goes MObile - MEasurements and MOdelling) project and has received funding from the European Union's Horizon 2020 research and innovation programme under the Marie Sklodowska-Curie grant agreement No 722479.

Disclosure statement. The authors declare no competing interests.

Data availability statement. The data that support the findings of this study are available from the corresponding author upon request.

Chapter 3

Use of high-frequency atmospheric isotopic composition measurements for deriving information about model-measurement mismatches

3.1 Preamble

3.1.1 Context and aim of the study

In Chapter 2, we estimated errors connected to transport models and emission inventories. This chapter deals with the limitation regarding the scarcity of quasi-continuous atmospheric measurements of methane isotopologues across Europe (Section 1.6, page 24) and focuses on potential factors that can cause differences between measurements and simulations of atmospheric CH_4 mixing ratios and its stable isotopic ratios. The two potential main reasons, besides transport model errors, can be incorrect emission inventories and isotopic source signatures used for modelling atmospheric δ^{13}C and δ^{2}H isotopic ratios. This is investigated for δ^{2}H and δ^{13}C at the location of the coastal monitoring site Lutjewad in the Netherlands. Discrepancies between measured and simulated δ^{13}C are also examined at the continental site Heidelberg in Germany and the isotopic signature of the dominant source is determined.

3.1.2 Quasi-continuous isotopic measurements at a coastal monitoring site

Quasi-continuous measurements of CH_4 mixing ratios and stable isotopic ratios, δ^{13}C and δ^{2}H, were carried out from 3 November 2016 to 31 March 2017 at the Dutch monitoring site Lutjewad (Figure 3.2), located in the northern part of the Netherlands on the Wadden Sea coast. The measurements were carried out using an isotope measurement system based on a continuous flow isotope ratio mass spectrometry system (CF-IRMS, Röckmann et al., 2016; Menoud et al., 2020b). The measurements were analysed within the MEMO^{2} project by Menoud et al. (2020b). In Menoud et al. (2020b), measurements of CH_4 mixing ratios and δ^{13}C and δ^{2}H were investigated by Malika Menoud at the Institute for Marine and Atmospheric research Utrecht (IMAU). To support and further analyse the findings of Malika Menoud, simulations of CH_4 mixing ratios, as well as δ^{2}H and δ^{13}C isotope ratios were carried out using the atmospheric transport models FLEXPART-COSMO (Stohl et al., 2005; Baldauf et al., 2011) and CHIMERE. The simulations with FLEXPART-COSMO were performed by Randulph Morales at the Swiss Federal Laboratories for Materials Science and Technology (Empa), while the simulations with CHIMERE were carried out by me.

Menoud et al. (2020b) performed an in-depth analysis of the δ^{13}C and δ^{2}H measurements in order to identify the main sources of CH_4 in the region. A Keeling plot approach was used to obtain isotopic source signatures of pollution events during the measurement period. To do so, they applied a moving time window with a width of 12 hours and moving steps of 1 hour and selected suitable datasets by taking at least 5 data points and CH_4 mixing ratios enhancement of at least 200 ppb above background. The obtained average isotopic source signature based on the measurements of δ^{13}C and δ^{2}H for the five-month period is -59.5 ± 0.1‰ and -287 ± 1‰ for δ^{13}C and δ^{2}H, respectively. These are typical values for microbial CH_4 origin (agriculture and waste). It corresponds well to the type of land-use in the area around Lutjewad and in the Netherlands in general. The region is characterised by intensive agriculture and it has a high amount of livestock.

Furthermore, Menoud et al. (2020b) compared the measured isotopic composition to isotopic composition simulated by the two above mentioned CTMs using two anthropogenic emission inventories EDGARv4.3.2 and TNO-MACC_III. The source signatures were derived for the simulations as well, which were in good agreement with the measurements on the dominant CH_4 source type. Both δ^{13}C and δ^2H source signatures obtained from the measurements were overestimated by the models. Using one of the models, CHIMERE, the isotopic source signatures were for δ^{13}C -57.2 ± 0.2‰ and -55.2 ± 0.2 with EDGAR and TNO-MACC, respectively (Figure 3.1). The δ^2H source signature derived from simulations with EDGAR and TNO-MACC were -266 ± 2‰ and -254 ± 2‰, respectively. This suggests that either the δ^{13}C and δ^2H isotopic source signatures used for modelling are too high or that the emission in the two inventories are too low. This is investigated in Section 3.2.

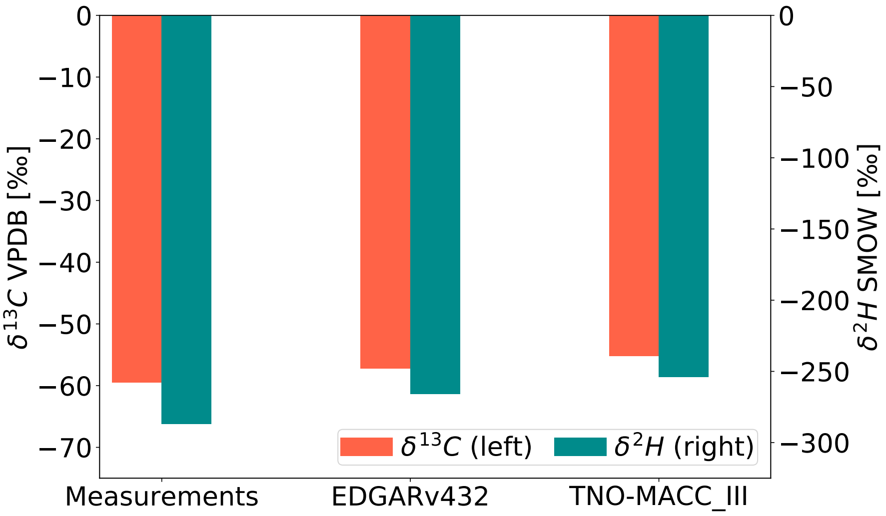

Figure 3.1: δ^{13}C and δ^2H source isotopic signatures derived from measurement and simulations of CH_4 mixing ratios and its isotopic composition for the coastal monitoring site Lutjewad (Menoud et al., 2020b). Simulations are performed with CHIMERE using the EDGARv4.3.2 and TNO-MACC_III anthropogenic emission inventories.

3.1.3 Quasi-continuous isotopic measurements at a continental monitoring site

Quasi-continuous time-series of CH_4 mixing ratios and its stable isotopic contents of δ^{13}C were measured from 12 November 2016 to 31 March 2017 in Heidelberg (Figure 3.2), located on the river Neckar in the state of Baden-Württemberg in South-West Germany. The land use around Heidelberg is mainly characterised by urban fabrics and farming (Jokar Arsanjani et al., 2013). The measurements were carried out using an analyser based on cavity ring down spectroscopy (CRDS) at the Institute of Environmental Physics of the Heidelberg University. The analyser continuously measures ambient air in the laboratory, regularly using calibration gas and quality control gas injections (Hoheisel et al., 2019).

Hoheisel et al. (2019) carried out surveys around Heidelberg and in North Rhine-Westphalia to characterise the δ^{13}C isotopic signature of several CH_4 sources. Samples were taken and mobile measurements were performed to study CH_4 sources from a natural gas distribution network, from a biogas plant, from dairy farms, a landfill, a waste water treatment plant, natural gas facilities and coal mines. The Miller-Tans approach combined with the York fit was used to obtain δ^{13}C isotopic signatures and corresponding uncertainties of the surveyed sources. The resulting mean δ^{13}C signatures are listed in Table 3.1.

Table 3.1: δ^{13}C source isotopic signatures determined in the study of Hoheisel et al. (2019), which are used as input for computing time-series of atmospheric δ^{13}C isotope ratios in the study presented in Section 3.3.

Source type	**Mean δ^{13}C [‰]**
Dairy farms	-63.9 ± 0.9
Biogas plant	-62.4 ± 1.2
Landfill	-58.7 ± 3.3
Waste-water treatment plant	-52.5 ± 1.4
Active deep coal mine	-56.0 ± 2.3
Natural gas	-43.3 ± 0.8

3.1.4 Overview of the study

We use the CTM CHIMERE in a domain covering mainly Northern France, the BENELUX and Western Germany (Figure 3.2). The size of the domain is reduced to avoid high computational costs as the simulations are carried out with a relatively high horizontal resolution of $0.1°\times0.1°$. The isotopic ratios of δ^{13}C and δ^{2}H are computed by combining simulated CH_4 mixing ratios of the main CH_4 sources and corresponding isotopic source signatures. This was done by applying the Equations 1.10 to 1.13 in Section 1.4 (page 19).

We analyse the measurements and simulations of CH_4 mixing ratios, δ^{2}H and δ^{13}C using wind roses. Wind roses provide a good insight on the general model performance and quality of the modelled wind fields and can be an asset for evaluating the magnitude and placement of sources in inventories. To conclude on the main cause(s) for discrepancies between measurements and simulations, we carry out different sensitivity analyses.

Our study in Section 3.2 complements the study of Menoud et al. (2020b)

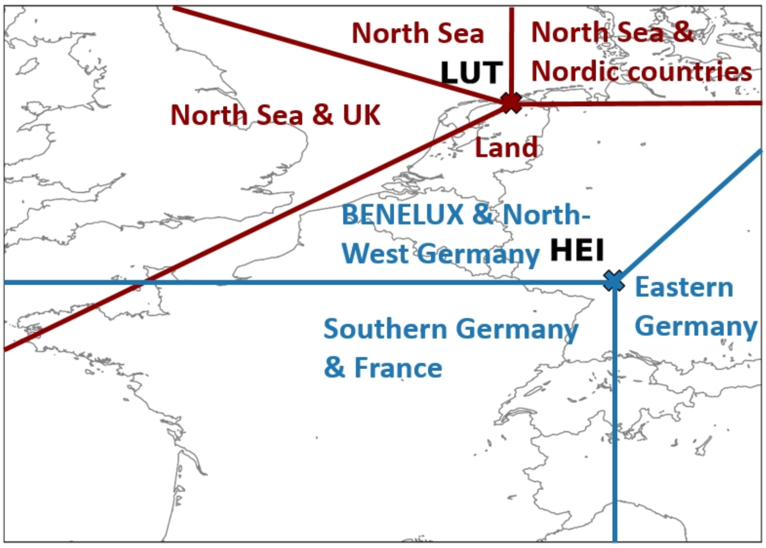

Figure 3.2: Model domain covering parts of Northwestern Europe, showing the locations of the measurement sites Lutjewad (LUT) and Heidelberg (HEI) and the geographical zones used in the studies in Sections 3.2 and 3.3. The colours of the lines depicting the geographical zones correspond to the measurement sites: blue=Heidelberg, red=Lutjewad.

and further investigates the simulation performance of CHIMERE combined with evaluating emission inventories, while analysing the influence of the modelled wind field and CH_4 boundary mixing ratios on the simulated values.

In Section 3.3, we further evaluate the emission inventories using δ^{13}C measurements of the same five-month period at the continental site Heidelberg. The isotopic source signatures determined by Hoheisel et al. (2019) are taken as input for modelling δ^{13}C isotopic ratios. Besides the wind rose analysis, we determine the dominant source by applying the Miller-Tans approach.

As a complement to the wind rose analyses in Sections 3.2 and 3.3, Figures A1 and A2 in the Appendix section A.1 illustrate the time series of the measured and modelled CH_4 mixing ratios and δ^{13}C isotope ratios for the German monitoring site Heidelberg, as well as CH_4 mixing ratios and δ^{13}C and δ^{2}H isotope ratios for the Dutch monitoring site Lutjewad. The figures also include the relative source contributions to the total simulated CH_4 mixing ratios above the simulated CH_4 boundary mixing ratios.

3.2 What can we learn about methane emissions from the comparison of measured and simulated methane isotopic ratios at a coastal monitoring site?

Article in preparation:

Barbara Szénási[1], Antoine Berchet[1], Isabelle Pison[1], Grégoire Broquet[1], Malika Menoud[2], Carina vander Veen[2], Bert Scheeren[3], Huilin Chen[3], Thomas Röckmann[2], and Philippe Bousquet[1]

[1] Laboratoire des Sciences du Climat et de l'Environnement, LSCE-IPSL (CEA-CNRS-UVSQ), Université Paris-Saclay, Gif-sur-Yvette, France

[2] Institute for Marine and Atmospheric Research Utrecht (IMAU), Utrecht University, the Netherlands

[3] Centre of Isotope Research, University of Groningen, the Netherlands

Abstract. The stable isotope (^{13}C and ^{2}H) contents of atmospheric methane (CH_4) are valuable tools to discriminate different types of CH_4 emissions. Isotope ratios of δ^{13}C and δ^{2}H, in addition to CH_4 mixing ratios, can improve the estimation of CH_4 emissions and their source attribution in atmospheric inversion studies. However, high-frequency, long-term measurements of isotope ratios remain scarce. In this study, we compare five-month long quasi-continuous measurements of CH_4 mixing ratios and its isotopic compositions δ^{13}C and δ^{2}H made at the Dutch coastal monitoring site Lutjewad to simulation outputs. Model-measurements mismatches are analysed through an ensemble of sensitivity tests. The simulations of CH_4 mixing ratios are performed using two anthropogenic inventories for a domain covering parts of Northwestern Europe. The δ^{2}H and δ^{13}C are computed using source contributions to the total simulated CH_4 mixing ratios, combined with their corresponding source isotopic signatures. Our results suggest that the isotopic source signatures used in the model are generally appropriate for the sources and that discrepancies between measurements and simulations are due to mismatches in emissions. Furthermore, the emissions of agricultural origin are underestimated in the inventories, whereas the fossil fuel emissions are overestimated. The comparison at a single site has limitations; mainly that our conclusions may not be representative for the entire domain studied here and most certainly not for all of Europe. Therefore, more long-term measurements of isotope ratios are needed to draw solid conclusions and bring more constraints on the CH_4 budget through atmo-

spheric inversions.

3.2.1 Introduction

Atmospheric methane (CH_4) is a potent greenhouse gas that is emitted through various anthropogenic activities, representing about 60% of global emissions, and through natural sources accounting for about 40% of global total emissions (Saunois et al., 2020). In Europe, $\sim$80% of emissions are anthropogenic and $\sim$20% are emitted through natural sources (Saunois et al., 2016a,b). Major European anthropogenic sources include landfills, waste water treatment plants, agricultural activities, enteric fermentation of cattle and other ruminants, non-industrial combustion (e.g. heating), as well as fossil fuel extraction, distribution and production (EEA, 2019). The dominant natural source in Europe is natural wetlands.

CH_4 emissions originate from complex processes, have many different sources and their emission factors highly vary in space and time, which poses challenges for emission quantification. This, paired with a relatively low density of sites measuring atmospheric CH_4 both on the global and European scale, leads to uncertainties in the sources and their estimates. Emissions are primarily estimated and characterised by bottom-up and top-down approaches. Bottom-up estimates of anthropogenic CH_4 emissions aggregate economic statistical information with the aid of activity data and average emission factors. Atmospheric inversion approaches are increasingly used to help improve and complement inventories. They optimally merge atmospheric measurements, atmospheric chemistry-transport modelling and prior knowledge on emissions.

However, there are considerable differences between bottom-up and top-down estimates of emissions. In the latter, the characterisation of emission sources often relies only on the knowledge gained from CH_4 mixing ratio measurements. This can make it difficult to attribute emissions to their specific source, especially if multiple types of sources (e.g. waste and gas) are close to each other or downwind of a measurement site. The stable isotope ratios of CH_4, quantified as $\delta^{13}C$ and $\delta^{2}H$, are, in principle, a valuable asset in addition to CH_4 mixing ratios to improve source discrimination of CH_4 emissions in atmospheric inversions (Mikaloff-Fletcher et al., 2004; Bousquet et al., 2006; Berchet et al., 2020; Gromov et al., 2017). This could improve source estimates of top-down studies and help decrease the discrepancies between bottom-up and top-down estimates.

The isotope signature in the background atmosphere, i.e. air containing lowest level of emissions, is appr. -47‰ in case of δ^{13}C and appr. -85‰ in case of δ^{2}H (Dlugokencky et al., 2011). The isotopic composition of the emitted CH_4 from different sources depends on the isotopic composition of the substrates and the isotope effects associated with the production process. Biogenic CH_4 is produced from organic matter by anaerobic bacteria and is generally more depleted in ^{13}C than the background atmosphere. Such anthropogenic sources, e.g. domestic animals, waste water treatment and wetlands, have isotope signatures between -74‰ and -46‰ for δ^{13}C and between -358‰ and -281‰ for δ^{2}H (Sherwood et al., 2017). Thermogenic CH_4, e.g. fossil fuel production and natural gas seeps, is generated from the breakdown of organic matter at high temperatures and high pressure, and the isotope signatures usually range ranges between -87‰ and -15‰ for δ^{13}C, and between -415‰ and -62‰ for δ^{2}H. Pyrogenic CH_4 is formed by incomplete combustion of biomass (wild fires), of biofuels (domestic wood burning) and fossil fuels. Pyrogenic CH_4 sources are enriched in heavy isotopes relative to the background atmosphere and to both biogenic and thermogenic sources. Wetlands have typical signatures between -79‰ and -48‰ for δ^{13}C and between -450‰ and -288‰ for δ^{2}H.

Atmospheric measurements of isotopic signatures of sources have been used to characterise emissions from various sources (e.g. Zazzeri et al., 2017; Townsend-Small et al., 2016; Lowry et al., 2001). Such measurements are often carried out by collecting air samples on ground or on small aircrafts that are later measured in laboratory. For example, Zazzeri et al. (2017) sampled CH_4 emission plumes in the London area and found that CH_4 emissions are underestimated and spatially not well characterised in the inventory they evaluated. However, there is a lack of measured signatures of emission sources. Due to that, the spatial and temporal variability, as well as the possible range of signatures of the specific source types in different locations is yet to be surveyed and remains, therefore, uncertain. This is one of the limitations in the use of isotopes to improve our understanding of the CH_4 cycle. Isotopic signatures of CH_4 sources are also used to tune CTM's for forward simulation of δ^{2}H and/or δ^{13}C. Those simulations are usually compared to measurements for interpreting the data gained from measurements and demonstrating the regional influence of emission sources (e.g. Thonat et al., 2019; Warwick et al., 2016; Monteil et al., 2011).

To date, measurements of methane isotope ratios δ^{13}C and δ^{2}H, especially long-term or quasi-continuous in-situ measurements are even scarcer both globally and in Europe than isotopic source signature measurements (e.g. Menoud et al., 2020b; Röckmann et al., 2016; Tyler et al., 1999). This is another major limitation. However, isotopic ratios assimilated in atmospheric inversions have the potential to constrain the CH_4 budget and reduce uncertainties of sources when combined with measurements of CH_4 mixing ratios (e.g. Quay et al., 1999; Mikaloff-Fletcher et al., 2004; Rigby et al., 2012).

Menoud et al. (2020b) presented quasi-continuous isotope measurements of atmospheric CH_4, δ^{13}C and δ^{2}H, that were performed at the atmospheric monitoring site Lutjewad (LUT), the Netherlands, at the North Sea coast. This data set is one of the very few high-frequency isotopic measurements available in Europe. They showed that the main sources of CH_4 emissions in the surroundings of LUT are associated with agricultural practices. In addition to their extensive analysis of the isotopic signatures, they compared the measurements to the simulations made by two transport models, each using two anthropogenic emission inventories. The isotopic ratios were computed from simulated source sector contributions of CH_4 mixing ratios combined with isotopic signatures of the particular sources. The source signatures were taken from several available literature. Even though the simulations generally underestimated the measurements of CH_4 mixing ratios and overestimated the δ^{13}C and δ^{2}H isotope ratios, they correlated well with the measurements. The study of Menoud et al. (2020b) indicates that it is important to use isotope source signatures that are representative for the respective study area; global average numbers are often not sufficient.

Here, following Menoud et al. (2020b) using the same modelling set-up, we investigate discrepancies between measurements and simulation outputs at LUT in more detail by conducting an ensemble of analysis and sensitivity tests. In this forward modelling study, we focus on the contribution of main emission sources (agriculture, waste, fossil fuel and natural wetland) to the total CH_4 mixing ratios and their impact on the computed isotopic composition at LUT. The importance of the modelled boundary conditions connected to the computed isotopic signatures is investigated as well.

The measurements at LUT and the modelling framework, including the method for computing the isotopic compositions δ^{13}C and δ^{2}H, are described in Section 2. Section 3 deals with the analysis tools used in this study. The results are presented and discussed in Section 4 with a focus on the influence of the emissions and the isotopic source signatures on the computed isotopic time series at LUT.

3.2.2 Measurements and modelling framework

3.2.2.1 Measurements

Measurements of CH_4 mixing ratio and its isotopic compositions $\delta^{13}C$-CH_4 and δ^2H-CH_4 were carried out at the atmospheric measurement site Lutjewad from November 3 2016 to March 31 2017 (Menoud et al., 2020b). The site is equipped with a 60m-tall tower and is located in the northern part of the Netherlands on the Wadden Sea coast (Figure 3.3). The land-use in the studied domain (Figure 3.3) can be characterised by intensive agriculture, including dairy farms and vegetables. Furthermore, natural gas is extracted from sandstone layers at about 3 km depth. In the North Sea, a large number of oil and gas extraction platforms are located west and north-west from LUT.

The measurements were performed using an isotope measurement system based on a continuous flow isotope ratio mass spectrometry system (CF-IRMS) that was set up at the Lutjewad site. $\delta^{13}C$ and δ^2H were measured alternatively by one IRMS instrument, after conversion to CO_2 and H_2, respectively. The system, the extraction process and the data handling is described in detail in Menoud et al. (2020b) and in Röckmann et al. (2016). The resulting time series of $\delta^{13}C$ and δ^2H have a non-regular temporal resolution of 51 minutes on average. During an isotope measurement, the CH_4 mixing ratios were also determined. Therefore, the measurement process lead to two time series of CH_4 mixing ratio; one time series when $\delta^{13}C$ was measured and a second one when δ^2H was measured.

The meteorological data collected at LUT were incomplete, therefore, wind measurements at 10m height are used from the monitoring site Lauwersoog. Lauwersoog is located about 10 km from LUT and is operated by The Royal Netherlands Meteorological Institute (KNMI). Menoud et al. (2020b) analysed the incomplete wind data measured at LUT and the wind data from Lauwersoog and found that the two data sets are very similar in wind characteristics.

3.2.2.2 Modelling framework

We use the regional transport model CHIMERE (Menut et al., 2013, Mailler et al., 2017) driven by the PYVAR system developed for forward comparison of model outputs and observations and variational inversions (Fortems-Cheiney et al., 2019). The model domain covers parts of Northwestern Europe; [43.6° - 55.6°] in latitude and [5° - 12°] in longitude (Figure 3.3). The main characteristics of the model and its configuration are described in Table 3.2.

We carried out simulations at a horizontal resolution of 0.1°×0.1°. The meteorological data used to drive the model are obtained from the European Centre for Medium-Range Weather Forecast (ECMWF) operational forecast product. The boundary and initial conditions are taken from the analysis and forecasting system developed in the Monitoring Atmospheric Composition and Climate (MACC) project (Marécal et al., 2015). The global concentration fields and the meteorological products are spatially and temporally interpolated to our model grid.

Most CTMs incorporate only basic planetary boundary layer (PBL) parameterisations. Due to that, the mixed layer depth of the PBL is not always well represented in transport models, which negatively affects the vertical mixing (Dabberdt et al., 2004). This mainly occurs during night with the mixed layer depth not being shallow enough in CTMs. The vertical mixing is usually largest and better represented in the afternoon. This PBL representation issue is a known and significant source of transport model error. In order to limit the impact of this error on the simulation outputs, we have analysed at which time of the day the measurements are best reproduced by CHIMERE. We have compared the measured and simulated CH_4 mixing ratios sampled at the grid-cell matching the location of LUT during morning, afternoon and night. Following it, we select measurements in the afternoon between 12 and 17 UTC that we compare to simulations sampled at the location of LUT in this study.

Emissions

The annual mean anthropogenic emissions driving the model are taken from the TNO-MACC_III (Kuenen et al., 2014) and the EDGARv4.3.2 (Janssens-Maenhout et al., 2017) emission inventories. When we conducted this study, the inventories did not include the study years 2016 and 2017 so that we use the anthropogenic emissions from the most recent available year in each inventory (Table 3.3). We group the emissions into Selected Nomenclature for Air Pollution (SNAP) level-1 sectors to have a common ground for the inventories, as they use different classifications. The main emitting sectors of CH_4 in the study area are agriculture (SNAP 10) and waste (SNAP 9). Other relev-

Table 3.2: Setup of the atmospheric transport model CHIMERE for the simulations between November 2016 and March 2017. The resolutions indicated for "Meteorology" and "Boundary and initial conditions" are the original ones, from which the data are interpolated on the horizontal and vertical resolution of the domain grid.

Meteorology	ECMWF
Horizontal resolution	10×10 km
Frequency of data availability	3 hours
Boundary and initial conditions	MACC
Vertical levels	71
Horizontal resolution	0.653° × 0.653°
Frequency of data availability	3 hours
Number of levels	29
Top pressure	300 hPa
Anthropogenic emissions	EDGARv4.3.2 and TNO-MACC_III
Natural emissions	ORCHIDEE-WET
Horizontal resolution	0.1° × 0.1°
Period simulated	12 November 2016 - 31 March 2017

ant emission sources for CH_4 are non-industrial combustion plants (SNAP 2) and the production, extraction and distribution of fossil fuels (SNAP 5). These two sectors are added into one category and named "fossil fuel related emissions" hereafter. Emissions from sources other than the above mentioned are named "other" anthropogenic sources. As wetlands are the main natural CH_4 source in Europe, we include natural wetland emissions in the simulations. We obtain the yearly natural wetland emissions from the ORCHIDEE-WET model (Ringeval et al., 2011). The annual average anthropogenic and wetland emissions used in the study for the model domain are shown in Figure 3.3.

Table 3.3: Description of the anthropogenic emission inventories and the wetland emissions

Inventory/model	TNO-MACC_III	EDGARv4.3.2	ORCHIDEE-WET
Coverage	Europe	Global	Global
Spatial resolution	0.125°×0.0625°	0.1°×0.1°	1°×1°
Temporal resolution	Yearly	Monthly and yearly (yearly used)	Yearly
Available years	2000-2011	1970-2012	1935-2009
Years used	2011	2011	2009

Due to the paucity of information on high-resolution activity data of CH_4, the temporal variability of CH_4 sources is not yet well understood. As a result, CH_4 emissions do not have high temporal, e.g. hourly, profiles. Hence, the hourly variation of the simulation outputs depends only on the meteorology, as well as the boundary and initial conditions. This is another source of transport model error that can contribute to mismatches between simulations and measurements.

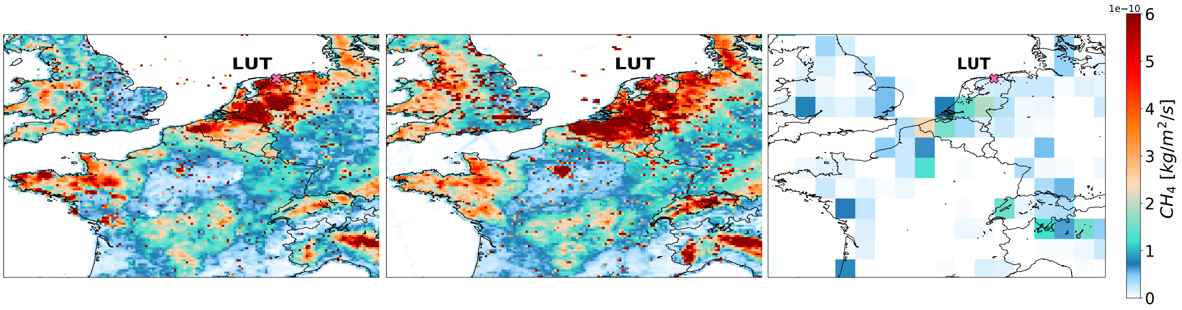

(a) TNO-MACC_III **(b)** EDGARv4.3.2 **(c)** ORCHIDEE-WET

Figure 3.3: Total anthropogenic methane emissions in the emission inventories in our domain for 2011 in case of TNO-MACC and EDGAR, and the wetland emissions from ORCHIDEE-WET for 2010. The study site Lutjewad is indicated by the rose-coloured circle and its three-letter code "LUT".

Computation of the isotopic ratios δ^{13}C and δ^{2}H

The δ^{13}C and δ^{2}H isotope ratios are computed by combining for each hour the simulated CH_4 mixing ratios per source category and the corresponding source signatures. The used input source signatures and the average simulated CH_4 mixing ratios per source are listed in Table 3.4. As the study of Menoud et al. (2020b) indicated that their source signatures, obtained as the average of several global studies, are not representative enough for the region around LUT, we adjusted the source signatures of some sources in our domain, based on source signatures derived from measurements within the MEMO^2 project (Menoud et al., 2020a).

Table 3.4: Summary of the absolute CH_4 mixing ratios [ppb $\pm$ 1σ], their relative contribution [% $\pm$ 1σ] to the total mixing ratios in the grid-cell matching the location of Lutjewad and the corresponding characteristic source isotopic values used as input for the computation of the isotopic compositions δ^{13}C and δ^{2}H. The δ^{13}C source isotopic value for the boundary mixing ratios represents the mean value of the LMDz simulations of δ^{13}C used as background δ^{13}C values. Note that the relative contributions of the sources indicate the source contributions to CH_4 mixing ratios above background, and that the relative contribution of the background indicates the contribution to the total mixing ratios.

Source sector	CH_4 [ppb] EDGARv4.3.2 & ORCHIDEE-WET	CH_4 [ppb] TNO-MACC_III & ORCHIDEE-WET	Contribution [%] EDGARv4.3.2 & ORCHIDEE-WET	Contribution [%] TNO-MACC_III & ORCHIDEE-WET	δ^{13}C [‰]	δ^{2}H [‰]
Agriculture	71 ± 67	65 ± 60	63 ± 14	60 ± 13	-64.0	-301
Waste	26 ± 29	24 ± 29	18 ± 10	17 ± 8	-58.0	-285
Fossil fuel related emissions	14 ± 17	18 ± 22	11 ± 6	14 ± 7	-40.0	-175
Other anthropogenic sources	3 ± 3	4 ± 5	2 ± 1	3 ± 2	-35.0	-150
Wetland	7 ± 8	7 ± 8	6 ± 3	6 ± 3	-71.0	-330
Boundary mixing ratios	1947 ± 45		95 ± 4		-47.7 (mean)	-87 (mean)

Based on the results of Menoud et al. (2020b), we have changed some of the source isotopic signatures. We use δ^{13}C and δ^{2}H signatures for agricultural sources being by 4‰ and 18‰, respectively, heavier than the ones in Menoud et al. (2020b). For the waste sources, we apply 8‰ heavier δ^{2}H and 3‰ lighter δ^{13}C isotopic source signatures. We increased the δ^{2}H isotopic signature by 25‰ for the "other" anthropogenic sources, while we decreased the δ^{13}C isotopic signature by 2‰ for wetlands.

The isotopic ratios used for the background in combination with the simulated CH_4 boundary mixing ratios are taken from global simulations of δ^{13}C and δ^{2}H from Thanwerdas et al. (2019). These isotopic simulations are carried out with the Laboratoire de Meteorologie Dynamique (LMDz) global model (Hourdin et al., 2006) and have 3-hourly temporal resolution outputs. We use the δ^{13}C and δ^{2}H time series obtained from a model grid-cell above the North Atlantic as background as the air masses in Europe often originate from that direction. As the spatial variation of δ^{13}C and δ^{2}H is low in the North Atlantic, we consider these δ^{13}C and δ^{2}H simulations adequate for the background conditions of our Western European domain. In the study of Menoud et al. (2020b), offsets were applied to the simulated background δ^{13}C and δ^{2}H to better match the isotope scales identified in an international inter-comparison (Umezawa et al., 2018). We apply the same offsets of -0.3‰ for δ^{13}C and +12‰ for δ^{2}H in this study, that lead to an average background of -47.7‰ for δ^{13}C and -87‰ for δ^{2}H.

3.2.3 Analysis tools

We compare the simulations of CH_4 mixing ratios and of δ^{13}C and δ^{2}H values to the measurements and evaluate the model performance computing the Pearson correlation coefficient r, the mean bias error (MBE) and the root mean squared error (RMSE). The MBE is computed in ppb and in percentage, compared to the average measured CH_4 mixing ratios, δ^{13}C and δ^{2}H at LUT, respectively. When analysing the CH_4 mixing ratios, we use the combination of the two measured CH_4 time series (Section 3.2.2.1). For the analysis of CH_4 mixing ratios and isotopic ratios at the same time, we use the CH_4 time series that were taken during the extraction of the corresponding isotopic composition.

3.2.3.1 Analysis of the modelled wind fields

Before analysing the simulated mixing ratios and isotopic compositions in Section 3.2.4, we shortly compare the modelled wind fields to the measured wind fields in Figure 3.4 to assess whether it contributes to the measurement-simulation mismatch. The measured wind fields are generally well reproduced by the model with a correlation coefficient of r=0.9 for both the wind direction and the wind speed. The standard deviation (SD) of the simulated wind speed and direction is similar to that of the measured ones. The modelled wind direction is misaligned by appr. 3° on average compared to the observed wind direction. The measured wind speed is underestimated by 0.5 ms^{-1} on average by the model. In general, there are only 5 cases out of the total 3330 data points with high speeds (> 15 ms^{-1}) in the modelled wind field.

To reduce the impact of discrepancies between the measured and modelled wind fields on the simulations, we analyse the measured and simulated CH_4 mixing ratios and isotope ratios using wind roses, i.e. function of the wind speed and direction. Doing so, we can investigate whether the simulations are generally in agreement with the measurements regarding location and magnitude of the sources, even if some pollution events at given times are not well reproduced by the model.

For wind roses, we categorise the wind direction and speed with a bin size of 2.4 ms^{-1} and 22.5°, respectively. This is done by combining the measured wind direction and speed with the measured CH_4 mixing ratios, δ^{13}C and δ^{2}H isotope ratios, as well as by combining the simulated wind direction and speed with the simulated CH_4 mixing ratios, δ^{13}C and δ^{2}H isotope ratios.

Using such wind roses, geographical zones are defined in the study domain to evaluate the model performance on the placement of sources. The geographical zones correspond to the following wind directions:

- Land, including the BENELUX and Germany: 90° - 225°
- North Sea & UK: 225° - 292.5°
- North Sea: 292.5° - 359°
- North Sea & Nordic countries (Denmark and Norway): 0° - 90°

3.2.4 Results and discussion

3.2.4.1 General investigation of the model performance

The comparison of measured and simulated CH_4 mixing ratios is shown in Figure 3.5 as a function of wind direction and speed. Large measured CH_4 mixing ratios originate from the land (South) with a maximum value of about 2875 ppb, while the lowest measured mixing ratios of about 1900 ppb, associated with background, come from the North Sea (Northwest). Simulations made with both inventories agree with the measurements and produce max-

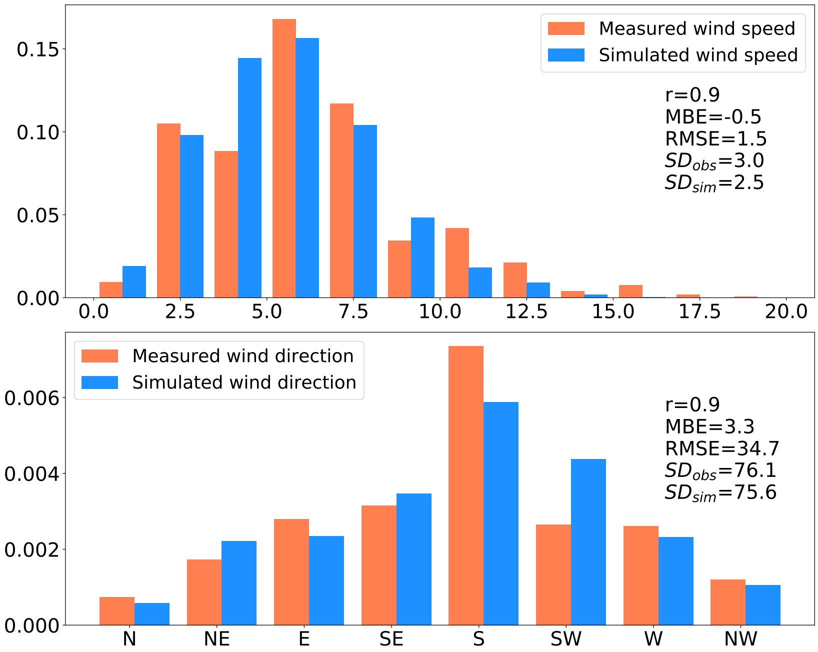

Figure 3.4: Comparison of the measured and simulated 10m-wind speed in ms^{-1} (top panel) and direction in ° (bottom panel). Furthermore, the statistical measures Pearson correlation coefficient (r), mean bias error (MBE), root mean squared error (RMSE) and standard deviation (SD) are displayed.

imum CH_4 mixing ratios of about 2590 ppb and 2550 ppb with EDGARv4.3.2 and TNO-MACC_III, respectively, over land, and minimum CH_4 mixing ratios of about 1900 ppb with both inventories, originating from the North Sea direction. Table 3.5 summarises the results of the statistical analyses carried out on measured and simulated data. The simulations underestimate the measured CH_4 mixing ratios by appr. 37 ppb (EDGARv4.3.2) and 39 ppb (TNO-MACC_III) and correlate well with the measurements (correlation coefficient of 0.83 for EDGAR and 0.82 for TNO-MACC).

The wind roses of the measured and simulated isotopic compositions δ^{13}C and δ^{2}H are shown in Figure 3.6. The correlation coefficients are good; 0.83 and 0.81 for δ^{13}C, as well as 0.79 and 0.78 for δ^{2}H for the EDGARv4.3.2 and TNO-MACC_III inventories, respectively. In general, the simulated isotopic ratios are not depleted enough compared to the measured ones. The measured isotopic ratios are overestimated on average by 0.27‰ and 0.33‰ for δ^{13}C and by 4.62‰ and 5.2‰ for δ^{2}H in case of EDGAR and TNO-MACC, respectively. The mean bias values for δ^{13}C are less than 1% compared to the average of the measured δ^{13}C, while it is up to 7% for δ^{2}H (Table 3.5). Röckmann et al. (2016) consistently found that the simulations made using previous versions of these inventories (EDGARv4.2 FT2010 and TNO-MACC_II)

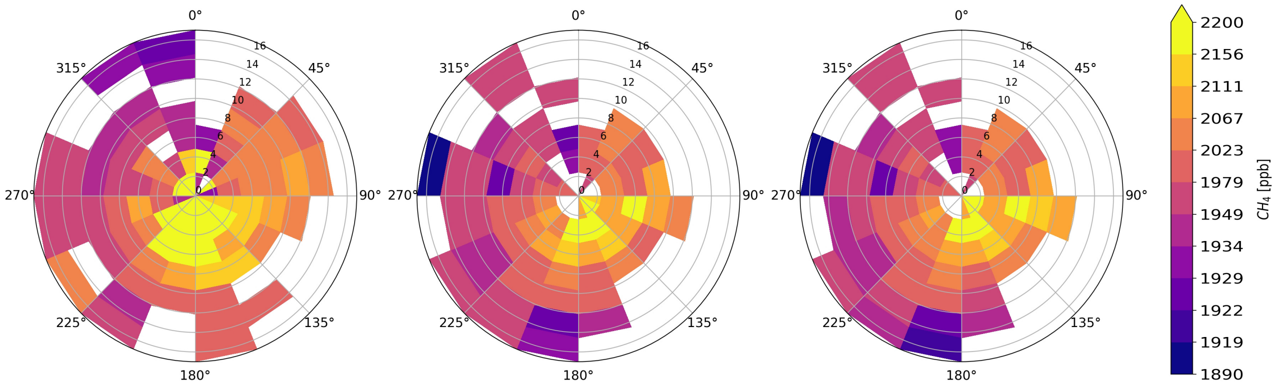

(a) Measurements **(b)** EDGARv4.3.2 **(c)** TNO-MACC_III

Figure 3.5: Hourly afternoon data of the total CH_4 mixing ratios as function of wind speed and wind direction for the period November 2016 - March 2017. The measurements are shown in sub-figure a) and the simulations made using the EDGARv4.3.2 and TNO-MACC_III inventories in sub-figures b) and c), respectively.

underestimated the measured CH_4 mixing ratios and produced simulated $\delta^{13}C$ and $\delta^{2}H$ too enriched compared to the measurements at another Dutch monitoring site, Cabauw. The versions of inventories used in this study still underestimate the different CH_4 mixing ratios, which could be the reason for the measurement-simulation mismatches in the isotopic composition. The largest differences between measurements and simulations of isotopic composition occur for the land origin, as for the CH_4 mixing ratios of Figure 3.5. However, the correlation between simulations and measurements is best for the land origin, while it is poorest for values from the North Sea. It could indicate issues with CH_4 boundary conditions as mostly background air is transported to LUT from this direction, according to the measurements.

Comparing the simulation performance for $\delta^{13}C$ and $\delta^{2}H$ in Table 3.5 shows that simulated $\delta^{13}C$ are in better agreement with measured $\delta^{13}C$ than for $\delta^{2}H$. An explanation can be that we use more realistic input isotopic values for $\delta^{13}C$ than for $\delta^{2}H$ for the dominating sources, as $\delta^{2}H$ signatures have been less studied so far.

3.2.4.2 Analysis of model-measurement mismatches by sensitivity analysis and source contributions of CH_4 mixing ratios

The underestimation of the CH_4 mixing ratios from the land zone, leading to too enriched isotopic ratios as shown in Section 3.2.4.1, could come from the underestimation of emissions in the inventories. Yet, too enriched isotopic source values can also contribute to or even be the main cause of the overestimation of the isotopic measurements. A detailed analysis of the

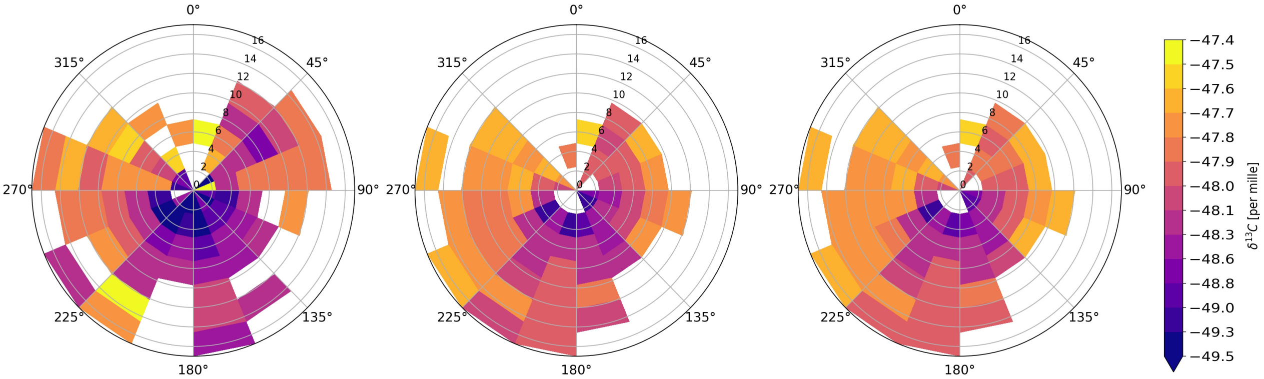

(a) δ^{13}C measurements **(b)** δ^{13}C EDGARv4.3.2 **(c)** δ^{13}C TNO-MACC_III

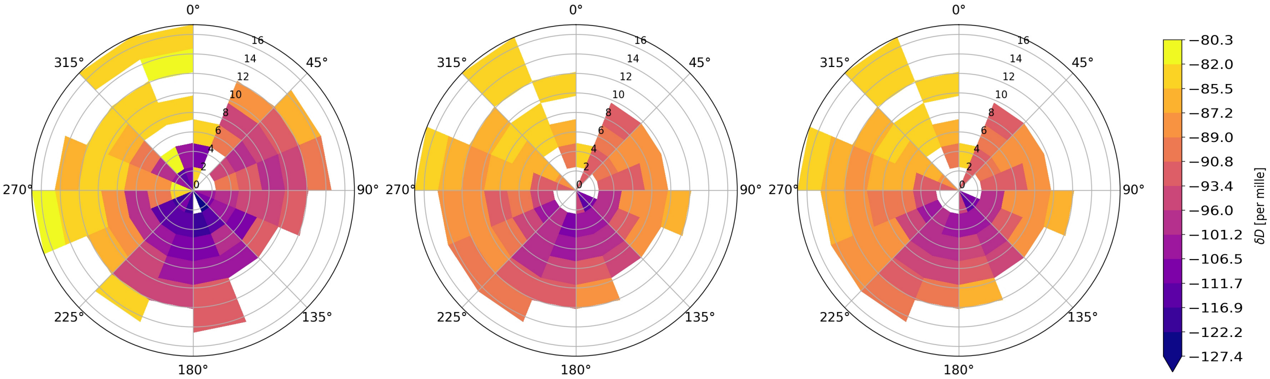

(e) δ^{2}H measurements **(f)** δ^{2}H EDGARv4.3.2 **(g)** δ^{2}H TNO-MACC_III

Figure 3.6: Hourly afternoon data of the measured isotope ratios of δ^{13}C and δ^{2}H (sub-figures a) and d), respectively) and simulated isotope ratios of δ^{13}C and δ^{2}H with the EDGARv4.3.2 and TNO-MACC_III inventories (sub-figures b) and e), c) and f), respectively) as function of wind speed and wind direction for the period November 2016 - March 2017.

mismatches between simulations and measurements is conducted in this section based on the contributions of the boundary mixing ratios and each source sector to the simulated total CH_4 mixing ratios (Figure 3.7).

Moreover, to further investigate causes of model-measurement mismatches in the isotopic ratios of δ^{13}C and δ^{2}H, we carry out three sensitivity analyses:

1. The correlation between simulations and measurements of CH_4 mixing ratios is poorest in the North Sea and the North Sea & Nordic countries geographical zones, which indicates an issue connected with the CH_4 boundary mixing ratios. Therefore, we perform two analyses concerning this issue, in which we compute averages of the lowest 10th percentile of the measured CH_4 mixing ratios over a 10-day and a 7-day rolling window. We then replace the simulated CH_4 boundary mixing ratios by the 10-day and 7-day rolling averages of the lowest 10th percentile of the measured CH_4 mixing ratios. The 7- and 10-day averages are chosen as this amount of days exceeds the synoptic time scale

Table 3.5: Statistics for the measured and modelled CH_4 mixing ratio and δ^{13}C and δ^{2}H isotopic ratios in the four geographical zones around Lutjewad (Section 3.2.3). The mean bias error (MBE) is presented as both absolute value in ppb and relative value in % compared to the mean of the measurements at Lutjewad in each geographical zone.

Geographical zones	**Correlation coefficient r**		**Mean bias error (MBE)**		**Root-mean-square error (RMSE)**	
	EDGARv4.3.2	**TNO-MACC_III**	**EDGARv4.3.2**	**TNO-MACC_III**	**EDGARv4.3.2**	**TNO-MACC_III**
CH_4 mixing ratios [ppb]						
All data	0.83	0.82	-37 (1.8%)	-39 (1.9%)	97	99
North Sea & Nordic countries	-0.20	-0.14	-17 (0.8%)	-16 (0.8%)	96	95
Land	0.81	0.8	-47 (2.3%)	-47 (2.3%)	79	80
North Sea & UK	0.69	0.73	-27 (1.3%)	-31 (1.5%)	66	65
North Sea	0.39	0.43	-48 (2.4%)	-48 (2.4%)	93	92
δ^{13}C [‰]						
All data	0.83	0.81	0.3 (0.6%)	0.3 (0.6%)	0.5	0.6
North Sea & Nordic countries	0.14	0.03	0.1 (0.2%)	0.2 (0.4%)	0.4	0.4
Land	0.78	0.76	0.3 (0.6%)	0.4 (0.8%)	0.5	0.6
North Sea & UK	0.87	0.87	0.3 (0.6%)	0.3 (0.6%)	0.5	0.5
North Sea	0.85	0.86	0.3 (0.6%)	0.3 (0.6%)	0.5	0.4
δ^{2}H [‰]						
All data	0.79	0.79	4.3 (4.4%)	4.8 (4.9%)	9.9	10.2
North Sea & Nordic countries	-0.89	-0.85	6.0 (6.2%)	6.2 (6.4%)	9.8	9.9
Land	0.86	0.85	6.7 (6.4%)	7.2 (6.9%)	8.7	9.1
North Sea & UK	0.76	0.74	-0.8 (0.9%)	-0.4 (0.4%)	5.7	5.8
North Sea	0.81	0.84	5.5 (6.0%)	5.4 (5.9%)	9.1	9.0

(about 5 days) and can be considered representative of background conditions.

2. To analyse the underestimation of emissions, we increase the CH_4 mixing ratios of each source sector by 20% (background by 2%). Doing so assists in determining whether the emissions are underestimated in the inventories used in this study.

   The modifications for the background are chosen to be smaller than those of other source sectors. This is necessary as the contribution of boundary mixing ratios is about 95% of the total CH_4 mixing ratios.
3. To analyse the overestimation of δ^{13}C and δ^{2}H isotopic ratios, we decrease the input isotopic signatures of each source sector by 10% (background by 1%). This leads to the simulated isotopic ratios becoming more depleted and the extent of overestimation smaller. As both δ^{2}H and δ^{13}C are overestimated, a reduction of the input source signatures will always lead to an improvement of the simulations. This can be misleading. However, if the decrease of the input source signatures results in an improvement of the simulated isotopic composition that cannot be explained by the underestimation of the CH_4 mixing ratios, then the used isotopic signatures are indeed too enriched.

The sensitivity analyses are performed on the time series of simulated CH_4 mixing ratios, δ^{13}C and δ^{2}H isotopic ratios but investigated using wind roses and the introduced geographical zones. The outcome and impact of the sensitivity analyses on the total δ^{13}C and δ^{2}H is evaluated by the RMSE and the MBE compared to the RMSE and MBE computed from the original simulations. The Pearson correlation coefficient is analysed as well. However, as the changes in the correlation coefficients are negligible, they are not further discussed when presenting the sensitivity analyses results. In the following sections, the issues concerning the simulated boundary conditions and the source contributions to the total CH_4 mixing ratios are discussed first, followed by the examination of corresponding sensitivity analyses.

Evaluation of the methane boundary mixing ratios

The simulated CH_4 mixing ratio from boundary conditions, shown in Figure 3.7f, is highest in the East (67.5° - 112.5°; part of the Land and Nordic countries zones). At this direction, the simulations of total CH_4 mixing ratio in Figure 3.5 often overestimate the measurements. This could indicate too high simulated boundary conditions. In the North Sea & Nordic countries zone, the correlation coefficients of -0.2 and -0.14 are the poorest, indicating that the simulated CH_4 mixing ratios are only weakly correlated to the measured ones. On the other hand, the MBE for both inventories is the smallest with about 0.8%. This again could mean that the boundary mixing ratios are too large in the North Sea & Nordic countries zone as the CH_4 mixing ratios from any source are low.

In the North Sea zone, the measured CH_4 mixing ratios are underestimated to a large extent with an MBE=2.4% and very low correlation coefficients. Since the source contributions are very low and mostly background air is advected from this direction, the simulated boundary conditions are probably too low in the North Sea zone. The MBE of δ^{2}H of appr. 6% are the largest in both the North Sea and North Sea & Nordic countries zones. Hence, the poor model performance in these zones is likely to be explained by the boundary conditions not being representative enough.

Giordano et al. (2015) analysed the influence of the MACC boundary conditions on the simulation quality of the long-lived species O_3 and CO, among others. They found that some biases between ground station observations and simulation outputs can be traced back to the performance of the MACC boundary conditions. The same may occur in the CH_4 boundary conditions of MACC.

The performance of the simulated CH_4 boundary mixing ratios is examined by all three sensitivity analyses. In Figures 3.8 and 3.9, the left and middle

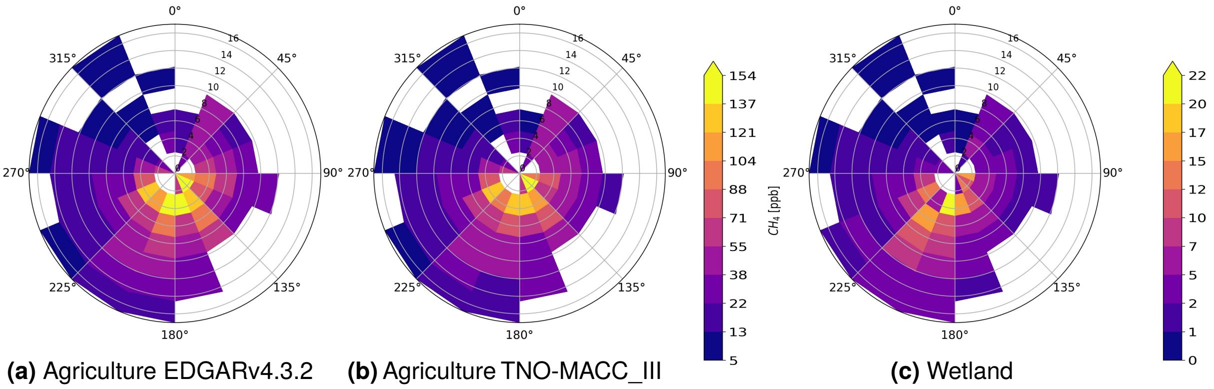

(a) Agriculture EDGARv4.3.2 **(b)** Agriculture TNO-MACC_III **(c)** Wetland

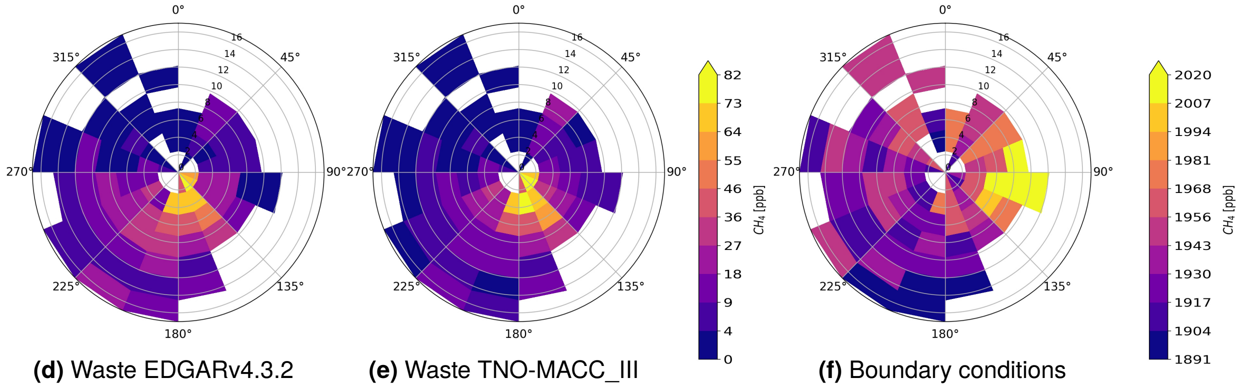

(d) Waste EDGARv4.3.2 **(e)** Waste TNO-MACC_III **(f)** Boundary conditions

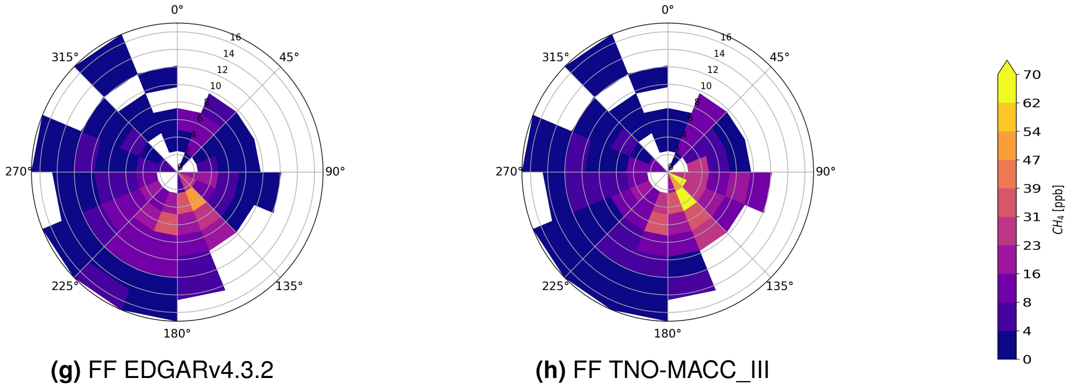

(g) FF EDGARv4.3.2 **(h)** FF TNO-MACC_III

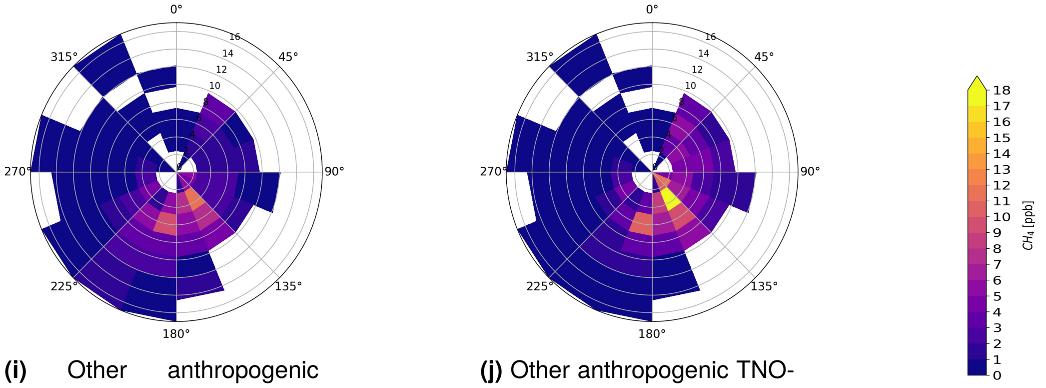

(i) Other anthropogenic EDGARv4.3.2 **(j)** Other anthropogenic TNO-MACC_III

Figure 3.7: Contributions of source sectors to the simulated total CH_4 mixing ratios for the simulations made using the EDGARv4.3.2 and TNO-MACC_III anthropogenic inventories. The wetland and boundary condition contributions are not dependent on the anthropogenic inventories. Note that the colour scale differs per source type.

panels illustrate the results of the sensitivity analyses 2 and 3. When modifying the contribution to the total CH_4 mixing ratios, the worsening of the RMSE and MBE for most geographical zones for both δ^2H and δ^{13}C indicate that the original boundary conditions are large enough or even too large. This contradicts the above mentioned findings but confirms the need for more analysis.

The right panels of Figures 3.8 and 3.9 illustrate the results of the boundary condition sensitivity analysis (analysis 1) on the simulated δ^{13}C and δ^2H, respectively. Our analysis shows that replacing the simulated boundary CH_4 mixing ratios by the 7-day and 10-day rolling averages of the lowest 10th percentile of the measured CH_4 mixing ratios has only a minor influence on the simulated δ^{13}C but a larger influence on the simulated δ^2H in all four geographical zones and both inventories. This difference between the influence on δ^2H and δ^{13}C could be due to the general difference in the model performance on δ^{13}C and δ^2H.

The largest difference between the original simulations of both δ^{13}C and δ^2H and the modified ones is in the Land zone. While the MBE of δ^{13}C for the 7-day average indicates an improvement, the RMSE becomes worse compared to the original simulations. This, together with the results for δ^2H, demonstrates that modifying the boundary mixing ratios does not improve the simulations of δ^{13}C and δ^2H and is not the key reason for the mismatches between simulations and measurements. However, analyses that apply more sophisticated background extraction approaches may bring more insight to better represent background conditions as they constitute most of the atmospheric ratios.

Analysis of the methane sources

We now evaluate the influence of the source contributions to the simulated total CH_4 mixing ratios and the effects of the sensitivity analyses 2 and 3 on the simulated isotopic compositions δ^{13}C and δ^2H. In general, the contributions from any emission sources are largest in the Land zone and lowest from the North Sea (Figure 3.7). The highest CH_4 mixing ratios on land are mainly associated with contributions from biogenic sources (waste and agriculture sources, wetlands to a smaller extent).

Both sensitivity analyses (Figures 3.8 and 3.9) result in a better agreement with the measurements for both inventories. The changes in the simulated isotopic ratios caused by both the increase of CH_4 mixing ratio and the decrease of input isotopic signatures are largest when more land is involved (zones Land and North Sea & Nordic countries). This is due to the higher amount of emissions and thus larger contributions to CH_4 mixing ratios. Furthermore, this leads to larger differences between the simulated isotopic ratios issued from the two inventories as they contain different magnitudes of emissions.

Agriculture sources. Both inventories agree that the largest contributor of the total CH_4 mixing ratios at LUT is agricultural activities (Figure 3.7a and Figure 3.7b). Although the EDGAR inventory has 3% larger contribution of the agriculture sources than TNO-MACC, there is no specific direction from which the agriculture contribution in EDGAR is much higher than in TNO-MACC.

The sensitivity analyses in Figure 3.8 show that in the Land zone, the modification of the input source signature for agriculture results in the largest improvement for δ^{13}C. This is likely to be a consequence of the fact that the agriculture has the largest contribution to the total CH_4 mixing ratios at LUT. The increase of the CH_4 mixing ratios also improves the simulated isotopic composition. These findings suggest that the agriculture sources are underestimated in the inventories. The only degradation is found for δ^2H results for the North Sea & UK zone (Figure 3.9): the RMSE is worse when both increasing the CH_4 mixing ratios and reducing the input source signature. This occurs in most source sectors as the original simulations of δ^2H underestimate the measurements in this geographical zone (Figure 3.6). The underestimation can be explained by the isotopic source signatures paired with the simulated boundary conditions not being suitable for δ^2H. The used source signatures are likely too low for the background, which can cause lower total δ^2H isotope ratios and the negative sensitivity analyses results for the sources.

Fossil fuel related sources. Between 90° and 157.5° (in Figure 3.5, part of the Land zone), the TNO-MACC CH_4 mixing ratios are on average by 14 ppb lower than the measured mixing ratios and about 12 ppb larger than the EDGAR ones. This can be due to the higher contribution of FF related sources and "other" anthropogenic sources in the TNO-MACC inventory (Figures 3.7h and 3.7j). It also contributes to the more enriched simulated δ^{13}C, and thus to a larger overestimation of the measurements with TNO-MACC (MBE=0.45) than with EDGAR (MBE=0.33) in this direction. Although there is no indication of it in the simulated δ^2H signatures with the MBE being similar (7.1 for TNO-MACC and 7.3 for EDGAR), it points towards too large emis-

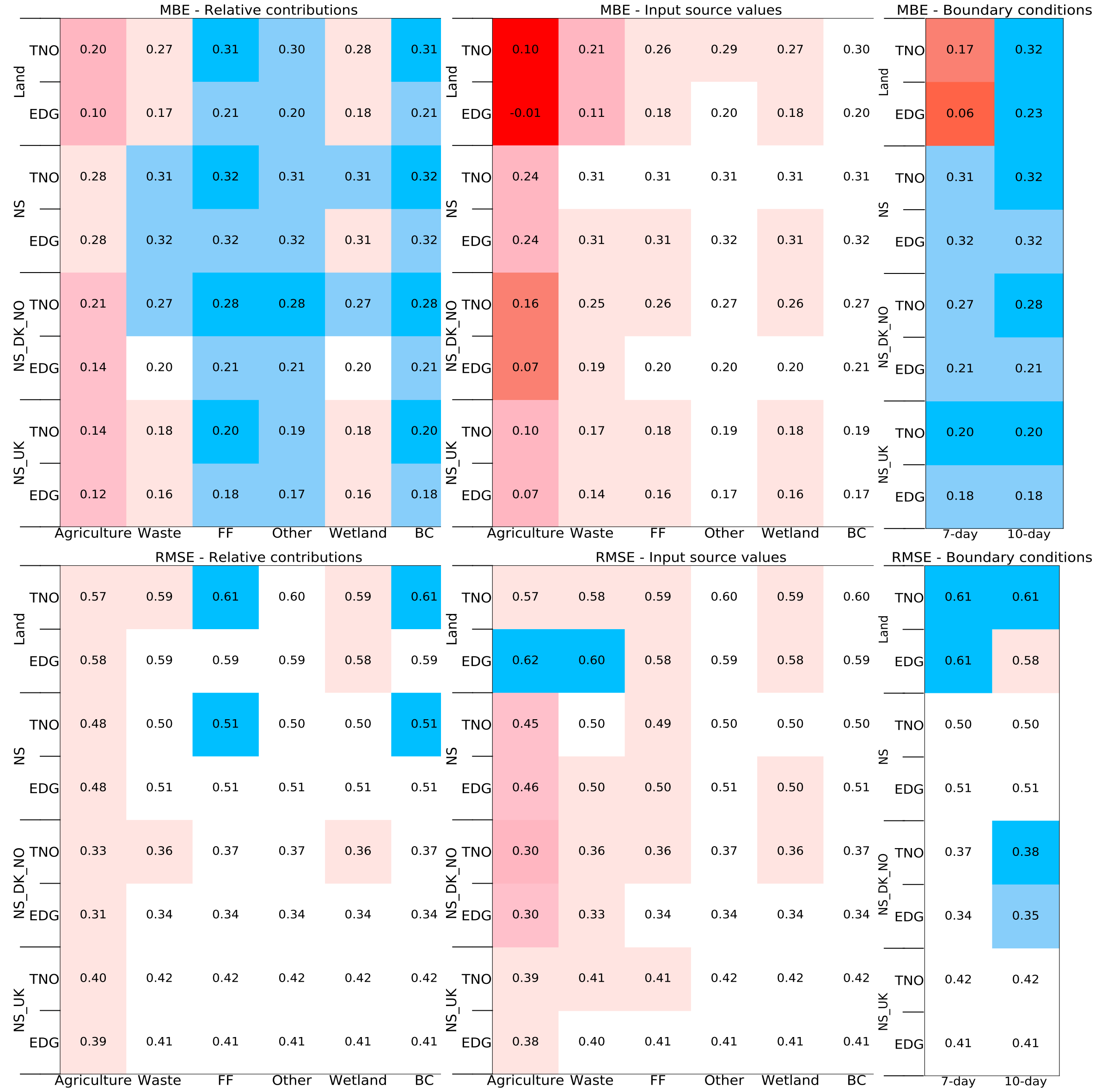

		Agriculture	Waste	FF	Other	Wetland	BC
MBE - Relative contributions							
Land	TNO	0.20	0.27	0.31	0.30	0.28	0.31
Land	EDG	0.10	0.17	0.21	0.20	0.18	0.21
NS	TNO	0.28	0.31	0.32	0.31	0.31	0.32
NS	EDG	0.28	0.32	0.32	0.32	0.31	0.32
NS_DK_NO	TNO	0.21	0.27	0.28	0.28	0.27	0.28
NS_DK_NO	EDG	0.14	0.20	0.21	0.21	0.20	0.21
NS_UK	TNO	0.14	0.18	0.20	0.19	0.18	0.20
NS_UK	EDG	0.12	0.16	0.18	0.17	0.16	0.18
MBE - Input source values							
Land	TNO	0.10	0.21	0.26	0.29	0.27	0.30
Land	EDG	-0.01	0.11	0.18	0.20	0.18	0.20
NS	TNO	0.24	0.31	0.31	0.31	0.31	0.31
NS	EDG	0.24	0.31	0.31	0.32	0.31	0.32
NS_DK_NO	TNO	0.16	0.25	0.26	0.27	0.26	0.27
NS_DK_NO	EDG	0.07	0.19	0.20	0.20	0.20	0.21
NS_UK	TNO	0.10	0.17	0.18	0.19	0.18	0.19
NS_UK	EDG	0.07	0.14	0.16	0.17	0.16	0.17
RMSE - Relative contributions							
Land	TNO	0.57	0.59	0.61	0.60	0.59	0.61
Land	EDG	0.58	0.59	0.59	0.59	0.58	0.59
NS	TNO	0.48	0.50	0.51	0.50	0.50	0.51
NS	EDG	0.48	0.51	0.51	0.51	0.51	0.51
NS_DK_NO	TNO	0.33	0.36	0.37	0.37	0.36	0.37
NS_DK_NO	EDG	0.31	0.34	0.34	0.34	0.34	0.34
NS_UK	TNO	0.40	0.42	0.42	0.42	0.42	0.42
NS_UK	EDG	0.39	0.41	0.41	0.41	0.41	0.41
RMSE - Input source values							
Land	TNO	0.57	0.58	0.59	0.60	0.59	0.60
Land	EDG	0.62	0.60	0.58	0.59	0.58	0.59
NS	TNO	0.45	0.50	0.49	0.50	0.50	0.50
NS	EDG	0.46	0.50	0.50	0.51	0.50	0.51
NS_DK_NO	TNO	0.30	0.36	0.36	0.37	0.36	0.37
NS_DK_NO	EDG	0.30	0.33	0.34	0.34	0.34	0.34
NS_UK	TNO	0.39	0.41	0.41	0.42	0.42	0.42
NS_UK	EDG	0.38	0.40	0.41	0.41	0.41	0.41

		7-day	10-day
MBE - Boundary conditions			
Land	TNO	0.17	0.32
Land	EDG	0.06	0.23
NS	TNO	0.31	0.32
NS	EDG	0.32	0.32
NS_DK_NO	TNO	0.27	0.28
NS_DK_NO	EDG	0.21	0.21
NS_UK	TNO	0.20	0.20
NS_UK	EDG	0.18	0.18
RMSE - Boundary conditions			
Land	TNO	0.61	0.61
Land	EDG	0.61	0.58
NS	TNO	0.50	0.50
NS	EDG	0.51	0.51
NS_DK_NO	TNO	0.37	0.38
NS_DK_NO	EDG	0.34	0.35
NS_UK	TNO	0.42	0.42
NS_UK	EDG	0.41	0.41

Figure 3.8: Results of the sensitivity analyses made for the EDGARv4.3.2 (EDG) and TNO-MACC_III (TNO) inventories: Mean bias error (MBE) and root-mean-square error (RMSE) for the δ^{13}C isotope ratios compared to the measured ones after modifying the CH_4 mixing ratios (left panel) and the input signatures (middle panel) of the sources, and the boundary conditions (right panel) by the 7-day and 10-day rolling averages of the lowest 10th percentile of the measured CH_4 mixing ratios for the period November 2016 - March 2017. The cell colours indicate the MBE and RMSE changed by the sensitivity analyses compared to the original MBE and RMSE; with decline in blue, improvement in red, no change in white. The darker the colour, the largest the decline/improvement. Note that the largest decline (-0.03) is smaller than the largest improvement (+0.21). These results are analysed by geographical zones: Land, North Sea (NS), North Sea & Nordic countries (NS_DK_NO) and North Sea & UK (NS_UK).

sions from the FF related sources and the "other anthropogenic" sources in both inventories. However, the overestimation of the emissions seems larger in the TNO-MACC_III inventory than in EDGAR around LUT. Similarly, in the study of Röckmann et al. (2016), the FF contribution was too large with a previous version of the EDGAR inventory.

Increasing the FF related mixing ratios leads to worsening of the simulated δ^{13}C in all geographical zones (Figure 3.8). This means that there is no need for more FF emissions in the inventories. Perhaps even a reduction of the FF emissions could be considered, particularly in the TNO-MACC inventory, which is indicated by the largest degradation in Figure 3.8 (darker blue colour). The decrease of the input isotopic signatures contributes to an improvement of the simulated δ^{13}C but δ^{2}H remains unchanged. Indeed, it makes the total simulated isotopic ratios more depleted. This improvement is noticeable as the FF related sources are the third largest contributor to the total CH_4 mixing ratio at LUT and suggests that the used input source values for δ^{13}C and δ^{2}H for this sector are too enriched.

Waste sources. Contributions from waste sources are the second largest to the total CH_4 mixing ratios (Figure 3.7d and Figure 3.7e) which is confirmed by the analysis of the measured isotopic ratios by Menoud et al. (2020b). The extent of the contribution from waste sources is similar for both inventories, the only difference being the location of the sources. The TNO-MACC_III inventory has larger CH_4 mixing ratios between 135° and 180° (Land zone) and lower mixing ratios between 180° and 270° (partly Land, partly North Sea & UK zone) than the EDGAR inventory. The simulated δ^{2}H in the North Sea & UK zone underestimates the measured δ^{2}H which may suggest that the waste emissions in EDGARv4.3.2 are overestimated in this area. However, there is no indication for it in the sensitivity analyses in Figures 3.8 and 3.9. Thus, we reject this hypothesis. Other results of the sensitivity analyses concerning the waste sector are inconclusive (e.g. decline of the MBE of δ^{13}C in the North Sea zone but there is no indication for it in the RMSE and δ^{2}H results).

Other anthropogenic sources. The lowest contributions to the total CH_4 mixing ratios come from the "other" anthropogenic sources (Figure 3.7i and Figure 3.7j). Between 90° and 157.5° (part of the Land zone), the CH_4 mixing ratios of the "other" anthropogenic sources in the inventories contribute to the generally higher mixing ratios that lead to a smaller underestimation of the measured mixing ratios and to a more enriched simulated δ^{13}C due to the enriched source signature of this source sector. Just as in the case of the FF related sources, this indicates that the emissions in the "other" anthropogenic source sector are large enough or too large in both inventories around LUT. The sensitivity analyses in Figures 3.8 and 3.9 indicate that the emissions in the "other" anthropogenic sources are indeed overestimated. It is shown by the worsening of the MBE for δ^{13}C and of the RMSE for δ^{2}H when increasing the CH_4 mixing ratios of this source.

Wetland sources. The wetland sources have a small contribution to the total CH_4 mixing ratios (Figure 3.7c). In the Land zone, the increase of CH_4 mixing ratios and the decrease of the isotopic signatures for any biogenic sources, including wetlands, results in an improvement (Figures 3.8 and 3.9). This is because biogenic sources have lower signatures than other source types and thus, they improve the simulated δ^{13}C and δ^{2}H signatures which are too enriched compared to the measurements. In the other geographical zones, the changes due to both sensitivity analyses are small and can be positive or negative.

3.2.5 Conclusions

In this study, we have compared quasi-continuous measurements of CH_4 mixing ratios and isotopic ratios of δ^{13}C and δ^{2}H to simulation outputs at the Lutjewad monitoring site, located in the Netherlands, at the North Sea coast. Using wind rose plots and sensitivity analyses, we have examined whether the emissions in the study domain are well characterised by the EDGARv4.3.2 and TNO-MACC_III inventories. Moreover, the simulated CH_4 boundary mixing ratios and their impact on the simulated isotopic ratios have been analysed.

Our analysis shows that the MACC CH_4 boundary mixing ratios that were used as the background CH_4 mixing ratios in this study need further investigation. They are perhaps too high on the land and too low over the sea. However, they are not the key reason for the model-measurement mismatches of the methane isotopic ratios.

With the sensitivity analyses proposed here, we have shown that an adjustment of the CH_4 mixing ratios and of the input isotopic source signatures leads to a better agreement between the measured and simulated δ^{2}H and δ^{13}C. We have found that the simulation quality for δ^{2}H is generally lower, suggesting that the input isotopic source signatures are not suitable for the studied region. To have more information on typical iso-

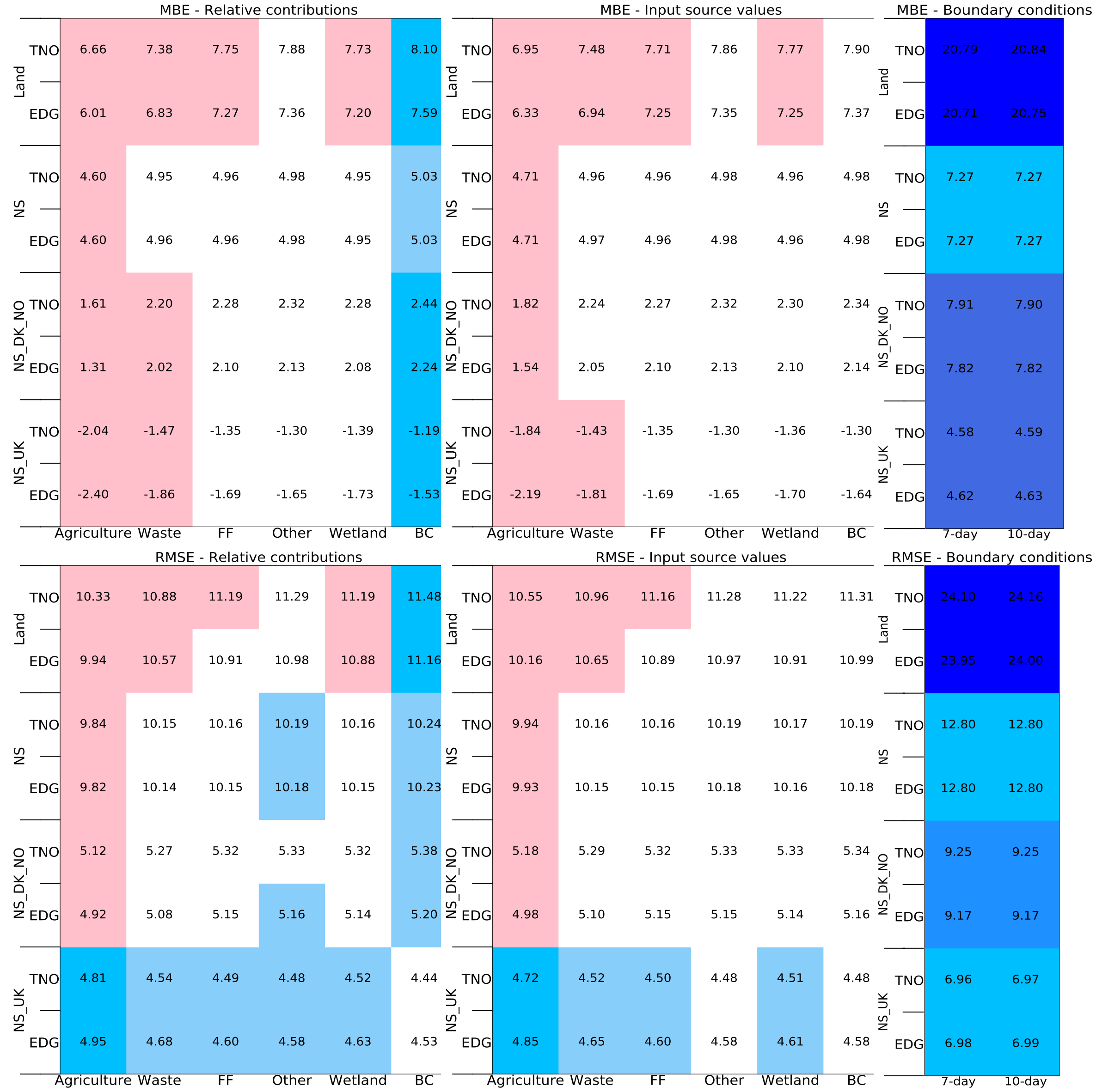

MBE - Relative contributions

		Agriculture	Waste	FF	Other	Wetland	BC
Land	TNO	6.66	7.38	7.75	7.88	7.73	8.10
	EDG	6.01	6.83	7.27	7.36	7.20	7.59
NS	TNO	4.60	4.95	4.96	4.98	4.95	5.03
	EDG	4.60	4.96	4.96	4.98	4.95	5.03
NS_DK_NO	TNO	1.61	2.20	2.28	2.32	2.28	2.44
	EDG	1.31	2.02	2.10	2.13	2.08	2.24
NS_UK	TNO	-2.04	-1.47	-1.35	-1.30	-1.39	-1.19
	EDG	-2.40	-1.86	-1.69	-1.65	-1.73	-1.53

MBE - Input source values

		Agriculture	Waste	FF	Other	Wetland	BC
Land	TNO	6.95	7.48	7.71	7.86	7.77	7.90
	EDG	6.33	6.94	7.25	7.35	7.25	7.37
NS	TNO	4.71	4.96	4.96	4.98	4.96	4.98
	EDG	4.71	4.97	4.96	4.98	4.96	4.98
NS_DK_NO	TNO	1.82	2.24	2.27	2.32	2.30	2.34
	EDG	1.54	2.05	2.10	2.13	2.10	2.14
NS_UK	TNO	-1.84	-1.43	-1.35	-1.30	-1.36	-1.30
	EDG	-2.19	-1.81	-1.69	-1.65	-1.70	-1.64

MBE - Boundary conditions

		7-day	10-day
Land	TNO	20.79	20.84
	EDG	20.71	20.75
NS	TNO	7.27	7.27
	EDG	7.27	7.27
NS_DK_NO	TNO	7.91	7.90
	EDG	7.82	7.82
NS_UK	TNO	4.58	4.59
	EDG	4.62	4.63

RMSE - Relative contributions

		Agriculture	Waste	FF	Other	Wetland	BC
Land	TNO	10.33	10.88	11.19	11.29	11.19	11.48
	EDG	9.94	10.57	10.91	10.98	10.88	11.16
NS	TNO	9.84	10.15	10.16	10.19	10.16	10.24
	EDG	9.82	10.14	10.15	10.18	10.15	10.23
NS_DK_NO	TNO	5.12	5.27	5.32	5.33	5.32	5.38
	EDG	4.92	5.08	5.15	5.16	5.14	5.20
NS_UK	TNO	4.81	4.54	4.49	4.48	4.52	4.44
	EDG	4.95	4.68	4.60	4.58	4.63	4.53

RMSE - Input source values

		Agriculture	Waste	FF	Other	Wetland	BC
Land	TNO	10.55	10.96	11.16	11.28	11.22	11.31
	EDG	10.16	10.65	10.89	10.97	10.91	10.99
NS	TNO	9.94	10.16	10.16	10.19	10.17	10.19
	EDG	9.93	10.15	10.15	10.18	10.16	10.18
NS_DK_NO	TNO	5.18	5.29	5.32	5.33	5.33	5.34
	EDG	4.98	5.10	5.15	5.15	5.14	5.16
NS_UK	TNO	4.72	4.52	4.50	4.48	4.51	4.48
	EDG	4.85	4.65	4.60	4.58	4.61	4.58

RMSE - Boundary conditions

		7-day	10-day
Land	TNO	24.10	24.16
	EDG	23.95	24.00
NS	TNO	12.80	12.80
	EDG	12.80	12.80
NS_DK_NO	TNO	9.25	9.25
	EDG	9.17	9.17
NS_UK	TNO	6.96	6.97
	EDG	6.98	6.99

Figure 3.9: Results of the sensitivity analyses made for the EDGARv4.3.2 (EDG) and TNO-MACC_III (TNO) inventories: Mean bias error (MBE) and root-mean-square error (RMSE) for the δ^2H isotope ratios compared to the measured ones after modifying the CH_4 mixing ratios (left panel) and the input signatures (middle panel) of the sources, and the boundary conditions (right panel) by the 7-day and 10-day rolling averages of the lowest 10th percentile of the measured CH_4 mixing ratios for the period November 2016 - March 2017. The cell colours indicate the MBE and RMSE changed by the sensitivity analyses compared to the original MBE and RMSE; with decline in blue, improvement in red, no change in white. The darker the colour, the largest the decline/improvement. Note that the largest improvement (+1.36) is smaller than the largest decline (-13.01). These results are analysed by geographical zones: Land, North Sea (NS), North Sea & Nordic countries (NS_DK_NO) and North Sea & UK (NS_UK).

topic source signatures that can be used for modelling isotopic ratios, more campaign-like, local measurements are required that target the estimation of specific source signatures. The importance of this is well demonstrated by the fact that adjusting the input source isotopic signatures based on the MEMO^2 campaigns measurements has improved the δ^2H and δ^{13}C simulations, compared to those in (Menoud et al., 2020b).

As the sensitivity analysis for modifying the input source signatures results either in an improvement or no change compared to the original simulations of δ^2H and δ^{13}C, most of the discrepancies between the measured and simulated CH_4 mixing ratios, δ^{13}C and δ^2H are the result of incorrect emissions and/or their spatial distribution in the inventories. The general underestimation of the measured CH_4 mixing ratios and the overestimation of δ^{13}C and δ^2H by CHIMERE is mainly due to the underestimation of the biogenic sources, especially agriculture sources, in both the EDGARv4.3.2 and the TNO-MACC_III inventory.

Even though the measured CH_4 mixing ratio is generally underestimated by the simulations, the fossil fuel related emissions and emissions from "other" anthropogenic sources are likely overestimated in both inventories. However, the results suggest that the overestimation of these sources is larger in TNO-MACC, particularly South-East from LUT (Land zone), suggesting too large sources in Eastern Netherlands and North-West Germany. Therefore, the EDGAR inventory contains more reasonable emission amounts and emission distribution for these source sectors. Moreover, we found indications that the δ^{13}C isotopic source signature for fossil fuel related emissions is too high. Hence, δ^{13}C isotopic source signatures of approximately -44‰, as in the sensitivity analysis, would likely better match the conditions around Lutjewad.

One of the main limitations of this study is that the measurements were carried out only in winter months. Therefore, seasonal effects and even more the inter-annual variability of sources cannot be assessed. Further limitations are introduced by the fact that simulations of this study are compared to measurements made at one location only. The geographical features, as well as amount and type of sources at larger distances from and at LUT can be widely different from those of other sites and regions in Europe. LUT is a coastal site whose mixing ratios are strongly influenced by winds from West and North-West advecting background air. Moreover, the Netherlands is a relatively well mapped country regarding CH_4 sources, which is also demonstrated by the similarities of the two inventories. This may not be the case for other countries or regions. Hence, our results may not be representative for the full studied domain.

Although source attribution through forward modelling can pinpoint issues with emissions as the main reason for mismatches between measurements and simulations, the combination of CH_4 mixing ratios and isotope ratios in atmospheric inversion approaches appears to be more powerful. Indeed, such an approach can help reduce the uncertainties associated with bottom-up estimates of sources. Furthermore, with more measurements, the inter-annual variability of CH_4 sources could be assessed, which is usually not provided by inventories. Therefore, long-term high-frequency measurements of CH_4 isotope ratios at multiple locations could improve the current estimates of CH_4 emissions and their attribution to specific sources in top-down approaches. Consequently, it would help broaden our knowledge on the atmospheric CH_4 cycle in Europe.

Acknowledgements. This project is part of the MEMO^2 (MEthane goes MObile - MEasurements and MOdelling) project and has received funding from the European Union’s Horizon 2020 research and innovation programme under the Marie Sklodowska-Curie grant agreement No 722479. We are grateful to the colleagues at TNO for their valuable support. Calculations were performed using the resources of LSCE, maintained by François Marabelle and the LSCE IT team.

3.3 Analysis of quasi-continuous carbon isotopic ratios at a continental monitoring site

To further investigate the value of quasi-continuous isotopic composition measurements for source attribution, we conduct an analysis similar to the previous study in Section 3.2. This study uses quasi-continuous measurements of δ^{13}C carried out in Heidelberg (HEI), South-West Germany for the same five-month period as in Lutjewad. Heidelberg is a good target for complementing the study in Section 3.2 as it is located deeper on the continent and thus the prevailing meteorological conditions differ from those around Lutjewad.

As the study in Section 3.2 revealed, the main reason for the discrepancies between measurements and simulations is incorrect emissions in the inventories. Therefore, we focus here on the dominant sources of CH_4 and the evaluation of emission inventories around HEI.

3.3.1 Material and methods

3.3.1.1 Modelling framework

The same modelling framework, including the study domain and emission inventories, as in Section 3.2 is used in this study to simulate CH_4 mixing ratios and compute $\delta^{13}C$ isotopic ratios for the location of HEI (see Figure 3.2 on page 69). The $\delta^{13}C$ isotopic source signatures used for the computation of $\delta^{13}C$ isotope ratios are described below.

3.3.1.2 Measurements

The University Heidelberg, Germany, has made $\delta^{13}C$ isotopic ratio measurements of five months available for members of the MEMO^2 project. The time period is the same as for the measurements carried out at the site Lutjewad: 12 November 2016 to 31 March 2017. The measuring instrument used is an analyser based on cavity ring down spectroscopy (Hoheisel et al., 2019). The instrument is set up to continuously measure CH_4 mixing ratios and $\delta^{13}C$ isotopic composition, using regularly calibration gas and quality control gas injection. The repeatability of the analyser, determined by the Allan variance (Werle et al., 1993), is 0.08 ppb for atmospheric CH_4 mixing ratios and 0.2‰ for atmospheric $\delta^{13}C$ isotopic ratios. A more detailed description about the analyser and the data handling can be found in the study of Hoheisel et al. (2019).

3.3.1.3 Source isotopic signatures

The $\delta^{13}C$ source isotopic signatures used here for the main CH_4 sources are listed in Table 3.6, including the contribution of each source sector to the total CH_4 mixing ratios in the grid-cell corresponding to the location of Heidelberg. The $\delta^{13}C$ signatures for waste, agriculture and fossil fuel related emissions are taken from the study of Hoheisel et al. (2019), while the $\delta^{13}C$ signatures for the "other" anthropogenic sources and wetland emissions are the same as in Section 3.2. To better match the isotope scales identified in an international inter-comparison by Umezawa et al. (2018), we apply offsets of -0.2‰ for the simulated $\delta^{13}C$ background from LMDz in this study, which lead to an average background of -47.4‰.

Table 3.6: Summary of the absolute CH_4 mixing ratios [ppb $\pm$ 1σ], their relative contribution [% $\pm$ 1σ] to the total mixing ratios in the grid-cell matching the location of Heidelberg and the corresponding characteristic source isotopic values used as input for the computation of the isotopic composition δ^{13}C. The δ^{13}C source isotopic value for the boundary mixing ratios represents the mean value of the LMDz simulations of δ^{13}C used for the background. Note that the relative contributions of the sources indicate the source contributions to CH_4 mixing ratios above background (boundary mixing ratios), and that the relative contribution of the background indicates its contribution to the total mixing ratios.

Source sector	CH_4 [ppb] EDGARv4.3.2 & ORCHIDEE-WET	CH_4 [ppb] TNO-MACC_III & ORCHIDEE-WET	Contribution [%] EDGARv4.3.2 & ORCHIDEE-WET	Contribution [%] TNO-MACC_III & ORCHIDEE-WET	δ^{13}C [‰]
Agriculture	31 ± 22	31 ± 23	43 ± 12	53 ± 11	-64.0
Waste	28 ± 29	11 ± 10	31 ± 8	17 ± 6	-55.0
Fossil fuel related emissions	10 ± 13	10 ± 10	12 ± 6	15 ± 5	-47.0
Other anthropogenic sources	7 ± 7	6 ± 7	7 ± 2	7 ± 4	-35.0
Wetland	6 ± 6	6 ± 6	6 ± 3	8 ± 4	-71.0
Boundary mixing ratios	1952 ± 51		96 ± 3	97 ± 2	-47.4 (mean)

3.3.1.4 Analysis tools

Analogue to the study in Section 3.2, we compare simulations of CH_4 mixing ratios and of δ^{13}C isotope ratios to measurements and evaluate the model performance computing the Pearson correlation coefficient r, the mean bias error (MBE) and the root mean squared error (RMSE). The comparison between measurements and simulations helps evaluating the TNO-MACC_III and EDGARv4.3.2 emission inventories used in this study.

As discussed in Section 3.2, most CTMs use basic planetary boundary layer parameterisations, which negatively affects the vertical mixing (Dabberdt et al., 2004) in transport models, especially during night. Therefore, we have compared measured and simulated CH_4 mixing ratios sampled at the grid-cell matching the location of HEI during morning, afternoon and night to examine which time of the day is better reproduced by CHIMERE (comparison not shown). Subsequently, we select measurements in the afternoon between 12 and 17 UTC that we compare to simulations sampled from the grid-cell matching the location of HEI in this study.

Similarly to Section 3.2, we shortly compare the modelled wind fields to the measured wind fields in Figure 3.10 to investigate whether discrepancies between the modelled and measured wind fields contribute to the measurement-simulation mismatches of CH_4 mixing ratios and δ^{13}C and δ^2H isotopic ratios. The modelled wind speed correlates with the measured wind speed with a correlation coefficient of r=0.7 and underestimates the measured wind speed on average by 0.1 ms^{-1}. The modelled wind direction differs by 28° on average from the measured wind direction and weakly correlates by r=0.4 with the measured wind direction. However, the standard deviation (SD) of the simulated wind speed and direction is similar to that of the measured ones.

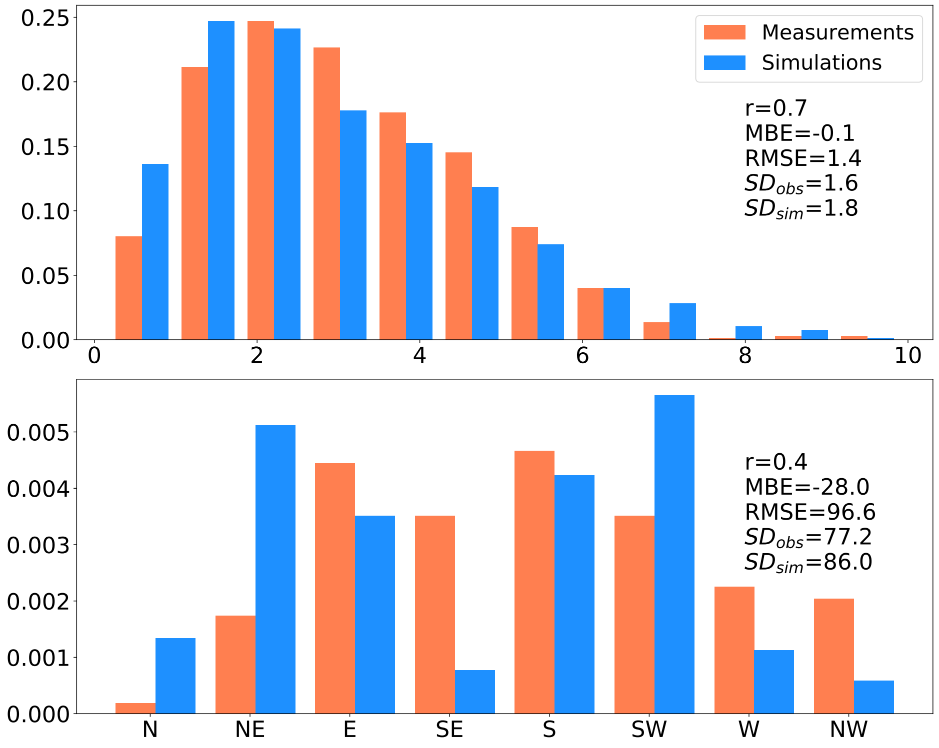

Figure 3.10: Comparison of measured and simulated wind speed in ms^{-1} (top panel) and direction in ° (bottom panel). Furthermore, the statistical measures Pearson correlation coefficient (r), mean bias error (MBE), root mean squared error (RMSE) and standard deviation (SD) are displayed.

For wind roses, the same categorisation of the wind direction and speed are used as in Section 3.2: a bin size of 2.4 ms^{-1} and 22.5°, respectively. The measured wind direction and speed are combined with the measured CH_4 mixing ratios, $\delta^{13}C$ and $\delta^{2}H$ isotope ratios, the simulated wind direction and speed with the simulated CH_4 mixing ratios, $\delta^{13}C$ and $\delta^{2}H$ isotope ratios. To evaluate the model performance associated with the placement of sources, we define geographical zones in the model domain. The geographical zones correspond to the following wind directions (Figure 3.2):

- Eastern Germany: 45° - 179°
- Southern Germany & France: 180° - 269°
- BENELUX & North-West Germany: 270° - 44°

The dominant source type for the five-month study period is determined by the Miller-Tans approach (see Equation 1.6 in Section 1.3 on page 14), combined with an orthogonal distance regression fit that takes the uncertainties in the X and Y variables into account. As the background values for both measurements and simulations of CH_4 mixing ratios and $\delta^{13}C$ isotope ratios need to be specified, we take the lower 10th percentile of the measured CH_4 mixing ratios and the average of the CH_4 boundary conditions. Correspondingly for $\delta^{13}C$, we use the highest 10th percentile of the measured $\delta^{13}C$ isotope ratios and the average of the LMDz $\delta^{13}C$ simulations used as background in this study. Note that a more sophisticated background extraction approach may produce more reliable $\delta^{13}C$ isotopic source signatures.

3.3.2 Results and discussion

3.3.2.1 General comparison of measurements and simulations

The comparison of measured and simulated CH_4 mixing ratios and $\delta^{13}C$ isotope ratios is shown in Figure 3.11 as a function of wind direction and wind speed. The measured minimum and maximum CH_4 mixing ratios are 1926 ppb, originating from South at high wind speeds, and 2285 ppb, from South at wind speeds of about 5 ms^{-1}. Simulated minimum and maximum CH_4 mixing ratios are 1908 ppb and 2429 ppb for EDGAR and 1906 ppb and 2316 ppb for TNO-MACC, respectively. Table 3.7 summarises the results of the statistical analyses carried out on measured and simulated data. The simulated CH_4 mixing ratios underestimate the measured CH_4 mixing ratios by approximately 20 ppb (TNO-MACC_III) and 5 ppb (EDGARv4.3.2) and, in general, correlate well with the measurements (correlation coefficient of 0.67 for TNO-MACC and of 0.72 for EDGAR). The CH_4 mixing ratio simulations with EDGAR are higher than with TNO-MACC. This difference between them is likely due to the higher contribution of waste sources to the total CH_4 mixing ratios in the EDGAR inventory (Table 3.6) as the contributions of other sources to the total mixing ratios are similar with both inventories. The highest correlation coefficients of r=0.91 and r=0.92 for EDGAR and TNO-MACC, respectively, are reached when the wind is from the Southern Germany & France geographical zone. The poorest correlation coefficients of r=0.46 for EDGAR and of r=0.42 for TNO-MACC occurs in the BENELUX & NW Germany zone, in which both simulations overestimate the measured CH_4 mixing ratios. It suggests an overestimation of the CH_4 sources in this zone.

Regarding the $\delta^{13}C$ isotope ratios, the simulated isotopic ratios are generally not as depleted as the measured ones. The simulated $\delta^{13}C$ with both inventories overestimates the measured $\delta^{13}C$ by only 0.1‰. However, the

Table 3.7: Statistics for the measured and simulated CH_4 mixing ratio and $\delta^{13}C$ isotopic ratios in the three geographical zones around Heidelberg (Section 3.3.1).

Geographical zones	Correlation coefficient r		Mean bias error (MBE)		Root-mean-square error (RMSE)	
	EDGARv4.3.2	TNO-MACC_III	EDGARv4.3.2	TNO-MACC_III	EDGARv4.3.2	TNO-MACC_III
CH_4 mixing ratios [ppb]						
All data	0.72	0.67	-5	-20	47	52
Eastern Germany	0.5	0.45	-5	-21	31	36
Southern Germany & France	0.91	0.92	8	-7	23	18
BENELUX & North-West Germany	0.46	0.42	38	21	60	48
$\delta^{13}C$ [‰]						
All data	0.28	0.25	0.1	0.1	0.4	0.4
Eastern Germany	-0.09	-0.11	0.1	0.1	0.2	0.2
Southern Germany & France	0.01	0.04	0.1	0.1	0.3	0.2
BENELUX & North-West Germany	-0.22	-0.25	0.1	0.2	0.4	0.4

correlation coefficients are poor; 0.28 for EDGAR and 0.25 for TNO-MACC. In the Southern Germany & France geographical zone, there is no correlation between simulated and measured $\delta^{13}C$, which is in contrast with the high correlations for the CH_4 mixing ratios. The correlations between measured and simulated CH_4 mixing ratio are even negative and the RMSE is the largest for the BENELUX & NW Germany zone.

These findings indicate issues with CH_4 emissions in inventories, as well as with the assigned $\delta^{13}C$ isotopic signatures for sources used for simulations. In sensitivity analyses similar to the ones in Section 3.2, we examine these issues. In one of them, we decrease the $\delta^{13}C$ isotopic source signatures used as input for modelling by 10% (background 1%) to analyse whether the used isotopic source signatures cause the overestimation of measured $\delta^{13}C$ isotope ratios. In another sensitivity analysis, we increase the CH_4 mixing ratio of each source by 20% (boundary conditions 2%) to investigate whether the emissions are too low that cause the underestimation of measured CH_4 mixing ratios and/or the overestimation of measured $\delta^{13}C$ isotope ratios.

However, none of the sensitivity analyses lead to significant changes in comparison between the simulated total $\delta^{13}C$ isotope ratios and the measured $\delta^{13}C$ isotope ratios. Thus, the main reason for mismatches between measured and simulated $\delta^{13}C$ must be another underlying issue.

Uncertainties in modelled wind fields and boundary conditions surely contribute to the mismatches between simulations and measurements but as the measured CH_4 mixing ratios are relatively well reproduced by the model (r=0.67 and r=0.72 for TNO-MACC and EDGAR, respectively) in contrast to $\delta^{13}C$ isotope ratios, they cannot be the main driver for the mismatches between measured and simulated $\delta^{13}C$.

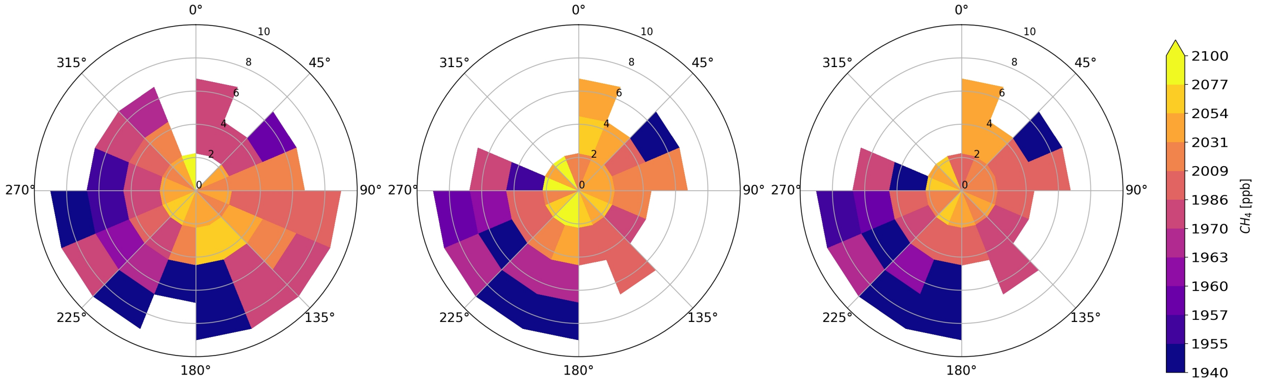

(a) CH_4 measurements **(b)** CH_4 EDGARv4.3.2 **(c)** CH_4 TNO-MACC_III

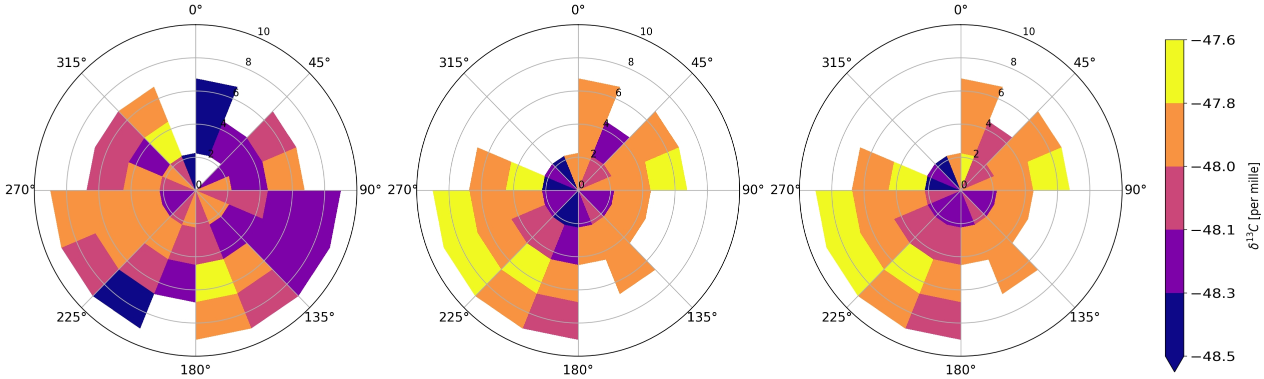

(e) δ^{13}C measurements **(f)** δ^{13}C EDGARv4.3.2 **(g)** δ^{13}C TNO-MACC_III

Figure 3.11: Hourly afternoon data of the measured CH_4 mixing ratios and δ^{13}C isotope ratios (sub-figures a) and d), respectively) and simulated CH_4 mixing ratios and δ^{13}C isotope ratios with the EDGARv4.3.2 and TNO-MACC_III inventories (sub-figures b) and e), as well as c) and f), respectively) as function of wind speed and wind direction for the period November 2016 - March 2017.

Contrariwise to LUT, Heidelberg is a town where the transport of sources is different, more complex than at a site like LUT, which is more difficult to reproduce by a model with a horizontal resolution of 0.1°×0.1°. This horizontal resolution is high for regional studies but not appropriate for the city-scale.

The precision of the CRDS instrument used for measuring δ^{13}C at HEI may play a role in the mismatches between measured and simulated δ^{13}C.

Although the impact of the emissions has been investigated by the sensitivity analysis when increasing CH_4 mixing ratios, the low model performance for δ^{13}C isotope ratios can still be partly due to emissions. If the source sector distribution and/or placement of emissions in the inventories is not representative enough for the area around Heidelberg, that can lead to incorrect modelled total δ^{13}C isotope ratios as the modelled δ^{13}C is computed using one isotopic source signature per source combined with CH_4 mixing ratios of that source. Therefore, we compare the measured and simulated CH_4 mixing ratios and δ^{13}C isotopic ratios by examining the source contributions to the total simulated CH_4 mixing ratios in the following sections.

3.3.2.2 Determination of the dominant source type

The Miller-Tans plots used for determining the dominant source type around Heidelberg are shown in Figure 3.12. The average δ^{13}C isotopic source signature derived from the measurements is -53.5 ± 0.5‰, implying that the dominant source around Heidelberg is of microbial origin, possibly waste. However, this δ^{13}C source isotopic signature could also be due to a mixing of microbial and thermogenic sources.

The δ^{13}C isotopic source signatures defined from the simulations with EDGAR and TNO-MACC are -55.0 ± 0.3 and -54.2 ± 0.4, respectively. They could also imply a microbial origin. The δ^{13}C source isotopic signatures used as input for the source sectors and the source contributions to the simulated total CH_4 mixing ratios (Table 3.6), however, implies a mixing of agriculture and FF related sources: agricultural sources have a larger contribution to the simulated total CH_4 mixing ratios with both inventories than waste sources.

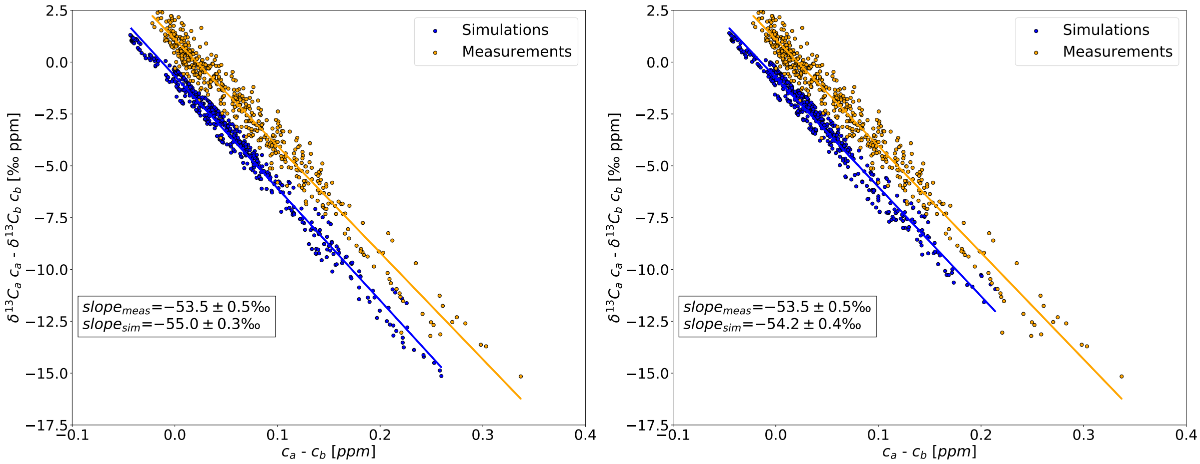

(a) EDGARv4.3.2

(b) TNO-MACC_III

Figure 3.12: Miller-Tans plots based on measured and simulated CH_4 mixing ratios and δ^{13}C isotopic ratios for the period November 2016 - March 2017.

The measured source signature is underestimated by both simulations. However, the derived δ^{13}C source signature with TNO-MACC_III is higher and thus closer to the measured isotopic source signature than that with EDGARv4.3.2. The difference between the regression lines of the measurements and simulations is likely due to issues with the simulations used for the background in this study: the LMDz simulations of δ^{13}C and/or the simulated CH_4 boundary mixing ratios. We test this hypothesis with simplified methods for the TNO-MACC inventory, in which we replace:

(i) the simulated CH_4 boundary mixing ratios by the lowest 10th percentile of the measured CH_4 mixing ratios in a 10-day running window (similar to Section 3.2.4.2, page 84);

(ii) the LMDz simulations of $\delta^{13}C$ by the highest 10th percentile of the measured $\delta^{13}C$ isotope ratios in a 10-day running window.

The modification of the LMDz $\delta^{13}C$ simulations (Figure 3.13a) results in a 1‰-lower average $\delta^{13}C$ source isotopic ratio of -55.2 $\pm$ 0.4‰, while modifying the CH_4 boundary mixing ratios (Figure 3.13b) leads to a higher average $\delta^{13}C$ source isotopic ratio of -54.0 $\pm$ 0.4‰. The latter is even in the range of the uncertainty of the average $\delta^{13}C$ source isotopic ratio derived from the measurements. The improvement caused by replacing the CH_4 boundary mixing ratios indicates that there are indeed issues with the simulated CH_4 boundary mixing ratios as shown in Section 3.2.4.2. The further decrease of the average $\delta^{13}C$ source isotopic ratio derived from simulations when replacing the LMDz simulations of $\delta^{13}C$ implies that the highest 10th percentile of the measured $\delta^{13}C$ is not optimal for combination with the original simulated CH_4 boundary mixing ratios or the isotopic signatures of sources (Table 3.1) used for simulating the total atmospheric $\delta^{13}C$ isotope ratios. Both the LMDz simulations of $\delta^{13}C$ and the simulated CH_4 boundary mixing ratios need further, in-depth analyses to learn more about the underlying issues.

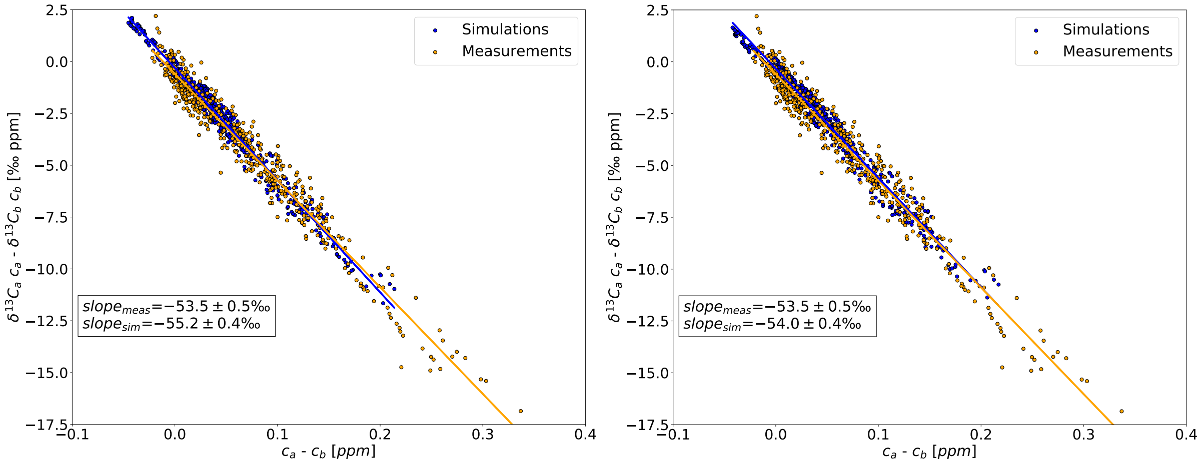

(a) Modified $\delta^{13}C$ isotope ratio

(b) Modified CH_4 boundary mixing ratio

Figure 3.13: Miller-Tans plots based on modified simulated $\delta^{13}C$ isotope ratios (**a**) and CH_4 mixing ratios (**b**) used for simulating the background for the period November 2016 - March 2017. The Miller-Tans plots are made by using simulations with the TNO-MACC_III inventory.

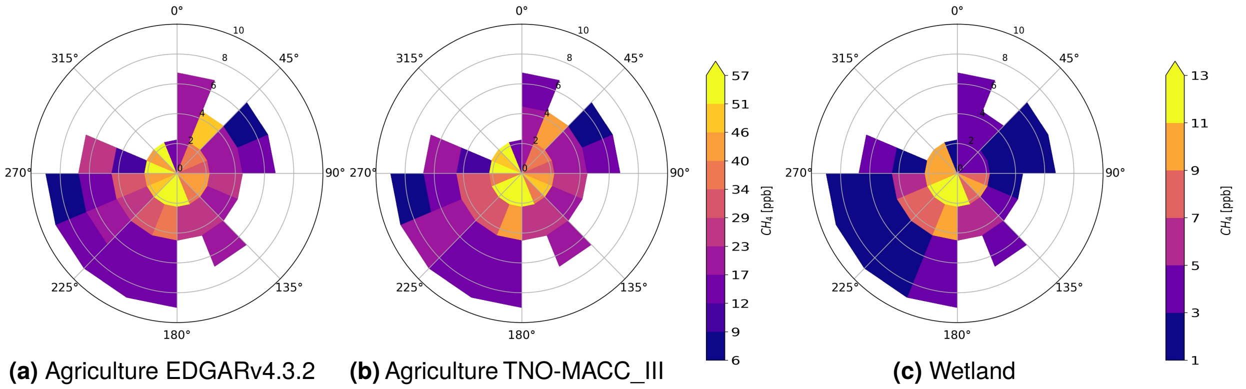

(a) Agriculture EDGARv4.3.2 **(b)** Agriculture TNO-MACC_III **(c)** Wetland

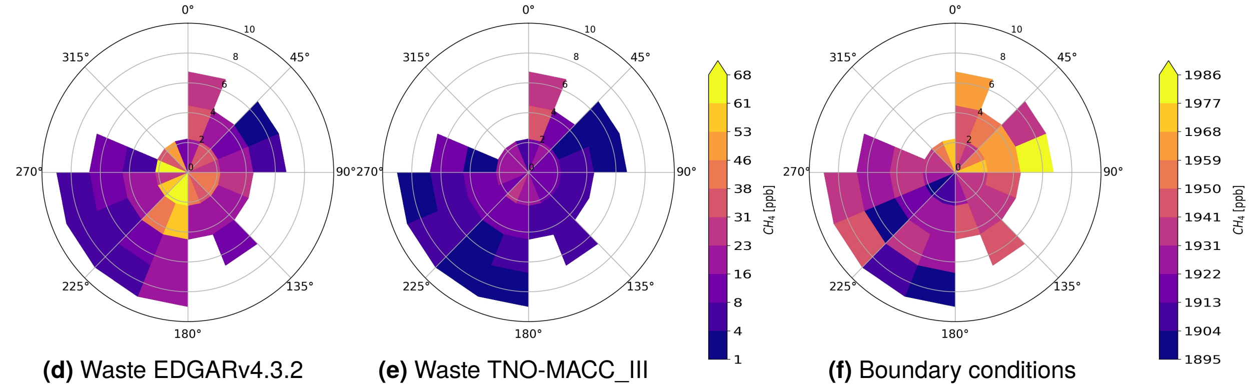

(d) Waste EDGARv4.3.2 **(e)** Waste TNO-MACC_III **(f)** Boundary conditions

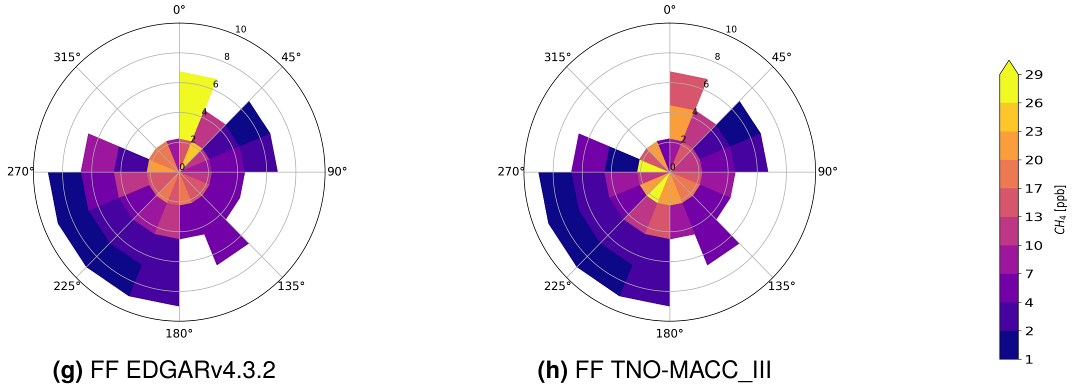

(g) FF EDGARv4.3.2 **(h)** FF TNO-MACC_III

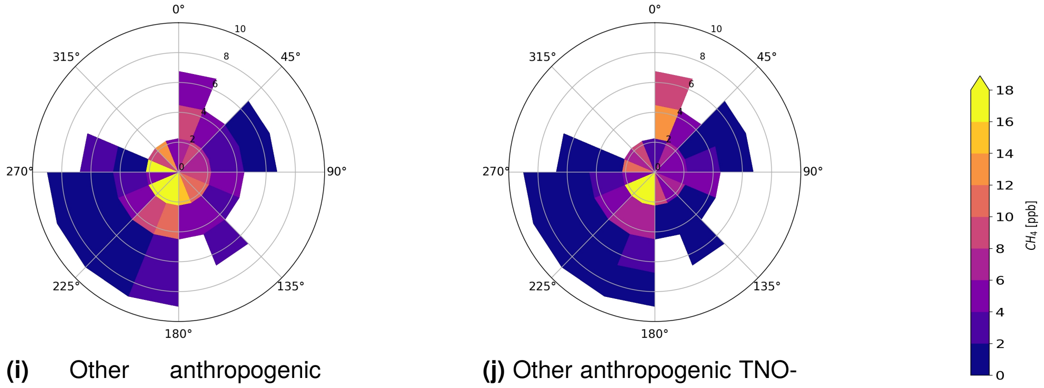

(i) Other anthropogenic EDGARv4.3.2 **(j)** Other anthropogenic TNO-MACC_III

Figure 3.14: Contributions of source sectors to the simulated total CH_4 mixing ratios for the simulations made using the EDGARv4.3.2 and TNO-MACC_III anthropogenic inventories. The wetland and boundary condition contributions are not dependent on the anthropogenic inventories. Note that the colour scale differs per source type.

3.3.2.3 Investigating model-measurement mismatches by source contributions to CH_4 mixing ratios

In this section, the source contributions to the simulated total CH_4 mixing ratios are analysed based on the mismatches between measured and simulated CH_4 mixing ratio and $\delta^{13}C$ isotope ratio. The source contributions to the simulated total CH_4 mixing ratios are displayed in Figure 3.14.

Agriculture. The overestimation of measured CH_4 mixing ratios in the BENELUX & NW Germany zone can be due to large agriculture contributions to the simulated total CH_4 mixing ratios (Figures 3.14a and 3.14b). As the measured $\delta^{13}C$ is usually underestimated by the simulated $\delta^{13}C$ in this zone, it confirms the possible overestimation of agriculture sources in the inventories. Based on the Figures 3.14a and 3.14b, the inventories generally agree on the magnitude of contributions to the total agriculture mixing ratios and on the location of agriculture sources in the model domain.

Fossil fuel related sources. Fossil fuel related sources (Figures 3.14g and 3.14h) also contribute to the overestimation of the measured CH_4 mixing ratios in the BENELUX & NW Germany zone, especially between 0° and 22.5°. The contributions of these sources to the total mixing ratios is larger with EDGAR, while the location of them in both inventories is similar. The overestimation of the FF related sources in North is in agreement with the findings of the study in Section 3.2 that indicates too large FF related sources South-East from Lutjewad. The measured $\delta^{13}C$ isotope ratio in North is low, indicating sources of microbial origin rather than thermogenic.

Waste. Waste sources are the second largest contributor to the simulated total CH_4 mixing ratios with EDGAR (Figure 3.14d). It likely places too large sources South from HEI between 180° and 225° in the Southern Germany & France zone as EDGAR simulations of CH_4 mixing ratios overestimate the measurements in this direction when wind speed is under 5 ms^{-1}. It is supported by the fact that simulations of CH_4 mixing ratios using TNO-MACC emissions (Figure 3.14e) lead to smaller waste contribution to the total simulated mixing ratios and thus to an underestimation of the measurements in the same area. In addition, the measured $\delta^{13}C$ isotope ratio is underestimated in this same area by the simulated $\delta^{13}C$ with EDGAR, which further supports the hypothesis that EDGAR overestimates waste sources there.

Other anthropogenic sources. Other anthropogenic sources are one of the smallest sources in the domain (Figures 3.14i and 3.14j). However, as their contribution to the simulated total CH_4 mixing ratios is largest in the Southern Germany & France zone at wind speeds under 2.5 ms^{-1}, indicating sources in or close by Heidelberg, they are also responsible for the overestimation of measured CH_4 mixing ratios, especially with the EDGAR inventory.

Wetlands. Wetland sources have a small contribution to the total simulated CH_4 mixing ratios (Figure 3.14c). Their contribution is largest in the Southern Germany & France zone. The impacts of this contribution is similar to the ones of the other anthropogenic sources.

Boundary conditions. The boundary conditions are largest when wind is coming from North-West (Figure 3.14f). However, the simulated CH_4 mixing ratios performed with both inventories underestimate the measurements between 45° and 90° in the "Eastern Germany" zone, indicating that sources are missing in this direction that may be close to the domain borders based on the average wind speed of about 7 ms^{-1} for the five-month period in this wind rose area. Indeed, the contributions of any sources to CH_4 mixing ratios is small in this direction. In this geographical zone "Eastern Germany", the measured δ^{13}C is overestimated by the simulated δ^{13}C with both inventories, which confirms that sources are missing and that missing sources are likely of microbial origin based on relatively low measured δ^{13}C isotope ratios.

3.3.3 Conclusions

In this study, we have compared quasi-continuous measurements of CH_4 mixing ratios and δ^{13}C isotopic ratios to simulation outputs at Heidelberg, located in South-West Germany. We have used wind roses to investigate possible origins of discrepancies between measurements and simulations. Our results suggest that emissions are misplaced and emission magnitudes are inaccurate in the TNO-MACC_III and EDGARv4.3.2 emission inventories. However, this conclusion is drawn only from the comparison of the measured and simulated CH_4 mixing ratios and δ^{13}C isotope ratios, combined with the examination of the source contribution to the simulated total CH_4 mixing ratios. Differences in the simulated CH_4 mixing ratios per source of two inventories is usually the result of differences in the magnitude and/or spatial distribution of CH_4 emissions of the inventories and isotopic composition can be useful for evaluating this.

As in the study in Section 3.2, we have carried out sensitivity analyses to investigate whether the δ^{13}C isotopic source signatures used as input for simulations or emissions are the main cause for simulation-measurement mismatches around Heidelberg. However, the sensitivity analyses did not lead to significant changes compared to the original simulations and could not be used to draw conclusions. Yet, based on the findings of this study, it can be assumed that the δ^{13}C isotopic source signatures used as input for simulations are possibly not well suited for the region around HEI and CHIMERE is less able to reproduce CH_4 mixing ratios in a dense area as well as at other locations such as Lutjewad. However, the LMDz δ^{13}C values used for background conditions seem to have a significant impact on the simulated total δ^{13}C isotope ratios, as shown in Figures 3.13a and 3.12b, and they need to be further analysed using a more sophisticated method.

Our findings indicate that agriculture sources in the BENELUX & NW Germany geographical zone are overestimated by both inventories. In the same zone North from HEI, FF related sources are overestimated. It also strengthens the findings in the study described in Section 3.2 that FF related sources are overestimated South-East from Lutjewad, which points towards North-West Germany. Furthermore, South from Heidelberg between 180° and 225° in the Southern Germany & France zone, the EDGAR inventory possibly overestimates waste sources. In addition to emission overestimation in the inventories, they likely miss sources in the geographical zone "Eastern Germany" at some distance from Heidelberg, indicated by missing sources occurring at larger wind speeds.

The average measured δ^{13}C isotopic source signature was defined by the Miller-Tans approach and resulted in -53.5 ± 0.5‰, indicating microbial sources or a mixing of microbial and thermogenic sources as dominant around Heidelberg. Simulations with both inventories agree with the source type(s) but underestimate the source signature. However, the δ^{13}C isotopic source signature derived from the simulations with TNO-MACC is closer to the measured δ^{13}C source signature.

Using information from quasi-continuous δ^{13}C in addition to CH_4 mixing ratios provided a benefit to evaluate emission inventories. However, as some results of this study are inconclusive, more quasi-continuous or long-term measurements of δ^{13}C would bring more constraints on the findings. This is well demonstrated by the fact that an overestimation of FF related emissions is confirmed from this study and the study in Section 3.2.

3.4 Conclusions and impact

As a conclusion from the analysis of the simulations and measurements carried out for the Dutch coastal site Lutjewad, we have found that the main reason for the discrepancies between measured and simulated δ^{2}H and δ^{13}C is incorrect emissions of the TNO-MACC_III and EDGARv4.3.2 inventories. Both inventories used for this study underestimate agricultural sources and overestimate fossil fuel emissions. The isotopic source signatures used as input for the simulations seems to be well-suited for δ^{13}C, except for fossil fuel emissions, for which the analysis suggests lower signatures than -40‰. However, for δ^{2}H, the simulation performance was in general lower than for δ^{2}H, implying that the isotopic source signatures used for δ^{2}H are less suitable. Therefore, campaign-like measurements of δ^{2}H (and δ^{13}C) at multiple locations and during different seasons are needed to derive characteristic isotopic signatures of the various CH_4 sources. This is one of the main objectives of the MEMO^2 project and various regions in Europe have been surveyed, which will be of great value for future studies on atmospheric methane in Europe.

The results of the study analysing measured and simulated CH_4 mixing ratios and δ^{13}C isotope ratios at the continental site Heidelberg lead to conclusions that emissions of the main anthropogenic CH_4 sources (agriculture, waste and FF related emissions) are incorrectly estimated and spatially distributed in the inventories. Both inventories overestimate agricultural and FF related sources North from Heidelberg, a region that is known for intensive agriculture. Analysing the measured δ^{13}C isotope ratios at Heidelberg in addition to the analysis of δ^{13}C at Lutjewad helped confirm that FF related sources are overestimated in North-West Germany.

Our results from both case studies show that source partitioning through forward modelling can be useful for discovering the main cause for discrepancies between measurements and simulations and for evaluating emission inventories. Hence, more long-term, high-frequency measurements of both δ^{13}C and δ^{2}H at multiple locations could help better identify and quantify CH_4 sources.

Chapter 4

Investigating the potential of isotopic measurements for methane source detection in a modelling framework

4.1 Introduction

The results in Chapter 3 reveal that inaccurate magnitudes and placement of methane emissions in the inventories is the main reason for the differences between measured and modelled δ^{13}C and δ^{2}H and that measurements of isotopologues in addition to mixing ratios can be an asset for gaining more information about CH_4 emissions. δ^{13}C and δ^{2}H measurements are usually available as flask-sampled data with a low frequency of several days to weeks, while high-frequency ($\sim$ hourly) data of isotopic composition have been demonstrated to be able to reduce uncertainties on emissions estimated through atmospheric inversions (Rigby et al., 2012). However, the global scarcity of high-frequency, long-term measurements of δ^{13}C and δ^{2}H limits their application in emission estimation methods, such as atmospheric inversions.

Therefore in this chapter, we investigate through experiments with synthetic data the importance of high-frequency δ^{13}C and δ^{2}H data to be assimilated in atmospheric inversions, alongside with CH_4 mixing ratios, to improve CH_4 emission estimates. While awaiting availability of more high-frequency atmospheric isotopic measurements of several months or years in Europe, the evaluation is made at monitoring sites of the ICOS network. ICOS is chosen as the sites in this network already provide measurements of atmospheric CH_4 mixing ratios and it could represent a possible CH_4 isotopologue monitoring network.

Furthermore, we address the limitation on CH_4 source detection due to limited precisions of instruments measuring atmospheric isotopic composition (Schaefer, 2019), as referred to in Section 1.6 (page 24). Following Thonat et al. (2019), we analyse a set of current instrument precisions for δ^2H and δ^{13}C analyses and investigate from what type of CH_4 sources atmospheric δ^{13}C and δ^2H signals would be detectable with given instrument precisions. A further aim of this analysis is to provide ICOS sites or alternative locations that would be best suited for long-term monitoring of CH_4 isotopologues.

4.2 Methodology

The synthetic experiments are performed for one year from 1 July 2016 to 30 June 2017 using the same modelling framework as in Chapter 3.

4.2.1 Computation of isotopic ratios

δ^{13}C and δ^2H time series are computed with an hourly temporal resolution based on simulated CH_4 mixing ratios for the four main CH_4 source categories as in Chapters 2 and 3. Using Equations 1.10 to 1.13 (page 19), the simulated CH_4 mixing ratios per source are combined with their corresponding δ^2H and δ^{13}C isotopic source signatures. The atmospheric CH_4 mixing ratios, as well as δ^2H and δ^{13}C isotope ratios are computed for the locations of measurement sites (Section 4.4.1) and for the domain (Section 4.4.4) using emissions from two anthropogenic emission inventories to tackle uncertainties in emissions and their impact on the simulations of atmospheric CH_4 mixing ratios and δ^{13}C and δ^2H isotope ratios.

We use simulations of atmospheric δ^2H and δ^{13}C isotope ratios sampled in grid-cells matching the monitoring sites locations of the ICOS network (Figure 4.1). Presently, there are 23 monitoring sites in our full European domain that are part of the ICOS network. We also include ten additional sites that are in the labelling process to become part of the ICOS network as described in Section 1.3. Detailed information on the ICOS sites in our domain can be found in Table 4.1.

As discussed in previous chapters, most transport models use basic planetary boundary layer parameterisations, which affects the vertical mixing in models (Dabberdt et al., 2004). Therefore, we have examined whether the conclusions of this study, described in Section 4.5, are affected by us-

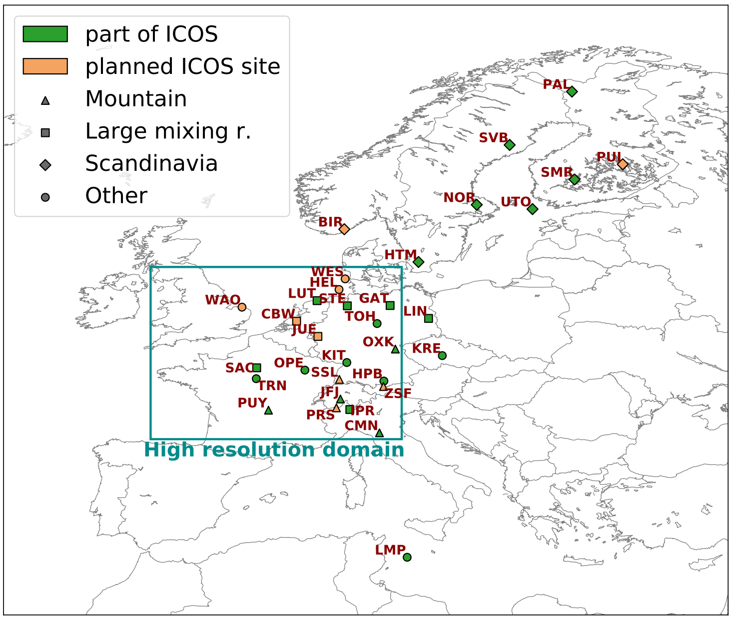

Figure 4.1: Simulation domains covering whole Europe and part of Europe (turquoise square). Locations of the monitoring sites that are already part of the ICOS network are shown in green and sites being in the labelling process are orange. Mountain sites are indicated by triangles, sites with usually large mixing ratios by squares, sites in Scandinavia by diamonds and any other sites by circles.

ing mixing ratios and isotopic ratios of only the morning, afternoon or night time. Based on this analysis (not shown), the conclusions are not affected and we use hourly simulations of atmospheric CH_4 mixing ratios as well as δ^{13}C and δ^{2}H isotopic ratios of entire days in this study, without selecting specific hours of the day.

We group the measurement sites in four categories (Figure 4.1):

- Large mixing ratio: sites whose average CH_4 mixing ratio in the study year is above 1980 ppb
- Scandinavia: sites located in Scandinavia, where most of the European wetlands are
- Mountain: sites located at an altitude above 900 m above sea level
- Other: sites that do not fit in the above mentioned categories

4.2.2 Determination of average source isotopic signatures

We derive δ^{2}H and δ^{13}C source isotopic signatures from time series of atmospheric δ^{2}H and δ^{13}C isotope ratios to identify the average source type at locations of all measurement sites over the study year (Section 4.4.2). To do so, the Keeling plot approach (Equation 1.5 in Section 1.3) is applied on atmospheric CH_4 mixing ratios and δ^{13}C and δ^{2}H isotope ratios in combination with an orthogonal distance regression that accounts for the uncertainty in

Table 4.1: List of monitoring sites in the ICOS network within our European domain.

3-letter code of site	Name of site	Country	Altitude [m a.s.l + inlet height]	part of ICOS
Large mixing ratio sites				
CBW	Cabauw	The Netherlands	0 + 200	in process
GAT	Gartow	Germany	70 + 341	yes
IPR	Ispra	Italy	210 + 100	yes
JUE	Jülich	Germany	98 + 120	in process
LUT	Lutjewad	The Netherlands	1 + 60	yes
SAC	Saclay	France	160 + 100	yes
STE	Steinkimmen	Germany	29 + 252	yes
Scandinavia sites				
BIR	Birkenes Observatory	Norway	219 + 224	in process
HTM	Hyltemossa	Sweden	115 + 150	yes
NOR	Norunda	Sweden	46 + 100	yes
PAL	Pallas	Finland	565 + 12	yes
PUI	Puijo	Finland	316 + 84	in process
SMR	Hyytiälä	Finland	181 + 127	yes
SVB	Svartberget	Sweden	267 + 150	yes
UTO	ICOS Utö - Baltic sea	Finland	8 + 57	yes
Mountain sites				
CMN	Monte Cimone	Italy	2165 + 8	yes
JFJ	Jungfraujoch	Switzerland	3572 + 10	yes
OXK	Ochsenkopf	Germany	1015 + 163	yes
PRS	Plateau Rosa	Italy	3480 + 9	in process
PUY	Puy de Dome	France	1465 + 10	yes
SSL	Schauinsland	Germany	1205 + 12	in process
ZSF	Zugspitze	Germany	2666 + 3	in process
Other sites				
HEL	Helgoland	Germany	43 + 110	in process
HPB	Hohenpeissenberg	Germany	934 + 131	yes
KIT	Karlsruhe	Germany	110 + 200	yes
KRE	Křešín u Pacova	Czech Republic	534 + 250	yes
LIN	Lindenberg	Germany	73 + 98	yes
LMP	Lampedusa	Italy	45 + 8	yes
OPE	Observatoire Pérenne de l'Environnement	France	392 + 120	yes
TOH	Torfhaus	Germany	801 + 147	yes
TRN	Trainou	France	131 + 180	yes
WES	Westerland	Germany	12 + 11	in process
WAO	Weybourne Atmospheric Observatory	United Kingdom	15 + 10	in process

both the X (1/CH_4 mixing ratio) and Y (isotopic composition) variables.

4.2.3 Detection of methane sources

Following Thonat et al. (2019), we compute the standard deviations (SD) of simulated daily (1-day mean) total atmospheric δ^2H and δ^{13}C time series over 3-day, 7-day and 14-day running windows, i.e. running time intervals, to be in the range of the synoptic time scale (about 5 days). We test a set of instrument precisions, i.e. thresholds for signal detection. If a threshold is exceeded by the running SDs of the total atmospheric δ^2H and δ^{13}C signals, we compute the SDs of the individual CH_4 sources over the same running windows. Even though total atmospheric signals consist of various sources that have different isotopic signatures, we consider only the source with the highest running SD as detectable for a given day. The exceedance of a threshold indicates that the synoptic variability of atmospheric signals can be detected, in which case a measuring instrument is considered to be able to provide useful information for regional atmospheric inversions. To conclude on how often signals from CH_4 sources are detectable in a year, the number of days when signals are detectable are added up over the one year study period.

4.2.3.1 Detection thresholds

The thresholds for δ^2H and δ^{13}C are chosen according to precisions of current instruments and compatibility targets defined by the WMO IAEA (World Meteorological Organization - International Atomic Energy Agency) (WMO, 2018). The latter are for δ^2H and δ^{13}C, respectively, ±1‰ and ±0.02‰ for global studies, as well as ±5‰ and ±0.2‰ for regionally aimed studies (Section 1.3). The thresholds used in this study for δ^2H are 0.5‰, 1.0‰, 3.0‰ and 5.0‰. For δ^{13}C, we use the thresholds of 0.02‰, 0.05‰, 0.1‰ and 0.2‰.

The instrument used by Röckmann et al. (2016) and Menoud et al. (2020b) is based on a continuous flow isotope ratio mass spectrometry system (CF-IRMS) and has a precision of 1.0‰ for δ^2H and 0.1‰ for δ^{13}C. According to Lowe et al. (2002), the IRMS of the National Institute of Water and Atmospheric Research, Wellington, New Zealand reaches a precision of 0.02‰ and the Scripps Institution of Oceanography, University of California San Diego, uses an IRMS with an experimental uncertainty of 1.0-3.0‰ for δ^2H and 0.05-0.1‰ for δ^{13}C. Similarly, Fisher et al. (2006) achieved a precision of 0.05‰ for δ^{13}C using a CF-IRMS. Bergamaschi et al. (1998a) performed δ^2H analyses in CH_4 samples with the aid of their tunable diode laser based Methane ISOtopomer Spectrometer (MISOS) with an overall precision of 0.5‰.

4.2.3.2 Confirmation of detectable sources

In Section 4.4.5, we analyse whether source types indicated as detectable by the detection method described above are indeed likely to be detected. For that, we select the dominant detectable source, i.e. the source that is detectable on most of the days in the study year, at the sites and apply the Keeling approach on the hourly data of the days on which the dominant source is detectable. We carry out this analysis for the sources that can be detectable by measuring instruments with 0.02‰ and 0.5‰ precisions for δ^{13}C and δ^{2}H, respectively.

If the derived average δ^{13}C and δ^{2}H source isotopic signatures are within the range of the dominant detectable source type, which are based on MEMO^2 campaigns (Menoud et al., 2020a, more details in Section 4.3.1) and studies listed in Szénási and Bousquet (2019), it gives insights that a specific source at a given site is indeed likely to be detected by an instrument with the given precisions. For example, if the dominant detectable source is waste and the derived δ^{13}C and δ^{2}H source isotopic signatures indicate a microbial source type at a given site, we assume that waste sources are likely to be detected at that given site.

4.2.3.3 Seasonal detection analysis

We also analyse in which season the various sources are more expected to be detected. Doing so can reveal which season is most suited to perform intensive measurement campaigns of several days to weeks or quasi-continuous measurements (e.g. Röckmann et al., 2016; Menoud et al., 2020b) if there is no possibility for measurements of at least a year. This is especially helpful if the source of interest is detectable only on a low number of days ($\sim$ one month or less) during a year. The results are presented and discussed in Section 4.4.6.

4.2.4 Investigating the impact of horizontal resolution on simulation outputs

The study of Locatelli et al. (2013) demonstrates that different model horizontal resolution configurations can lead to differences in top-down estimated CH_4 emissions. Emissions, especially from point sources or small area sources, are more concentrated in grid-cells with a high horizontal resolution. This leads to larger spatial and temporal gradients of simulated mixing ratios within a smaller grid-cell compared to simulations made with a lower horizontal resolution. Additionally, the results in Chapter 2 have shown that it is important to analyse the influence of the model's horizontal resolution on the simulation outputs. The sensitivity of atmospheric δ^{2}H and δ^{13}C isotope ratios could be analysed to different horizontal resolutions with similar methods. However, such an analysis requires information on source isotopic signatures in more detail than it is currently available (for example, country or region specific isotopic signatures of different sources).

Although an exhaustive analysis is not yet possible due to a lack of information on source isotopic signatures, we start investigating the influence of the model's horizontal resolution on the simulated atmospheric δ^2H and δ^{13}C isotopic ratios as well as the source detectability in Section 4.4.7. For that, simulations at two horizontal resolutions are carried out: 0.5°×0.5° over the entire European domain and 0.1°×0.1° over the sub-domain covering parts of Northwestern Europe (Figure 4.1).

4.3 Material

4.3.1 Source isotopic signatures

The δ^{13}C and δ^2H source isotopic signatures used as input for computing time series of atmospheric δ^{13}C and δ^2H isotopic compositions are assumed homogeneous in time and space over the domains. They are chosen with the aid of several literature studies and the MEMO^2 measurements (Menoud et al., 2020a) and are summarised in Table 4.2. Although MEMO^2 campaigns have been carried out at several locations in Europe and they have brought valuable information on typical isotopic source signatures, the locations of the measurement sites we focus on do not overlap with the MEMO^2 campaign locations. The areas of interest in MEMO^2 are large emission areas, whereas the sites of the ICOS network used in this study are located in rather low emission areas to be representative at large spatial scales.

For methane of microbial origin, enteric fermentation is a major source and its signature varies depending on the type of animal and their diet. For example, Klevenhusen et al. (2010) found δ^{13}C signatures of -68‰ for a C3 plant diet of cows (e.g. barley, wheat) and -57‰ for a C4 plant diet (e.g. maize, sugarcane). Signatures of agricultural sources derived from measurements using Keeling or Miller-Tans approaches in MEMO^2 range between -65.5‰ and -56.8‰ for δ^{13}C and between -379‰ and -168‰ for δ^2H in the Netherlands. One signature per country for Romania, Poland, and the United Kingdom is available that are for δ^{13}C -62.6‰, -61.5‰ and -63.4‰, respectively. In case of δ^2H, these are -252‰, -356‰ and -301‰ for the three countries, respectively. Corresponding to these values and values found in other studies listed in Table 4.2, we use -63.5‰ for δ^{13}C and -306‰ for δ^2H

Table 4.2: Characteristic source isotopic signatures used as input for the computation of the atmospheric isotopic compositions δ^{13}C and δ^2H, including the ranges of values found in the listed references. The δ^{13}C and δ^2H values for the boundary mixing ratios demonstrate the mean value as they vary over time.

Source sector	δ^{13}C [‰]	δ^2H [‰]	References
Agriculture	-63.5 [-74.4 – -50.3]	-306 [-442 – -168]	Menoud et al. (2020a), Levin et al. (1993), Klevenhusen et al. (2010), Sherwood et al. (2017), Bréas et al. (2001), Bilek et al. (2001), Röckmann et al. (2016), Uzaki et al. (1991), Tyler et al. (1997)
Waste	-54.9 [-73.9 – -45.4]	-290 [-347 – -172]	Bergamaschi et al. (1998b), Levin et al. (1993), Zazzeri et al. (2015), Röckmann et al. (2016), Menoud et al. (2020a), Games and Hayes (1976), Sherwood et al. (2017)
Fossil fuel related emissions	-46.4 [-87.0 – -14.8]	-185 [-415 – -56]	Levin et al. (1999), Röckmann et al. (2016), Menoud et al. (2020a), Sherwood et al. (2017), Lowry et al. (2001), Thielemann et al. (2004), Zazzeri et al. (2016)
Other anthropogenic sources	-38.3 [-64.4 – -12.5]	-206 [-308 – -110]	Menoud et al. (2020a), Röckmann et al. (2016), Levin et al. (1999), Chanton et al. (2000), Nakagawa et al. (2005), Sherwood et al. (2017)
Wetland	-68.2 [-96.5 – -48.0]	-337 [-450 – -288]	Menoud et al. (2020a), Sherwood et al. (2017), Tyler et al. (1987), Smith et al. (2000), Fisher et al. (2017), Galand et al. (2010), Happell et al. (1995), Martens et al. (1992), Bilek et al. (2001), Sugimoto and Fujita (2006), Quay et al. (1999)
Boundary mixing ratios	-47.0 (mean)	-86 (mean)	Thanwerdas et al. (2019)

for the agriculture sector.

Waste signatures typically vary between -73.9‰ and -45.5‰ for δ^{13}C and between -312‰ and -281‰ for δ^2H at the global scale (Sherwood et al., 2017). According to the MEMO^2 measurements in Europe, the ranges are similar with -63.6‰ – -45.4‰ for δ^{13}C and -347‰ – -173‰ for δ^2H, with the lowest values found in France and the highest in Poland and the United Kingdom. Therefore, we use signatures of -54.9‰ and -290‰ for δ^{13}C and δ^2H, respectively.

Typical, global signature ranges for wetland sources are -70.1‰ – -48.0‰ in case of δ^{13}C and -442‰ – -288‰ in case of δ^2H (Sherwood et al., 2017). In the MEMO^2 project, most measurements were carried out in Swedish wetlands and one measurement in Romania. In Sweden, the signatures vary between -96.5‰ and -54.9‰ for δ^{13}C and between -380‰ and -255‰ for δ^{2}H. In Romania, the derived δ^{13}C and δ^{2}H source signatures are -64.2‰ and -237.3‰, respectively. In this study, the signatures used for wetlands are -68.2‰ and -337‰ in case of δ^{13}C and δ^{2}H, respectively.

Thermogenic CH_4 sources (e.g. from fossil fuel production) typically have isotopic signatures that vary widely between -87‰ and -15‰ for δ^{13}C, and between -415‰ and -62‰ for δ^{2}H (Sherwood et al., 2017). The range of signatures derived from the MEMO^2 measurements is similarly wide: -73.3‰ – -18.3‰ for δ^{13}C and -369‰ – -56‰ for δ^{2}H. Based on these and values found in other studies, the used source signatures for δ^{13}C and δ^{2}H are -46.4‰ and -185‰, respectively.

Pyrogenic CH_4 is usually more enriched in heavy isotopes compared to microbial and thermogenic sources. For biomass burning, the signatures typically are between -32.4‰ and -12.5‰ in case of δ^{13}C, and between -232‰ and -195‰ in case of δ^{2}H, according to the global inventory of Sherwood et al. (2017). The source category named "other anthropogenic sources" in this study is a mixture of mainly pyrogenic and some thermogenic sources. Thus, we use signatures for the "other anthropogenic sources" of -38.3‰ and -206‰ for δ^{13}C and δ^{2}H, respectively.

For the background, i.e. air with very low emission levels, the simulated CH_4 boundary mixing ratios are combined with isotopic composition time series obtained from δ^{13}C and δ^{2}H simulations of Thanwerdas et al. (2019) as in Chapter 3. The average of the δ^{13}C and δ^{2}H simulations for the one year period is -47.0‰ and -98‰, respectively. Since the average of the δ^{2}H LMDz simulations is much lower than the global average of δ^{2}H in background air (-86‰ by Rigby et al., 2012), we offset the δ^{2}H simulations by +12‰ to meet the global average and have realistic source signatures for the background.

4.3.2 Emission data

4.3.2.1 Methane emissions

We use anthropogenic emissions from the TNO-MACC_III (Kuenen et al., 2014) and the EDGARv4.3.2 (Janssens-Maenhout et al., 2017) inventories and use the same classifications for CH_4 source sectors as in Chapters 2 and 3. Natural wetland emissions are obtained from the ORCHIDEE-WET model (Ringeval et al., 2011) with a monthly time profile. The anthropogenic and wetland emissions over the European domain with a horizontal resolution of 0.5°×0.5° are illustrated in Figure 4.2 and Table 4.3 contains the magnitude of the total and sector emissions of the inventories.

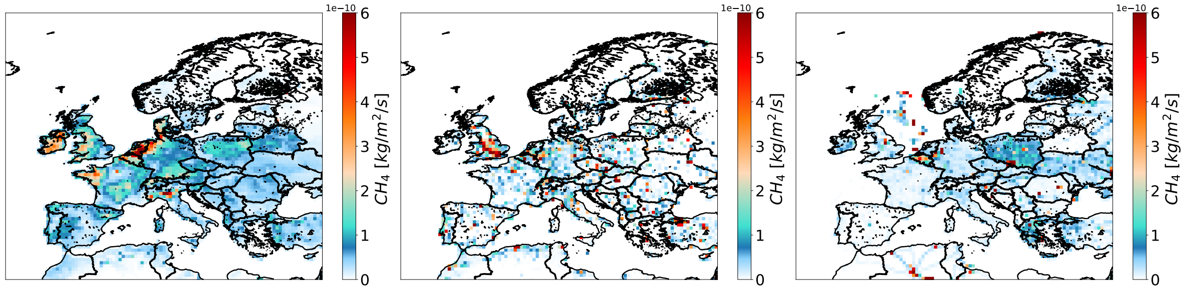

(a) Agriculture - EDGARv4.3.2 **(b)** Waste - EDGARv4.3.2 **(c)** Fossil fuel related - EDGARv4.3.2

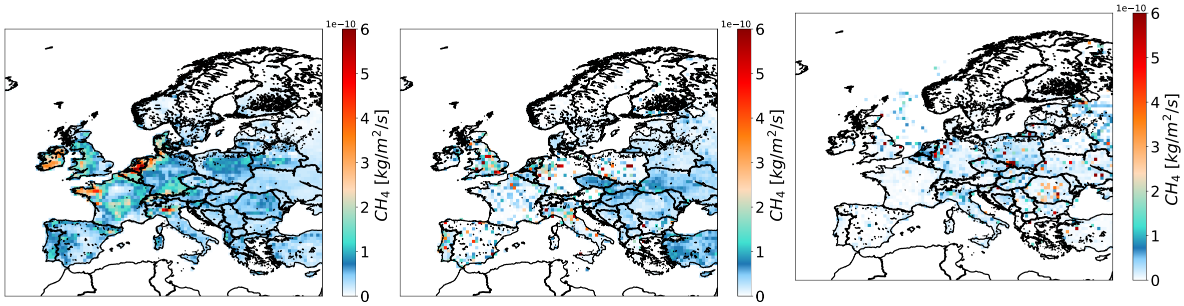

(d) Agriculture - TNO-MACC_III **(e)** Waste - TNO-MACC_III **(f)** Fossil fuel related - TNO-MACC_III

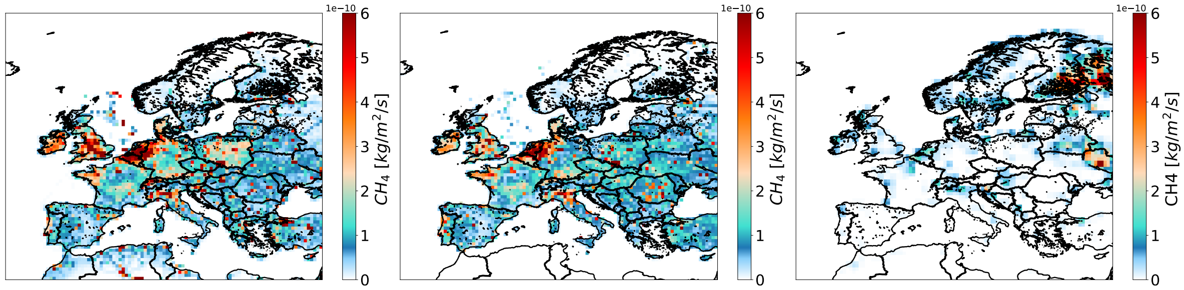

(g) Total - EDGARv4.3.2 **(h)** Total - TNO-MACC_III **(i)** Wetland - ORCHIDEE

Figure 4.2: Anthropogenic emissions per sector (**a-f**) contributing to the total CH_4 emissions of the EDGARv4.3.2 (**g**) and TNO-MACC_III (**h**) inventory, as well as emissions from natural wetlands (**i**) obtained from the ORCHIDEE-WET model.

4.3.2.2 Methane isotopic maps

Based on the main emission sectors and emission inventories used in this study, we produce maps of δ^{13}C and δ^{2}H of CH_4 sources for Europe to analyse emissions with the aid of isotopic information. Such maps provide more insight on the source distribution and dominant source types over the domain than, for example, maps of total CH_4 emissions. The δ^{13}C and δ^{2}H maps are made by using weighted emission averages of emission sectors from the inventories in combination with corresponding δ^{13}C and δ^{2}H source

Table 4.3: Emissions [TgCH$_4$year^{-1}] per category of the TNO-MACC_III and EDGARv4.3.2 anthropogenic inventories, as well as of natural wetlands in the full European domain. The relative contribution [%] of the sources to the total anthropogenic emissions is displayed in the column "Percentage of the total anthropogenic emissions".

SNAP code	SNAP name	Name in this study	Quantity (TgCH$_4$year^{-1})		Percentage [%] of the total anthropogenic emissions	
			TNO-MACC_III	EDGARv4.3.2	TNO-MACC_III	EDGARv4.3.2
Anthropogenic sources						
2, 5	Non-industrial combustion plants & Distribution of fossil fuels and geothermal energy	Fossil fuel related emissions	6.1	7.3	24.0	23.9
9	Waste treatment and disposal	Waste	7.7	10.8	30.3	35.3
10	Agriculture	Agriculture	10.9	12.1	42.9	39.5
1, 3, 4, 6, 7, 8		Other anthropogenic sources	0.7	0.4	2.8	1.3
Total anthropogenic			25.4	30.6	100.0	100.0
Wetland emissions						
11	Natural emissions	Wetland	7.8	7.8		
Total			33.2	38.4		

isotopic signatures (from Section 4.3.1).

Figure 4.3 shows the δ^{13}C and δ^{2}H emission maps for the European domain. Through the δ^{13}C and δ^{2}H values, a general spatial distribution of CH$_4$ sources is easily recognisable. The prevailing values of about -60‰ for δ^{13}C and -300‰ for δ^{2}H in both inventories indicate that CH$_4$ from agriculture sources dominates in Europe. In most of the capitals and larger cities, the δ^{13}C and δ^{2}H values are higher, pointing out sources connected to fossil fuels and residential combustion (e.g. heating). Such isotopic maps highlight the differences in spatial and sector distribution of sources between the inventories (e.g. Figure 4.3a and Figure 4.3b). The TNO-MACC_III inventory contains a higher ratio of FF related emissions from point sources than EDGAR, indicated by the higher δ^{13}C and δ^{2}H values in multiple single grid-cells in the TNO-MACC maps. The sources in EDGAR appear to be more diffuse, indicating a larger proportion of area sources than in TNO-MACC. This difference may be due to different definitions and treatment of point and area sources in the inventories. Another difference between the inventories is the inclusion of shipping paths in the EDGAR inventory, which are not present in the TNO-MACC inventory.

The combination of CH$_4$ emissions (Figure 4.2) and their isotopic signatures provide a full insight on the differences of the emission magnitudes between the inventories (Table 4.3). The TNO-MACC inventory includes in

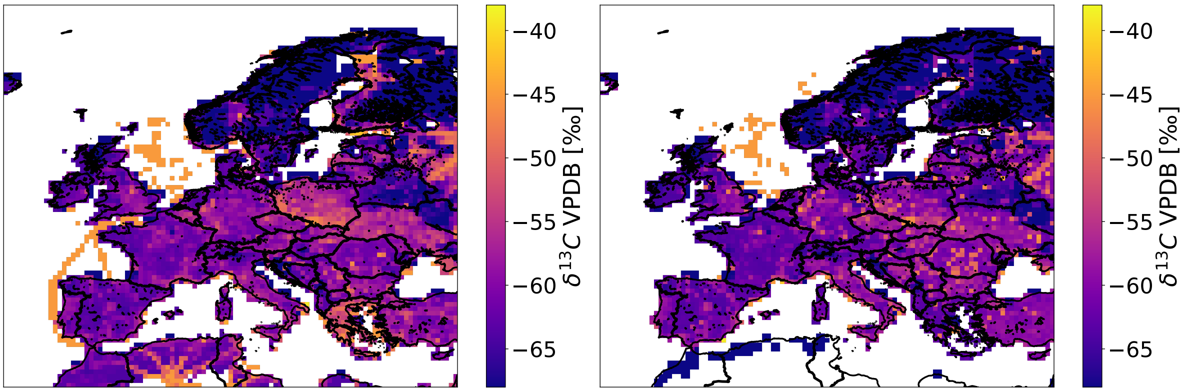

(a) EDGARv4.3.2 - δ^{13}C **(b)** TNO-MACC_III - δ^{13}C

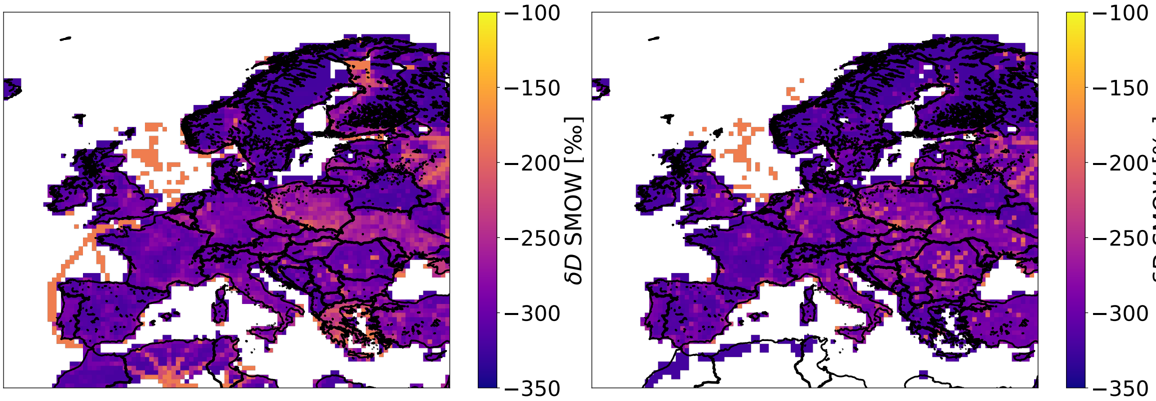

(c) EDGARv4.3.2 - δ^{2}H **(d)** TNO-MACC_III - δ^{2}H

Figure 4.3: Maps of δ^{13}C (top panel) and δ^{2}H (bottom panel) made from the EDGARv43.2. (left panel) and TNO-MACC_III (right panel) anthropogenic emission inventories and ORCHIDEE-WET wetland emissions as weighted average for the full European domain with a horizontal resolution of 0.5°×0.5°.

general more agriculture and less waste emissions than EDGAR over our European domain, which is indicated in the maps of Figure 4.3 by TNO-MACC having more values under approximately -62‰. This is due to the agriculture sources having lower signatures assigned than waste sources. Furthermore, EDGAR having more waste sources likely contributes to the higher δ^{13}C and δ^{2}H in larger cities where waste and FF related emissions are usually the largest sources of methane.

As described in Section 4.2.4 and demonstrated in Chapter 2, the horizontal resolution of the model affects, among others, the emissions used as input for the model. Hence, the δ^{13}C and δ^{2}H emission maps are computed for the higher horizontal resolution configuration of 0.1°×0.1°. Figure 4.4 shows the δ^{13}C and δ^{2}H of emission sources over the sub-domain covering parts of Northwestern Europe, which illustrates well the effect of the horizontal resolution configuration. The spatial distribution of δ^{13}C and δ^{2}H is finer than in the low horizontal resolution configuration (Figure 4.3).

Hot-spots and point sources are better defined. A good example is the offshore gas and oil distribution network in the North Sea, which appear as point sources in Figure 4.4 instead of clusters as in Figure 4.3. Moreover, the difference in the proportions of area and point sources between the two inventories is even more apparent than in the low horizontal resolution configuration.

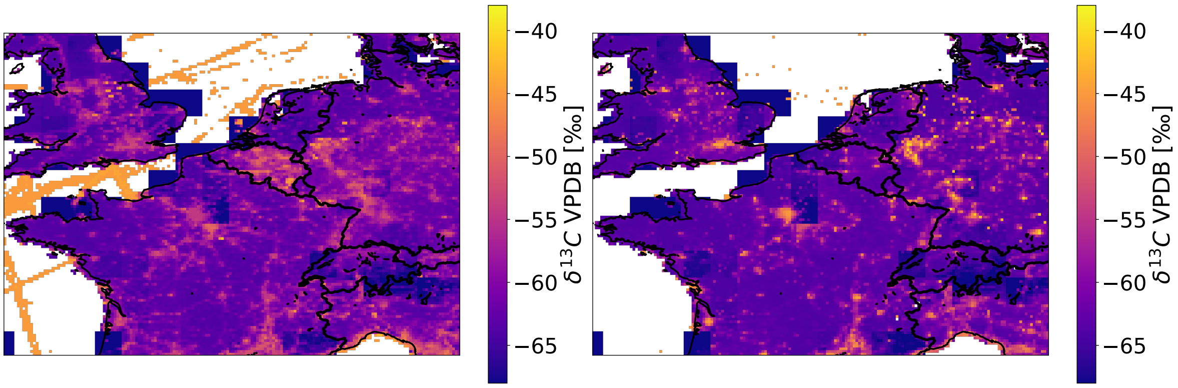

(a) EDGARv4.3.2 - δ^{13}C **(b)** TNO-MACC_III - δ^{13}C

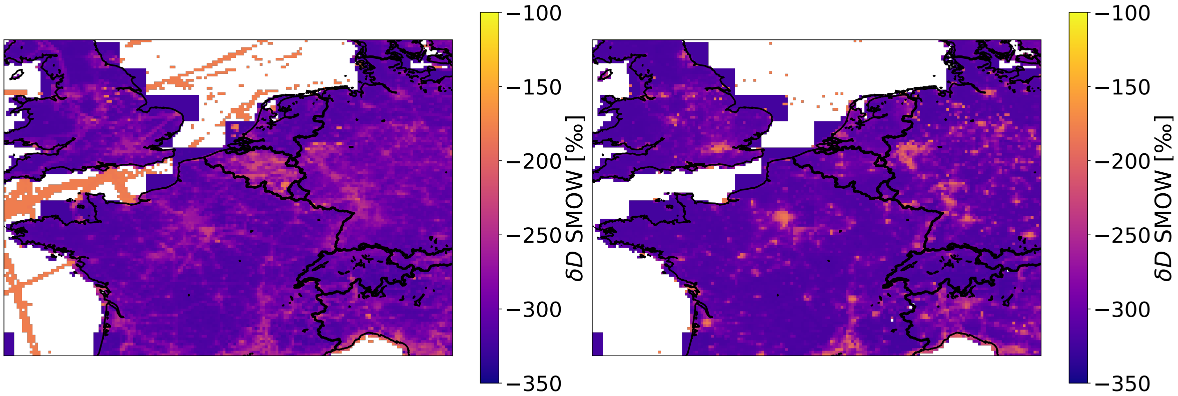

(c) EDGARv4.3.2 - δ^{2}H **(d)** TNO-MACC_III - δ^{2}H

Figure 4.4: Maps of δ^{13}C (top panel) and δ^{2}H (bottom panel) made from the EDGARv43.2. (left panel) and TNO-MACC_III (right panel) anthropogenic emission inventories and ORCHIDEE-WET wetland emissions as weighted average for the domain covering parts of Northwestern Europe with a horizontal resolution of 0.1°×0.1°.

4.4 Results and discussion

4.4.1 Analysing time series of methane mixing ratios and its stable isotopic content

In this section, analyses of atmospheric CH_4 mixing ratios as well as δ^{2}H and δ^{13}C isotope ratios are carried out to demonstrate how δ^{13}C and δ^{2}H isotope ratios can be useful to indicate the extent of contribution of the various CH_4 sources to total CH_4 mixing ratios. As the boundary mixing ratios are the largest contributor (approximately 95%) to the total CH_4 mixing ratios, the source contributions to the total CH_4 mixing ratios are shown above the boundary mixing ratios in this section. As an example, we show the time series of two monitoring sites: Steinkimmen (STE) in Figure 4.5 and Weybourne Atmospheric Observatory (WAO) in Figure 4.6.

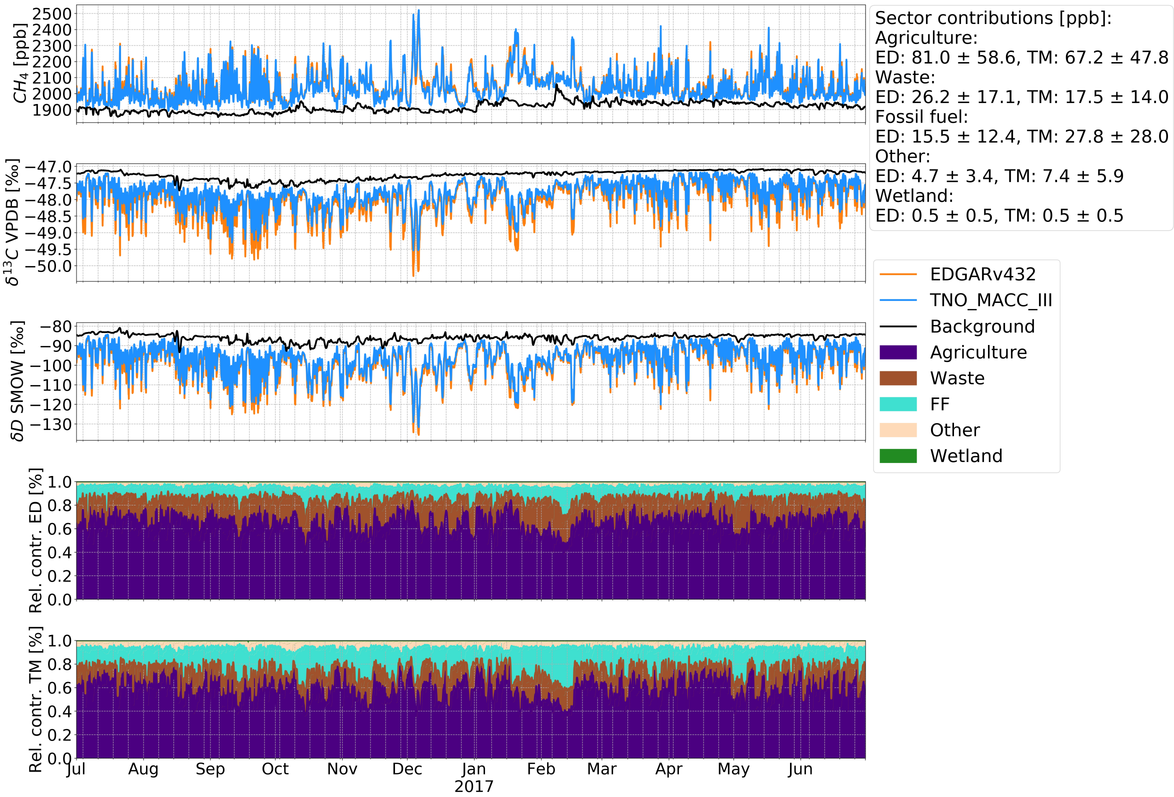

Figure 4.5: Time series of CH_4 mixing ratios (top panel), $\delta^{13}C$ (second panel from top) and $\delta^{2}H$ (middle panel) at the monitoring site Steinkimmen (STE) in the domain covering whole Europe. The relative contributions [%] (bottom two panels) indicate the CH_4 mixing ratio contributions of the sources to the total CH_4 mixing ratios using the EDGARv4.3.2 and the TNO-MACC_III inventories. The absolute CH_4 mixing ratios of the sources [ppb] are indicated in text form on the top right corner of the figure.

At STE, the CH_4 mixing ratios made by using the TNO-MACC_III inventory are generally larger than those made by using the EDGAR inventory. However, the $\delta^{2}H$ and especially the $\delta^{13}C$ time series indicate differences in the CH_4 source contributions to the total CH_4 mixing ratios. If both inventories contained a similar source apportionment and they differed only in the amount of emissions (and thus in the total CH_4 mixing ratios), the $\delta^{13}C$ with TNO-MACC would be lower than that with EDGAR. Indeed, the bottom two panels of Figure 4.5 show that the total CH_4 mixing ratio simulations with the

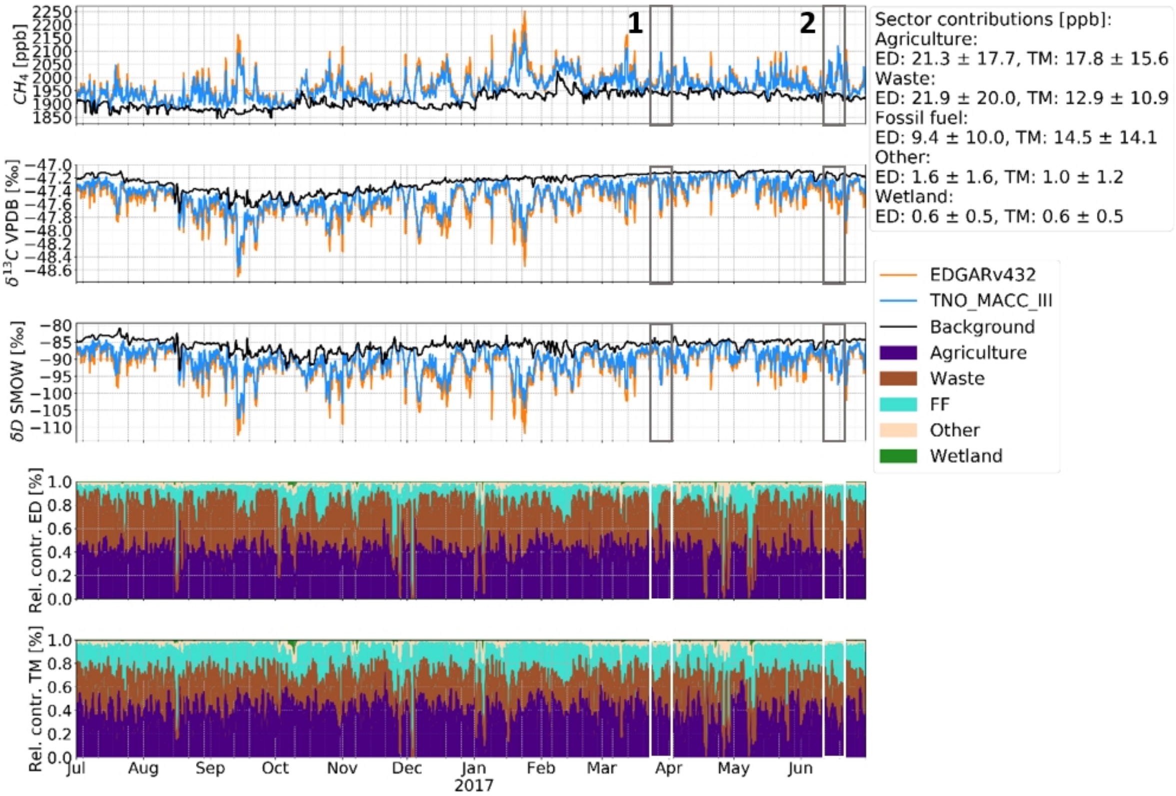

Sector contributions [ppb]:
Agriculture:
ED: 21.3 ± 17.7, TM: 17.8 ± 15.6
Waste:
ED: 21.9 ± 20.0, TM: 12.9 ± 10.9
Fossil fuel:
ED: 9.4 ± 10.0, TM: 14.5 ± 14.1
Other:
ED: 1.6 ± 1.6, TM: 1.0 ± 1.2
Wetland:
ED: 0.6 ± 0.5, TM: 0.6 ± 0.5

Figure 4.6: Time series of CH$_4$ mixing ratios (top panel), δ^{13}C (second panel from top) and δ^2H (middle panel) computed by using the TNO-MACC_III and EDGARv4.3.2. emission inventories at the monitoring site Weybourne Atmospheric Observatory (WAO) in the domain covering whole Europe. The relative contributions [%] (bottom two panels) indicate the CH$_4$ mixing ratio contributions of the sources to the total CH$_4$ mixing ratios using the EDGARv4.3.2 and the TNO-MACC_III inventories. The absolute CH$_4$ mixing ratios of the sources [ppb] are indicated in text form on the top right corner of the figure. The squares numbered 1 and 2 highlight events when δ^{13}C and δ^2H pinpoint differences in the source apportionment of the TNO-MACC_III and EDGARv4.3.2. inventories.

TNO-MACC inventory have a larger contribution of FF related sources than EDGAR, while the total CH$_4$ mixing ratios with EDGAR contain mainly agriculture and waste sources. Since the input isotopic signatures used for the FF related sources are higher than those used for the agriculture and waste sources, the total δ^{13}C and δ^2H values become more enriched in heavy isotopes when the FF related sources dominate.

For WAO, the CH$_4$ mixing ratios made by using the EDGAR inventory are larger than those made by using TNO-MACC. Accordingly, the δ^{13}C and δ^2H values are generally lower with EDGAR than with TNO-MACC. Yet, there are events when the CH$_4$ mixing ratio with TNO-MACC is larger than with EDGAR but the δ^{13}C values are still more depleted with EDGAR than with TNO-MACC. These events are marked with the numbers 1 and 2 in Figure 4.6. In both events, the main sources contributing to the total CH$_4$ mixing ratio with TNO-MACC are FF related and "other" anthropogenic sources, whereas with EDGAR, the waste and agriculture sources dominate, making the δ^{13}C lower than with TNO-MACC.

These two examples show differences in the magnitudes, source partitioning and spatial distribution of the emissions in the inventories, leading to discrepancies in the total CH_4 mixing ratios as well as the δ^2H and δ^{13}C isotope ratios. Just as the results in Chapter 3, they underpin the need for high-frequency, long-term isotopic composition measurements to detect differences between simulations with the two inventories, in other words between two atmospheric signals, in order to perform relevant atmospheric inversions.

4.4.2 Determination of average source isotopic signatures

In order to obtain the average source type at all measurement sites of the ICOS network over the study year, we derive δ^2H and δ^{13}C source isotopic signatures from atmospheric δ^2H and δ^{13}C time series. The determined δ^{13}C and δ^2H source isotopic signatures are shown in Figure 4.7, in which the sites are coloured depending on their site category (Section 4.2.2). Most of the sites in each category have similar isotopic source signatures. Most sites in the Scandinavia, Mountain and Other categories have typical average source signatures that correspond to background values. In the Large mixing ratio category, simulations made using the EDGAR inventory are of microbial origin at most sites, while the source isotopic signatures derived from simulations made using TNO-MACC are higher and only two sites are within the microbial category. This is due to TNO-MACC having mainly lower CH_4 emissions than EDGAR and therefore lower CH_4 mixing ratios, which results in a higher δ^2H and δ^{13}C.

The determined δ^2H and δ^{13}C isotopic source signatures at the measurement sites are close to a straight line in Figure 4.7. This is because δ^{13}C and δ^2H time series are computed from sectoral CH_4 mixing ratios combined with only one δ^{13}C and δ^2H source isotopic signature per source (Table 4.2) for each hour in the study year. Only the background source isotopic signatures include an hourly time profile. Under real conditions, the determined average source isotopic signatures at sites would have a more dispersed distribution. However, as long as there is a lack of knowledge on typical source isotopic signatures and their spatial and temporal distribution, simplifications (such as one isotopic signature per source for each hour) have to be made in modelling frameworks.

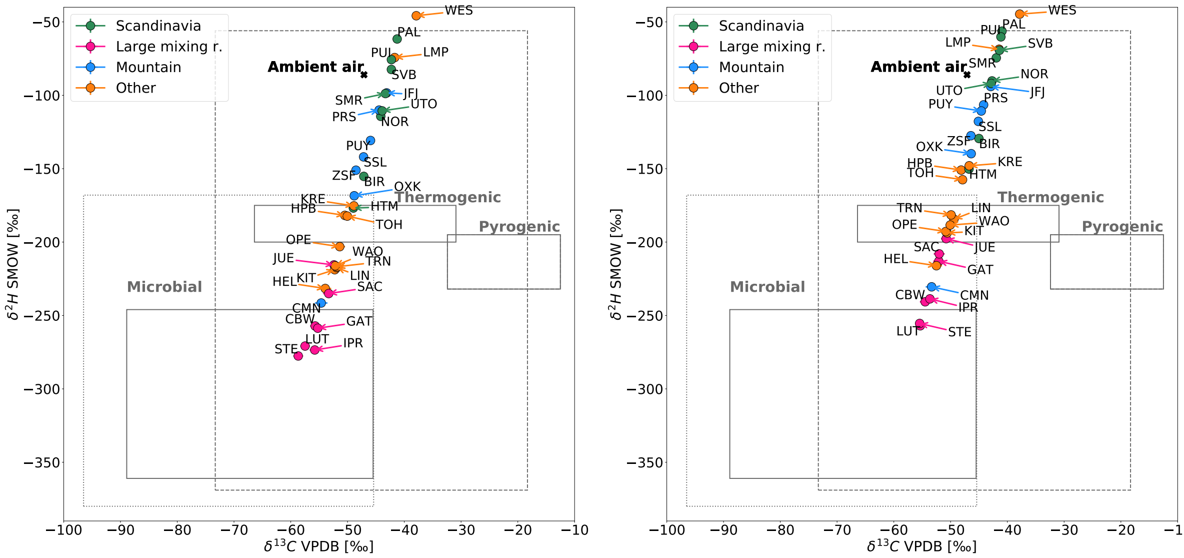

(a) EDGARv4.3.2

(b) TNO-MACC_III

Figure 4.7: Average δ^{13}C and δ^2H isotopic source signatures determined by the Keeling approach using simulations made with the EDGARv4.3.2 (**a**) and TNO-MACC_III (**b**) inventories for each monitoring site of the ICOS network in the full European domain for the year between July 2016 and June 2017. The ranges for CH_4 source types (microbial, thermogenic, pyrogenic) indicated by solid grey lines are taken from studies listed in Szénási and Bousquet (2019). The dashed grey box represents the range for thermogenic CH_4 sources taken from MEMO^2 campaigns (Menoud et al., 2020a). The dotted grey box indicates the range for microbial CH_4 sources obtained from MEMO^2 campaigns (Menoud et al., 2020a). The black cross represents the global average δ^2H and δ^{13}C isotopic signatures in ambient (background) air (Rigby et al., 2012).

4.4.3 Detectability of methane sources at ICOS sites

This section investigates whether δ^{13}C and δ^2H signals from CH_4 sources can be detected by isotopic instruments of different precisions, and if so, on how many days of the study year specific sources are likely to be detected. Figures 4.8 and 4.9 show the number of days between July 2016 and June 2017 when the SDs of simulated daily CH_4 source contributions to δ^2H and δ^{13}C, using the TNO-MACC_III inventory, at ICOS sites are above the four different thresholds. The results are shown for 3-day, 7-day and 14-day running windows and the colours of the bars indicate the source types that exceed a given threshold on a day. The figures for the EDGARv4.3.2 inventory can be found in the Appendix (Figures A4, A5).

The thresholds for both δ^{13}C and δ^2H are exceeded on less days with the 3-day running window compared to when using the 7-day and 14-day running windows. In general, the lower the running window, the lower the

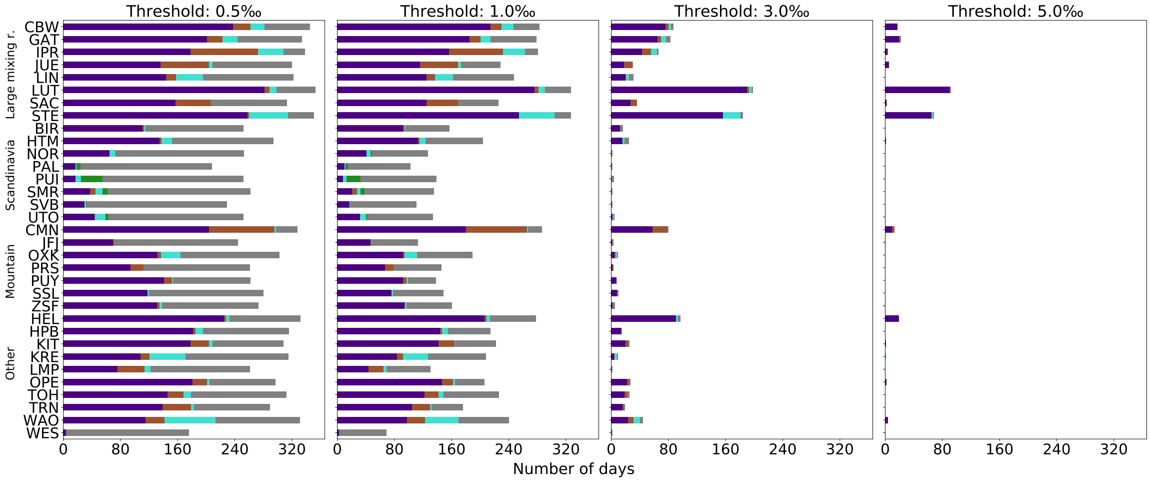

(a) 3-day window, TNO-MACC_III

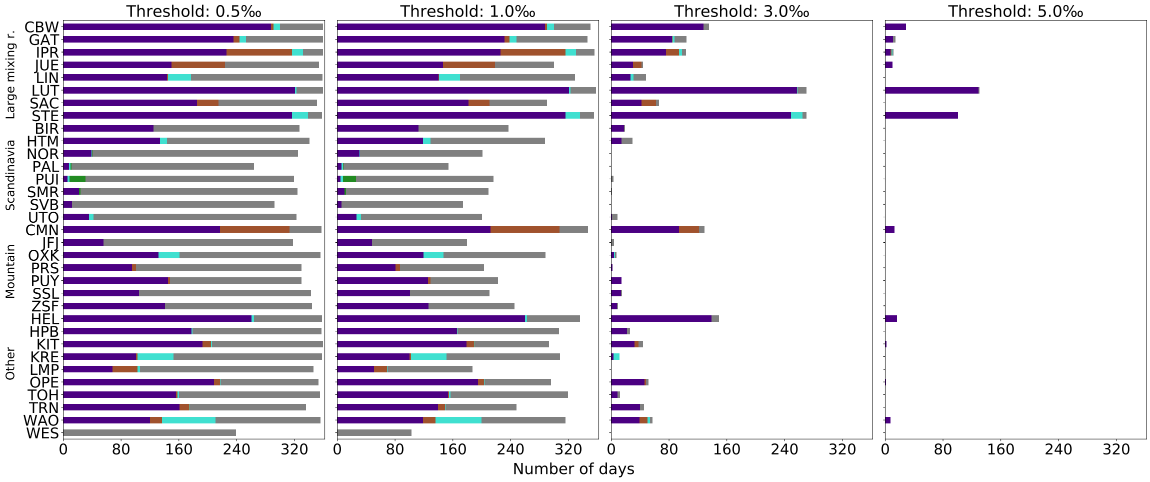

(b) 7-day window, TNO-MACC_III

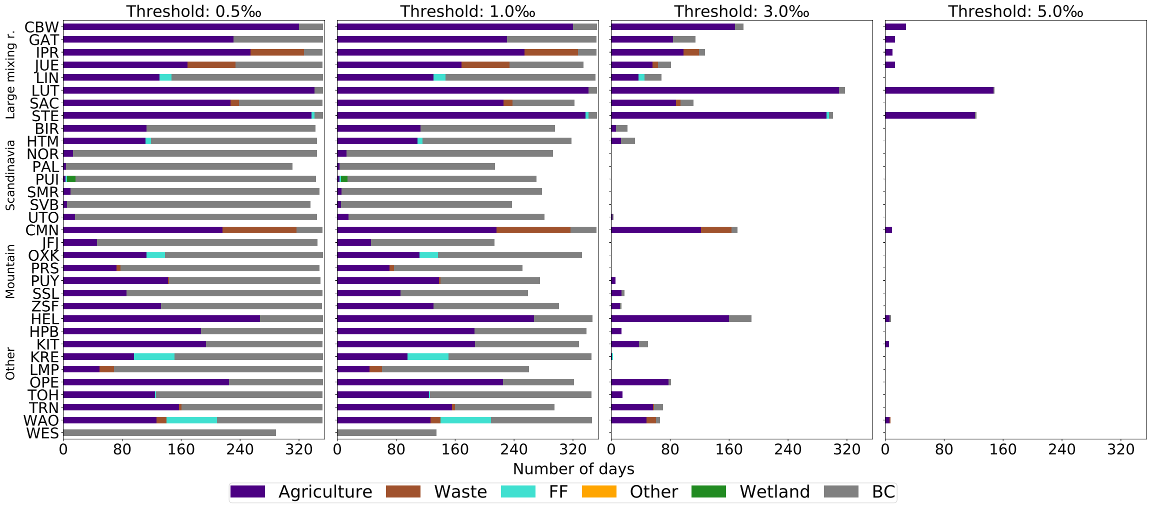

(c) 14-day window, TNO-MACC_III

Figure 4.8: Number of days in the study year when simulated daily source contributions to δ^2H at ICOS sites are above given thresholds, computed from standard deviations over the 3-day, 7-day and 14-day running windows, for the TNO-MACC_III inventory in the domain covering whole Europe. Colours indicate detectable source types.

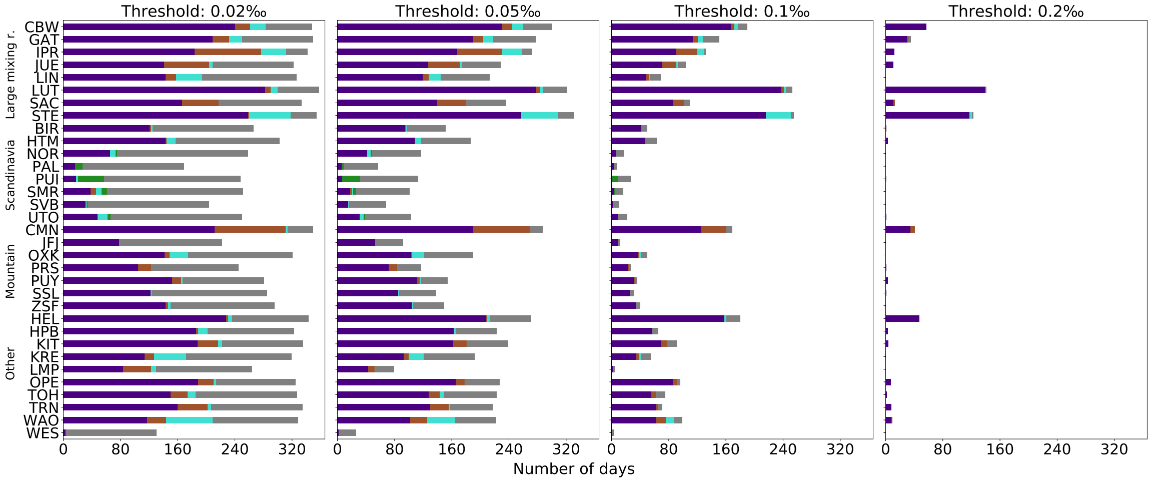

(a) 3-day window, TNO-MACC_III

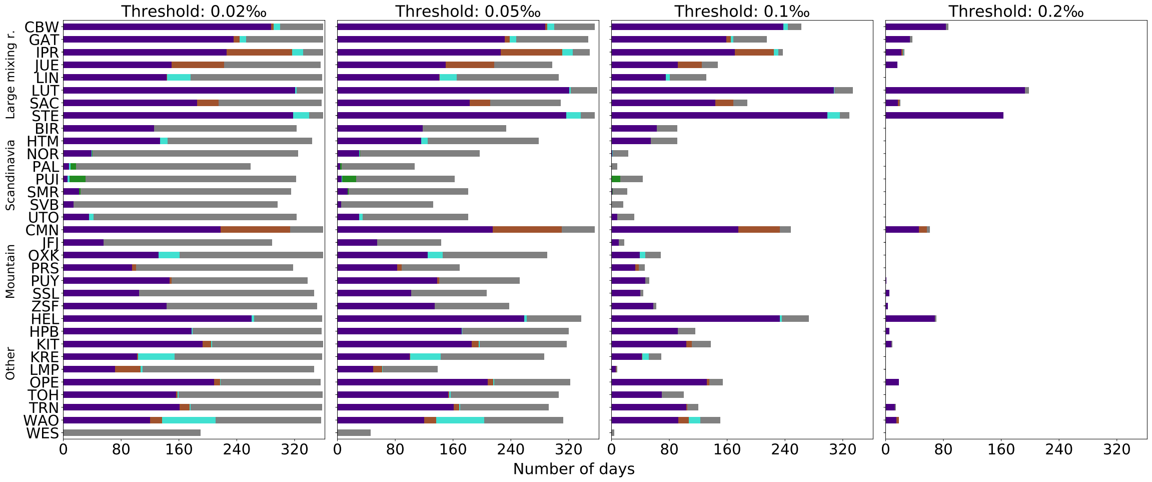

(b) 7-day window, TNO-MACC_III

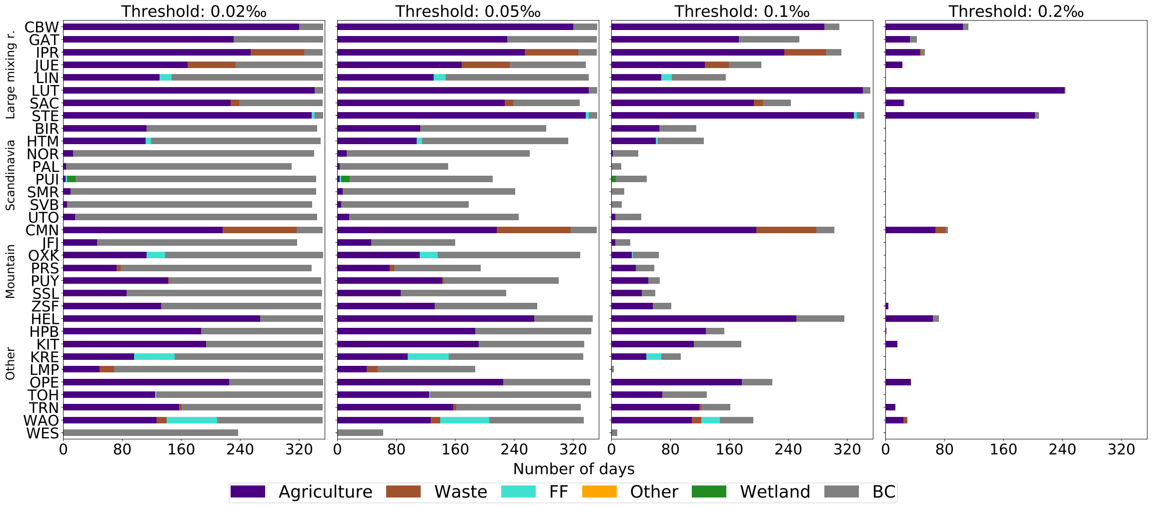

(c) 14-day window, TNO-MACC_III

Figure 4.9: Number of days in the study year when simulated daily source contributions to δ^{13}C at ICOS sites are above given thresholds, computed from standard deviations over the 3-day, 7-day and 14-day running windows, for the TNO-MACC_III inventory in the domain covering whole Europe. Colours indicate detectable source types.

number of days when the thresholds are exceeded and thus sources can be detected. This occurs because variations in the simulated daily δ^{13}C and δ^{2}H isotope ratios are lower in a smaller running window than in a larger running window. In order to present a lower bound on the source detection, we only study the 3-day running SD results in the following.

For δ^{2}H, signals generated with both emission inventories can be detected with the lowest detectability threshold (i.e. highest instrument precision) of 0.5‰ at all sites on at least 175 days, while on average, signals can be detected during about 80% of the year. With the second lowest threshold of 1.0‰, the minimum number of days on which signals are detectable is 67 days at the German site Westerland (WES). On average, signals are detectable for about 57% of the year at the sites. However, the two highest thresholds (i.e. two lowest instrument precisions) of 3.0‰ and 5.0‰ are exceeded on average only for about 10% and 5% of the year, respectively. With the highest thresholds, there are only 6 and 2 sites at which signals are detectable for at least 28 days ($\sim$ one month) when using the EDGAR and TNO-MACC inventories, respectively. The number of sites is larger with EDGAR as it contains generally larger emission amounts than TNO-MACC.

For δ^{13}C, the lowest threshold of 0.02‰ is exceeded on at least 130 days (at the site WES), while the threshold is exceeded on average at the sites for about 80% of the year. The number of detection events is reduced with the second lowest measurement uncertainty of 0.05‰: signals can be detected at all sites but only for about 54% of the year. The detection capability with the second largest threshold of 0.10‰ is limited compared to the lower thresholds of 0.02‰ and 0.05‰ as the number of days on which signals are detectable is about 85 days on average at the sites and the minimum number of such days is only 4 days (at WES). The largest threshold of 0.20‰ is barely exceeded during the year: there are 9 and 6 sites at which signals can be detectable for at least 28 days when using EDGAR and TNO-MACC, respectively. Moreover, there are only 26 and 22 sites with EDGAR and TNO-MACC, respectively, at which signals exceed the threshold on at least 1 day during the year. Based on these results, potential instruments should have a precision of at least 1.0‰ for δ^{2}H and 0.05‰ for δ^{13}C to be able to detect sources at 50% of the ICOS sites on about 85% of the year.

Thus, we further analyse the detectability using the two lowest thresholds (two highest precisions): 0.5‰ and 1.0‰ for δ^{2}H, as well as 0.02‰ and 0.05‰ for δ^{13}C. Figure 4.10 shows the number of days in the study year

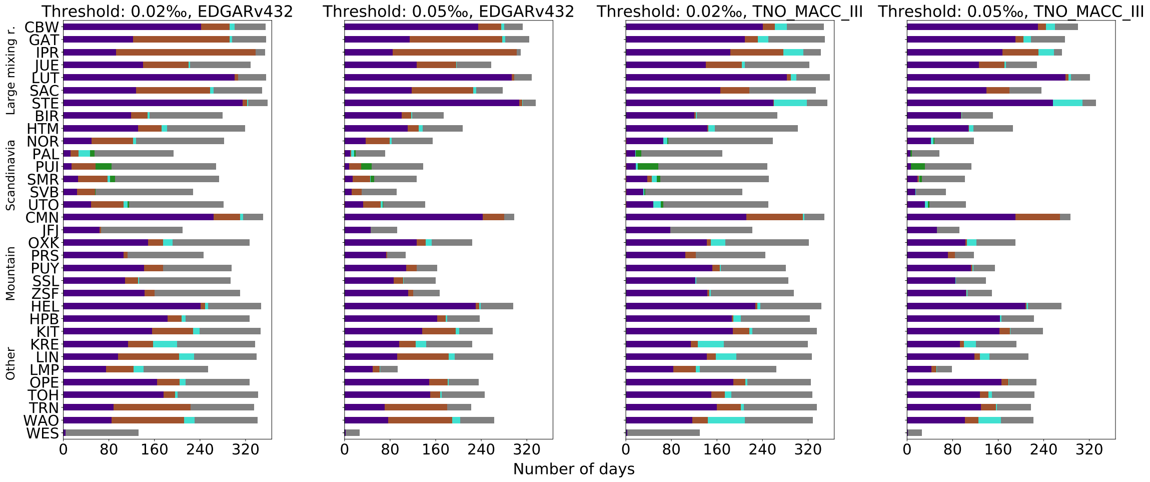

(a) δ^{13}C

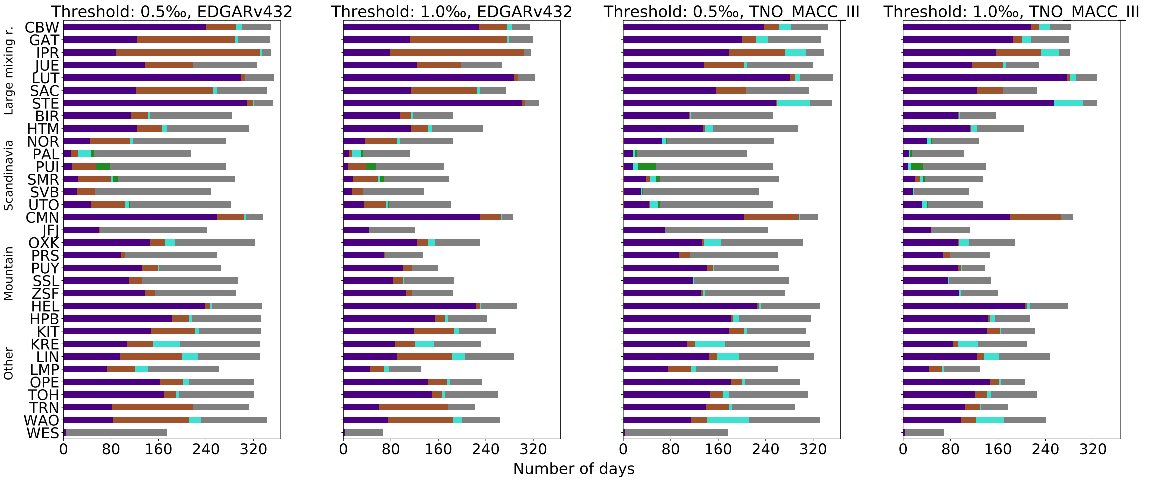

(b) δ^{2}H

Figure 4.10: Number of days in the study year when simulated daily source contributions to δ^{13}C at ICOS sites are above given thresholds, computed from standard deviations over the 3-day running window, for the TNO-MACC_III and EDGARv4.3.2 inventory in the domain covering whole Europe. Colours indicate detectable source types.

when simulated daily CH_4 source contributions to δ^{2}H and δ^{13}C, using the TNO-MACC and EDGAR inventories, at ICOS sites are above the two lowest thresholds for δ^{2}H and δ^{13}C. When comparing the results for δ^{2}H and δ^{13}C, approximately the same types of sources may be detected at the same monitoring sites. Examples for this are the large number of agriculture source detection events at Lutjewad (LUT), Cabauw (CBW), Monte Cimone (CMN) and Helgoland (HEL), or the low number of days on which wetland sources are detectable at Puijo (PUI) and Hyytiälä (SMR). As the possible ranges of δ^{13}C and δ^{2}H for the various source types are large and sometimes overlap, it is advantageous to analyse both δ^{2}H and δ^{13}C together so that sources can be more certainly attributed to a specific source type. The source types that are mainly detectable at ICOS sites are agriculture and boundary mixing ratios. Each is detectable using both inventories on about 40% of the total number of days on which any sources are detectable.

The magnitude and the location of the sources in the inventories determine whether a type of source is dominant enough at a site to exceed a given detectability threshold. Hence, the differences between the number of detection events and the dominant sources when using the EDGAR or TNO-MACC inventories can be linked to different magnitudes and locations of specific sources in the inventories. Differences occur, for example, at the site Utö - Baltic sea (UTO) where waste sources could not be detected at all according to TNO-MACC, whereas the number of detectable waste sources with EDGAR using the two lowest precisions, respectively, is 57 and 31 days for δ^{13}C, as well as 57 and 37 days for δ^{2}H. Similarly at WAO, FF related sources can be detected on about 30% more days with TNO-MACC than with EDGAR. The differences between the emissions in the inventories highlight the importance and need for a much more accurate knowledge on CH_4 emissions. El Yazidi (2018) found that the spatial distribution of the CH_4 emission budget over France bears significant uncertainties when studying the sensitivity of CH_4 mixing ratios to emissions using the CHIMERE model with the EDGARv4.2 and the IER (produced by Institute for Energy Economics and the Rational Use of Energy, University Stuttgart) anthropogenic emission inventories. Similarly, Wunch et al. (2019) inferred CH_4 emissions in Europe by total column measurements and found that the spatial disaggregation of the emissions in the EDGAR v4.3.1 and TNO-MACC_III inventories is highly uncertain.

4.4.4 Detectability of methane sources across the domain

Since agriculture and boundary mixing ratios are the primarily detectable source types at ICOS sites, we analyse the detectability over the European domain as well to investigate whether there are other locations that could prove useful for detecting other types of sources. The maps in Figures 4.11 and 4.12 showing the dominant source types and the number of days when simulated daily source contributions to δ^{2}H and δ^{13}C exceed the thresholds can be a good indication for where long-term isotopic measurements could be carried out in the future. We show only the detectable source type in a model grid-cell that dominates over the one year period. For example, if waste sources exceed a given threshold on 300 days in a grid-cell and other types of sources exceed that same given threshold on the remaining days of the year, only the waste source is shown as dominant detectable source for that grid-cell. However, the corresponding number of days in that grid-cell represents the total number of days on which any source is detectable. Doing so, we are able to deduce the most potential locations or areas in Europe, in which sites could be installed for detecting CH_4 sources through measurements of atmospheric δ^{13}C and δ^{2}H isotope ratios.

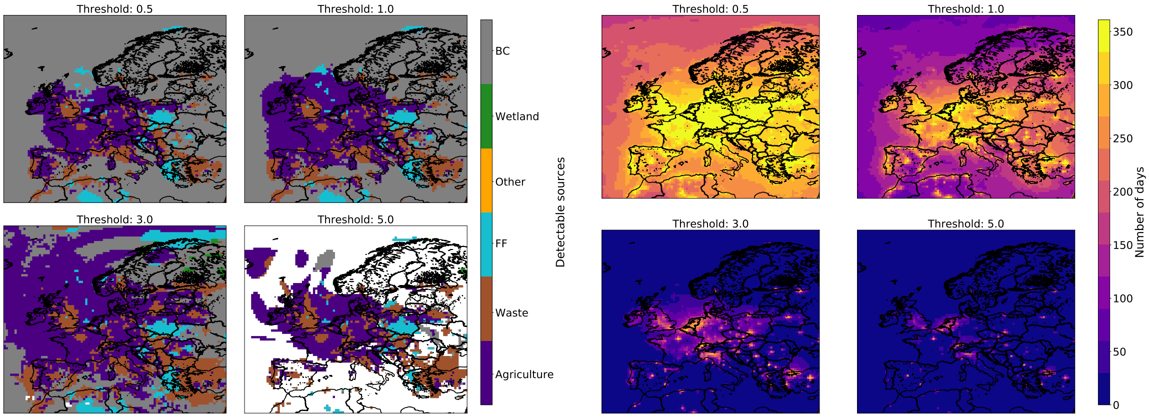

(a) Source types - EDGARv4.3.2

(b) Number of days - EDGARv4.3.2

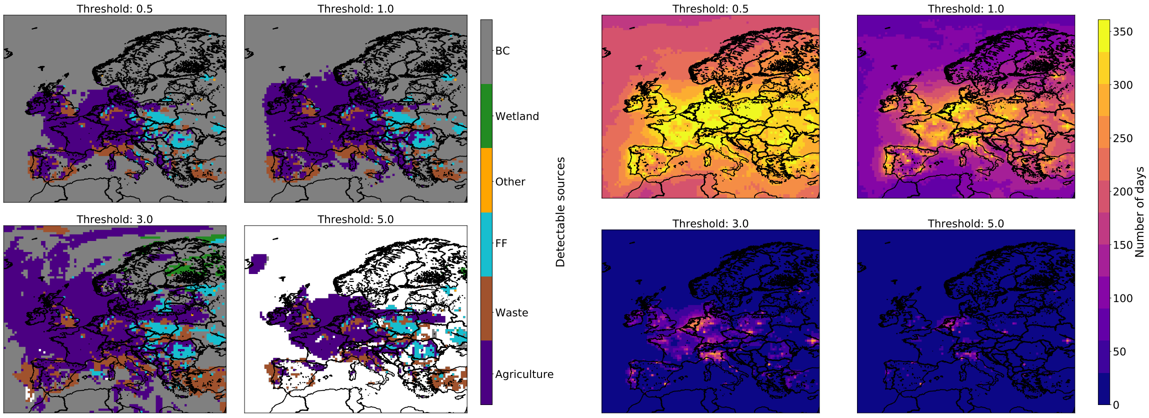

(c) Source types - TNO-MACC_III

(d) Number of days - TNO-MACC_III

Figure 4.11: Number of days in the study year (**b** and **d**) and source types (**a** and **c**) when simulated daily source contributions to δ^{2}H at ICOS sites are above given thresholds, computed from 3-day running standard deviations. Results are shown for the EDGARv4.3.2 (**a** and **b**) and TNO-MACC_III (**c** and **d**) inventories in the domain covering whole Europe.

The number of days on which thresholds are exceeded for EDGAR is similar to that in case of TNO-MACC (Figures 4.11d, 4.11b, 4.12d, and 4.12b). With the highest instrument precisions, both δ^{13}C and δ^{2}H isotope ratios exceed the thresholds all year around over Europe and signals are detectable during approximately two third of the year over the whole domain, even

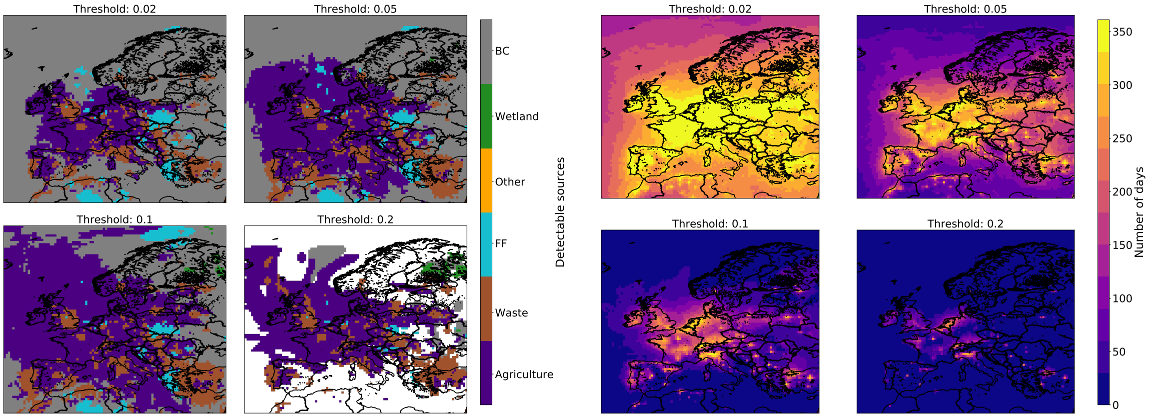

(a) Source types - EDGARv4.3.2 **(b)** Number of days - EDGARv4.3.2

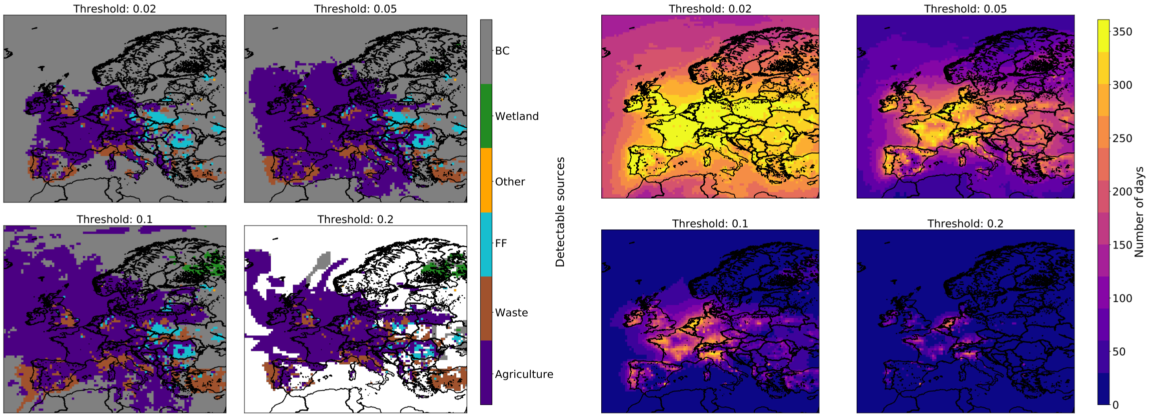

(c) Source types - TNO-MACC_III **(d)** Number of days- TNO-MACC_III

Figure 4.12: Number of days in the study year (**b** and **d**) and source types (**a** and **c**) when simulated daily source contributions to δ^{13}C at ICOS sites are above given thresholds, computed from 3-day running standard deviations. Results are shown for the EDGARv4.3.2 (**a** and **b**) and TNO-MACC_III (**c** and **d**) inventories in the domain covering whole Europe.

over sea grid-cells. This is due to the air being well transported over the domain during the study year. The second highest threshold of 1‰ for δ^2H and of 0.05‰ for δ^{13}C is exceeded over most regions in Europe during at least half of the year. For δ^2H, with the second lowest instrument precision of 3.0‰, signals only from large source areas can be detected on approximately 200 days or more. These regions are large emission regions in the inventories in Figure 4.2; for example, the BENELUX, the Po-Valley in Italy and several larger cities, such as Paris and Madrid. The δ^{13}C from larger sources, as the above mentioned ones, is detectable with the second lowest instrument precision of 0.1‰ on about 250 days in the study year. The lowest thresholds for both δ^{13}C and δ^2H are exceeded over very few areas on max. 291 (EDGAR) and 260 (TNO-MACC) days, as well as 274 (EDGAR) and 254 (TNO-MACC) days, respectively. Such areas are e.g. the BENELUX, North-Western Germany, the Po-Valley, Brittany in North-Western France, the Southern part of the UK and larger cities, such as Minsk and Budapest.

The placement of sources in the inventories determines the patterns in the dominant source types, which is well visible through the differences between the results for EDGAR and TNO-MACC in Figures 4.11 and 4.12. The inventories agree that West from Poland (e.g. Germany, France, Italy), mostly agriculture and some waste sources are detectable over Europe, while there are differences in the inventories regarding the FF related sources. With EDGAR, FF related sources exceed the thresholds of 0.5‰, 1‰ and 3‰ for δ^2H over the North Sea, pointing towards the oil and gas platforms. This is not the case in TNO-MACC, in which only agriculture sources are detectable over the North Sea. These detected sources are emitted over the surrounding land and transported to the North Sea during the study year. Moreover, the detection capability of FF related sources differs the most for the two inventories in Eastern Europe. For example, there are larger areas in Romania in which FF related sources are dominant detectable with TNO-MACC than with EDGAR. Another example is Greece where FF related sources are the main dominant detectable source according to the simulations with EDGAR, whereas using TNO-MACC, the dominant detectable source is agriculture. Wetland sources are detectable with all precisions for δ^2H and δ^{13}C but they are not the dominant detectable source in higher northern latitudes with the two highest precisions (two lowest thresholds) and hence not visible in the figures. The dominant detectable source is boundary mixing ratios in higher latitudes with the two highest precisions. When the precision is not high enough to detect boundary mixing ratios, i.e. lowest two precisions of δ^{13}C and δ^2H, wetlands become the dominant detectable source in some areas. Such areas are Southern part of Finland and the far northwest of Russia.

Regions that could be targeted for long-term isotopic measurements are regions with discrepancies in the dominant source types with the two inventories (e.g. Greece) and regions where FF related sources (e.g. Silesia in Poland) and wetland sources (e.g. Southern Finland) dominate during the year as sites detecting these two sources are scarce in the ICOS network.

4.4.5 Confirmation of detectable sources at ICOS sites

To strengthen the findings on dominant sources in the previous sections, we investigate whether the dominant sources are indeed likely to be detected at ICOS sites with the highest instrument precisions of 0.5‰ for δ^2H and 0.02‰ for δ^{13}C. As described in Section 4.2.3 (page 111), we use the Keeling approach to determine the average isotopic source signatures of atmospheric δ^2H and δ^{13}C (Figure 4.13) for days on which the dominant source is detectable.

According to the simulations performed using EDGARv4.3.2 (Figure 4.13a), only agriculture and waste sources, as well as boundary mixing ratios dominate at ICOS sites during the year, whereas with TNO-MACC (Figure 4.13b) only agriculture and boundary conditions dominate. However, with both inventories, the determined δ^{13}C and δ^2H isotopic source signatures can confirm the dominant source only at a small number of sites. These sites are the ones within the square of the microbial source type and around the average of ambient air for boundary conditions.

To be able to compare the results of this analysis to the ones in Figure 4.7 (Section 4.4.2, page 123), Figures 4.13c and 4.13d show sites at which the derived δ^2H and δ^{13}C isotopic source signatures have changed by more than ± 10‰ or ± 2‰, respectively. Even though the source isotopic signatures have changed, the corresponding source type remained the same. However, the sites whose dominant detectable source is agriculture and waste have moved towards lower δ^{13}C and δ^2H values, i.e. towards more typical microbial source values. These changes occurred mainly due to changes in the δ^2H source isotopic signatures, which is expected as the ranges of the different source types are larger for δ^2H than for δ^{13}C. Hence, analysing only days on which a dominant source is detectable can lead to changes in the average source isotopic signature compared to when analysing every day in the study year.

Although the above mentioned source types dominate over the year at specific sites, it is still not certain that any source above background or a source of interest will be detected by instruments with even a high precision of 0.02‰ and 0.5‰ for δ^{13}C and δ^2H, respectively. As one of the goals of these analyses is to contribute to a better understanding of the various CH_4 sources, we analyse whether it is possible to detect signals from sources other than the dominant source type. Hence, we apply two criteria to obtain sites at which specific sources could be detected with a higher possibility:

(i) We select the top 10 sites at which agriculture and waste are detectable, the top 5 sites at which FF related sources are detectable and the top 2 sites at which wetlands are detectable. The number of sites is

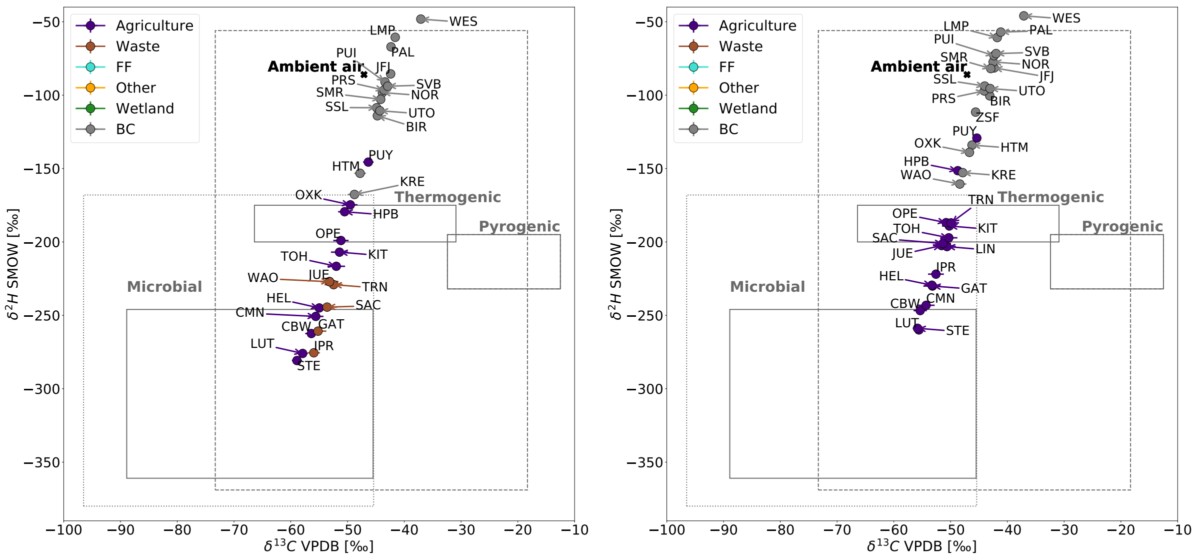

(a) EDGARv4.3.2 **(b)** TNO-MACC_III

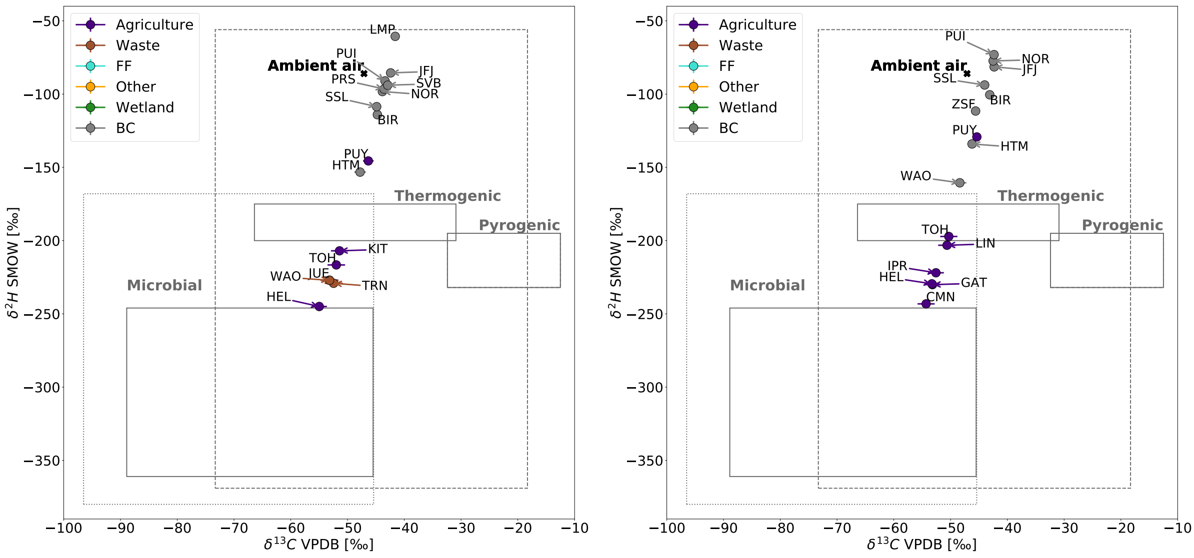

(c) Comparison to Figure 4.7a - EDGARv4.3.2 **(d)** Comparison to Figure 4.7b - TNO-MACC_III

Figure 4.13: Determined average δ^{13}C and δ^2H source isotopic signatures using simulations made with the EDGARv4.3.2 (**a**) and TNO-MACC_III (**b**) inventories for each monitoring site of ICOS in the European domain for days on which specific sources are detectable, indicated by the colour of circles. Figures (**c**) and (**d**) show sites at which average δ^{13}C and δ^2H source isotopic signatures changed compared to Figure 4.7. Ranges for CH_4 sources (microbial, thermogenic, pyrogenic) indicated by solid grey lines are taken from studies listed in Szénási and Bousquet (2019). The dashed grey box represents the range for thermogenic CH_4 sources and the dotted grey box the range for microbial sources, obtained from MEMO^2 campaigns (Menoud et al., 2020a). The black cross represents the global average δ^2H and δ^{13}C isotopic signatures in ambient (background) air (Rigby et al., 2012).

determined by the initial number of sites at which the specific sources are detectable (Section 4.4.3).

(ii) A given source type at a given site is only taken into account if the number of days, on which that given source is detectable, exceeds 28 days to ensure a sufficient number of data for this analysis.

These two criteria can lead to some sites representing more than one source category. The result of this analysis is illustrated in Table 4.4 and Figure 4.14. For wetlands, only one site PUI passed both criteria, for FF related sources with EDGARv4.3.2, only two sites, Křešín u Pacova (KRE) and Lindenberg (LIN), and for waste sources with TNO-MACC_III only six sites CMN, Ispra (IPR), Jülich (JUE), Saclay (SAC), Trainou (TRN) and Lampedusa (LMP).

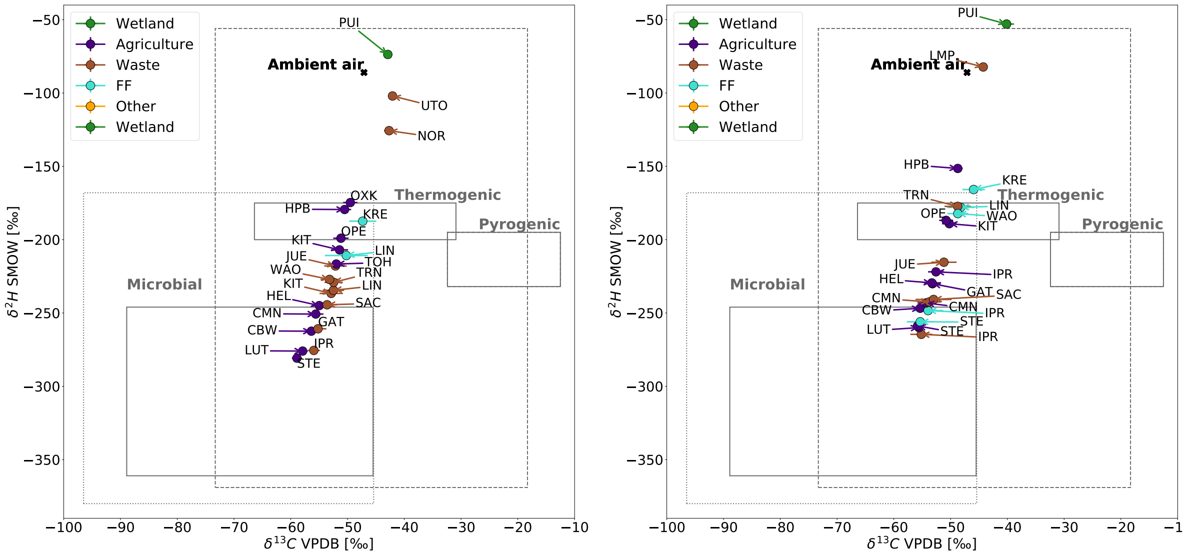

(a) EDGARv4.3.2 **(b)** TNO-MACC_III

Figure 4.14: Determined average δ^{13}C and δ^2H source isotopic signatures using simulations made with the EDGARv4.3.2 (**a**) and TNO-MACC_III (**b**) inventories in the full European domain. The analysis is performed for days on which specific sources are dominant detectable, indicated by the colour of circles, with the criteria that those days account for at least 28 days. The ranges for CH_4 source types (microbial, thermogenic, pyrogenic) indicated by solid grey lines are taken from studies listed in Szénási and Bousquet (2019). The dashed grey box represents the range for thermogenic CH_4 sources and the dotted grey box the range for microbial CH_4 sources, obtained from MEMO^2 campaigns (Menoud et al., 2020a). The black cross represents the global average δ^2H and δ^{13}C isotopic signatures in ambient (background) air (Rigby et al., 2012).

For the top 10 sites in the agriculture and waste source types, this analysis with simulations using both inventories leads to the same source isotopic signatures as the previous analysis. The sites, which are within the solid square indicating microbial sources, remained the same, with one exception: waste sources appear to be detectable at IPR with the TNO-MACC simulations. Thus, agriculture and waste sources are more certain to be detected by high-precision instruments at the following sites, suggested by simulations with both inventories: CBW, LUT, IPR and STE. Accoring to

EDGAR, two more sites show potential for the detection of agriculture and waste sources: CMN and Gartow (GAT), respectively. CBW, LUT, IPR and STE are in the Large mixing ratio category, which is another reason to expect that sources can be detected at these sites as signals from larger sources are generally easier to detect at any instrument precision. Indeed, CBW and LUT have been surveyed by Röckmann et al. (2016) and Menoud et al. (2020b) and provided useful information for evaluating CH_4 emission inventories.

For wetlands, even the one site PUI passing the two criteria does not prove to be a potential site for detecting signals from wetlands as the derived δ^2H and δ^{13}C source isotopic signatures are representative for background conditions.

For the thermogenic source type, KRE and LIN are likely to provide useful atmospheric δ^2H and δ^{13}C measurements during about a month as indicated by the simulations with both inventories.

4.4.6 Analysis of the seasonal detection

In order to capture sources with a limited number of detectable days, seasonal variations of the detectability should be analysed. This section investigates the seasonal variation of the detectability at ICOS sites and discusses the results for the detection thresholds of 1‰ for δ^2H and 0.05‰ for δ^{13}C as these precisions are possibly more often available for instruments. The seasonal detection is shown in Figures 4.15 and 4.16 for δ^2H and δ^{13}C, respectively. Since only the boundary mixing ratios and wetland emissions have a temporal variation and other source types are constant over the year in the model, the seasonal variations are due to meteorology, boundary conditions and wetlands.

The number of days on which sources are detectable and the types of detectable sources are similar for δ^2H and δ^{13}C. The number of days on which any source exceeds the given thresholds is generally largest in autumn. The detectability of agriculture and waste sources has only a small seasonal variation over winter, spring and summer, while FF related sources and boundary conditions exceed the thresholds mainly in autumn and winter. Thus, if the source of interest is fossil fuel related sources or background and if there is no possibility to deploy instruments to measure isotopic composition of CH_4 over an entire year, it is most beneficial to perform measurements during autumn and winter.

Table 4.4: ICOS sites at which the four main sources of methane can be detectable for more than 28 days within our European domain. Number of detection days is indicated for the atmospheric δ^{13}C and δ^{2}H isotopic ratio simulations made with the EDGARv4.3.2 and TNO-MACC_III emission inventories.

Site EDGARv4.3.2	**Number of days**		**Site TNO-MACC_III**	**Number of days**	
	δ^{13}**C**	δ^{2}**H**		δ^{13}**C**	δ^{13}**C**
Agriculture					
STE	315	310	LUT	283	282
LUT	301	299	STE	259	258
CMN	264	258	CBW	241	238
CBW	242	240	HEL	228	225
HEL	241	239	CMN	212	204
HPB	183	183	GAT	209	201
TOH	176	170	OPE	189	181
OPE	165	163	KIT	188	178
KIT	156	148	HPB	186	182
OXK	149	145	IPR	184	178
Waste					
IPR	245	244	CMN	99	92
GAT	169	166	IPR	93	95
TRN	136	136	JUE	63	68
SAC	130	129	SAC	51	50
WAO	127	127	TRN	42	40
LIN	107	104	LMP	39	38
JUE	80	81			
NOR	73	73			
KIT	72	68			
UTO	57	58			
Fossil fuel related sources					
KRE	42	45	WAO	65	71
LIN	28	28	STE	58	55
			KRE	45	50
			LIN	36	38
			IPR	35	35
Wetlands					
PUI	28	28	PUI	36	30

Although wetland sources are dominant only on a few days during the study period, they exceed the thresholds mainly in summer and autumn. Therefore, campaigns aimed at measuring δ^{13}C and δ^{2}H from wetlands over a few months should be carried out in the summer and autumn months. This is consistent with the campaigns performed by Fisher et al. (2017) at northern European wetlands mainly during summer months.

The seasonality of the detection capability for the FF related sources differs for EDGAR and TNO-MACC. In general, there are more sites at which the thresholds are exceeded by FF related sources with TNO-MACC and more sites at which waste sources exceed the thresholds with EDGAR. With EDGAR, waste sources exceed the thresholds of δ^2H and δ^{13}C mostly in summer and autumn, while with TNO-MACC, the number of days when waste sources exceed the 1‰ threshold is highest in winter. As the relative contribution of the waste sources to the total anthropogenic emissions is larger in EDGAR, waste sources tend to exceed the thresholds on more days than with TNO-MACC. The seasonality differences between the results using the two inventories could be due to the different spatial allocation of sources in them. In-

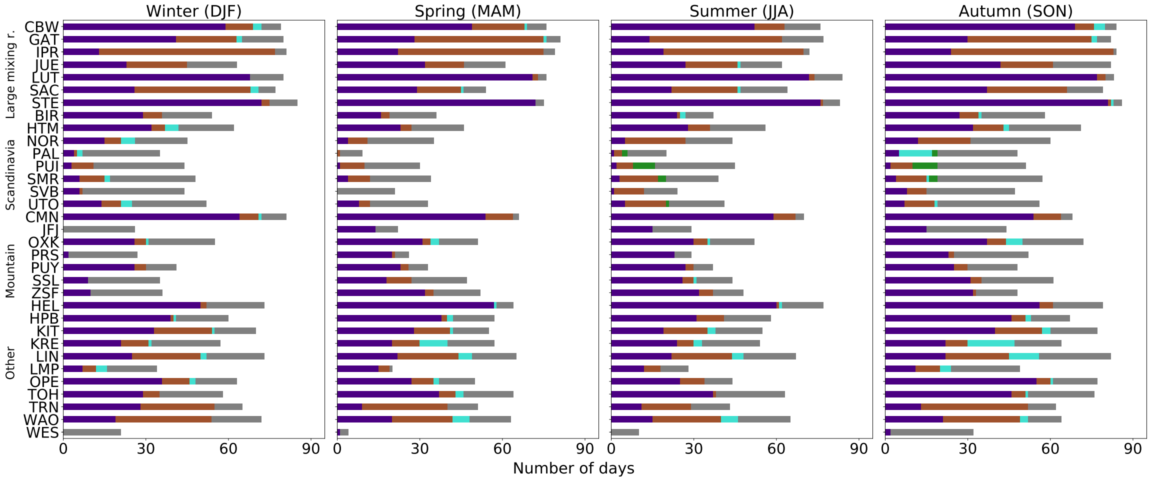

(a) EDGARv4.3.2

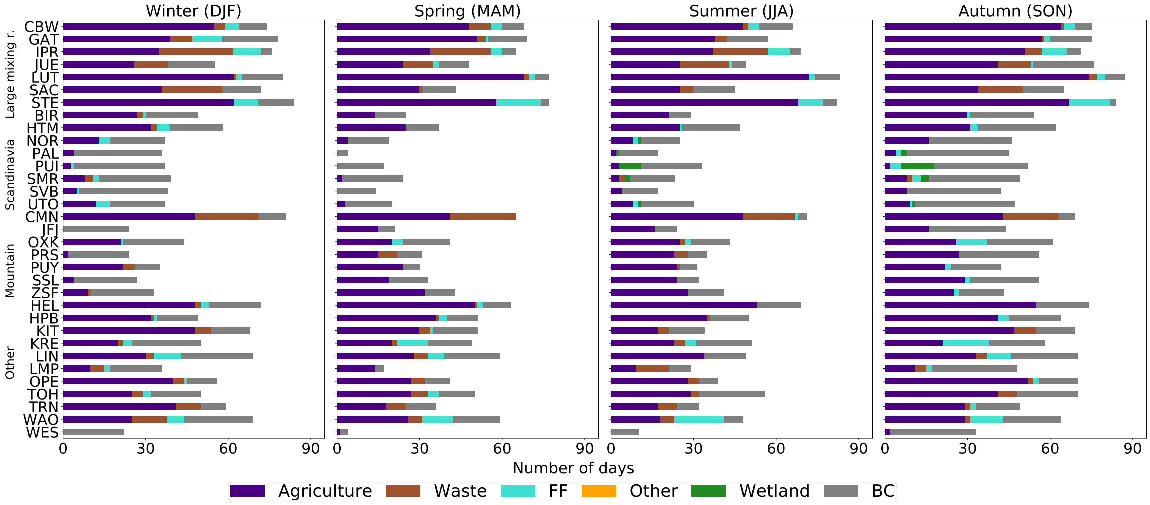

(b) TNO-MACC_III

Figure 4.15: Seasonality of simulated daily source contributions to δ^2H at ICOS sites being above the 1‰ threshold, computed from 3-day running standard deviations. Colours indicate detectable source types. Results are shown for using the EDGARv4.3.2 (**a**) and TNO-MACC_III (**b**) inventories in the domain covering Europe.

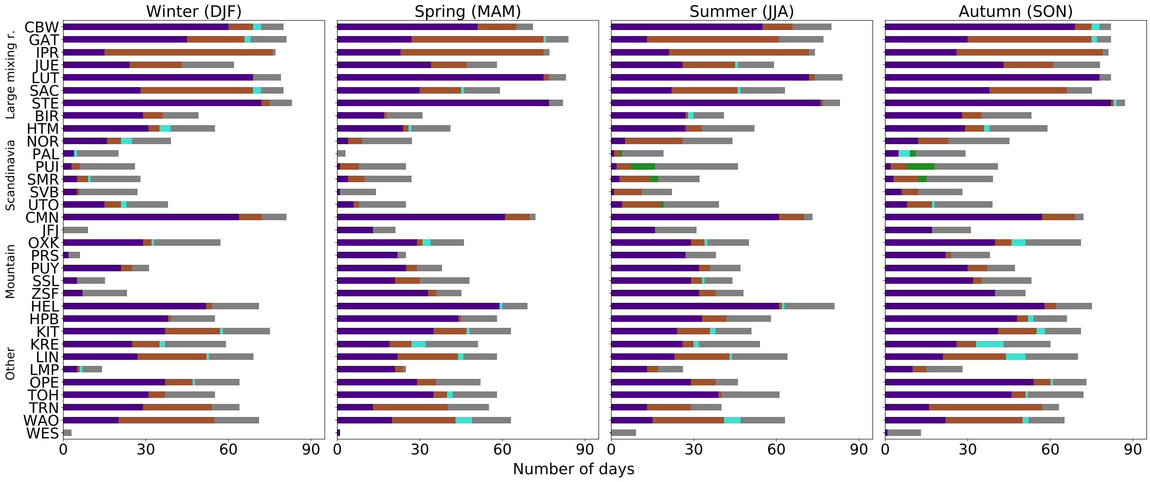

(**a**) EDGARv4.3.2

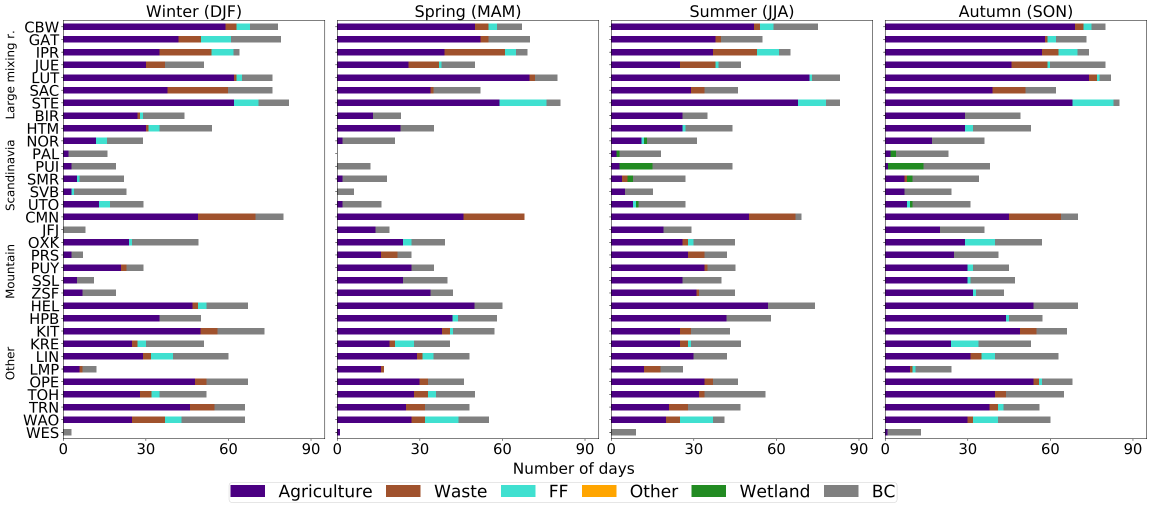

(**b**) TNO-MACC_III

Figure 4.16: Seasonality of simulated daily source contributions to δ^{13}C at ICOS sites being above the 0.05‰ threshold, computed from 3-day running standard deviations. Colours indicate detectable source types. Results are shown for using the EDGARv4.3.2 (**a**) and TNO-MACC_III (**b**) inventories in the domain covering Europe.

deed, prevailing wind directions can be different depending on the season and thus, different sources can be advected depending on their locations.

4.4.7 Impact of horizontal resolution on simulation outputs

4.4.7.1 Analysing time series of methane mixing ratios and its stable isotopic content

The horizontal resolution influences the CH_4 emissions and simulated mixing ratios, which affect the computed atmospheric δ^2H and δ^{13}C isotopic ratios. As an example, the impact of the horizontal resolution on the simulated time series of STE is illustrated in Figure 4.17. Agriculture sources are more dominant in the lower horizontal resolution configuration (Figure 4.5) compared to the higher horizontal resolution configuration. This occurs because agriculture is an area source that is the main source of methane in Europe and other sources, such as FF related sources that are mainly point sources, become more concentrated in smaller grid cells. Therefore, point sources can be more dominant when using high horizontal resolutions and the differences between simulations with two inventories can be more obvious.

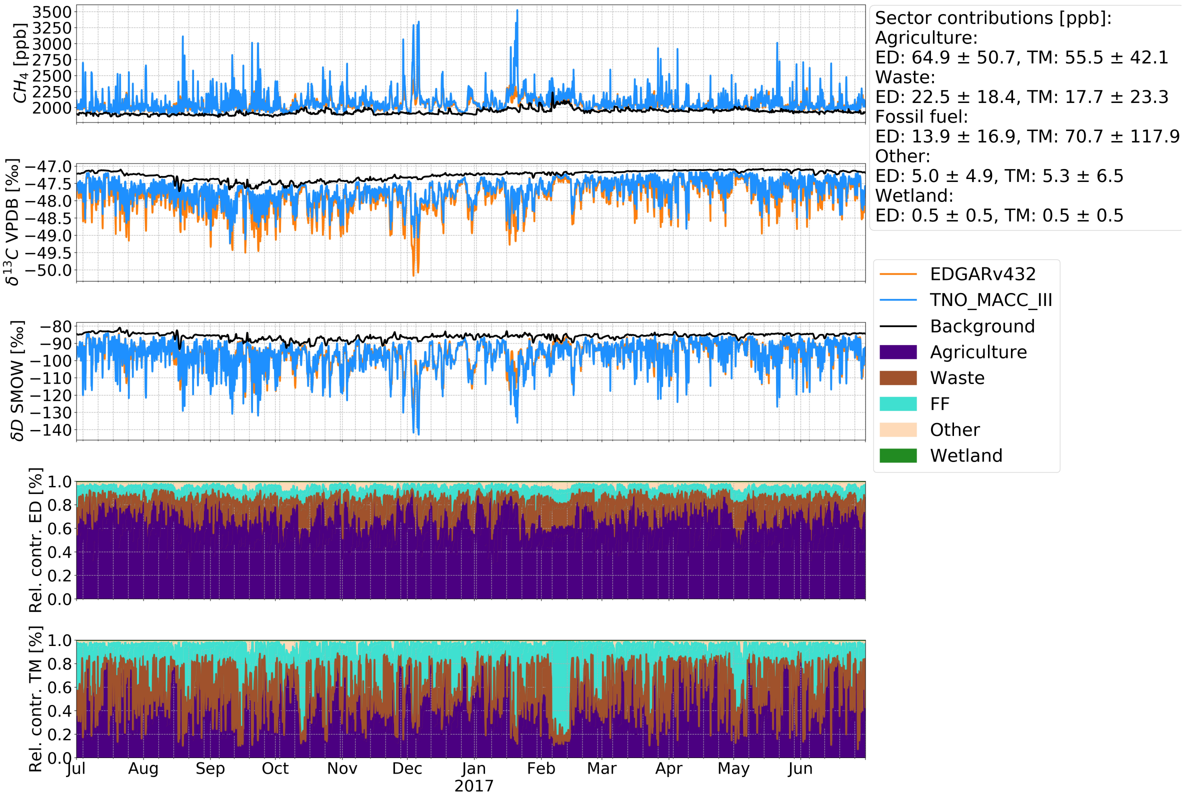

Figure 4.17: Time series of CH_4 mixing ratios (top panel), δ^{13}C (second panel from top) and δ^2H (middle panel) at the monitoring site Steinkimmen (STE) in the domain covering parts of Northwestern Europe (horizontal resolution: 0.1°×0.1°). The relative contributions [%] (bottom two panels) indicate the CH_4 mixing ratio contributions of the sources to the total CH_4 mixing ratios using the EDGARv4.3.2 and the TNO-MACC_III inventories. The absolute CH_4 mixing ratios of the sources [ppb] are indicated in text form on the top right corner of the figure.

4.4.7.2 Detectability of methane sources at ICOS sites

The comparison between simulations of the two horizontal resolution configurations demonstrates the influence of the horizontal resolution on the detection capability. Figure 4.18 illustrates the results for δ^{13}C signal detection from CH_4 sources with the higher horizontal resolution configuration at ICOS sites. The figures for δ^2H can be found in the Appendix (Figure A6). We show only the 3-day running SD results as 3-day averages are sufficient to target synoptic scale variations and, as stated in Section 4.4.3, we present a lower bound for the detectability of methane sources.

There are specific sites whose dominant source differs with the two resolutions. For example, at the site SAC, the dominant source with the low horizontal resolution simulations using EDGAR is agriculture but with the high horizontal resolution simulations, more waste sources are detectable. Other examples are STE and WAO: using the higher horizontal resolution simulations with TNO-MACC, FF related sources become the dominant source, instead of agriculture in the low horizontal resolution simulations.

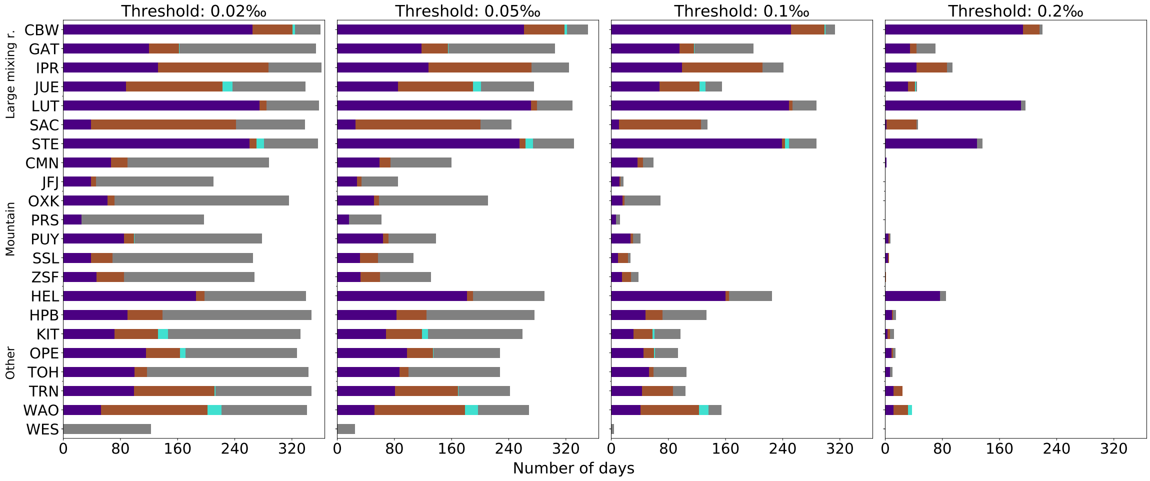

(a) EDGARv4.3.2

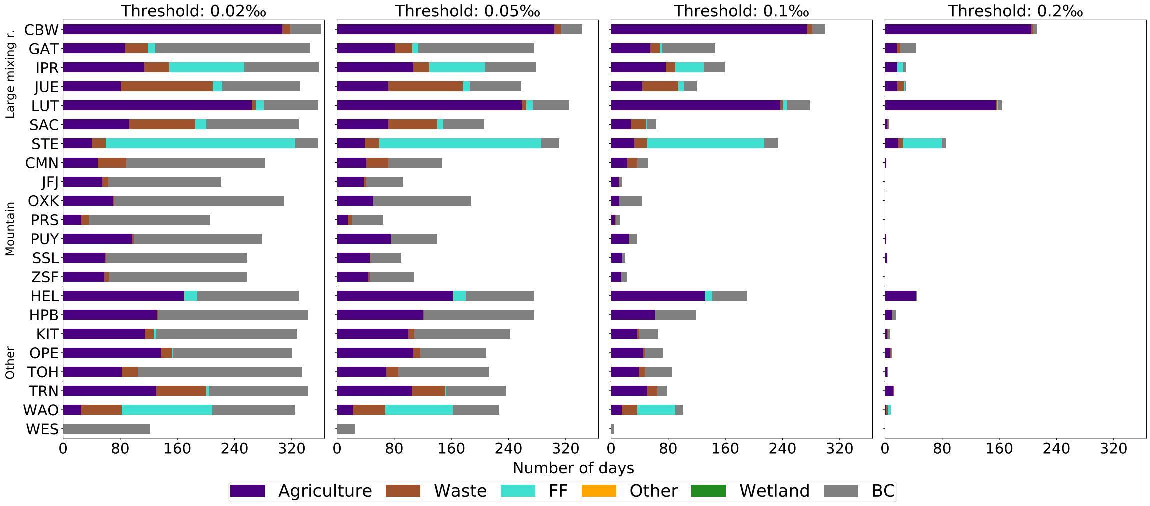

(b) TNO-MACC_III

Figure 4.18: Number of days in the study year when simulated daily source contributions to δ^{13}C at ICOS sites are above given thresholds, computed from 3-day running standard deviations. Colours indicate detectable source types. Results are shown for using the EDGARv4.3.2 (**a**) and TNO-MACC_III (**b**) inventories in the domain covering parts of Northwestern Europe.

4.4.7.3 Detectability of methane sources across the domain

A similar effect is apparent when analysing the detection capability for δ^{13}C over the domain. Figure 4.19 shows the number of days and the source types when the simulated daily source contributions to δ^{13}C are above the instrument precision thresholds in the sub-domain covering parts of Northwestern Europe. As in the previous section, only the 3-day running SD results are shown. As the results for δ^{2}H lead to similar conclusions, confirming the detectable source types, the corresponding figures are shown only in the Appendix (Figure A3).

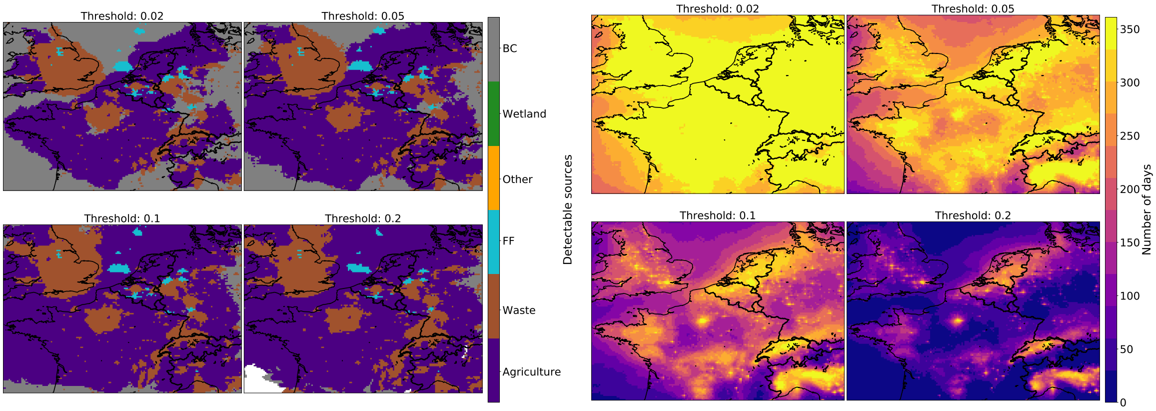

(a) Source types - EDGARv4.3.2

(b) Number of days - EDGARv4.3.2

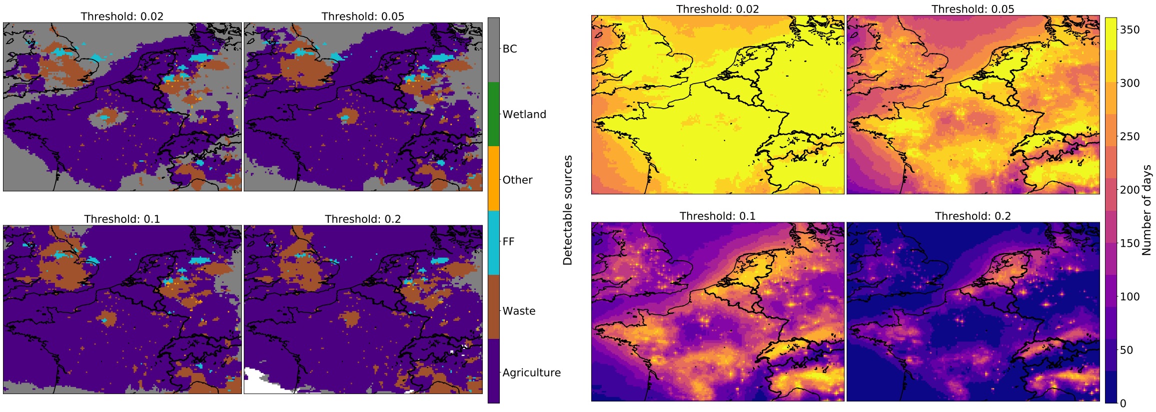

(c) Source types - TNO-MACC_III

(d) Number of days - TNO-MACC_III

Figure 4.19: Number of days in the study year (**b** and **d**) and source types (**a** and **c**) when simulated daily source contributions to δ^{13}C are above given thresholds, computed from 3-day running standard deviations. Results are shown for the EDGARv4.3.2 (**a** and **b**) and TNO-MACC_III (**c** and **d**) inventories in the domain covering parts of Northwestern Europe.

The FF related sources and waste sources are more dominant in the high resolution domain. The maximum number of days on which the lowest thresholds are exceeded are higher with 344 (EDGAR) and 335 (TNO-MACC) days for δ^2H, as well as 342 (EDGAR) and 339 (TNO-MACC) days for δ^{13}C, than with the low horizontal resolution, which results in max. 274 (EDGAR) and 254 (TNO-MACC) days for δ^2H, as well as 291 (EDGAR) and 260 (TNO-MACC) days for δ^{13}C.

4.5 Conclusions

We have analysed which instrument precision would be necessary to detect sources at already existing monitoring sites of the ICOS network and over our European domain. Our results indicate that the requirements on instrument precisions are high. The precision targets defined by the WMO IAEA (WMO, 2018) for δ^{13}C and δ^2H are 0.2‰ and 5‰, respectively, for regionally oriented studies. However, our analysis implies that the 0.2‰ and 5‰ precisions are sufficient for detecting sources only from large emitting areas, such as the Po-Valley in Italy or the Silesian coal basin in Poland, during about six months of the year. The second highest precisions of 1‰ for δ^2H analyses and 0.05‰ for δ^{13}C analyses have been demonstrated to be more useful for providing information on CH_4 sources in regional atmospheric inversions: sources could be detected at about half of the ICOS sites during 85% of the year. The highest precisions of 0.5‰ for δ^2H analyses and 0.02‰ for δ^{13}C analyses could yield even more days on which sources can be detected. Such precisions, however, are quite ambitious and require strict laboratory protocols.

We have shown that seasonal variations exist in the detectability of CH_4 sources. However, it is important to note that seasonal variations of sources occur mainly due to the meteorology and boundary mixing ratios in this study as the applied anthropogenic sources are constant over the year. Agriculture and waste sources are mainly detectable in autumn and they are approximately uniformly detectable during the rest of the year. Although wetland sources exceed the detection thresholds only at a few high-latitude sites on a few days during the year, the best possibility to detect them would be during summer and autumn months. Perhaps, an even higher instrument precision than the ones analysed here would yield satisfactory detection results. For the best detectability of FF related sources and boundary mixing ratios, the seasonality analysis suggests winter and autumn months.

It should be noted that the source detection method used in this study is optimistic as we consider only the source with the highest SD as detectable, while atmospheric signals consist of contributions from different sources.

The number of detection events can be lower than in our study as signals can cancel each other out for some events. Furthermore, sources that have been indicated as detectable in our study highly depend on the emissions' magnitude and spatial distribution in the inventories used.

Our results show that at most ICOS sites, mainly background and agricultural sources would be detectable. While background sites are valuable for monitoring the general atmospheric evolution of sources and sinks of GHGs at larger regional scales, sites and regions where signals from CH_4 sources would be detectable, could be useful to improve our understanding on specific methane sources and their temporal and spatial distribution. For example, sites and regions with controversial source detectability for EDGAR and TNO-MACC could be considered for long-term monitoring of δ^{13}C and δ^{2}H isotope ratios. A good example is the monitoring site Steinkimmen (STE) in Germany, at which simulations with TNO-MACC suggest that FF related sources are detectable, whereas simulations with EDGAR do not indicate FF related sources as detectable. Our study performed with the low horizontal resolution configuration indicates that the detection of FF related sources over a month is not likely at any ICOS sites. However, the analysis of the source detection using simulations with the higher horizontal resolution and the TNO-MACC inventory implies that FF related sources may be detectable at STE for over half a year. Furthermore, long-term monitoring of CH_4 mixing ratios and δ^{13}C and δ^{2}H isotope ratios or at least measurement campaigns of several months would be beneficial in Eastern Europe as the emissions in the two inventories and the resulting detectability have substantial discrepancies and there are currently no ICOS sites in operation there.

We have analysed which sites have the most potential for detecting δ^{13}C and δ^{2}H signals from CH_4 sources. Based on our analyses using simulations with both inventories, the sites at which the possibility is high for detecting agriculture sources for at least six months are STE, CBW and LUT. For the detection of waste sources during at least six months, IPR appears to be promising. The analysis with the EDGAR simulations suggests also CMN and GAT as potential sites for detecting signals from primarily agriculture and waste sources, respectively. The highest possibility to detect waste and agriculture sources is in autumn. FF related sources may be detectable at KRE and LIN for about a month mainly during autumn and winter. None of the current ICOS sites have been indicated to be suited for capturing signals from wetlands. Southern Finland is likely to be a good target for carrying out measurements of at least a few months in summer and autumn to detect signals from wetlands.

Even though this study has been performed for one year only, we assume that the results apply for the years after 2017 as emission hot-spots and large emission areas will likely remain at similar locations in Europe. Moreover, most CH_4 emissions in Europe do not have a high inter-annual variability, due to which we can assume that our results will still apply in the near future. Hence, δ^2H and δ^{13}C data sets can be implemented in atmospheric inversions of CH_4 emission over Europe, once a sufficient amount of δ^2H and δ^{13}C data with sufficient instrument precision are available. However, as our study showed, even higher precisions than 0.02‰ for δ^{13}C and 0.5‰ for δ^2H may be necessary to detect sources. This may be the case especially for wetland and FF related sources. Alternatively, atmospheric inversions could further investigate the value of long-term isotopic data by using synthetic measurements of δ^2H and δ^{13}C over multiple years.

Chapter 5

Summary and outlook

5.1 Summary and conclusions

The general aim of this thesis is to improve our knowledge on European methane sources by using atmospheric modelling of CH_4 mixing ratios, as well as δ^{13}C and δ^{2}H isotopic ratios. This work is motivated by the importance of atmospheric CH_4 in climate change and the increasingly available CH_4 mixing ratio measurements in Europe that are valuable for emission quantification. This thesis addresses uncertainties in the European CH_4 budget by focusing on several elements used in atmospheric inversions. The accuracy of CH_4 emission estimates derived from top-down atmospheric inversions depends on the performance of the transport model, the uncertainties connected to its input data, such as emissions and boundary and initial conditions, the precision of instruments measuring CH_4 mixing ratios and δ^{2}H and δ^{13}C isotope ratios as well as the number and location of such measurements.

In the first part of this thesis, we assessed several errors in transport models and emission inventories by comparing simulations of CH_4 mixing ratios that were carried out using different configurations, transport models and input data. These error estimates can be used in regional atmospheric inversions to derive CH_4 emissions in Europe. The second step of this work involved the use of information obtained from quasi-continuous measurements and simulations of CH_4 isotopic composition to explore possible causes for mismatches between measurements and simulations, with the final aim to deduce information on emissions of the main CH_4 sources. The main limitation of the study is that quasi-continuous, high-frequency measurements of δ^{13}C and δ^{2}H are available from only two monitoring sites in our European domain. This leads to the third study of this thesis with the aim to investigate the value of long-term in-situ isotopic measurements at operational monitoring sites in Europe. To do so, we analyse the instrument precision needed for detecting signals from CH_4 sources.

In the following, the main conclusions of these studies are summarised and the research questions posed at the beginning of this thesis answered. The main findings are summarised in Figure 5.1.

Research question 1: *How can we quantify errors in transport models and emission inventories for atmospheric inversions of methane emissions in Europe?*
In Chapter 2, we estimated various errors in transport modelling and emission inventories, which can be used to set up atmospheric inversions of methane emissions in Europe. The aim was to gain insights into how these errors could be consistently treated and included in a data assimilation system for inverting CH_4 emissions in Europe. A simple method (Wang et al., 2017) was used that consists of performing multiple simulations using two limited-area transport models at three different horizontal resolutions with inputs based on three emission inventories and two sets of boundary and initial conditions.

We found that the background error features a homogeneous structure and low variability, due to which it can be discriminated from other types of errors. Hence, it can be controlled alongside emissions in an inversion framework, which is consistent with other regional inversion studies. The representation error can also be included in the observation error statistics. Our analyses suggest that the sources of the transport error may better be controlled alongside the emissions. However, the optimisation of the transport together with the emissions is challenging in most inversion systems. In addition, it showed spatial and temporal correlations, which increase the difficulties to include the transport error in the emission space due to the technical challenges of inverting large non-diagonal matrices.

The error in emission inventories is heterogeneous and depends on the country and source sector. The inventories differ mainly in the waste and fossil fuel related sources over Europe. This is due to assumptions used for spatially disaggreagting area and point sources in inventories, which leads to differences in the magnitudes and locations of emissions.

Research question 2: *Are isotopic measurements useful as constraints*

on CH_4 sources?
In Chapter 3, we investigated causes for mismatches between measured and simulated methane mixing ratios, as well as its isotopic ratios δ^2H and δ^{13}C at two measurement sites: the coastal site Lutjewad in the Netherlands and the continental site Heidelberg in Germany. The aim of this study was to analyse whether such mismatches can be associated with inaccurate magnitudes and/or spatial distributions of emission in inventories or with improper δ^{13}C and δ^2H isotopic source signatures used for modelling atmospheric δ^{13}C and δ^2H isotope ratios.

The analysis of the measurement-simulation mismatches around Lutjewad indicated that the key reason for the mismatches is inaccurate magnitudes and spatial distribution of emissions in the domain covering parts of Northwestern Europe. The underestimation of the measured CH_4 mixing ratios and the overestimation of δ^{13}C and δ^2H by CHIMERE is primarily due to the underestimation of biogenic sources, especially agriculture sources, in both the EDGARv4.3.2 and the TNO-MACC_III inventory. Moreover, the sensitivity analyses suggested that fossil fuel related emissions are overestimated in both inventories, especially South-East from Lutjewad. The comparison of measured and simulated CH_4 mixing ratios and δ^{13}C isotope ratios around Heidelberg lead to the conclusion that emissions are likely misplaced and emission magnitudes are inaccurate in both emission inventories. A possible reason for the low model performance for atmospheric δ^{13}C isotopic ratios is improper δ^{13}C source isotopic signatures used for the area around Heidelberg. Nevertheless, our results indicate, among others, that fossil fuel related sources are overestimated North from Heidelberg. This confirms the similar findings based on the analysis around Lutjewad that fossil fuel related emissions possibly in North-Western Germany are overestimated.

Research question 3: *Which instrument precisions and sites are needed for isotopic measurements to be used in atmospheric inversion studies at the European scale?*
In Chapter 4, we have investigated the importance of long-term isotopic measurements of atmospheric δ^{13}C and δ^2H for improved CH_4 emission estimates in Europe. As long-term isotopic measurements are presently scarce in Europe, simulations of atmospheric δ^{13}C and δ^2H isotope ratios are used in this synthetic study. The simulations were carried out for monitoring sites of the European ICOS network for one year. This study was focused on the instrument precision needed to detect signals from the main CH_4 sources and

on measurement sites, at which the potential to detect signals is highest.

Through the investigation of the instrument precision, we found that a precision of at least 1‰ for δ^2H analyses and 0.05‰ for δ^{13}C analyses would be needed to detect sources at most sites during at least six months. The ICOS sites Steinkimmen (DE), Cabauw (NL), Lutjewad (NL) and IPR (IT) have been implied by simulations with both inventories as potential sites for isotopic signal detection during at least six months of the year. The main detectable confirmed source at these sites is agriculture, which is detectable by most sites. At IPR, waste sources are the dominant detectable source. The sites KRE (CZ) and LIN (DE) appear to be promising for the detection of FF related sources for about a month.

In order to learn more about CH_4 sources and sinks, it would be advantageous to measure CH_4 isotopic composition at sites and in regions with controversial source detectability indicated by the simulations using two inventories (e.g. WAO (UK) and STE), as well as in further regions where waste and fossil fuel related sources can be detectable. Such regions are, for example, Southern part of the UK and Eastern Europe, respectively. As none of the ICOS sites is indicated to be a potential site for detecting signals from wetlands, other higher latitude regions, such as Southern Finland, could be a good target for measuring δ^2H and δ^{13}C isotope ratios and CH_4 mixing ratios from wetlands.

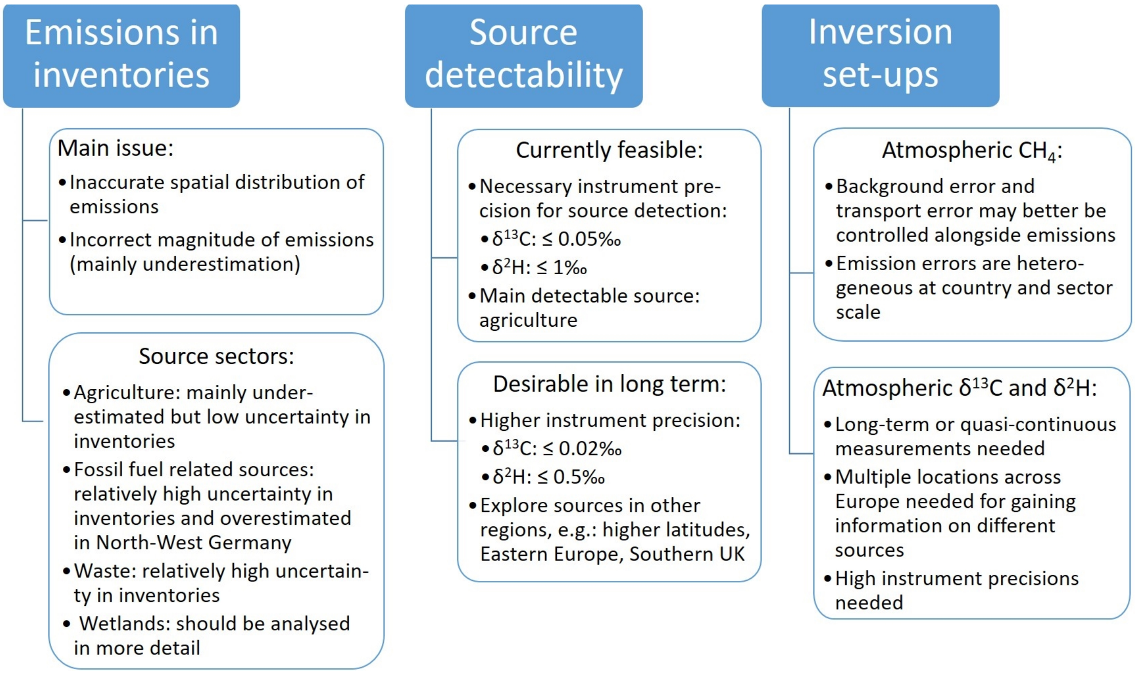

Main issue:
- Inaccurate spatial distribution of emissions
- Incorrect magnitude of emissions (mainly underestimation)

Source sectors:
- Agriculture: mainly underestimated but low uncertainty in inventories
- Fossil fuel related sources: relatively high uncertainty in inventories and overestimated in North-West Germany
- Waste: relatively high uncertainty in inventories
- Wetlands: should be analysed in more detail

Currently feasible:
- Necessary instrument precision for source detection:
  - δ^{13}C: ≤ 0.05‰
  - δ^2H: ≤ 1‰
- Main detectable source: agriculture

Desirable in long term:
- Higher instrument precision:
  - δ^{13}C: ≤ 0.02‰
  - δ^2H: ≤ 0.5‰
- Explore sources in other regions, e.g.: higher latitudes, Eastern Europe, Southern UK

Atmospheric CH_4:
- Background error and transport error may better be controlled alongside emissions
- Emission errors are heterogeneous at country and sector scale

Atmospheric δ^{13}C and δ^2H:
- Long-term or quasi-continuous measurements needed
- Multiple locations across Europe needed for gaining information on different sources
- High instrument precisions needed

Figure 5.1: Summary of the main findings in this thesis.

The research in this thesis found that inaccurate spatial distributions and magnitudes of CH_4 emissions are the primary reason for mismatches between measured and simulated atmospheric CH_4 mixing ratios and isotopic composition. The largest uncertainties were detected in the waste and fossil fuel related source sectors of the inventories used in this thesis. Our studies showed that the application of $\delta^{13}C$ and $\delta^{2}H$ isotopic ratios in addition to CH_4 mixing ratios can help identify discrepancies between the magnitude and spatial distribution of emissions in the inventories and help improve them. Furthermore, long-term (> 1 year) or quasi-continuous (< 1 year) measurements of $\delta^{13}C$ and $\delta^{2}H$ can be an asset for source discrimination in atmospheric inversions. However, such measurements should be carried out by instruments with a precision of at least 0.05‰ for $\delta^{13}C$ and 1‰ for $\delta^{2}H$ in order to be useful in inversions. Moreover, inversion studies should carefully asses the errors in transport models and emission inventories.

5.2 Outlook

5.2.1 Emission estimation

As the results of the study in Chapter 2 showed, the spatial distribution of emissions in anthropogenic methane emission inventories is uncertain. Although our analysis of emissions provides valuable insights into emission inventories and uncertainties connected to them, a more comprehensive study on estimating errors in CH_4 emission inventories would likely yield more reliable emission estimates in atmospheric inversion frameworks. The estimation of the errors in emission inventories and the transported-emission errors could be improved by adding other emission inventories if available, or new versions of the used inventories, including updated emission magnitudes and spatial distribution, as well as seasonal and/or diurnal time profiles.

Time profiles based on atmospheric processes driving CH_4 production (e.g. higher temperatures increase methane formation in landfills; Javadinejad et al., 2019) would potentially help reduce discrepancies between measurements and simulation outputs. The impact of applying temporal profiles on simulation outputs of CH_4 mixing ratios should, however, be examined as improper time profiles could lead to even larger discrepancies between measurements and simulations. Furthermore, an in-depth analysis on the spatial distribution of emissions, as well as the assumptions and proxies used for spatially distributing them would contribute to lower emission uncertainties. Such analyses would provide valuable information for preparing emission inventories.

Throughout the whole thesis, the same version of the anthropogenic emission inventories TNO-MACC_III and EDGARv4.3.2 from the year 2011 was used. Since the beginning of this thesis, new versions of these inventories have become available and Table 5.1 shows a comparison of TNO-MACC_III and EDGARv4.3.2 to their newer versions: CAMS-REG v4.2 and EDGARv5.0 for 2011 and the most recent available year 2015. The comparison of the EDGAR inventory's versions for 2011 shows a more than 2 Tg total CH_4 emission increase in EDGARv5.0, which is mainly due to the almost 4 Tg increase of CH_4 in the waste sector and a 1.3 Tg CH_4 decrease of the fossil fuel related emissions. In 2015 in EDGARv5.0, the waste emissions became 1 Tg smaller compared to 2011 in the same inventory version, while agriculture emissions slightly increased by 0.4 Tg, resulting in a total emission reduction of 0.5 Tg CH_4. In the CAMS-REG v4.2 inventory, the total CH_4 emission increased by 1.5 Tg with an enhancement of emissions in the agriculture, waste and fossil fuel related emissions for 2011, compared to TNO-MACC_III. Comparing 2011 and 2015 of CAMS-REG v4.2 shows a decrease in the waste and fossil fuel related emissions and a slight 0.2 Tg enhancement of agriculture emissions, which leads to a total 1.3 Tg CH_4 emission reduction in 2015. In Chapter 3, we found that fossil fuel related emissions are overestimated in TNO-MACC_III and EDGARv4.3.2 in a domain covering parts of Northwestern Europe. Thus, the decrease of fossil fuel related emissions in the newer versions, especially in CAMS-REG v4.2 for 2015, suggests an improvement of the emission magnitudes. Consequently, in future studies on atmospheric CH_4, newer versions could provide updated emission magnitudes and possibly updated spatial distributions.

Even though emissions from natural wetlands in Europe are small compared to anthropogenic emissions (Saunois et al., 2016b), their role in the European atmospheric CH_4 budget is substantial, especially in higher northern latitudes. Their contribution to the European CH_4 budget should be further investigated and their errors could be studied using the same method as in Chapter 2.

Each of these suggestions are feasible in short or medium term as most of the tools are available.

Table 5.1: Emissions [TgCH$_4$year^{-1}] per source category of TNO-MACC_III (2011) and EDGARv4.3.2 (2011) anthropogenic emission inventories compared to their newer versions CAMS-REG v4.2 and EDGARv5.0 for the years 2011 and 2015.

SNAP code	Source sector in this study	TNO-MACC_III	CAMS-REG v4.2		EDGARv4.3.2	EDGARv5.0	
		2011	2011	2015	2011	2011	2015
2, 5	Fossil fuel related emissions	6.1	6.3	5.6	7.3	6.0	6.0
9	Waste	7.7	8.6	7.7	10.8	14.5	13.5
10	Agriculture	10.9	11.3	11.5	12.1	12.0	12.4
1, 3, 4, 6, 7, 8	Other anthropogenic sources	0.7	0.7	0.8	0.4	0.4	0.5
Total		25.4	26.9	25.6	30.6	32.9	32.4

5.2.2 Atmospheric modelling

The study in Chapter 3, investigating reasons for mismatches between measurements and simulations, indicated issues with the MACC boundary and initial conditions (Marécal et al., 2015). The impact of the MACC boundary conditions on the simulation quality of the long-lived species O$_3$ and CO was analysed in the study of Giordano et al. (2015). They found that biases between ground-based measurements and simulation outputs exist due to the performance of the MACC boundary conditions. Similarly, the influence of the CH$_4$ boundary conditions on the simulation outputs of CH$_4$ mixing ratios could be investigated in the short term.

The vertical mixing of CH$_4$ mixing ratios in CHIMERE was not examined in this thesis. However, it is known to be a source of error in meteorological inputs used in transport models (Gerbig et al., 2008). It highlights the need to analyse uncertainties contained by meteorological inputs. Brunner et al. (2015) analysed the performance of atmospheric models due to meteorological inputs and found that the simulation of some meteorological parameters, e.g. planetary boundary layer height, is indeed subject to uncertainties. The influence of meteorological inputs on the simulation of CH$_4$ mixing ratios could be investigated in a similar study or by the method described in Chapter 2. Such a study could analyse the influence of e.g. the PBL height on simulations of atmospheric CH$_4$ mixing ratios and could point out what could potentially be improved in atmospheric CTMs to further enhance their performance. Moreover, increasing the vertical resolution could lead to more accurate simulation outputs as it could improve the representation of vertical gradients and decrease misrepresentations of the vertical mixing of CH$_4$ mixing ratios.

5.2.3 Measurements of isotopic composition

In Chapter 4, we have used homogeneous δ^{13}C and δ^{2}H isotopic source signatures as input for computing atmospheric δ^{13}C and δ^{2}H isotope ratios. However, isotopic source signatures of a given source depend on the actual parameters of CH_4 formation processes, such as the diet type of cattle, which can be different from region to region. To start investigating this issue, we shortly study the detectability, analogue to the method used in Chapter 4, for the highest instrument precisions at the ICOS site Steinkimmen in Germany. We modify the δ^{13}C and δ^{2}H source isotopic signatures of the agriculture and fossil fuel related sources as these are the sources that were indicated dominant detectable by simulations with the TNO-MACC inventory in our study in Chapter 4. The δ^{13}C and δ^{2}H source isotopic signatures have been modified to lower source signatures of -66‰ and -330‰, respectively, for the agriculture sector and to higher source signatures of -40‰ and -160‰, respectively, for FF related sources. The resulting detectable sources and number of days on which they are detectable are compared in Table 5.2 to the ones determined in Chapter 4. Even though modified input source isotopic signatures seem to have only a marginal influence on the detectability of CH_4 sources at Steinkimmen, heterogeneous source isotopic signatures would likely result in more realistic δ^{13}C and δ^{2}H time series. However, more spatially well distributed δ^{2}H and δ^{13}C source isotopic signatures derived from measurements are needed to provide more realistic signatures over a domain as large as Europe.

Table 5.2: Number of days on which sources are detectable at the ICOS site Steinkimmen (Germany) when modifying the δ^{2}H and δ^{13}C source isotopic signatures for the agriculture and fossil fuel (FF) related sources in simulations using the TNO-MACC_III emission inventory.

Source sector	**δ^{13}C [‰]**		**δ^{2}H [‰]**	
	original	**modified**	**original**	**modified**
Agriculture	259	260	258	255
Waste	1	1	2	2
FF related sources	58	60	55	60
Other anthropogenic sources	0	0	0	0
Wetlands	0	0	0	0
BC	36	41	36	40

In order to gain more information on typical δ^{13}C and δ^{2}H source isotopic signatures in Europe, more local mobile isotopic measurements are required that target the estimation of isotopic source signatures, which has been a focus in recent studies (e.g. Fisher et al., 2017; Zazzeri et al., 2017; Assan, 2017) and would thus be feasible in medium term. The MEMO^2 project is a great initiative, whose objective is the identification of various CH_4 sources in different locations in Europe. The target areas of MEMO^2 includes mainly Western European countries. Although MEMO^2 participated in intensive measurement campaigns in Poland and Romania, other parts of Eastern Europe are, to date, not well explored.

This was also indicated by the analyses in Chapter 4 that demonstrated discrepancies in emissions of the TNO-MACC_III and EDGARv4.3.2 inventories. Currently, there is no ICOS site in operation in Eastern Europe, it would hence be beneficial to carry out quasi-continuous measurements of CH_4 mixing ratios and its isotopic ratios for at least several months.

As most European CH_4 emissions do not feature high year-to-year variations as demonstrated in Table 5.1, it is reasonable to assume that our results in Chapter 4 will apply at least in the near future. While there are uncertainties in the spatial allocation of emissions in inventories, the spatial uncertainties of emissions have been addressed by using two emission inventories. Therefore, atmospheric inversions could implement δ^{13}C and δ^{2}H data, once the availability of such data has sufficiently increased. To overcome limitations of the use of isotopic data in atmospheric inversions, more long-term or at least quasi-continuous isotopic measurements are needed in Europe. It will possibly take many years to reach a sufficient amount of long-term or quasi-continuous isotopic measurements. However, the data availability is not the only limiting factor to implement isotopic data in inversion frameworks. The requirements on instrument precisions that would yield valuable measurements for atmospheric inversions remain challenging. Therefore, measurement projects could target ICOS sites that seem to be most advantageous to detect sources: for example, Steinkimmen in Germany or Ispra in Italy as indicated by our study.

5.2.4 Atmospheric inversions of methane emissions

In this thesis, we have addressed some of the main uncertainties in atmospheric inversions of CH_4 emissions; errors in transport models and emissions from simulation outputs of CH_4 mixing ratios and precision requirements for instruments measuring CH_4 isotopic composition. Furthermore, we explored the advantages when using isotopic information to gain knowledge about emissions and isotopic source signatures. These analyses have shown what would be necessary for an atmospheric inversion framework to be able to estimate reliable methane emissions from atmospheric measurements of CH_4 mixing ratios and its stable isotopic composition in Europe. Such an inversion framework would be of great importance for future studies on methane emissions, it would thus be relevant to validate that in simplified atmospheric inversions, while aiming to take into account as much of the recommendations in our studies as possible regarding computational challenges and costs, as well as data availability.

An example for an inversion system that could be used for this purpose is currently being developed and tested at the global scale, which is designed to assimilate measurements of specific CH_4 tracers and their corresponding isotopic data (Thanwerdas et al., In preparation).

As long as the number of available CH_4 isotopic measurements is not sufficient in Europe, synthetic measurements of δ^2H and δ^{13}C could be included in Observing System Simulation Experiments (OSSEs) that would make possible to investigate the performance of atmospheric inversions with isotopic data within a shorter time range.

Appendix

A.1 Use of high-frequency atmospheric isotopic composition measurements for deriving information about model-measurement mismatches

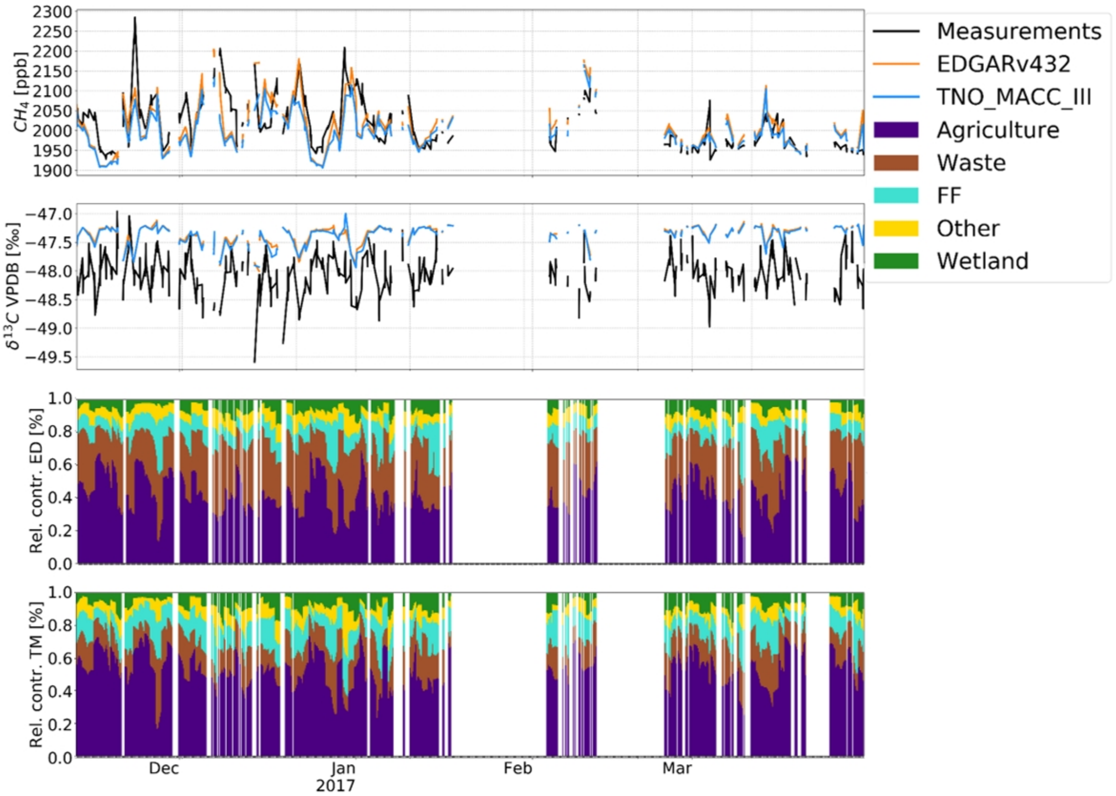

Figure A1: Time series of the measured and simulated CH_4 mixing ratios and δ^{13}C isotope ratios at the German monitoring site Heidelberg for the period November 2016 to March 2017. Simulations made by using the EDGARv4.3.2 inventory are illustrated with orange lines, simulations made by using the TNO-MACC_III inventory are illustrated with blue lines. Furthermore, the relative source contributions to the total simulated CH_4 mixing ratios above the simulated CH_4 boundary mixing ratios are shown by different colours at the bottom of the figure.

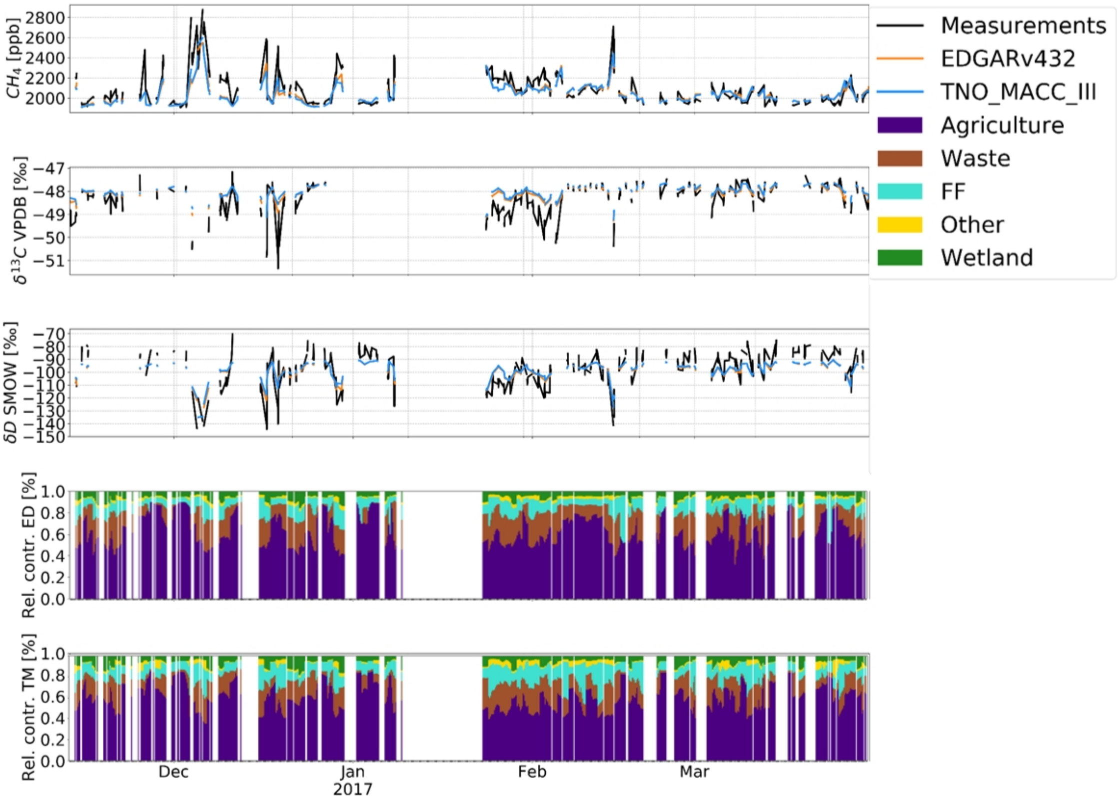

Figure A2: Time series of the measured and simulated CH_4 mixing ratios as well as δ^{13}C and δ^{2}H isotope ratios at the Dutch monitoring site Lutjewad for the period November 2016 to March 2017. Simulations made by using the EDGARv4.3.2 inventory are illustrated with orange lines, simulations made by using the TNO-MACC_III inventory are illustrated with blue lines. Furthermore, the relative source contributions to the total simulated CH_4 mixing ratios above the simulated CH_4 boundary mixing ratios are shown by different colours at the bottom of the figure.

A.2 Investigating the potential of isotopic measurements for methane source detection in a modelling framework

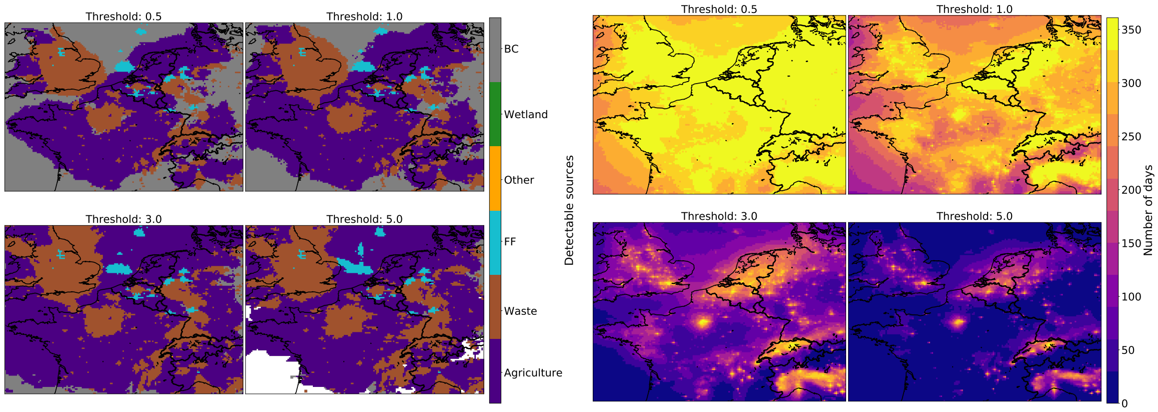

(a) Source types - EDGARv4.3.2

(b) Number of days - EDGARv4.3.2

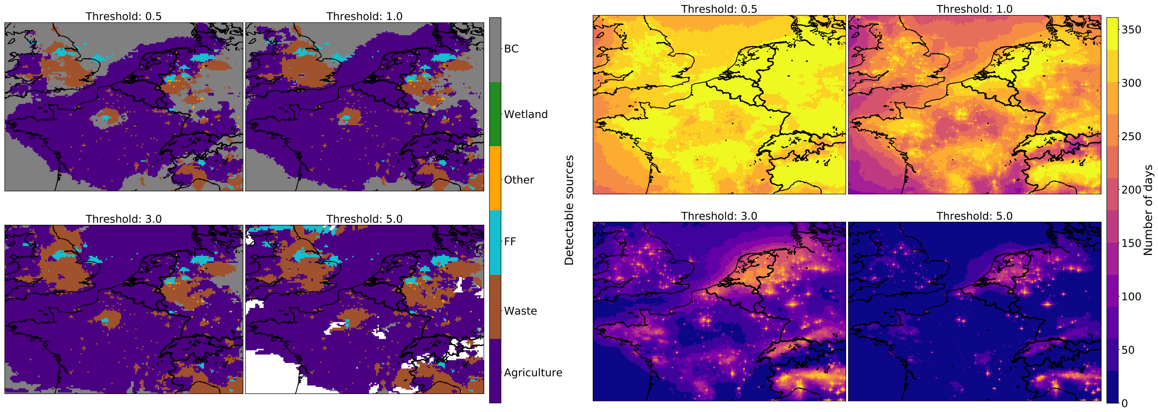

(c) Source types - TNO-MACC_III

(d) Number of days - TNO-MACC_III

Figure A3: Number of days in the study year (**b**, **d**) and source types (**a** and **c**) when simulated daily source contributions to δ^2H at ICOS sites are above given thresholds, computed from 3-day running standard deviations. Results are shown for the EDGARv4.3.2 (**a**) and TNO-MACC_III (**c**) inventories in the domain covering parts of Northwestern Europe.

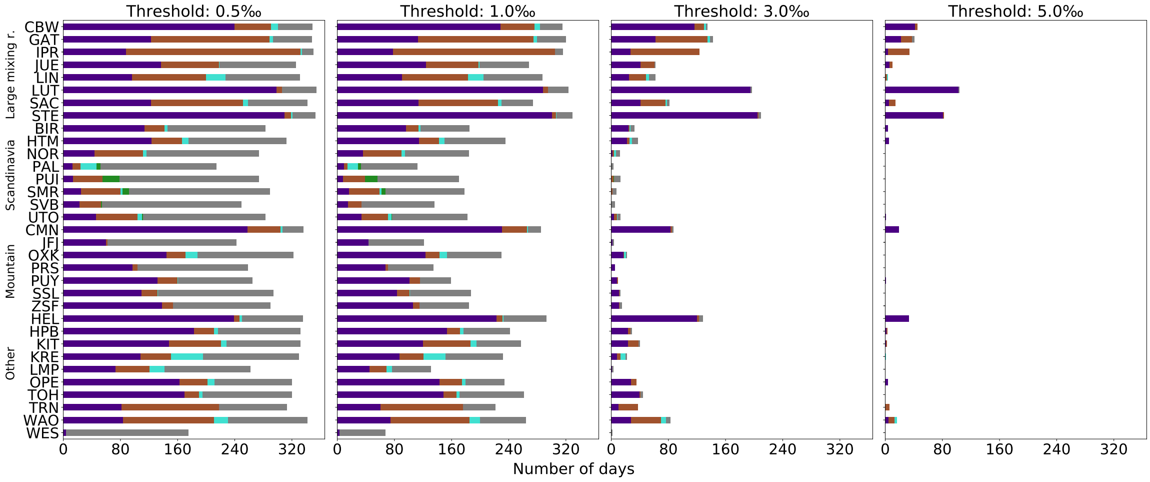

(a) 3-day window, EDGARv4.3.2

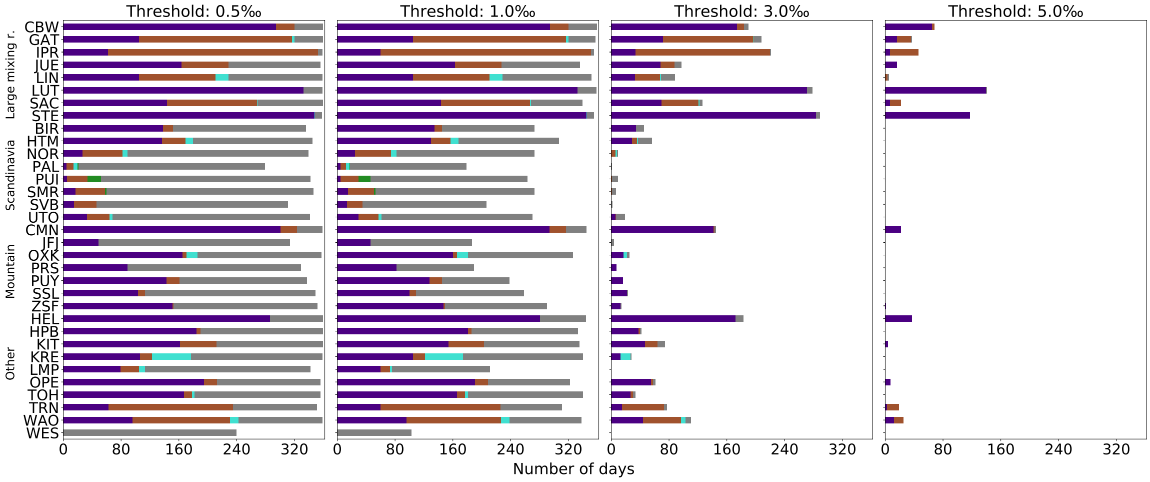

(b) 7-day window, EDGARv4.3.2

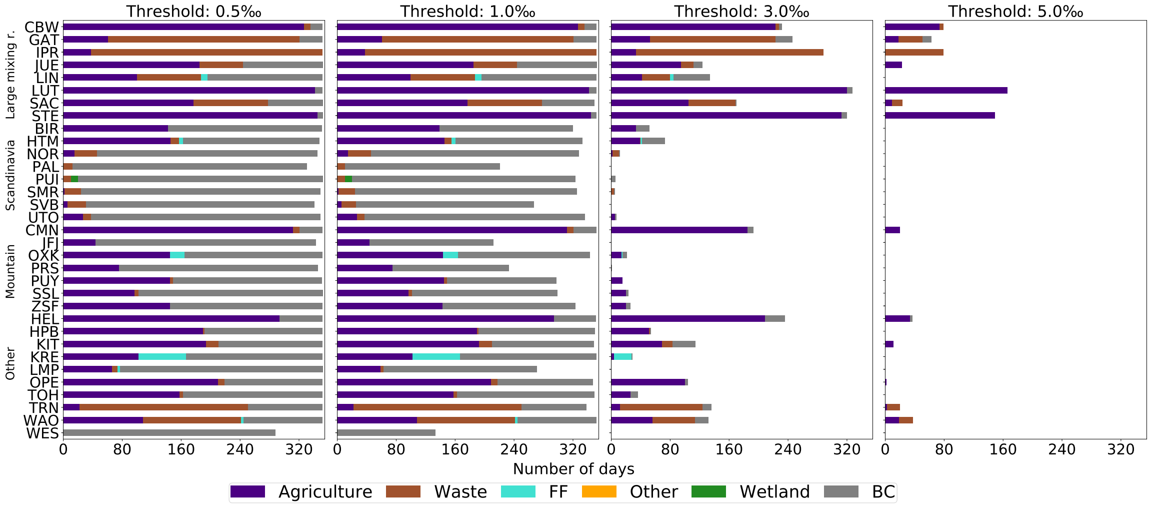

(c) 14-day window, EDGARv4.3.2

Figure A4: Number of days in the study year when simulated daily source contributions to δ^2H at ICOS sites are above given thresholds, computed from standard deviations over 3-day, 7-day and 14-day running windows, for the EDGARv4.3.2 inventory in the domain covering whole Europe. Colours indicate detectable source types.

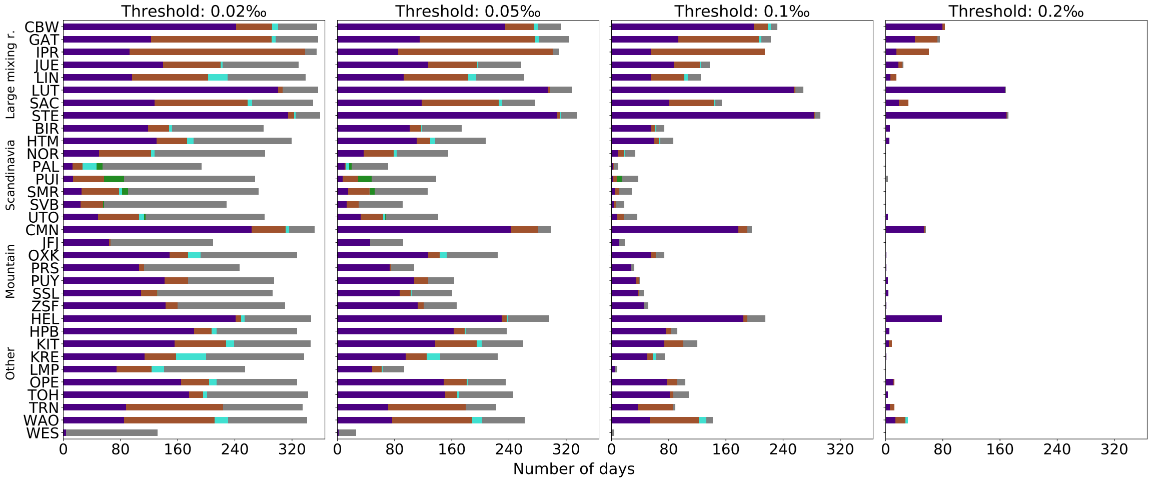

(a) 3-day window, EDGARv4.3.2

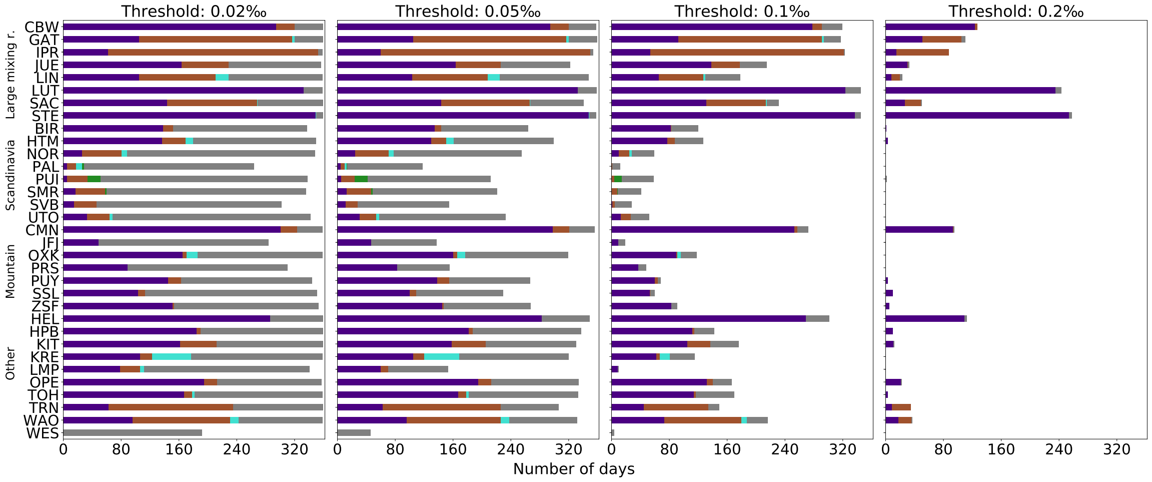

(b) 7-day window, EDGARv4.3.2

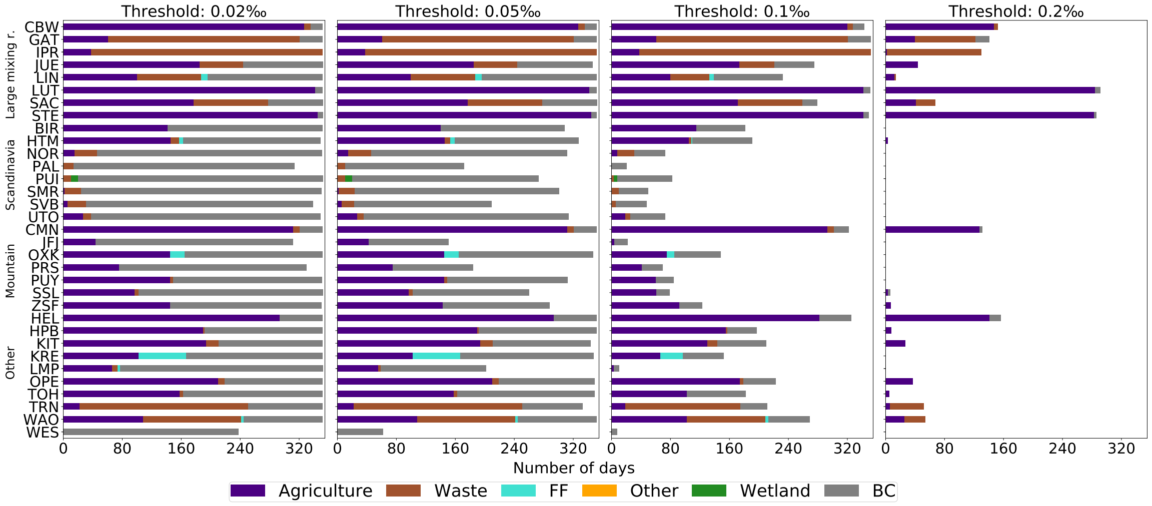

(c) 14-day window, EDGARv4.3.2

Figure A5: Number of days in the study year when simulated daily source contributions to δ^{13}C at ICOS sites are above given thresholds, computed from standard deviations over 3-day, 7-day and 14-day running windows, for the EDGARv4.3.2 inventory in the domain covering whole Europe. Colours indicate detectable source types.

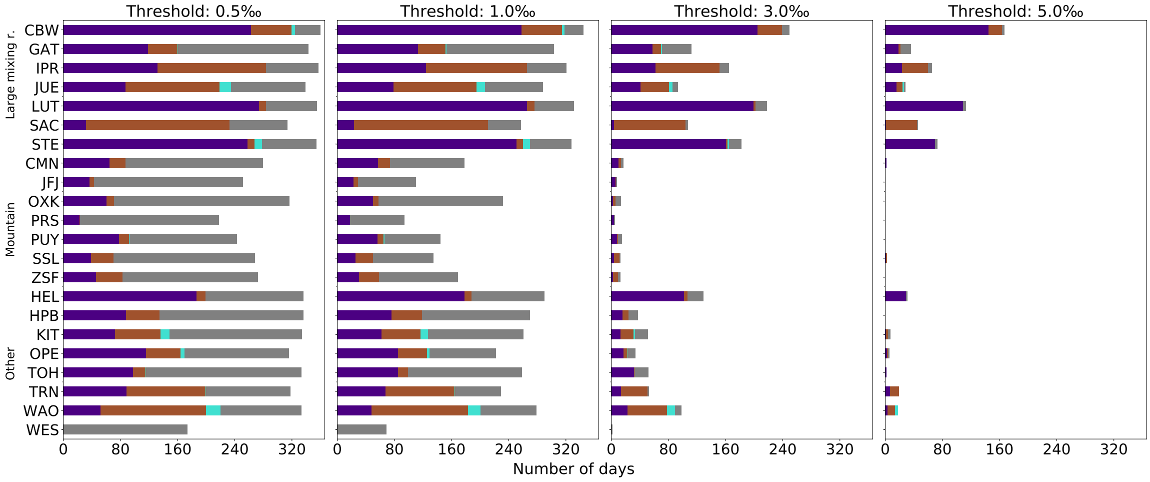

(a) EDGARv4.3.2

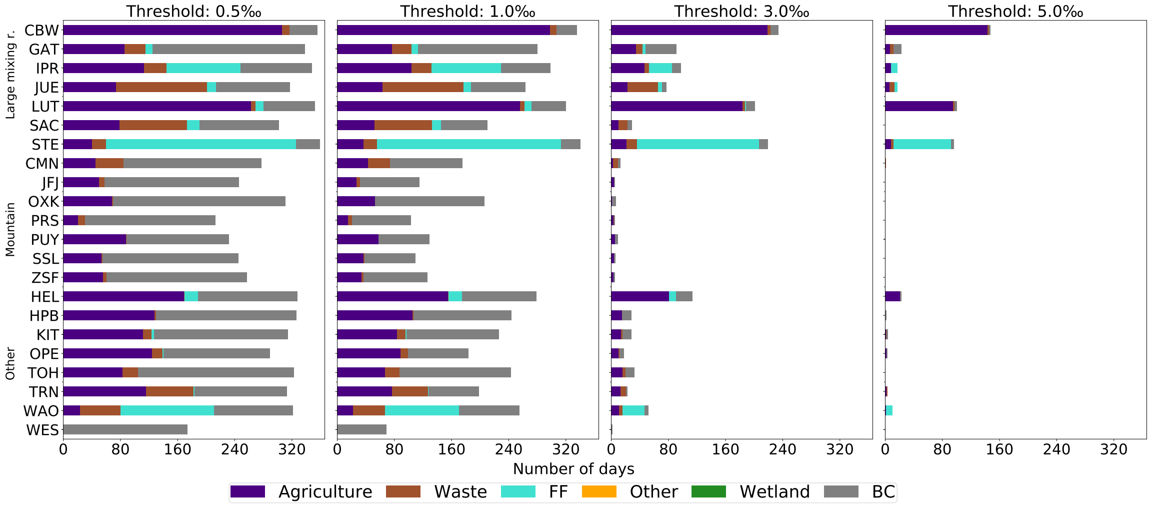

(b) TNO-MACC_III

Figure A6: Number of days in the study year when simulated daily source contributions to δ^2H at ICOS sites are above given thresholds, computed from 3-day running standard deviations. Colours indicate detectable source types. Results are shown for using the EDGARv4.3.2 (**a**) and TNO-MACC_III (**b**) inventories in the domain covering parts of Northwestern Europe.

A.3 Publication list

- **Barbara Szénási**, Antoine Berchet, Grégoire Broquet, Arjo Segers, Hugo Denier van der Gon, Maarten Krol, Joanna J.S. Hullegie, Anja Kiesow, Dirk Günther, A.M. Roxana Petrescu, Marielle Saunois, Philippe Bousquet, and Isabelle Pison: A Pragmatic Protocol for Characterising Errors in Atmospheric Inversions of Methane Emissions over Europe. *Tellus B: Chemical and Physical Meteorology*. Submitted on 13 August 2020
- Malika Menoud, Carina van der Veen, Bert Scheeren, Huilin Chen, **Barbara Szénási**, Randulph P. Morales, Isabelle Pison, Philippe Bousquet, Dominik Brunner, and Thomas Röckmann: Characterisation of methane sources in Lutjewad, The Netherlands, using quasi-continuous isotopic composition measurements. *Tellus B: Chemical and Physical Meteorology*. Nov. 2020. 72:1, 1-19, DOI: 10.1080/16000889.2020.1823733
- **Barbara Szénási**, Antoine Berchet, Isabelle Pison, Grégoire Broquet, Malika Menoud, Carina van der Veen, Bert Scheeren, Huilin Chen, Thomas Röckmann, and Philippe Bousquet: What can we learn about methane emissions from the comparison of measured and simulated methane isotopic ratios at a coastal monitoring site?. In preparation

A.4 Training and network activities

Secondments

- Wageningen University and Research in Wageningen, The Netherlands
  Duration: 19 February 2018 - 19 March 2018
  Objectives: Model development and inter-model comparison using MicroHH, a computational fluid dynamics code for the simulation of turbulent flows in the atmosphere, and the CHIMERE chemistry-transport model
- Netherlands Organisation for Applied Scientific Research (TNO) in Utrecht, The Netherlands
  Duration: 17 June 2019 - 12 July 2019
  Objectives: Characterisation of errors in transport modelling and emission inventories
- Institute for Marine and Atmospheric research Utrecht (IMAU) of the Utrecht University in Utrecht, The Netherlands
  Duration: 9 December 2019 - 20 December 2019
  Objectives: Perform sensitivity analyses to improve understanding of modelled atmospheric isotopic ratios
- Netherlands Organisation for Applied Scientific Research (TNO) in Utrecht, The Netherlands
  Duration: 13 January 2020 - 24 January 2020
  Objectives: Prepare study for investigating the need of atmospheric isotopic measurements in Europe

Training events and courses

- University course *Greenhouse gases (GHGs): challenges and observations* at Ecole Polytechnique in Palaiseau, France
  Duration: October 2017 - December 2017
  Objectives: Introduction to GHGs and atmospheric observation techniques
- University course *Biogeochemical cycles and interactions with the biosphere at global scale* at AgroParisTech in Paris, France
  Duration: October 2017 - December 2017
  Objectives: Introduction to biogeochemical cycles
- First MEMO^2 school in Schoorl, The Netherlands
  Duration: 5 February 2018 - 16 February 2018

Objectives: First meeting with MEMO^2 members and acquire basics about atmospheric CH_4 mixing ratios and its stable isotopologues

- Workshop about CH_4 isotopologues at Royal Holloway University of London in Egham, United Kingdom
  Duration: 17 - 19 September 2018
  Objectives: Acquire fundamentals on CH_4 isotopologues
- Dispersion modelling workshop at Institute of Environmental Physics of the Heidelberg University in Heidelberg, Germany
  Duration: 9 - 10 October 2018
  Objectives: Understanding essential know-how on dispersion modelling
- University course *Scientific writing* at University Paris-Saclay in Saclay, France
  Duration: 12 - 13 February 2019
  Objectives: Improve scientific writing
- Second MEMO^2 school at University of Versailles Saint-Quentin-en-Yvelines in Gouyancourt, France
  Duration: 18 - 20 February 2019
  Objectives: Learn about how CH_4 and the society are connected
- LOTOS-EUROS modelling workshop
  Duration: 15-16 January 2020
  Objectives: Update LOTOS-EUROS user community about progress in atmospheric modelling

Meetings and conferences

- First MEMO^2 annual meeting at Swiss Federal Laboratories for Materials Science and Technology in Dübendorf, Switzerland
  Duration: 22 - 23 March 2018
  Objectives: Update each other about project progress and plans
- Conference EGU in Vienna, Austria
  Duration: 9 - 13 April 2018
  Presentation form and title: Poster presentation "Atmospheric monitoring of methane emission at the European scale"
  Authors: Barbara Szénási, Isabelle Pison, Antoine Berchet, Gregoire Broquet, Philippe Bousquet, Marielle Saunois
- Second MEMO^2 annual meeting
  Duration: 21 - 22 February 2019

Objectives: Update each other about project progress and plans

- Conference EGU in Vienna, Austria
  Duration: 7 - 12 April 2019
  Presentation form and title: PICO presentation "Evaluation of methane emission inventories at the European scale by comparing atmospheric transport models and measurements"
  Authors: Barbara Szénási, Antoine Berchet, Gregoire Broquet, Marielle Saunois, Hugo Denier van der Gon, Arjo Segers, Malika Menoud, Thomas Röckmann, Randulph Morales, Dominik Brunner, Philippe Bousquet, and Isabelle Pison
- Conference NCGG8 in Amsterdam, The Netherlands
  Duration: 12 - 14 June 2019
  Presentation form and title: Oral presentation "Evaluation of methane emission inventories by comparing atmospheric transport models and measurements"
  Authors: Barbara Szénási, Antoine Berchet, Gregoire Broquet, Marielle Saunois, Hugo Denier van der Gon, Arjo Segers, Malika Menoud, Thomas Röckmann, Randulph Morales, Dominik Brunner, Philippe Bousquet, and Isabelle Pison
- Third MEMO^2 annual meeting
  Duration: 10 - 11 February 2020
  Objectives: Update each other about project progress and plans

A.5 Résumé

L'objectif général de cette thèse est d'améliorer nos connaissances sur les sources européennes de méthane en utilisant la modélisation atmosphérique du rapport de mélangeatmosphérique de CH_4, ainsi que des rapports isotopiques δ^{13}C et δ^{2}H. Ce travail est motivé par l'importance du CH_4 atmosphérique dans le changement climatique et par la disponibilité de mesures de plus en plus nombreuses du rapport de mélange de CH_4 en Europe, mesures qui sont précieuses pour la quantification des émissions. Cette thèse aborde les incertitudes du bilan européen de CH_4 en se concentrant sur plusieurs éléments utilisés dans les inversions atmosphériques. La précision des estimations d'émissions de CH_4 dérivées des inversions atmosphériques (méhodes descendantes) dépend de la performance du modèle de transport utilisé, des incertitudes liées à ses données d'entrée, telles que les inventaires d'émissions et les conditions aux limites et initiales, de la précision des instruments mesurant les rapports de mélange de CH_4 et les rapports isotopiques δ^{2}H et δ^{13}C ainsi que du nombre et de l'emplacement de ces mesures.

Dans la première partie de cette thèse, nous avons évalué plusieurs erreurs dans les modèles de transport et les inventaires d'émissions en comparant des simulations du rapport de mélange de CH_4 effectuées en utilisant différentes configurations, différents modèles de transport et différents jeux de données d'entrée. Ces estimations d'erreurs peuvent être utilisées dans des inversions atmosphériques régionales pour estimer les émissions de CH_4 en Europe. La deuxième étape de ce travail a consisté à utiliser les informations obtenues à partir de mesures quasi-continues de la composition isotopique du CH_4 atmosphérique pour explorer les causes possibles des décalages entre les mesures et les simulations. Le but est d'en déduire des informations sur les principales sources de CH_4. La principale limite de l'étude est que les mesures quasi-continues et à haute fréquence de δ^{13}C et δ^{2}H ne sont disponibles que pour deux sites dans notre domaine européen. Ceci conduit à la troisième partie de cette thèse: son le but est d'étudier l'apport des mesures isotopiques in-situ à long terme aux sites opérationnels en Europe. Pour ce faire, nous analysons la précision des instruments nécessaire à la détection des signaux provenant de sources de CH_4.

Dans ce qui suit, nous résumons les principales conclusions et répondons aux questions de recherche posées au début de cette thèse. Les principales conclusions sont résumées dans la Figure 5.1.

Question de recherche 1: *Comment pouvons-nous quantifier les erreurs dans les modèles de transport et les inventaires d'émissions utilisés pour les inversions atmosphériques des émissions de méthane en Europe?* Dans le chapitre 2, nous avons estimé diverses erreurs dans la modélisation du transport et les inventaires d'émissions, qui peuvent être utilisées pour mettre en place des inversions atmosphériques des émissions de méthane en Europe. L'objectif était de comprendre comment ces erreurs pourraient être traitées de manière cohérente et incluses dans un système d'assimilation de données pour inverser les émissions de méthane en Europe. Les erreurs ont été évaluées aux emplacements des sites de mesure européens et sur le domaine européen modélisé pour 2015. Une méthode simple (Wang et al., 2017) a été utilisée: elle consiste à effectuer des simulations multiples à l'aide de deux modèles de transport à aire limitée à trois résolutions horizontales différentes avec des entrées basées sur trois inventaires d'émissions et deux ensembles de conditions aux limites et initiales. L'avantage d'une telle méthode d'estimation des erreurs est qu'elle est flexible et peut être utilisée avec n'importe quel modèle de transport et pour toute étude locale, régionale ou mondiale, ainsi que pour acquérir davantage de connaissances sur d'autres espèces atmosphériques que le méthane. À partir de l'ensemble des simulations, nous avons pu estimer quatre erreurs du modèle de transport : l'erreur de fond, l'erreur de représentation, l'erreur de transport, l'erreur dues aux émissions transportées. Le rapport entre l'erreur dues auxémissions transportées et les trois autres erreurs, leur amplitude et leur structure ont été utilisés pour examiner si les émissions ciblées peuvent être traitées par une inversion atmosphérique. En outre, nous avons estimé l'erreur des inventaires d'émissions en utilisant trois inventaires, ce qui nous a permis d'étudier les incertitudes spatiales des inventaires et les incertitudes liées aux amplitudes des émissions.

Nous avons constaté que l'erreur de fond présente une structure homogène et une faible variabilité, ce qui permet de la distinguer des autres types d'erreurs. Par conséquent, elle peut être contrôlée en même temps que les émissions dans le cadre de l'inversion, ce qui est cohérent avec d'autres études d'inversion régionales. L'erreur de représentation peut également être incluse dans les statistiques d'erreur d'observation. Nos analyses suggèrent que les sources d'erreur de transport peuvent être contrôlées au mieux en même temps que les émissions. Cependant, l'optimisation du transport en même temps que les émissions est difficile dans la plupart des systèmes d'inversion. En outre, notre analyse a montré des corrélations spatiales et temporelles, qui augmentent les difficultés pourinclure l'erreur de transport dans l'espace des émissions en raison des défis techniques que soulève l'inversion de grandes matrices non-diagonales.

L'erreur dans les inventaires d'émissions est hétérogène et dépend du pays et du secteur source. Les inventaires diffèrent principalement en ce qui concerne les sources liées aux déchets et aux combustibles fossiles en Europe. Cela est dû aux hypothèses utilisées pour la désagrégation spatiale des sources surfaciques et ponctuelles dans les inventaires, qui entraînent des différences dans l'ampleur et la localisation des émissions. Les longueurs de corrélation spatiale pour les secteurs des déchets et des combustibles fossiles sont négligeables. Pour l'agriculture, elle est d'environ 100-150 km.

Question de recherche 2: *Les mesures isotopiques sont-elles utiles comme contraintes sur les sources de CH_4 ?*

Dans le chapitre 3, nous avons recherché les causes des inadéquations entre les rapports de mélange de méthane mesurés et simulés, ainsi qu'entre ses rapports isotopiques δ^2H et δ^{13}C sur deux sites de mesure : le site côtier de Lutjewad aux Pays-Bas et le site continental de Heidelberg en Allemagne. L'objectif de cette étude était d'analyser si de telles différences peuvent être associées à des amplitudes et/ou des distributions spatiales d'émissions inexactes dans les inventaires ou à des signatures de sources isotopiques δ^{13}C et δ^2H inappropriées utilisées pour modéliser les rapports isotopiques δ^{13}C et δ^2H atmosphériques.

L'analyse des différences entre les mesures et les simulations autour de Lutjewad indique que la raison principale en est l'imprécision de l'amplitude et de la répartition spatiale des émissions dans le domaine couvrant certaines parties de l'Europe du Nord-Ouest. La sous-estimation des rapports de mélange CH_4 et la surestimation de δ^{13}C et δ^2H par CHIMERE sont principalement dues à la sous-estimation des sources biogéniques, en particulier des sources agricoles, dans l'inventaire EDGARv4.3.2 et TNO-MACC_III. De plus, les analyses de sensibilité suggèrent que les émissions liées aux combustibles fossiles sont surestimées dans les deux inventaires, en particulier au sud-est de Lutjewad. La comparaison des rapports de mélange de CH_4 et des rapports isotopiques δ^{13}C mesurés et simulés autour de Heidelberg permet de conclure que les émissions sont probablement mal placées et que leur amplitude est inexacte dans les deux inventaires . Une raison possible de la faible performance du modèle pour les rapports isotopiques δ^{13}C atmosphériques est la mauvaise signature isotopique de la source δ^{13}C utilisée pour la zone autour de Heidelberg. Néanmoins, nos résultats indiquent, entre autres, que les sources liées aux combustibles fossiles sont surestimées au nord de Heidelberg. Cela confirme les résultats similaires basés sur l'analyse autour de Lutjewad, selon lesquels les émissions liées aux combustibles fossiles qui pourraient se trouver dans le nord-ouest de l'Allemagne sont surestimées.

Question de recherche 3: *Quelles sont les précisions des instruments et les sites nécessaires pour que les mesures isotopiques soient utilisées dans les études d'inversion atmosphérique à l'échelle européenne ?*

Dans le chapitre 4, nous avons étudié l'importance des mesures isotopiques à long terme des δ^{13}C et δ^{2}H atmosphériques pour améliorer les estimations des émissions de CH_4 en Europe. Comme les mesures isotopiques à long terme sont actuellement rares en Europe, des simulations des rapports isotopiques du δ^{13}C et du δ^{2}H atmosphériques sont utilisées dans cette étude synthétique. Les simulations ont été réalisées pour les sites de surveillance du réseau européen ICOS pendant un an. Cette étude s'est concentrée sur la précision des instruments nécessaire pour détecter les signaux des principales sources de CH_4 et sur les sites de mesureauxquels le potentiel de détection des signaux est le plus élevé.

En étudiant la précision de l'instrument, nous avons constaté qu'une précision d'au moins 1‰ pour les analyses δ^{2}H et de 0,05‰ pour les analyses δ^{13}C serait nécessaire pour détecter les sources sur la plupart des sites pendant au moins six mois. Des simulations avec les deux inventaires indiquent les sites ICOS de Steinkimmen (DE), Cabauw (NL), Lutjewad (NL) et IPR (IT) ont été par d comme sites potentiels pour la détection de signaux isotopiques pendant au moins six mois de l'année. La principale source détectable confirmée sur ces sites est l'agriculture, qui est détectable sur la plupart des sites. À IPR, les sources de déchets sont la principale source détectable. Les sites KRE (CZ) et LIN (DE) semblent prometteurs pour la détection de sources liées aux combustibles fossiles pendant environ un mois.

Afin d'en savoir plus sur les sources et les puits de CH_4, il serait avantageux de mesurer la composition isotopique du CH_4 sur les sites et dans les régions où la détectabilité des sources est controversée, comme l'indiquent les simulations utilisant deux inventaires (par exemple WAO (UK) et STE), ainsi que dans d'autres régions où les sources liées aux déchets et aux combustibles fossiles peuvent être détectées. Ces régions sont, par exemple, la partie sud du Royaume-Uni et l'Europe de l'Est, respectivement. Comme aucun des sites ICOS n'est indiqué comme étant un site potentiel pour la détection de signaux provenant de zones humides, d'autres régions de latitude plus élevée, comme le sud de la Finlande, pourraient constituer une bonne cible pour la mesure des rapports isotopiques δ^2H et δ^{13}C et des rapports de mélange CH_4 provenant de zones humides.

Les recherches menées dans le cadre de cette thèse ont révélé que les distributions spatiales et les amplitudes inexactes des émissions de CH_4 sont la principale raison des écarts entre les rapports de mélange et la composition isotopique du CH_4 atmosphérique mesurés et simulés. Les plus grandes incertitudes ont été détectées dans les secteurs des déchets et des sources liées aux combustibles fossiles pour les inventaires utilisés dans cette thèse. Nos études ont montré que l'utilisation des rapports isotopiques δ^{13}C et δ^2H en plus des rapports de mélange de CH_4 peut aider à identifier les causes des divergences entre l'ampleur et la distribution spatiale des émissions dans les inventaires et contribuer à les améliorer. En outre, les mesures à long terme (> 1 an) ou quasi-continues (< 1 an) de δ^{13}C et δ^2H peuvent constituer un atout pour différencier les sources dans les inversions atmosphériques. Cependant, pour être utiles dans les inversions, ces mesures doivent être effectuées par des instruments dont la précision est d'au moins 0,05 ‰ pour δ^{13}C et 1 ‰ pour δ^2H. En outre, les études d'inversion doivent évaluer soigneusement les erreurs des modèles de transport et des inventaires d'émissions.

List of Acronyms and Abbreviations

AD: activity data

BC: boundary conditions

BU: bottom-up

CAMS: Copernicus Atmosphere Monitoring Service

CF-IRMS: continuous flow isotope ratio mass spectrometry system

CHIMERE: name of a multi-scale limited-area Eulerian chemistry-transport model

CTM: chemistry-transport model

CH_4: methane

CO_2: carbon dioxide

COSMO: Consortium for Small-scale Modelling

CRDS: cavity ring-down spectroscopy

δ^2H: relative difference of the hydrogen isotope ratio of methane

δ^{13}C: relative difference of the carbon isotope ratio of methane

ECLIPSE: Evaluating the Climate and Air Quality Impacts of Short-Lived Pollutants

ECMWF: European Centre for Medium-Range Weather Forecasts

EDGAR: Emission Database for Global Atmospheric Research

EEA: European Environment Agency

EF: emission factor

Empa: Swiss Federal Laboratories for Materials Science and Technology

ESRL: Earth System Research Laboratory

FLEXPART: FLEXible PARTicle dispersion model

GHG: greenhouse gas

GMD: Global Monitoring Division

GWP: global warming potential

H_2O: water vapour

HEI: Heidelberg

IAEA: International Atomic Energy Agency

ICOS: Integrated Carbon Observation System

IMAU: Institute for Marine and Atmospheric research Utrecht

InGOS: Integrated non-CO2 Greenhouse gas Observing System

IPCC: Intergovernmental Panel on Climate Change

IRMS: isotope ratio mass spectrometry system

KNMI: The Royal Netherlands Meteorological Institute

LBC: lateral boundary condition

LMDz: Laboratoire de Météorologie Dynamique, zoom

LOTOS-EUROS: Long Term Ozone Simulation - European Operational Smog

LSCE: Laboratoire des Sciences du Climat et de l’Environnement

LUT: Lutjewad

MACC: Monitoring Atmospheric Composition and Climate

MBE: mean bias error

$MEMO^2$: MEthane goes MObile - MEasurements and MOdelling

MicroHH: name of a computational fluid dynamics code made for Direct Numerical Simulation (DNS) and Large-Eddy Simulation (LES) of turbulent flows in the atmos-pheric boundary layer

MISOS: Methane ISOtopomer Spectrometer

N_2O: nitrous oxide

NIR: national inventory report

NOAA: National Oceanic and Atmospheric Administration

NO_x: nitrogen oxides

O_3: ozone

OH: hydroxyl radical

ORCHIDEE-WET: Organising Carbon and Hydrology In Dynamic Ecosystems model version for modelling groundwater flow and wetlands

OSSE: Observing System Simulation Experiment

PBL: planetary boundary layer

PYVAR: PYthon based VARiational data assimilation framework

RMSE: root mean squared error

SD: standard deviation

SNAP: Selected Nomenclature for Air Pollution

TD: top-down

TNO: Netherlands Organisation for Applied Scientific Research

UNFCCC: United Nations Framework Convention on Climate Change

VPDB: Vienna Peedee Belemnite

VSMOW: Vienna Standard Mean Ocean Water

WMO: World Meteorological Organization

List of Figures

List of Tables

Bibliography

Michelle Allsopp, Richard Page, Paul Johnston, and David Santillo, editors. *Increasing Greenhouse Gas Emissions: Impacts on the Marine Environment*, pages 157–180. Springer Netherlands, Dordrecht, 2009. ISBN 978-1-4020-9116-2. doi: 10.1007/978-1-4020-9116-2_5.

Sabina Assan. Towards improved source apportionment of anthropogenic methane sources, 2017. EarthSciences. Université Paris Saclay (COmUE), NNT: 017SACLV079.

Michael Baldauf, Axel Seifert, Jochen Förstner, Detlev Majewski, Matthias Raschendorfer, and Thorsten Reinhardt. Operational Convective-Scale Numerical Weather Prediction with the COSMO Model: Description and Sensitivities. *Monthly Weather Review*, 139(12):3887–3905, Dec. 2011. ISSN 0027-0644. doi: 10.1175/MWR-D-10-05013.1. URL `https://doi.org/10.1175/MWR-D-10-05013.1`.

A. Berchet, I. Pison, F. Chevallier, P. Bousquet, J.-L. Bonne, and J.-D. Paris. Objectified quantification of uncertainties in Bayesian atmospheric inversions. *Geoscientific Model Development*, 8(5):1525–1546, 2015. doi: 10.5194/gmd-8-1525-2015. URL `https://www.geosci-model-dev.net/8/1525/2015/`.

A. Berchet, I. Pison, P. M. Crill, B. Thornton, P. Bousquet, T. Thonat, T. Hocking, J. Thanwerdas, J.-D. Paris, and M. Saunois. Using ship-borne observations of methane isotopic ratio in the arctic ocean to understand methane sources in the arctic. *Atmospheric Chemistry and Physics*, 20(6):3987–3998, 2020. doi: 10.5194/acp-20-3987-2020. URL `https://www.atmos-chem-phys.net/20/3987/2020/`.

P. Bergamaschi, C. A. M. Brenninkmeijer, M. Hahn, T. Röckmann, D. H. Scharffe, P. J. Crutzen, N. F. Elansky, I. B. Belikov, N. B. A. Trivett, and D. E. J. Worthy. Isotope analysis based source identification for atmospheric CH_4 and CO sampled across Russia using the Trans-Siberian railroad. *Journal* *of Geophysical Research: Atmospheres*, 103(D7):8227–8235, 1998a. doi: 10.1029/97JD03738. URL `https://agupubs.onlinelibrary.wiley.com/doi/abs/10.1029/97JD03738`.

P. Bergamaschi, C. Lubina, R. Königstedt, H. Fischer, A. C. Veltkamp, and O. Zwaagstra. Stable isotopic signatures (δ^{13}C, δD) of methane from European landfill sites. *Journal of Geophysical Research: Atmospheres*, 103(D7):8251–8265, 1998b. doi: 10.1029/98JD00105. URL `https://agupubs.onlinelibrary.wiley.com/doi/abs/10.1029/98JD00105`.

P. Bergamaschi, M. Krol, F. Dentener, A. Vermeulen, F. Meinhardt, R. Graul, M. Ramonet, W. Peters, and E. J. Dlugokencky. Inverse modelling of national and European CH_4 emissions using the atmospheric zoom model TM5. *Atmospheric Chemistry and Physics*, 5(9):2431–2460, 2005. doi: 10.5194/acp-5-2431-2005. URL `https://www.atmos-chem-phys.net/5/2431/2005/`.

P. Bergamaschi, M. Krol, J. F. Meirink, F. Dentener, A. Segers, J. van Aardenne, S. Monni, A. T. Vermeulen, M. Schmidt, M. Ramonet, C. Yver, F. Meinhardt, E. G. Nisbet, R. E. Fisher, S. O'Doherty, and E. J. Dlugokencky. Inverse modeling of European CH_4 emissions 2001–2006. *Journal of Geophysical Research: Atmospheres*, 115(D22), 2010. doi: 10.1029/2010JD014180. URL `https://agupubs.onlinelibrary.wiley.com/doi/abs/10.1029/2010JD014180`.

P. Bergamaschi, Matteo Corazza, U. Karstens, Maria Athanassiadou, R. Thompson, I. Pison, A. Manning, Philippe Bousquet, A.J. Segers, Alex Vermeulen, G. Janssens-Maenhout, Martina Schmidt, Michel Ramonet, F. Meinhardt, Tuula Aalto, L. Haszpra, J. Moncrieff, Elena Popa, David Lowry, and E. Dlugokencky. Top-down estimates of European CH_4 and N_2O emissions based on four different inverse models. *Atmospheric Chemistry and Physics*, 15:715–736, Jan. 2015. doi: 10.5194/acp-15-715-2015.

P. Bergamaschi, U. Karstens, A. J. Manning, M. Saunois, A. Tsuruta, A. Berchet, A. T. Vermeulen, T. Arnold, G. Janssens-Maenhout, S. Hammer, I. Levin, M. Schmidt, M. Ramonet, M. Lopez, J. Lavric, T. Aalto, H. Chen, D. G. Feist, C. Gerbig, L. Haszpra, O. Hermansen, G. Manca, J. Moncrieff, F. Meinhardt, J. Necki, M. Galkowski, S. O'Doherty, N. Paramonova, H. A. Scheeren, M. Steinbacher, and E. Dlugokencky. Inverse modelling of European CH_4 emissions during 2006-2012 using different inverse models and reassessed atmospheric observations. *Atmospheric Chem-*

istry and Physics, 18(2):901–920, 2018. doi: 10.5194/acp-18-901-2018. URL `https://www.atmos-chem-phys.net/18/901/2018/`.

R. S. Bilek, S. C. Tyler, M. Kurihara, and K. Yagi. Investigation of cattle methane production and emission over a 24-hour period using measurements of δ^{13}C and δD of emitted CH_4 and rumen water. *Journal of Geophysical Research: Atmospheres*, 106(D14):15405–15413, 2001. doi: 10.1029/2001JD900177. URL `https://agupubs.onlinelibrary.wiley.com/doi/abs/10.1029/2001JD900177`.

Donald Blake, Edward Mayer, Stanley Tyler, Yoshihiro Makide, Derek Montague, and F. Rowland. Global increase in atmospheric methane concentrations between 1978 and 1980. *Geophysical Research Letters - GEOPHYS RES LETT*, 9, Apr. 1982. doi: 10.1029/GL009i004p00477.

M. Bocquet, L. Wu, and F. Chevallier. Bayesian design of control space for optimal assimilation of observations. Part I: Consistent multiscale formalism. *Quarterly Journal of the Royal Meteorological Society*, 137(658): 1340–1356, 2011. doi: 10.1002/qj.837. URL `https://rmets.onlinelibrary.wiley.com/doi/abs/10.1002/qj.837`.

P. Bousquet, P. Ciais, J. B. Miller, E. J. Dlugokencky, D. A. Hauglustaine, C. Prigent, G. R. Van der Werf, P. Peylin, E.-G. Brunke, C. Carouge, R. L. Langenfelds, J. Lathière, F. Papa, M. Ramonet, M. Schmidt, L. P. Steele, S. C. Tyler, and J. White. Contribution of anthropogenic and natural sources to atmospheric methane variability. *Nature*, 443:439–443, 2006. doi: doi:10.1038/nature05132.

P. Bousquet, B. Ringeval, I. Pison, E. J. Dlugokencky, E.-G. Brunke, C. Carouge, F. Chevallier, A. Fortems-Cheiney, C. Frankenberg, D. A. Hauglustaine, P. B. Krummel, R. L. Langenfelds, M. Ramonet, M. Schmidt, L. P. Steele, S. Szopa, C. Yver, N. Viovy, and P. Ciais. Source attribution of the changes in atmospheric methane for 2006–2008. *Atmospheric Chemistry and Physics*, 11(8):3689–3700, 2011. doi: 10.5194/acp-11-3689-2011. URL `https://www.atmos-chem-phys.net/11/3689/2011/`.

Philippe Bousquet, Clémence Pierangelo, Cédric Bacour, Julia Marshall, Philippe Peylin, Pradeebane Vaittinada Ayar, Gerhard Ehret, François-Marie Bréon, Frédéric Chevallier, Cyril Crevoisier, Fabien Gibert, Patrick Rairoux, Christoph Kiemle, Raymond Armante, Caroline Bès, Vincent Cassé, Jordi

Chinaud, Olivier Chomette, Thibault Delahaye, Dimitri Edouart, Frédéric Estève, Andreas Fix, Achim Friker, Andrzej Klonecki, Martin Wirth, Mathias Alpers, and Bruno Millet. Error Budget of the MEthane Remote LIdar missioN and Its Impact on the Uncertainties of the Global Methane Budget. *Journal of Geophysical Research: Atmospheres*, 123(20):11,766–11,785, 2018. doi: 10.1029/2018JD028907. URL `https://agupubs.onlinelibrary.wiley.com/doi/abs/10.1029/2018JD028907`.

K. Brophy, H. Graven, A. J. Manning, E. White, T. Arnold, M. L. Fischer, S. Jeong, X. Cui, and M. Rigby. Characterizing uncertainties in atmospheric inversions of fossil fuel CO_2 emissions in California. *Atmospheric Chemistry and Physics*, 19(5):2991–3006, 2019. doi: 10.5194/acp-19-2991-2019. URL `https://acp.copernicus.org/articles/19/2991/2019/`.

Grégoire Broquet, Frédéric Chevallier, Peter Rayner, Céline Aulagnier, Isabelle Pison, Michel Ramonet, Martina Schmidt, Alex T. Vermeulen, and Philippe Ciais. A European summertime CO_2 biogenic flux inversion at mesoscale from continuous in situ mixing ratio measurements. *Journal of Geophysical Research: Atmospheres*, 116(D23), 2011. doi: 10.1029/2011JD016202. URL `https://agupubs.onlinelibrary.wiley.com/doi/abs/10.1029/2011JD016202`.

Dominik Brunner, Nicholas Savage, Oriol Jorba, Brian Eder, Lea Giordano, Alba Badia, Alessandra Balzarini, Rocío Baró, Roberto Bianconi, Charles Chemel, Gabriele Curci, Renate Forkel, Pedro Jimenez-Guerrero, Marcus Hirtl, Alma Hodzic, Luka Honzak, ulas im, Christoph Knote, Paul Makar, and Stefano Galmarini. Comparative analysis of meteorological performance of coupled chemistry-meteorology models in the context of AQMEII phase 2. *Atmospheric Environment*, 115:470–498, Aug. 2015. doi: 10.1016/j.atmosenv.2014.12.032.

O. Bréas, C. Guillou, F. Reniero, and E. Wada. The Global Methane Cycle: Isotopes and Mixing Ratios, Sources and Sinks. *Isotopes in Environmental and Health Studies*, 37(4):257–379, 2001. doi: 10.1080/10256010108033302. URL `https://doi.org/10.1080/10256010108033302`. PMID: 12723792.

Christopher A. Cantrell, Richard E. Shetter, Anthony H. McDaniel, Jack G. Calvert, James A. Davidson, David C. Lowe, Stanley C. Tyler, Ralph J. Cicerone, and James P. Greenberg. Carbon kinetic isotope effect in the oxidation of methane by the hydroxyl radical. *Journal of Geophysical Research: Atmospheres*, 95(D13):22455–22462, 1990. doi: 10.1029/JD095iD13p22455. URL https://agupubs.onlinelibrary.wiley.com/doi/abs/10.1029/JD095iD13p22455.

Jeffrey Chanton, Christine Rutkowski, Candace Schwartz, D. Ward, and Lindsay Boring. Factors influencing the stable carbon isotopic signature of methane from combustion and biomass burning. *Journal of Geophysical Research*, 105:1867–1877, Jan. 2000. doi: 10.1029/1999JD900909.

CHIMERE. Documentation of the chemistry-transport model CHIMERE, Jun. 2017. URL http://www.lmd.polytechnique.fr/chimere/.

Maria Custodio, Rosmeri Rocha, Tércio Ambrizzi, P.L. Vidale, and Marie-Estelle Demory. Impact of increased horizontal resolution in coupled and atmosphere-only models of the HadGEM1 family upon the climate patterns of South America. *Climate Dynamics*, 48, 07 2016. doi: 10.1007/s00382-016-3271-8.

Walter Dabberdt, Mary Carroll, Darrel Baumgardner, Gregory Carmichael, Ronald Cohen, Timothy Dye, James Ellis, Georg Grell, Christine Grimmond, Steven Hanna, John Irwin, Brian Lamb, Sasha Madronich, Jeffery Mcqueen, James Meagher, Mehmet Odman, Jonathan Pleim, Hans Schmid, and Douglas Westphal. Meteorological Research Needs for Improved Air Quality Forecasting: Report of the 11th Prospectus Development Team of the U.S. Weather Research Program. *Bulletin of the American Meteorological Society*, 85, Apr. 2004. doi: 10.1175/bams-85-4-563.

H. A. C. Denier van der Gon, R. Bergström, C. Fountoukis, C. Johansson, S. N. Pandis, D. Simpson, and A. J. H. Visschedijk. Particulate emissions from residential wood combustion in Europe – revised estimates and an evaluation. *Atmospheric Chemistry and Physics*, 15(11):6503–6519, 2015. doi: 10.5194/acp-15-6503-2015. URL https://acp.copernicus.org/articles/15/6503/2015/.

E. Dlugokencky. National Oceanic and Atmospheric Administration - Global Monitoring Laboratory (NOAA/GML). www.esrl.noaa.gov/gmd/ccgg/trends_ch4/, last accessed on 10 July 2020.

E. J. Dlugokencky, L. P. Steele, P. M. Lang, and K. A. Masarie. The growth rate and distribution of atmospheric methane. *Journal of Geophysical Research (Atmospheres)*, 99, Aug. 1994. doi: 10.1029/94JD01245.

Edward Dlugokencky, Euan Nisbet, Rebecca Fisher, and David Lowry. Global atmospheric methane: Budget, changes and dangers. *Philosophical transactions. Series A, Mathematical, physical, and engineering sciences*, 369: 2058–72, May 2011. doi: 10.1098/rsta.2010.0341.

Stephen Eckermann. Hybrid σ–p Coordinate Choices for a Global Model. *Monthly Weather Review*, 137(1):224–245, Jan. 2009. ISSN 0027-0644. doi: 10.1175/2008MWR2537.1. URL `https://doi.org/10.1175/2008MWR2537.1`.

ECMWF. *IFS Documentation CY47R1. PART III: Dynamics and Numerical Procedures*. Number 3 in IFS Documentation. ECMWF, 2020. URL `https://www.ecmwf.int/node/19747`.

EEA. Annual European Union greenhouse gas inventory 1990–2017 and inventory report 2019, 2019. URL `https://www.eea.europa.eu/publications/european-union-greenhouse-gas-inventory-2019`.

EEA. Annual European Union greenhouse gas inventory 1990–2018 and inventory report 2020, 2020. URL `https://www.eea.europa.eu//publications/european-union-greenhouse-gas-inventory-2020`.

D. H. Ehhalt. The atmospheric cycle of methane. *Tellus*, 26(1-2):58–70, 1974. doi: 10.1111/j.2153-3490.1974.tb01952.x. URL `https://onlinelibrary.wiley.com/doi/abs/10.1111/j.2153-3490.1974.tb01952.x`.

Abdelhadi El Yazidi. Estimation of the CO_2 and CH_4 fluxes in France using atmospheric concentrations from ICOS network and data-assimilation techniques, 2018. Meteorology. Université Paris-Saclay. NNT: 2018SACLV067.

I. G. Enting, C. M. Trudinger, and R. J. Francey. A synthesis inversion of the concentration and δ^{13}C of atmospheric CO_2. *Tellus B*, 47(1-2):35–52, 2 1995. ISSN 1600-0889. doi: 10.1034/j.1600-0889.47.issue1.5.x. URL `https://doi.org/10.1034/j.1600-0889.47.issue1.5.x`.

I.G. Enting, C.M. Trudinger, R.J. Francey, and H. Granek. Synthesis inversion of atmospheric CO_2 using the GISS tracer transport model. *CSIRO Aust Div Atmos Res Tech Paper*, 29:1–44, 1993.

Arlene Fiore, Jason West, Larry Horowitz, Vaishali Naik, and M. Schwarzkopf. Characterizing the tropospheric ozone response to methane emission controls and the benefits to climate and air quality. *Journal of Geophysical Research*, 113, Apr. 2008. doi: 10.1029/2007JD009162.

Rebecca Fisher, David Lowry, Owen Wilkin, Srimathy Sriskantharajah, and Euan Nisbet. High-precision, automated stable isotope analysis of atmospheric methane and carbon dioxide using continuous-flow isotope-ratio mass spectrometry. *Rapid Communications in Mass Spectrometry : RCM*, 20:200–8, Jan. 2006. doi: 10.1002/rcm.2300.

Rebecca Fisher, J. France, David Lowry, Mathias Lanoisellé, Rebecca Brownlow, John Pyle, Michelle Cain, Nicola Warwick, U. Skiba, Julia Drewer, Kerry Dinsmore, Sarah Leeson, Stéphane Bauguitte, Axel Wellpott, Sebastian O’Shea, Grant Allen, Martin Gallagher, Joseph Pitt, Carl Percival, and Euan Nisbet. Measurement of the ^{13}C isotopic signature of methane emissions from northern European wetlands. *Global Biogeochemical Cycles*, 31, Mar. 2017. doi: 10.1002/2016GB005504.

A. Fortems-Cheiney, F. Chevallier, I. Pison, P. Bousquet, M. Saunois, S. Szopa, C. Cressot, T. P. Kurosu, K. Chance, and A. Fried. The formaldehyde budget as seen by a global-scale multi-constraint and multi-species inversion system. *Atmospheric Chemistry and Physics*, 12(15):6699–6721, 2012. doi: 10.5194/acp-12-6699-2012. URL `https://www.atmos-chem-phys.net/12/6699/2012/`.

A. Fortems-Cheiney, I. Pison, G. Dufour, G. Broquet, A. Berchet, E. Potier, A. Coman, G. Siour, and L. Costantino. Variational regional inverse modeling of reactive species emissions with PYVAR-CHIMERE. *Geoscientific Model Development Discussions*, 2019:1–22, 2019. doi: 10.5194/gmd-2019-186. URL `https://www.geosci-model-dev-discuss.net/gmd-2019-186/`.

B Franco, E Mahieu, L K Emmons, Z A Tzompa-Sosa, E V Fischer, K Sudo, B Bovy, S Conway, D Griffin, J W Hannigan, K Strong, and K A Walker. Evaluating ethane and methane emissions associated with the development of oil and natural gas extraction in North America. *Environmental Research Letters*, 11(4):044010, Apr. 2016. doi: 10.1088/1748-9326/11/4/044010. URL `https://doi.org/10.1088/1748-9326/11/4/044010`.

Pierre Galand, Kim Yrjälä, and R. Conrad. Stable carbon isotope fractionation during methanogenesis in three boreal peatland ecosystems. *Biogeosciences*, 7, Nov. 2010. doi: 10.5194/bg-7-3893-2010.

L. M. Games and J. M. Hayes. On the mechanisms of CO_2 and CH_4 production in natural anaerobic environments. *Environmental Biogeochemistry*, pages 51–73, 1976.

A. L. Ganesan, M. Rigby, A. Zammit-Mangion, A. J. Manning, R. G. Prinn, P. J. Fraser, C. M. Harth, K.-R. Kim, P. B. Krummel, S. Li, J. Mühle, S. J. O'Doherty, S. Park, P. K. Salameh, L. P. Steele, and R. F. Weiss. Characterization of uncertainties in atmospheric trace gas inversions using hierarchical Bayesian methods. *Atmospheric Chemistry and Physics*, 14(8): 3855–3864, 2014. doi: 10.5194/acp-14-3855-2014. URL `https://www.atmos-chem-phys.net/14/3855/2014/`.

B. Gaubert, H. M. Worden, A. F. J. Arellano, L. K. Emmons, S. Tilmes, J. Barré, S. Martinez Alonso, F. Vitt, J. L. Anderson, F. Alkemade, S. Houweling, and D. P. Edwards. Chemical Feedback From Decreasing Carbon Monoxide Emissions. *Geophysical Research Letters*, 44(19):9985–9995, 2017. doi: 10.1002/2017GL074987. URL `https://agupubs.onlinelibrary.wiley.com/doi/abs/10.1002/2017GL074987`.

C. Gerbig, S. Körner, and J. C. Lin. Vertical mixing in atmospheric tracer transport models: error characterization and propagation. *Atmospheric Chemistry and Physics*, 8(3):591–602, 2008. doi: 10.5194/acp-8-591-2008. URL `https://acp.copernicus.org/articles/8/591/2008/`.

T Gierczak, R K Talukdar, S C Herndon, G L Vaghjiani, A R Ravishankara, and CO Univ. of Colorado, Boulder. Rate coefficients for the reactions of hydroxyl radicals with methane and deuterated methanes. *Journal of Physical Chemistry A: Molecules, Spectroscopy, Kinetics, Environment, amp General Theory*, 101(17), 4 1997. doi: 10.1021/jp963892r.

L. Giordano, Dominik Brunner, Johannes Flemming, C. Hogrefe, ulas im, Roberto Bianconi, Alba Badia, Alessandra Balzarini, Rocío Baró, Charles Chemel, Gabriele Curci, Renate Forkel, Pedro Jimenez-Guerrero, Marcus Hirtl, Alma Hodzic, Luka Honzak, Oriol Jorba, Christoph Knote, Jeroen Kuenen, and Stefano Galmarini. Assessment of the MACC reanalysis and its influence as chemical boundary conditions for regional air quality modeling in AQMEII-2. *Atmospheric Environment*, 115:371–388, 08 2015. doi: 10.1016/j.atmosenv.2015.02.034.

C. Granier, A. D'Angiola, H. Denier van der Gon, and J. Kuenen. Report on the update of anthropogenic surface emissions, MACC-II deliverable report D_22.1. *MACC deliverable*, Dec. 2012. Downloaded from http://www.aeris-data.fr/redirect/CAMS-REG-GHG.

S. Gromov, C. A. M. Brenninkmeijer, and P. Jöckel. Uncertainties of fluxes and $^{13}C/^{12}C$ ratios of atmospheric reactive-gas emissions. *Atmospheric Chemistry and Physics*, 17(13):8525–8552, 2017. doi: 10.5194/acp-17-8525-2017. URL `https://www.atmos-chem-phys.net/17/8525/2017/`.

James D. Happell, Jeffrey P. Chanton, and William J. Showers. Methane transfer across the water-air interface in stagnant wooded swamps of Florida: Evaluation of mass-transfer coefficients and isotropic fractionation. *Limnology and Oceanography*, 40(2):290–298, 1995. doi: 10.4319/lo.1995.40.2.0290. URL `https://aslopubs.onlinelibrary.wiley.com/doi/abs/10.4319/lo.1995.40.2.0290`.

P. Hausmann, Ralf Sussmann, and D. Smale. Contribution of oil and natural gas production to renewed increase in atmospheric methane (2007–2014): top–down estimate from ethane and methane column observations. *Atmospheric Chemistry and Physics*, 16, Mar. 2016. doi: 10.5194/acp-16-3227-2016.

Detlev Helmig, Sam Rossabi, Jacques Hueber, Pieter Tans, Stephen Montzka, Ken Masarie, Kirk Thoning, Christian Plass-Duelmer, Anja Claude, Lucy Carpenter, Alastair Lewis, Shalini Punjabi, Stefan Reimann, Martin Vollmer, Rainer Steinbrecher, James Hannigan, Louisa Emmons, Emmanuel Mahieu, Bruno Franco, and Andrea Pozzer. Reversal of global atmospheric ethane and propane trends largely due to US oil and natural gas production. *Nature Geoscience*, 9, Jun. 2016. doi: 10.1038/NGEO2721.

S. Henne, D. Brunner, B. Oney, M. Leuenberger, W. Eugster, I. Bamberger, F. Meinhardt, M. Steinbacher, and L. Emmenegger. Validation of the Swiss methane emission inventory by atmospheric observations and inverse modelling. *Atmospheric Chemistry and Physics*, 16(6):3683–3710, 2016. doi: 10.5194/acp-16-3683-2016. URL `https://www.atmos-chem-phys.net/16/3683/2016/`.

Daniel Hodyss and Nancy Nichols. The error of representation: basic understanding. *Tellus A: Dynamic Meteorology and Oceanography*, 67(1): 24822, 2015. doi: 10.3402/tellusa.v67.24822. URL `https://doi.org/10.3402/tellusa.v67.24822`.

A. Hoheisel, C. Yeman, F. Dinger, H. Eckhardt, and M. Schmidt. An improved method for mobile characterisation of $\delta^{13}CH_4$ source signatures and its application in Germany. *Atmospheric Measurement Techniques*, 12(2): 1123–1139, 2019. doi: 10.5194/amt-12-1123-2019. URL `https://www.atmos-meas-tech.net/12/1123/2019/`.

Christopher D. Holmes. Methane Feedback on Atmospheric Chemistry: Methods, Models, and Mechanisms. *Journal of Advances in Modeling Earth Systems*, 10(4):1087–1099, 2018. doi: 10.1002/2017MS001196. URL `https://agupubs.onlinelibrary.wiley.com/doi/abs/10.1002/2017MS001196`.

Frédéric Hourdin, Ionela Musat, Sandrine Bony, Pascale Braconnot, Francis Codron, Jean-Louis Dufresne, Laurent Fairhead, Marie-Angèle Filiberti, Pierre Friedlingstein, Jean-Yves Grandpeix, Gerhard Krinner, Phu Levan, Zhao-Xin Li, and François Lott. The LMDZ4 general circulation model: climate performance and sensitivity to parametrized physics with emphasis on tropical convection. *Climate Dynamics*, 27(7-8):787–813, Dec. 2006. doi: 10.1007/s00382-006-0158-0.

S. Houweling, M. Krol, P. Bergamaschi, C. Frankenberg, E. J. Dlugokencky, I. Morino, J. Notholt, V. Sherlock, D. Wunch, V. Beck, C. Gerbig, H. Chen, E. A. Kort, T. Röckmann, and I. Aben. A multi-year methane inversion using SCIAMACHY, accounting for systematic errors using TCCON measurements. *Atmospheric Chemistry and Physics*, 14(8):3991–4012, 2014. doi: 10.5194/acp-14-3991-2014. URL `https://acp.copernicus.org/articles/14/3991/2014/`.

Haili Hu, Jochen Landgraf, Rob Detmers, Tobias Borsdorff, Joost Aan de Brugh, Ilse Aben, André Butz, and Otto Hasekamp. Toward Global Mapping of Methane With TROPOMI: First Results and Intersatellite Comparison to GOSAT. *Geophysical Research Letters*, 45(8):3682–3689, 2018. doi: 10.1002/2018GL077259. URL `https://agupubs.onlinelibrary.wiley.com/doi/abs/10.1002/2018GL077259`.

IPCC. *IPCC Guidelines for National Greenhouse Gas Inventories, Prepared by the National Greenhouse Gas Inventories Programme*. Edited by H.S. Eggleston, L. Buendia, K. Miwa, T. Ngara and K. Tanabe. Institute for Global Environmental Strategies, Japan, 2006. ISBN 4-88788-032-4.

IPCC. Summary for Policymakers. In *Climate Change 2013: The Physical Science Basis. Contribution of Working Group I to the Fifth Assessment*

Report of the Intergovernmental Panel on Climate Change [Stocker, T.F., D. Qin, G.-K. Plattner, M. Tignor, S.K. Allen, J. Boschung, A. Nauels, Y. Xia, V. Bex and P.M. Midgley (eds.)], page 1–30, Cambridge, United Kingdom and New York, NY, USA, 2013. Cambridge University Press. ISBN 978-1-107-66182-0. doi: 10.1017/CBO9781107415324.004. URL `www.climatechange2013.org`.

IPCC. Climate Change 2014. In *Synthesis Report. Contribution of Working Groups I, II and III to the Fifth Assessment Report of the Intergovernmental Panel on Climate Change [Core Writing Team, R.K. Pachauri and L.A. Meyer (eds.)]*, Geneva, Switzerland, 2014. IPCC. ISBN 978-92-9169-143-2.

IPCC. Summary for Policymakers. In *Global Warming of 1.5°C. An IPCC Special Report on the impacts of global warming of 1.5°C above pre-industrial levels and related global greenhouse gas emission pathways, in the context of strengthening the global response to the threat of climate change, sustainable development, and efforts to eradicate poverty [V. Masson-Delmotte, P. Zhai, H.-O. Pörtner, D. Roberts, J. Skea, P.R. Shukla, A. Pirani, W. Moufouma-Okia, C. Péan, R. Pidcock, S. Connors, J.B.R. Matthews, Y. Chen, X. Zhou, M.I. Gomis, E. Lonnoy, T. Maycock, M. Tignor, and T. Waterfield (eds.)]*, Geneva, Switzerland, 2018. World Meteorological Organization.

ISAP. Integrated Sustainability Action Plan, 2019. URL `http://www.stpete.org/sustainability/integrated_sustainability_action_plan.php`.

G. Janssens-Maenhout, M. Crippa, D. Guizzardi, M. Muntean, E. Schaaf, F. Dentener, P. Bergamaschi, V. Pagliari, J. G. J. Olivier, J. A. H. W. Peters, J. A. van Aardenne, S. Monni, U. Doering, and A. M. R. Petrescu. EDGAR v4.3.2 Global Atlas of the three major Greenhouse Gas Emissions for the period 1970–2012. *Earth System Science Data Discussions*, 2017:1–55, 2017. doi: 10.5194/essd-2017-79. URL `https://www.earth-syst-sci-data-discuss.net/essd-2017-79/`.

S. Javadinejad, S. Eslamian, and K. Ostad-Ali-Askari. Investigation of monthly and seasonal changes of methane gas with respect to climate change using satellite data. *Applied Water Science*, 9(180), 2019. doi: https://doi.org/10.1007/s13201-019-1067-9.

Jamal Jokar Arsanjani, Marco Helbich, Mohamed Bakillah, and Lukas Loos.

The emergence and evolution of OpenStreetMap: A cellular automata approach. *International Journal of Digital Earth*, 8:1–30, Jan. 2013.

Matthias Jonas, Gregg Marland, Wilfried Winiwarter, Thomas White, Zbigniew Nahorski, Rostyslav Bun, and Sten Nilsson. *Benefits of dealing with uncertainty in greenhouse gas inventories: introduction. In Greenhouse Gas Inventories: Dealing With Uncertainty*, pages 3–18. Springer Netherlands, Dordrecht, 2011. ISBN 978-94-007-1670-4. doi: 10.1007/978-94-007-1670-4_2. URL `https://doi.org/10.1007/978-94-007-1670-4_2`.

Thomas Kaminski, P. Rayner, Martin Heimann, and Ian Enting. On aggregation errors in atmospheric transport inversion. *Journal of Geophysical Research*, 106, Mar. 2001. doi: 10.1029/2000JD900581.

Charles D Keeling. The concentration and isotopic abundances of atmospheric carbon dioxide in rural areas. *Geochimica et Cosmochimica Acta*, 13(4):322 – 334, 1958. ISSN 0016-7037. doi: https://doi.org/10.1016/0016-7037(58)90033-4. URL `http://www.sciencedirect.com/science/article/pii/0016703758900334`.

Stefanie Kirschke, Philippe Bousquet, Philippe Ciais, M. Saunois, Josep Canadell, Edward Dlugokencky, Peter Bergamaschi, Daniel Bergmann, Donald Blake, L. Bruhwiler, Philip Cameron-Smith, Simona Castaldi, Frederic Chevallier, Liang Feng, Annemarie Fraser, Martin Heimann, E. Hodson, Sander Houweling, B. Josse, and Guang Zeng. Three decades of global methane sources and sinks. *Nature Geoscience*, 6:813–823, Oct. 2013. doi: 10.1038/ngeo1955.

Fenja Klevenhusen, Stefano Bernasconi, M Kreuzer, and Carla Soliva. Experimental validation of the Intergovernmental Panel on Climate Change default values for ruminant-derived methane and its carbon-isotope signature. *Animal Production Science - ANIM PROD SCI*, 50, Jan. 2010. doi: 10.1071/AN09112.

E. Koffi, P. Bergamaschi, Ute Karstens, Maarten Krol, A.J. Segers, Martina Schmidt, Ingeborg Levin, Alex Vermeulen, R. Fisher, Victor Kazan, Henk Klein Baltink, David Lowry, G. Manca, Harro A.J. Meijer, J. Moncrieff, Sandip Pal, Michel Ramonet, and H.A. Scheeren. Evaluation of the boundary layer dynamics of the TM5 model. *Geoscientific Model Development Discussions*, pages 1–37, Mar. 2016. doi: 10.5194/gmd-2016-48.

J. J. P. Kuenen, A. J. H. Visschedijk, M. Jozwicka, and H. A. C. Denier van der Gon. TNO-MACC_II emission inventory; a multi-year (2003-2009) consistent high-resolution European emission inventory for air quality modelling. *Atmospheric Chemistry and Physics*, 14(20):10963–10976, 2014. doi: 10.5194/acp-14-10963-2014. URL `https://www.atmos-chem-phys.net/14/10963/2014/`.

Ingeborg Levin, Peter Bergamaschi, Helmut Dörr, and Dorothea Trapp. Stable isotopic signature of methane from major sources in Germany. *Chemosphere*, 26(1):161 – 177, 1993. ISSN 0045-6535. doi: https://doi.org/10.1016/0045-6535(93)90419-6. URL `http://www.sciencedirect.com/science/article/pii/0045653593904196`.

Ingeborg Levin, Holger Glatzel-Mattheier, Thomas Marik, Matthias Cuntz, Martina Schmidt, and Douglas Worthy. Verification of German methane emission inventories and their recent changes based on atmospheric observations. *Journal of Geophysical Research*, 104:3447–3456, Feb. 1999. doi: 10.1029/1998JD100064.

George P. Lithoxoos, Loukas D. Peristeras, Georgios C. Boulougouris, and Ioannis G. Economou. Monte Carlo simulation of carbon monoxide, carbon dioxide and methane adsorption on activated carbon. *Molecular Physics*, 110(11-12):1153–1160, 2012. doi: 10.1080/00268976.2012.659223. URL `https://doi.org/10.1080/00268976.2012.659223`.

R. Locatelli, Philippe Bousquet, F. Chevallier, A. Fortems-Cheney, S. Szopa, M. Saunois, Anna Agusti-Panareda, D. Bergmann, Huisheng Bian, P. Cameron-Smith, Martyn Chipperfield, Manuel Gloor, Sander Houweling, S. Kawa, Maarten Krol, P. Patra, Ronald Prinn, M. Rigby, Ryu Saito, and Christopher Wilson. Impact of transport model errors on the global and regional methane emissions estimated by inverse modelling. *Atmospheric Chemistry and Physics*, 13, Oct. 2013. doi: 10.5194/acp-13-9917-2013.

R. Locatelli, P. Bousquet, F. Hourdin, M. Saunois, A. Cozic, F. Couvreux, J.-Y. Grandpeix, M.-P. Lefebvre, C. Rio, P. Bergamaschi, S. D. Chambers, U. Karstens, V. Kazan, S. van der Laan, H. A. J. Meijer, J. Moncrieff, M. Ramonet, H. A. Scheeren, C. Schlosser, M. Schmidt, A. Vermeulen, and A. G. Williams. Atmospheric transport and chemistry of trace gases in LMDz5B: evaluation and implications for inverse modelling. *Geoscientific*

Model Development, 8(2):129–150, 2015. doi: 10.5194/gmd-8-129-2015. URL `https://gmd.copernicus.org/articles/8/129/2015/`.

D. Lowe, J. White, I. Levin, M. Wahlen, J.B. Miller, and P. Bergamaschi. Isotope measurement techniques for atmospheric methane (IAEA-TECDOC–1268), Jan. 2002. ISSN 1011-4289. International Atomic Energy Agency (IAEA).

David Lowry, Craig Holmes, Nigel Rata, Philip O'Brien, and Euan Nisbet. London methane emissions: Use of diurnal changes in concentration and δ^{13}C to identify urban sources and verify inventories. *J. Geophys. Res.*, 106, Apr. 2001. doi: 10.1029/2000JD900601.

M. F. Lunt, M. Rigby, A. L. Ganesan, and A. J. Manning. Estimation of trace gas fluxes with objectively determined basis functions using reversible-jump Markov chain Monte Carlo. *Geoscientific Model Development*, 9(9): 3213–3229, 2016. doi: 10.5194/gmd-9-3213-2016. URL `https://www.geosci-model-dev.net/9/3213/2016/`.

Po-Lun Ma, Philip J. Rasch, Minghuai Wang, Hailong Wang, Steven J. Ghan, Richard C. Easter, William I. Gustafson Jr., Xiaohong Liu, Yuying Zhang, and Hsi-Yen Ma. How does increasing horizontal resolution in a global climate model improve the simulation of aerosol-cloud interactions? *Geophysical Research Letters*, 42(12):5058–5065, 2015. doi: 10.1002/2015GL064183. URL `https://agupubs.onlinelibrary.wiley.com/doi/abs/10.1002/2015GL064183`.

S. Mailler, L. Menut, D. Khvorostyanov, M. Valari, F. Couvidat, G. Siour, S. Turquety, R. Briant, P. Tuccella, B. Bessagnet, A. Colette, L. Létinois, K. Markakis, and F. Meleux. CHIMERE-2017: from urban to hemispheric chemistry-transport modeling. *Geoscientific Model Development*, 10(6): 2397–2423, 2017. doi: 10.5194/gmd-10-2397-2017. URL `https://www.geosci-model-dev.net/10/2397/2017/`.

A. Manders, P.J.H. Builtjes, Lyana Curier, Hugo Gon, Carlijn Hendriks, Sander Jonkers, R. Kranenburg, Jeroen Kuenen, A.J. Segers, Renske Timmermans, A.J.H. Visschedijk, R.J. Wichink Kruit, W. Pul, Ferd Sauter, Eric Swaluw, Daan Swart, Ioannis Douros, Henk Eskes, Erik Meijgaard, and Martijn Schaap. Curriculum Vitae of the LOTOS-EUROS (v2.0) chemistry transport model. *Geoscientific Model Development Discussions*, pages 1–53, May 2017. doi: 10.5194/gmd-2017-88.

V. Marécal, V.-H. Peuch, C. Andersson, S. Andersson, J. Arteta, M. Beekmann, A. Benedictow, R. Bergström, B. Bessagnet, A. Cansado, F. Chéroux, A. Colette, A. Coman, R. L. Curier, H. A. C. Denier van der Gon, A. Drouin, H. Elbern, E. Emili, R. J. Engelen, H. J. Eskes, G. Foret, E. Friese, M. Gauss, C. Giannaros, J. Guth, M. Joly, E. Jaumouillé, B. Josse, N. Kadygrov, J. W. Kaiser, K. Krajsek, J. Kuenen, U. Kumar, N. Liora, E. Lopez, L. Malherbe, I. Martinez, D. Melas, F. Meleux, L. Menut, P. Moinat, T. Morales, J. Parmentier, A. Piacentini, M. Plu, A. Poupkou, S. Queguiner, L. Robertson, L. Rouïl, M. Schaap, A. Segers, M. Sofiev, L. Tarasson, M. Thomas, R. Timmermans, Á. Valdebenito, P. van Velthoven, R. van Versendaal, J. Vira, and A. Ung. A regional air quality forecasting system over Europe: the MACC-II daily ensemble production. *Geoscientific Model Development*, 8(9):2777–2813, 2015. doi: 10.5194/gmd-8-2777-2015. URL `https://www.geosci-model-dev.net/8/2777/2015/`.

Christopher S. Martens, Cheryl A. Kelley, Jeffrey P. Chanton, and William J. Showers. Carbon and hydrogen isotopic characterization of methane from wetlands and lakes of the Yukon-Kuskokwim delta, western Alaska. *Journal of Geophysical Research: Atmospheres*, 97(D15):16689–16701, 1992. doi: 10.1029/91JD02885. URL `https://agupubs.onlinelibrary.wiley.com/doi/abs/10.1029/91JD02885`.

J. McNorton, N. Bousserez, A. Agustí-Panareda, G. Balsamo, M. Choulga, A. Dawson, R. Engelen, Z. Kiping, and S. Lang. Representing Model Uncertainty for Global Atmospheric CO_2 Flux Inversions Using ECMWF-IFS-46R1. *Geoscientific Model Development Discussions*, 2020:1–30, 2020. doi: 10.5194/gmd-2019-314. URL `https://www.geosci-model-dev-discuss.net/gmd-2019-314/`.

Malika Menoud, Thomas Röckmann, Julianne Fernandez, Semra Bakkaloglu, David Lowry, Piotr Korben, Martina Schmidt, Mila Stanisavljevic, Jaroslaw Necki, Sara Defratyka, and Camille Yver Kwok. mamenoud/MEMO2_isotopes: v8.1 complete, Oct. 2020a. URL `https://doi.org/10.5281/zenodo.4062356`.

Malika Menoud, Carina van der Veen, Bert Scheeren, Huilin Chen, Barbara Szénási, Randulph P. Morales, Isabelle Pison, Philippe Bousquet, Dominik Brunner, and Thomas Röckmann. Characterisation of methane sources in Lutjewad, The Netherlands, using quasi-continuous isotopic composition measurements. *Tellus B: Chemical and Physical Meteorology*, 72(1):1–19, Nov. 2020b. doi: 10.1080/16000889.2020.1823733.

L. Menut, B. Bessagnet, D. Khvorostyanov, M. Beekmann, N. Blond, A. Colette, I. Coll, G. Curci, G. Foret, A. Hodzic, S. Mailler, F. Meleux, J.-L. Monge, I. Pison, G. Siour, S. Turquety, M. Valari, R. Vautard, and M. G. Vivanco. CHIMERE 2013: a model for regional atmospheric composition modelling. *Geoscientific Model Development*, 6(4):981–1028, 2013. doi: 10.5194/gmd-6-981-2013. URL `https://www.geosci-model-dev.net/6/981/2013/`.

Lina Mercado, Nicolas Bellouin, Stephen Sitch, Olivier Boucher, Chris Huntingford, Martin Wild, and Peter Cox. Impact of changes in diffuse radiation on the global land carbon sink. *Nature*, 458:1014–7, May 2009. doi: 10.1038/nature07949.

Sara Mikaloff-Fletcher, Pieter Tans, Lori Bruhwiler, John Miller, Martin Heimann, and Mikaloff Fletcher. CH_4 sources estimated from atmospheric observations of CH_4 and its $^{13}C/^{12}C$ isotopic ratios: 1. Inverse modeling of source processes. *Global Biogeochemical Cycles - GLOBAL BIOGEOCHEM CYCLE*, 18, Dec. 2004. doi: 10.1029/2004GB002223.

John B. Miller and Pieter P. Tans. Calculating isotopic fractionation from atmospheric measurements at various scales. *Tellus B*, 55(2):207–214, 2003. doi: 10.1034/j.1600-0889.2003.00020.x. URL `https://onlinelibrary.wiley.com/doi/abs/10.1034/j.1600-0889.2003.00020.x`.

G. Monteil, S. Houweling, E. J. Dlugockenky, G. Maenhout, B. H. Vaughn, J. W. C. White, and T. Röckmann. Interpreting methane variations in the past two decades using measurements of CH_4 mixing ratio and isotopic composition. *Atmospheric Chemistry and Physics*, 11(17):9141–9153, 2011. doi: 10.5194/acp-11-9141-2011. URL `https://www.atmos-chem-phys.net/11/9141/2011/`.

S.A. Montzka, M.C. Krol, E. Dlugokencky, B. Hall, P. Jöckel, and J. Lelieveld. Small Interannual Variability of Global Atmospheric Hydroxyl. *Science (New York, N.Y.)*, 331:67–9, Jan. 2011. doi: 10.1126/science.1197640.

V. Naik, A. Voulgarakis, A. M. Fiore, L. W. Horowitz, J.-F. Lamarque, M. Lin, M. J. Prather, P. J. Young, D. Bergmann, P. J. Cameron-Smith, I. Cionni, W. J. Collins, S. B. Dalsøren, R. Doherty, V. Eyring, G. Faluvegi, G. A. Folberth, B. Josse, Y. H. Lee, I. A. MacKenzie, T. Nagashima, T. P. C. van Noije, D. A.

Plummer, M. Righi, S. T. Rumbold, R. Skeie, D. T. Shindell, D. S. Stevenson, S. Strode, K. Sudo, S. Szopa, and G. Zeng. Preindustrial to present-day changes in tropospheric hydroxyl radical and methane lifetime from the Atmospheric Chemistry and Climate Model Intercomparison Project (ACCMIP). *Atmospheric Chemistry and Physics*, 13(10):5277–5298, 2013. doi: 10.5194/acp-13-5277-2013. URL `https://acp.copernicus.org/articles/13/5277/2013/`.

Fumiko Nakagawa, Urumu Tsunogai, Daisuke Komatsu, Keita Yamada, Naohiro Yoshida, Jun Moriizumi, Koichiro Nagamine, Takao Iida, and Yukimasa Ikebe. Automobile exhaust as a source of ^{13}C- and D-enriched atmospheric methane in urban areas. *Organic Geochemistry*, 36:727–738, May 2005. doi: 10.1016/j.orggeochem.2005.01.003.

National Academies of Sciences, Engineering, and Medicine. *Improving Characterization of Anthropogenic Methane Emissions in the United States, 4 Addressing Uncertainties in Anthropogenic Methane Emissions*. The National Academies Press, Washington, DC, 2018. ISBN 978-0-309-47050-6. doi: 10.17226/24987. URL `https://www.ncbi.nlm.nih.gov/books/NBK519298/`.

E. G. Nisbet, E. J. Dlugokencky, M. R. Manning, D. Lowry, R. E. Fisher, J. L. France, S. E. Michel, J. B. Miller, J. W. C. White, B. Vaughn, P. Bousquet, J. A. Pyle, N. J. Warwick, M. Cain, R. Brownlow, G. Zazzeri, M. Lanoisellé, A. C. Manning, E. Gloor, D. E. J. Worthy, E.-G. Brunke, C. Labuschagne, E. W. Wolff, and A. L. Ganesan. Rising atmospheric methane: 2007–2014 growth and isotopic shift. *Global Biogeochemical Cycles*, 30(9):1356–1370, 2016. doi: 10.1002/2016GB005406. URL `https://agupubs.onlinelibrary.wiley.com/doi/abs/10.1002/2016GB005406`.

E. G. Nisbet, M. R. Manning, E. J. Dlugokencky, R. E. Fisher, D. Lowry, S. E. Michel, C. Lund Myhre, S. M. Platt, G. Allen, P. Bousquet, R. Brownlow, M. Cain, J. L. France, O. Hermansen, R. Hossaini, A. E. Jones, I. Levin, A. C. Manning, G. Myhre, J. A. Pyle, B. H. Vaughn, N. J. Warwick, and J. W. C. White. Very Strong Atmospheric Methane Growth in the 4 Years 2014–2017: Implications for the Paris Agreement. *Global Biogeochemical Cycles*, 33(3):318–342, 2019. doi: 10.1029/2018GB006009. URL `https://agupubs.onlinelibrary.wiley.com/doi/abs/10.1029/2018GB006009`.

Atsumu Ohmura, Andreas Bauder, Hans Müller, and Giovanni Kappenberger.

Long-term change of mass balance and the role of radiation. *Annals of Glaciology*, 46:367–374, Oct. 2007. doi: 10.3189/172756407782871297.

Diane Pataki, James Ehleringer, Lawrence Flanagan, Dan Yakir, David Bowling, Christopher Still, Nina Buchmann, Jed Kaplan, and Joseph Berry. The application and interpretation of Keeling plots in terrestrial carbon cycle research. *Global Biogeochemical Cycles*, 17, Mar. 2003. doi: 10.1029/2001GB001850.

P. Patra, Tazu Saeki, Edward Dlugokencky, Kentaro Ishijima, Taku Umezawa, Akihiko Ito, Shuji Aoki, Shinji Morimoto, Eric Kort, Andrew Crotwell, Ravi Kumar Kunchala, and Takakiyo Nakazawa. Regional Methane Emission Estimation Based on Observed Atmospheric Concentrations (2002-2012). *Journal of the Meteorological Society of Japan*, 94:91–113, Mar. 2016. doi: 10.2151/jmsj.2016-006.

O. Peltola, T. Vesala, Y. Gao, O. Räty, P. Alekseychik, M. Aurela, B. Chojnicki, A. R. Desai, A. J. Dolman, E. S. Euskirchen, T. Friborg, M. Göckede, M. Helbig, E. Humphreys, R. B. Jackson, G. Jocher, F. Joos, J. Klatt, S. H. Knox, N. Kowalska, L. Kutzbach, S. Lienert, A. Lohila, I. Mammarella, D. F. Nadeau, M. B. Nilsson, W. C. Oechel, M. Peichl, T. Pypker, W. Quinton, J. Rinne, T. Sachs, M. Samson, H. P. Schmid, O. Sonnentag, C. Wille, D. Zona, and T. Aalto. Monthly gridded data product of northern wetland methane emissions based on upscaling eddy covariance observations. *Earth System Science Data*, 11(3):1263–1289, 2019. doi: 10.5194/essd-11-1263-2019. URL `https://www.earth-syst-sci-data.net/11/1263/2019/`.

I. Pison, A. Berchet, M. Saunois, P. Bousquet, G. Broquet, S. Conil, M. Delmotte, A. Ganesan, O. Laurent, D. Martin, S. O'Doherty, M. Ramonet, T. G. Spain, A. Vermeulen, and C. Yver Kwok. How a European network may help with estimating methane emissions on the French national scale. *Atmospheric Chemistry and Physics*, 18(5):3779–3798, 2018. doi: 10.5194/acp-18-3779-2018. URL `https://www.atmos-chem-phys.net/18/3779/2018/`.

Michael J. Prather, Christopher D. Holmes, and Juno Hsu. Reactive greenhouse gas scenarios: Systematic exploration of uncertainties and the role of atmospheric chemistry. *Geophysical Research Letters*, 39(9), 2012. doi: 10.1029/2012GL051440. URL `https://agupubs.onlinelibrary.wiley.com/doi/abs/10.1029/2012GL051440`.

Paul Quay, Johnny Stutsman, David Wilbur, Amy Snover, Ed Dlugokencky, and Tom Brown. The isotopic composition of atmospheric methane. *Global Biogeochemical Cycles*, 13:445–461, Jun. 1999. doi: 10.1029/1998GB900006.

M. Remaud, F. Chevallier, A. Cozic, X. Lin, and P. Bousquet. On the impact of recent developments of the LMDz atmospheric general circulation model on the simulation of CO_2 transport. *Geoscientific Model Development*, 11(11):4489–4513, 2018. doi: 10.5194/gmd-11-4489-2018. URL `https://gmd.copernicus.org/articles/11/4489/2018/`.

M. Rigby, A. J. Manning, and R. G. Prinn. The value of high-frequency, high-precision methane isotopologue measurements for source and sink estimation. *Journal of Geophysical Research: Atmospheres*, 117(D12), 2012. doi: 10.1029/2011JD017384. URL `https://agupubs.onlinelibrary.wiley.com/doi/abs/10.1029/2011JD017384`.

B. Ringeval, Pierre Friedlingstein, Charles Koven, Philippe Ciais, Nathalie de NOBLET, B. Decharme, and P. Cadule. Climate-CH_4 feedback from wetlands and its interaction with the climate-CO_2 feedback. *Biogeosciences*, 8:2137–2157, Aug. 2011. doi: 10.5194/bg-8-2137-2011.

Bruno Ringeval, Nathalie de Noblet-Ducoudré, Philippe Ciais, Philippe Bousquet, Catherine Prigent, Fabrice Papa, and William B. Rossow. An attempt to quantify the impact of changes in wetland extent on methane emissions on the seasonal and interannual time scales. *Global Biogeochemical Cycles*, 24(2), 2010. doi: 10.1029/2008GB003354. URL `https://agupubs.onlinelibrary.wiley.com/doi/abs/10.1029/2008GB003354`.

Thomas Röckmann, Simon Eyer, Carina Veen, Elena Popa, Béla Tuzson, Guillaume Monteil, Sander Houweling, Eliza Harris, Dominik Brunner, Hubertus Fischer, G. Zazzeri, David Lowry, Euan Nisbet, W. Brand, Jaroslaw Necki, Lukas Emmenegger, and Joachim Mohn. In situ observations of the isotopic composition of methane at the Cabauw tall tower site. *Atmospheric Chemistry and Physics*, 16:10469–10487, Aug. 2016. doi: 10.5194/acp-16-10469-2016.

C. Sarrat, J. Noilhan, P. Lacarrère, V. Masson, E. Ceschia, P. Ciais, A. Dolman, J. Elbers, C. Gerbig, and N. Jarosz. CO_2 budgeting at the regional scale using a Lagrangian experimental strategy and meso-scale modeling. *Biogeosciences*, 6, Jan. 2009.

M. Saunois, P. Bousquet, B. Poulter, A. Peregon, P. Ciais, J. G. Canadell, E. J. Dlugokencky, G. Etiope, D. Bastviken, S. Houweling, G. Janssens-Maenhout, F. N. Tubiello, S. Castaldi, R. B. Jackson, M. Alexe, V. K. Arora, D. J. Beerling, P. Bergamaschi, D. R. Blake, G. Brailsford, V. Brovkin, L. Bruhwiler, C. Crevoisier, P. Crill, K. Covey, C. Curry, C. Frankenberg, N. Gedney, L. Höglund-Isaksson, M. Ishizawa, A. Ito, F. Joos, H.-S. Kim, T. Kleinen, P. Krummel, J.-F. Lamarque, R. Langenfelds, R. Locatelli, T. Machida, S. Maksyutov, K. C. McDonald, J. Marshall, J. R. Melton, I. Morino, V. Naik, S. O'Doherty, F.-J. W. Parmentier, P. K. Patra, C. Peng, S. Peng, G. P. Peters, I. Pison, C. Prigent, R. Prinn, M. Ramonet, W. J. Riley, M. Saito, M. Santini, R. Schroeder, I. J. Simpson, R. Spahni, P. Steele, A. Takizawa, B. F. Thornton, H. Tian, Y. Tohjima, N. Viovy, A. Voulgarakis, M. van Weele, G. R. van der Werf, R. Weiss, C. Wiedinmyer, D. J. Wilton, A. Wiltshire, D. Worthy, D. Wunch, X. Xu, Y. Yoshida, B. Zhang, Z. Zhang, and Q. Zhu. The global methane budget 2000–2012. *Earth System Science Data*, 8(2): 697–751, 2016a. doi: 10.5194/essd-8-697-2016. URL `https://www.earth-syst-sci-data.net/8/697/2016/`.

M. Saunois, R. B. Jackson, P. Bousquet, B. Poulter, and J. G. Canadell. The growing role of methane in anthropogenic climate change. *Environmental Research Letters*, 11(12):120207, Dec. 2016b. doi: 10.1088/1748-9326/11/12/120207. URL `https://doi.org/10.1088/1748-9326/11/12/120207`.

M. Saunois, P. Bousquet, B. Poulter, A. Peregon, P. Ciais, J. G. Canadell, E. J. Dlugokencky, G. Etiope, D. Bastviken, S. Houweling, G. Janssens-Maenhout, F. N. Tubiello, S. Castaldi, R. B. Jackson, M. Alexe, V. K. Arora, D. J. Beerling, P. Bergamaschi, D. R. Blake, G. Brailsford, L. Bruhwiler, C. Crevoisier, P. Crill, K. Covey, C. Frankenberg, N. Gedney, L. Höglund-Isaksson, M. Ishizawa, A. Ito, F. Joos, H.-S. Kim, T. Kleinen, P. Krummel, J.-F. Lamarque, R. Langenfelds, R. Locatelli, T. Machida, S. Maksyutov, J. R. Melton, I. Morino, V. Naik, S. O'Doherty, F.-J. W. Parmentier, P. K. Patra, C. Peng, S. Peng, G. P. Peters, I. Pison, R. Prinn, M. Ramonet, W. J. Riley, M. Saito, M. Santini, R. Schroeder, I. J. Simpson, R. Spahni, A. Takizawa, B. F. Thornton, H. Tian, Y. Tohjima, N. Viovy, A. Voulgarakis, R. Weiss, D. J. Wilton, A. Wiltshire, D. Worthy, D. Wunch, X. Xu, Y. Yoshida, B. Zhang, Z. Zhang, and Q. Zhu. Variability and quasi-decadal changes in the methane budget over the period 2000–2012. *Atmospheric Chemistry and*

Physics, 17(18):11135–11161, 2017. doi: 10.5194/acp-17-11135-2017. URL https://acp.copernicus.org/articles/17/11135/2017/.

M. Saunois, A. R. Stavert, B. Poulter, P. Bousquet, J. G. Canadell, R. B. Jackson, P. A. Raymond, E. J. Dlugokencky, S. Houweling, P. K. Patra, P. Ciais, V. K. Arora, D. Bastviken, P. Bergamaschi, D. R. Blake, G. Brailsford, L. Bruhwiler, K. M. Carlson, M. Carrol, S. Castaldi, N. Chandra, C. Crevoisier, P. M. Crill, K. Covey, C. L. Curry, G. Etiope, C. Frankenberg, N. Gedney, M. I. Hegglin, L. Höglund-Isaksson, G. Hugelius, M. Ishizawa, A. Ito, G. Janssens-Maenhout, K. M. Jensen, F. Joos, T. Kleinen, P. B. Krummel, R. L. Langenfelds, G. G. Laruelle, L. Liu, T. Machida, S. Maksyutov, K. C. McDonald, J. McNorton, P. A. Miller, J. R. Melton, I. Morino, J. Müller, F. Murguia-Flores, V. Naik, Y. Niwa, S. Noce, S. O'Doherty, R. J. Parker, C. Peng, S. Peng, G. P. Peters, C. Prigent, R. Prinn, M. Ramonet, P. Regnier, W. J. Riley, J. A. Rosentreter, A. Segers, I. J. Simpson, H. Shi, S. J. Smith, L. P. Steele, B. F. Thornton, H. Tian, Y. Tohjima, F. N. Tubiello, A. Tsuruta, N. Viovy, A. Voulgarakis, T. S. Weber, M. van Weele, G. R. van der Werf, R. F. Weiss, D. Worthy, D. Wunch, Y. Yin, Y. Yoshida, W. Zhang, Z. Zhang, Y. Zhao, B. Zheng, Q. Zhu, Q. Zhu, and Q. Zhuang. The Global Methane Budget 2000–2017. *Earth System Science Data*, 12(3):1561–1623, 2020. doi: 10.5194/essd-12-1561-2020. URL https://essd.copernicus.org/articles/12/1561/2020/.

Hinrich Schaefer. On the Causes and Consequences of Recent Trends in Atmospheric Methane. *Current Climate Change Reports*, Aug. 2019. doi: 10.1007/s40641-019-00140-z.

Hinrich Schaefer, Sara Mikaloff-Fletcher, Cordelia Veidt, Keith Lassey, Gordon Brailsford, Tony Bromley, Edward Dlugokencky, Sylvia Michel, John Miller, Iosif Levin, Dave Lowe, Ross Martin, Bruce Vaughn, and James White. A 21^{st} century shift from fossil-fuel to biogenic methane emissions indicated by $^{13}CH_4$. *Science*, 352, Mar. 2016. doi: 10.1126/science.aad2705.

A. Segers and S. Houweling. Description of the CH_4 Inversion Production Chain. *ECMWF COPERNICUS REPORT*, page 27, 2017. Copernicus Atmosphere Monitoring Service.

O. A. Sherwood, S. Schwietzke, V. A. Arling, and G. Etiope. Global Inventory of Gas Geochemistry Data from Fossil Fuel, Microbial and Burning Sources, version 2017. *Earth System Science Data*, 9(2):639–656, 2017.

doi: 10.5194/essd-9-639-2017. URL https://essd.copernicus.org/articles/9/639/2017/.

A. J. Simmons and D. M. Burridge. An energy and angular-momentum conserving vertical finite- difference scheme and hybrid vertical coordinates. *Monthly Weather Review*, 109:758–766, 1981. doi: 10.1175/1520-0493(1981)109<0758:AEAAMC>2.0.CO;2.

L.K. Smith, W.M. Lewis, J.P. Chanton, Greg Cronin, and Stephen K. Hamilton. Methane emissions from the Orinoco River floodplain, Venezuela. *Biogeochemistry*, 51:113–140, 2000. doi: https://doi.org/10.1023/A:1006443429909.

A. Stohl, C. Forster, A. Frank, P. Seibert, and G. Wotawa. Technical note: The Lagrangian particle dispersion model FLEXPART version 6.2. *Atmospheric Chemistry and Physics*, 5(9):2461–2474, 2005. doi: 10.5194/acp-5-2461-2005. URL https://acp.copernicus.org/articles/5/2461/2005/.

A. Stohl, B. Aamaas, M. Amann, L. H. Baker, N. Bellouin, T. K. Berntsen, O. Boucher, R. Cherian, W. Collins, N. Daskalakis, M. Dusinska, S. Eckhardt, J. S. Fuglestvedt, M. Harju, C. Heyes, Ø. Hodnebrog, J. Hao, U. Im, M. Kanakidou, Z. Klimont, K. Kupiainen, K. S. Law, M. T. Lund, R. Maas, C. R. MacIntosh, G. Myhre, S. Myriokefalitakis, D. Olivié, J. Quaas, B. Quennehen, J.-C. Raut, S. T. Rumbold, B. H. Samset, M. Schulz, Ø. Seland, K. P. Shine, R. B. Skeie, S. Wang, K. E. Yttri, and T. Zhu. Evaluating the climate and air quality impacts of short-lived pollutants. *Atmospheric Chemistry and Physics*, 15(18):10529–10566, 2015. doi: 10.5194/acp-15-10529-2015. URL https://www.atmos-chem-phys.net/15/10529/2015/.

Roland B. Stull. *An Introduction to Boundary Layer Meteorology*. Springer Netherlands, 1988. ISBN 978-90-277-2768-8. doi: 10.1007/978-94-009-3027-8.

Atsuko Sugimoto and Noboru Fujita. Hydrogen Concentration and Stable Isotopic Composition of Methane in Bubble Gas Observed in a Natural Wetland. *Biogeochemistry*, 81:33–44, Oct. 2006. doi: 10.1007/s10533-006-9028-4.

Ingrid Super, Stijn Dellaert, A.J.H. Visschedijk, and Hugo Gon. Uncertainty analysis of a European high-resolution emission inventory of CO_2 and CO to support inverse modelling and network design. *Atmospheric Chemistry and Physics*, Sep. 2019. doi: 10.5194/acp-2019-696.

Barbara Szénási and Philippe Bousquet. Forward modelling simulations of CH_4 and isotopologues. MEMO^2 Deliverable 3.3, Sep.

2019. https://h2020-memo2.eu/wp-content/uploads/sites/198/2019/09/Deliverable_D3_3_final_version-SW.pdf.

J. Tang, Q. Zhuang, R. D. Shannon, and J. R. White. Quantifying wetland methane emissions with process-based models of different complexities. *Biogeosciences*, 7(11):3817–3837, 2010. doi: 10.5194/bg-7-3817-2010. URL https://bg.copernicus.org/articles/7/3817/2010/.

Albert Tarantola. *Inverse Problem Theory and Methods for Model Parameter Estimation*. Society for Industrial and Applied Mathematics, Philadelphia, PA, 2005.

J. Thanwerdas, M. Saunois, A. Berchet, I. Pison, D. Hauglustaine, M. Ramonet, C. Crevoisier, B. Baier, C. Sweeney, and P. Bousquet. Impact of atomic chlorine on the modelling of total methane and its $^{13}c:^{12}c$ isotopic ratio at global scale. *Atmospheric Chemistry and Physics Discussions*, 2019: 1–28, 2019. doi: 10.5194/acp-2019-925. URL https://www.atmos-chem-phys-discuss.net/acp-2019-925/.

Joël Thanwerdas, Marielle Saunois, Antoine Berchet, Isabelle Pison, and Philippe Bousquet. Design of a new 3-D variational inverse modelling system to assimilate δ^{13}C-CH_4 isotopic signal along with CH_4 observations. Personal communications in October 2020, In preparation.

Thomas Thielemann, Bernhard Cramer, and Axel Schippers. Coalbed methane in the Ruhr Basin, Germany: A renewable energy resource? *Organic Geochemistry*, 35:1537–1549, Nov. 2004. doi: 10.1016/j.orggeochem.2004.05.004.

R. L. Thompson, A. Stohl, L. X. Zhou, E. Dlugokencky, Y. Fukuyama, Y. Tohjima, S.-Y. Kim, H. Lee, E. G. Nisbet, R. E. Fisher, D. Lowry, R. F. Weiss, R. G. Prinn, S. O'Doherty, D. Young, and J. W. C. White. Methane emissions in East Asia for 2000–2011 estimated using an atmospheric Bayesian inversion. *Journal of Geophysical Research: Atmospheres*, 120(9):4352–4369, 2015. doi: 10.1002/2014JD022394. URL https://agupubs.onlinelibrary.wiley.com/doi/abs/10.1002/2014JD022394.

R. L. Thompson, M. Sasakawa, T. Machida, T. Aalto, D. Worthy, J. V. Lavric, C. Lund Myhre, and A. Stohl. Methane fluxes in the high northern latitudes for 2005–2013 estimated using a Bayesian atmospheric inversion. *Atmospheric Chemistry and Physics*, 17(5):3553–3572, 2017. doi: 10.5194/acp-17-3553-2017. URL `https://www.atmos-chem-phys.net/17/3553/2017/`.

T. Thonat, M. Saunois, I. Pison, A. Berchet, T. Hocking, B. F. Thornton, P. M. Crill, and P. Bousquet. Assessment of the theoretical limit in instrumental detectability of northern high-latitude methane sources using $\delta^{13}c_{\mathrm{CH4}}$ atmospheric signals. *Atmospheric Chemistry and Physics*, 19(19):12141–12161, 2019. doi: 10.5194/acp-19-12141-2019. URL `https://acp.copernicus.org/articles/19/12141/2019/`.

Renske M. A. Timmermans, Martijn Schaap, Peter Builtjes, Hendrik Elbern, Richard Siddans, Stephen Tjemkes, and Robert Vautard. An Observing System Simulation Experiment (OSSE) for Aerosol Optical Depth from Satellites. *Journal of Atmospheric and Oceanic Technology*, 26(12):2673–2682, Dec. 2009. ISSN 0739-0572. doi: 10.1175/2009JTECHA1263.1. URL `https://doi.org/10.1175/2009JTECHA1263.1`.

Amy Townsend-Small, E. Claire Botner, Kristine L. Jimenez, Jason R. Schroeder, Nicola J. Blake, Simone Meinardi, Donald R. Blake, Barkley C. Sive, Daniel Bon, James H. Crawford, Gabriele Pfister, and Frank M. Flocke. Using stable isotopes of hydrogen to quantify biogenic and thermogenic atmospheric methane sources: A case study from the colorado front range. *Geophysical Research Letters*, 43(21):11,462–11,471, 2016. doi: 10.1002/2016GL071438. URL `https://agupubs.onlinelibrary.wiley.com/doi/abs/10.1002/2016GL071438`.

I. Troen and L. Mahrt. A simple model of the atmospheric boundary layer; sensitivity to surface evaporation. *Boundary-Layer Meteorology*, 37:129–148, 1986.

A. Tsuruta, T. Aalto, L. Backman, J. Hakkarainen, I. T. van der Laan-Luijkx, M. C. Krol, R. Spahni, S. Houweling, M. Laine, E. Dlugokencky, A. J. Gomez-Pelaez, M. van der Schoot, R. Langenfelds, R. Ellul, J. Arduini, F. Apadula, C. Gerbig, D. G. Feist, R. Kivi, Y. Yoshida, and W. Peters. Global methane emission estimates for 2000–2012 from CarbonTracker Europe-CH_4 v1.0. *Geoscientific Model Development*, 10(3):1261–1289, 2017. doi: 10.5194/gmd-10-1261-2017. URL `https://www.geosci-model-dev.net/10/1261/2017/`.

Aki Tsuruta, Tuula Aalto, Leif Backman, Maarten C. Krol, Wouter Peters, Sebastian Lienert, Fortunat Joos, Paul A. Miller, Wenxin Zhang, Tuomas

Laurila, Juha Hatakka, Ari Leskinen, Kari E. J. Lehtinen, Olli Peltola, Timo Vesala, Janne Levula, Ed Dlugokencky, Martin Heimann, Elena Kozlova, Mika Aurela, Annalea Lohila, Mari Kauhaniemi, and Angel J. Gomez-Pelaez. Methane budget estimates in Finland from the CarbonTracker Europe-CH_4 data assimilation system. *Tellus B: Chemical and Physical Meteorology*, 71(1):1565030, 2019. doi: 10.1080/16000889.2018.1565030. URL https://doi.org/10.1080/16000889.2018.1565030.

S. C. Tyler, R. S. Bilek, R. L. Sass, and F. M. Fisher. Methane oxidation and pathways of production in a Texas paddy field deduced from measurements of flux, $\delta^{13}C$, and δD of CH_4. *Global Biogeochemical Cycles*, 11(3):323–348, 1997. doi: 10.1029/97GB01624. URL https://agupubs.onlinelibrary.wiley.com/doi/abs/10.1029/97GB01624.

Stanley C. Tyler, Donald R. Blake, and F. Sherwood Rowland. $^{13}C/^{12}C$ ratio in methane from the flooded Amazon forest. *Journal of Geophysical Research: Atmospheres*, 92(D1):1044–1048, 1987. doi: 10.1029/JD092iD01p01044. URL https://agupubs.onlinelibrary.wiley.com/doi/abs/10.1029/JD092iD01p01044.

Stanley C. Tyler, Henry O. Ajie, Mohan L. Gupta, Ralph J. Cicerone, Donald R. Blake, and Edward J. Dlugokencky. Stable carbon isotopic composition of atmospheric methane: A comparison of surface level and free tropospheric air. *Journal of Geophysical Research*, 104:13895–13910, 1999.

T. Umezawa, C. A. M. Brenninkmeijer, T. Röckmann, C. van der Veen, S. C. Tyler, R. Fujita, S. Morimoto, S. Aoki, T. Sowers, J. Schmitt, M. Bock, J. Beck, H. Fischer, S. E. Michel, B. H. Vaughn, J. B. Miller, J. W. C. White, G. Brailsford, H. Schaefer, P. Sperlich, W. A. Brand, M. Rothe, T. Blunier, D. Lowry, R. E. Fisher, E. G. Nisbet, A. L. Rice, P. Bergamaschi, C. Veidt, and I. Levin. Interlaboratory comparison of $\delta^{13}C$ and δD measurements of atmospheric CH_4 for combined use of data sets from different laboratories. *Atmospheric Measurement Techniques*, 11(2):1207–1231, 2018. doi: 10.5194/amt-11-1207-2018. URL https://www.atmos-meas-tech.net/11/1207/2018/.

M. Uzaki, H. Mizutani, and E. Wada. Carbon isotope composition of CH_4 from rice paddies in Japan. *Biogeochemistry*, 13:159–175, Apr. 1991. doi: https://doi.org/10.1007/BF00002775.

D. J. Varon, J. McKeever, D. Jervis, J. D. Maasakkers, S. Pandey, S. Houweling, I. Aben, T. Scarpelli, and D. J. Jacob. Satellite Discovery of Anomalously

Large Methane Point Sources From Oil/Gas Production. *Geophysical Research Letters*, 46(22):13507–13516, 2019. doi: 10.1029/2019GL083798. URL https://agupubs.onlinelibrary.wiley.com/doi/abs/10.1029/2019GL083798.

Fenjuan Wang, Shamil Maksyutov, Aki Tsuruta, Rajesh Janardanan, Akihiko Ito, Motoki Sasakawa, Toshinobu Machida, Isamu Morino, Yukio Yoshida, Johannes W. Kaiser, Greet Janssens-Maenhout, Edward J. Dlugokencky, Ivan Mammarella, Jost Valentin Lavric, and Tsuneo Matsunaga. Methane Emission Estimates by the Global High-Resolution Inverse Model Using National Inventories. *Remote Sensing*, 11(21), 2019. ISSN 2072-4292. doi: 10.3390/rs11212489. URL https://www.mdpi.com/2072-4292/11/21/2489.

Yilong Wang, Grégoire Broquet, Philippe Ciais, Frédéric Chevallier, Felix Vogel, Nikolay Kadygrov, Lin Wu, Yi Yin, Rong Wang, and Shu Tao. Estimation of observation errors for large-scale atmospheric inversion of CO_2 emissions from fossil fuel combustion. *Tellus B: Chemical and Physical Meteorology*, 69(1):1325723, 2017. doi: 10.1080/16000889.2017.1325723. URL https://doi.org/10.1080/16000889.2017.1325723.

N. J. Warwick, M. L. Cain, R. Fisher, J. L. France, D. Lowry, S. E. Michel, E. G. Nisbet, B. H. Vaughn, J. W. C. White, and J. A. Pyle. Using δ^{13}C-CH_4 and δD-CH_4 to constrain Arctic methane emissions. *Atmospheric Chemistry and Physics*, 16(23):14891–14908, 2016. doi: 10.5194/acp-16-14891-2016. URL https://acp.copernicus.org/articles/16/14891/2016/.

P. Werle, R. Mücke, and F. Slemr. The Limits of Signal Averaging in Atmospheric Trace-Gas Monitoring by Tunable Diode-Laser Absorption Spectroscopy (TDLAS). *Applied Physics B*, 57:131–139, 1993. doi: 10.1007/BF00425997.

Roland A. Werner and Willi A. Brand. Referencing strategies and techniques in stable isotope ratio analysis. *Rapid Communications in Mass Spectrometry*, 15(7):501–519, 2001. doi: 10.1002/rcm.258. URL https://onlinelibrary.wiley.com/doi/abs/10.1002/rcm.258.

Michael J. Whiticar. Carbon and hydrogen isotope systematics of bacterial formation and oxidation of methane. *Chemical Geology*, 161(1-3):291–314, Sep. 1999. doi: 10.1016/S0009-2541(99)00092-3.

Martin Wild, Doris Folini, Christoph Schär, Norman Loeb, Ellsworth Dutton, and Gert König-Langlo. The global energy balance from a surface perspective. *Climate Dynamics*, 40, Nov. 2012. doi: 10.1007/s00382-012-1569-8.

WMO. 19th WMO/IAEA Meeting on Carbon Dioxide, Other Greenhouse Gases, and Related Measurement Techniques (GGMT-2017) 27–31 August 2017, Dübendorf, Switzerland, Technical publications GAW Report No. 242, 2018. World Meteorological Organization, Geneva, Switzerland.

D. Wunch, D. B. A. Jones, G. C. Toon, N. M. Deutscher, F. Hase, J. Notholt, R. Sussmann, T. Warneke, J. Kuenen, H. Denier van der Gon, J. A. Fisher, and J. D. Maasakkers. Emissions of methane in Europe inferred by total column measurements. *Atmospheric Chemistry and Physics*, 19(6):3963–3980, 2019. doi: 10.5194/acp-19-3963-2019. URL `https://www.atmos-chem-phys.net/19/3963/2019/`.

G. Zazzeri, David Lowry, R.E. Fisher, J. France, Mathias Lanoisellé, and E.G. Nisbet. Plume mapping and isotopic characterisation of anthropogenic methane sources. *Atmospheric Environment*, 110, Jun. 2015. doi: 10.1016/j.atmosenv.2015.03.029.

G. Zazzeri, David Lowry, Rebecca Fisher, J. France, Mathias Lanoisellé, Bryce Kelly, Jaroslaw Necki, Charlotte Iverach, Elisa Ginty, Miroslaw Zimnoch, Alina Jasek-Kamińska, and Euan Nisbet. Carbon isotopic signature of coal-derived methane emissions to the atmosphere: From coalification to alteration. *Atmospheric Chemistry and Physics*, 16:13669–13680, Nov. 2016. doi: 10.5194/acp-16-13669-2016.

G. Zazzeri, David Lowry, R. E. Fisher, J. France, Mathias Lanoisellé, Christine Grimmond, and E. G. Nisbet. Evaluating methane inventories by isotopic analysis in the London region. *Scientific Reports*, 7, Jul. 2017. doi: 10.1038/s41598-017-04802-6.

Junfeng (Jim) Zhang, Yongjie Wei, and Zhangfu Fang. Ozone Pollution: A Major Health Hazard Worldwide. *Frontiers in Immunology*, 10:2518, 2019. ISSN 1664-3224. doi: 10.3389/fimmu.2019.02518. URL `https://www.frontiersin.org/article/10.3389/fimmu.2019.02518`.

Y. Zhao, M. Saunois, P. Bousquet, X. Lin, A. Berchet, M. I. Hegglin, J. G. Canadell, R. B. Jackson, D. A. Hauglustaine, S. Szopa, A. R. Stavert, N. L.

Abraham, A. T. Archibald, S. Bekki, M. Deushi, P. Jöckel, B. Josse, D. Kinnison, O. Kirner, V. Marécal, F. M. O'Connor, D. A. Plummer, L. E. Revell, E. Rozanov, A. Stenke, S. Strode, S. Tilmes, E. J. Dlugokencky, and B. Zheng. Inter-model comparison of global hydroxyl radical (OH) distributions and their impact on atmospheric methane over the 2000-2016 period. *Atmospheric Chemistry and Physics*, 19(21):13701–13723, 2019. doi: 10.5194/acp-19-13701-2019. URL `https://acp.copernicus.org/articles/19/13701/2019/`.

T. Zheng, N. H. F. French, and M. Baxter. Development of the WRF-CO2 4D-Var assimilation system v1.0. *Geoscientific Model Development*, 11(5):1725–1752, 2018. doi: 10.5194/gmd-11-1725-2018. URL `https://gmd.copernicus.org/articles/11/1725/2018/`.

ÉCOLE DOCTORALE
Sciences de
l'Environnement
d'Île-de-France (SEIF)

Titre: Surveillance atmosphérique des émissions de méthane en Europe

Mots clés: méthane, gaz à effet de serre, émission, Europe, isotope

Résumé: Les concentrations atmosphériques de gaz à effet de serre ont rapidement augmenté depuis la révolution industrielle, principalement en raison des activités anthropiques. Les études menées au cours des dernières décennies ont principalement porté sur le dioxyde de carbone (CO_2), qui est le principal responsable de la croissance du forçage radiatif mondial. Récemment, le méthane (CH_4), deuxième contributeur le plus important, a fait l'objet d'une attention scientifique croissante car il présente un important potentiel d'atténuation. En raison de sa durée de vie relativement courte (8 à 10 ans), les efforts d'atténuation peuvent être efficaces dans des délais relativement courts. Toutefois, les estimations actuelles des émissions de CH_4 à l'échelle mondiale et régionale sont très incertaines. Cette thèse vise à améliorer notre compréhension des émissions de CH_4 à l'échelle européenne en abordant les différentes sources d'incertitudes. Cette thèse présente le potentiel de réduction de l'incertitude des émissions par des inversions atmosphériques descendantes des émissions de méthane. Les émissions estimées par des approches descendantes dépendent de la performance des modèles de chimie-transport (MCT) et de la précision des mesures. Le potentiel des approches descendantes dans notre cadre des émissions de CH_4 en Europe est exploré par trois études, chacune se concentrant sur différentes sources d'incertitudes qui doivent être spécifiées dans les inversions atmosphériques. Dans la première étude, nous nous concentrons sur les performances de la MCT choisie en évaluant les erreurs dans la modélisation des transports et les émissions utilisées comme intrants dans la MCT. La deuxième étude cible d'autres causes possibles d'inadéquation entre les concentrations atmosphériques de CH_4 mesurées et simulées, ainsi que les rapports isotopiques atmosphériques de δ^{13}C et δ^{2}H. Entre autres, nous analysons si les inadéquations peuvent être associées aux signatures isotopiques des sources ou aux émissions utilisées ensemble comme données d'entrée dans le modèle de transport. Ces travaux démontrent que les informations obtenues à partir de mesures isotopiques, en plus des mesures des concentrations de CH_4, peuvent être utiles pour évaluer les inventaires d'émissions et estimer les émissions par inversion atmosphérique. Le potentiel des mesures de δ^{13}C et δ^{2}H dans les inversions atmosphériques est étudié en déterminant la précision de l'instrument nécessaire pour détecter les signaux de δ^{13}C et δ^{2}H provenant de diverses sources de CH_4. Cette précision est examinée à l'emplacement des sites de surveillance du réseau du système intégré d'observation du carbone (ICOS). Nos résultats indiquent des exigences de haute précision pour les instruments de mesure de δ^{13}C et δ^{2}H. Cependant, ils révèlent que les informations isotopiques, en plus des concentrations, pourraient améliorer la discrimination des sources de CH_4 lorsqu'elles sont mises en œuvre dans les inversions atmosphériques des émissions de CH_4. Les travaux de cette thèse offrent des aperçus sur la manière dont les cadres d'inversion pourraient être configurés et sur les éléments essentiels pour estimer de manière fiable les émissions de CH_4 à l'échelle européenne.

Title: Atmospheric monitoring of methane emissions at the European scale

Keywords: methane, greenhouse gas, emission, Europe, isotopologue

Abstract: Atmospheric mixing ratios of greenhouse gases have rapidly increased since the industrial revolution, mainly due to anthropogenic activities. Studies in the past decades have primarily targeted carbon dioxide (CO_2), being the largest contributor to the global radiative forcing growth. Recently, the second largest contributor, methane (CH_4), has received increasing scientific attention as it has a large mitigation potential. Due to its relatively short lifetime of 8-10 years, mitigation efforts can be effective within relatively short time ranges. However, current estimates of CH_4 emissions at both the global and regional scales are highly uncertain. This thesis aims at improving our understanding of CH_4 emissions at the European scale by addressing various sources of uncertainties.

This thesis presents the potential of emission uncertainty reduction by top-down atmospheric inversions of methane emissions. Emissions estimated by top-down approaches depend on the performance of chemistry-transport models (CTMs) and the precision of measurements. The potential of top-down approaches in our framework of CH_4 emissions in Europe is explored by three studies, each focusing on different sources of uncertainties that must be specified in atmospheric inversions. In the first study, we focus on the performance of the chosen CTM by assessing errors in transport modelling and emissions used as input in the CTM. The second study targets other possible causes for misfits between measured and simulated atmospheric CH_4 mixing ratios, as well as isotopic ratios $\delta^{13}C$ and $\delta^{2}H$. Among others, we analyse whether misfits can be associated with isotopic source signatures or emissions used together as input in the transport model. This work demonstrates that information gained from isotopic measurements, in addition to measurements of CH_4 mixing ratios, can be valuable for evaluating emission inventories and estimating emissions by atmospheric inversions.

The potential of $\delta^{13}C$ and $\delta^{2}H$ measurements in atmospheric inversions is investigated by determining the instrument precision needed to detect signals of $\delta^{13}C$ and $\delta^{2}H$ from various CH_4 sources. This is examined at the location of monitoring sites in the Integrated Carbon Observation System (ICOS) network. Our results indicate high precision requirements on instruments measuring $\delta^{13}C$ and $\delta^{2}H$. However, they reveal that isotopic information, on top of mixing ratios, could improve discrimination of CH_4 sources when implemented in atmospheric inversions of CH_4 emissions. The work in this thesis offers insights into how inversion frameworks could be configured and what are the essentials to reliably estimate CH_4 emissions at the European scale.

Maison du doctorat de l’Université Paris-Saclay
2ème étage aile ouest, Ecole normale supérieure Paris-Saclay
4 avenue des Sciences,
91190 Gif sur Yvette, France